# Properties of magnetotelluric transfer functions - with a case study from the Gaxun-Nur basin, NW-China

vorgelegt von
Diplom-Geowissenschaftler (Angewandte Geophysik)
**Michael Becken**
aus Landsberg am Lech

von der Fakultät VI
der Technischen Universität Berlin
zur Erlangung des akademischen Grades

Doktor der Naturwissenschaften
-Dr. rer. nat.-

genehmigte Dissertation

Promotionsausschuss:

Vorsitzender: Prof. W. Dominik
Berichter: Prof. H. Burkhardt
Berichter: Prof. L. B. Pedersen

Tag der wissenschaftlichen Aussprache: 1. Juli 2005

Berlin 2005
D83

# Zusammenfassung

Die Eigenschaften der elektromagnetischen Moden und des magnetotellurischen (MT) Impedanztensors werden im Rahmen von bei der Interpretation magnetotellurischer Daten auftretender Fragestellungen systematisch untersucht, und die methodischen Ergebnisse bei der Auswertung von Felddaten benutzt.

Unter Verwendung räumlicher Beziehungen aus der Elektrodynamik können für beliebige Leitfähigkeitsverteilungen nach Moden getrennte Übertragungsfunktionen abgeleitet werden, die dann ausschließlich Felder in der tangential-elektrischen (TE) oder tangential-magnetischen Mode (TM) enthalten. Obwohl räumliche Beziehungen auf praktische Felddaten aufgrund der unzureichenden flächenhaften Überdeckung nicht angewandt werden können, erweisen sich die abgeleiteten Beziehungen als nützlich zur Charakterisierung der Beiträge der einzelnen Moden zu aus Messdaten bestimmbaren Übertragungsfunktion. So sind die für anomale TE und TM Felder ursächlichen Leitfähigkeitsanomalien bei gleicher Periode unter Umständen nicht identisch, was im Falle von 3D Strukturen aufgrund der Überlagerungen beider Moden in jedem Element des Impedanztensors zu einem nicht zerlegbaren Gemisch verschiedener Effekte führt. Bei dem Versuch, MT Daten mit 3D Effekten durch ein zweidimensionales Modell zu erklären, werden insbesondere TM Anteile in der angenommenen E-Polarisation (reine TE Mode) und TE Anteile in der angenommenen B-Polarisation (reine TM Mode) angepasst, was dem physikalischen Hintergrund nicht Rechnung trägt und daher zu fehlerhaften Modellen führen muss. Vor diesem Hintergrund erscheint es vor allem sinnvoll, vertikale magnetische Übertragungsfunktionen (reine TE Mode) zu berücksichtigen sowie vertikale elektrische Übertragungsfunktionen (reine TM Mode), die in der Praxis allerdings nicht direkt aus Messdaten bestimmt werden können.

Sogenannte galvanische Verzerrung kann als Grenzfall betrachtet werden, indem an klein-räumigen Anomalien nur anomale TM Felder entstehen, und induktive Effekte vernachlässigt werden können. Das verzerrende elektrische Feld oszilliert dann mit gleicher Phase wie das regionale elektrische Feld, und ändert daher die Phasenlage des elektrischen Feldes nicht. Zur Beschreibung des Verzerrungseffektes empfiehlt sich daher die Betrachtung der Polarisations-zustände des elektromagnetischen Feldes und deren Entsprechung im Impedanztensor. Dieser Ansatz führt auf eine elliptische Parametrisierung der Spalten des Tensors. Die Existenz einer regionalen 2D Struktur kann bei geeigneter Drehung des Tensors in Richtung der Hauptachsen der Struktur aus verschwindenden Elliptizitäten behauptet werden. Die Orientierung der Ellipsen gibt dann die Verzerrungswinkel, d.h. die Richtung des linear polarisierten elektrischen Feldes in Bezug auf die Hauptachsen, an. Da sich alle Ellipsenparameter analytisch aus dem Tensor bestimmen lassen, ist die Implementierung eines Optimierungsalgorithmus zur Bestimmung des Koordinatensystems, das durch minimale Elliptizitäten gekennzeichnet ist, auch unter gleichzeitiger Berücksichtigung vieler Stationen und Frequenzen leicht und äußerst effektiv.

Breitbandige MT Daten, die während eines MT Experiments im Gaxun-Nur Becken in NW-China gemessen wurden, wurden einer solchen Elliptizitätsanalyse zur Bestimmung der Dimensionalität

des Untergrundes, der Streichrichtung zweidimensionaler Strukturen und der Identifikation galvanischer Verzerrung unterworfen. 1D und 2D Inversionrechnungen konnten nur für den kurzperiodischen Anteil durchgeführt werden. Bei längeren Perioden treten 3D Effekte auf, die zumindest für die magnetischen Übertragungsfunktionen mit 3D Modellrechnungen simuliert werden können. Aus den Leitfähigkeitsmodellen kann im Zusammenhang mit geologischen Geländeuntersuchungen und Satellitenbildinterpretationen eine geologisches Modell abgeleitet werden, das sich in den regionalen geologischen Kontext widerspruchsfrei einfügt. Aufgrund der Ergebnisse wird die Anlage zumindest von Teilen des heutigen Gaxun-Nur Beckens in das mittlere Mesozoikum gestellt, aus dem großräumige Krustenextension in Zentralasien bekannt ist, und auch im Untersuchungsgebiet zur Entwicklung tektonischer Gräben geführt hat. Eine spätere Reaktivierung mesozoischer Störungssysteme sowie dazu synthetisch angelegte Sekundärstörungen definieren im Känozoikum den südöstlichen Beckenrandbereich. Diese ebenfalls extensionellen Bewegungen scheinen bis heute aktiv zu sein, und haben wesentlichen Einfluss auf rezente Sedimentation und die hydrogeologische Situation im Untersuchungsgebiet.

# Summary

The properties of the electromagnetic modes and the magnetotelluric (MT) impedance tensor are systematically investigated in the course of MT data interpretation and the results are used for the analysis of actual field data.

Using spatial relations of electrodynamic theory, response functions separated into tangential-electric (TE) and tangential-magnetic modes (TM) are constructed for arbitrary conductivity models. Though the theory is at present only applicable in synthetic model studies due to insufficient spatial coverage of MT sites in practical measurements, it serves to a deeper understanding of MT transfer functions. The results of a synthetic model study prohibit a 2D inversion of impedance data which are not strictly 2D, since the modes, carrying information about structures at different depth, may in general not be separated by rotation or tensor decomposition, and TE- and TM-mode fields are attempted to be fitted in B-Polarization (pure TM-mode) and E-Polarization (pure TE-mode), respectively. In contrast, the purely TE-mode vertical magnetic transfer function is free of TM-mode distortion, and therefore more reliable in terms of 2D inversion. The purely TM-mode vertical electric transfer function would be a suitable measure of TM-mode fields, but it can not be determined in practice.

A limiting case of distorting TM-mode fields arising from shallow anomalies is commonly described in terms of galvanic distortion. Based upon the polarization states of principal electric and magnetic fields in presence of a regional 2D structure, a novel ellipse parameterization of the MT impedance tensor is developed, which reduces to the standard galvanic distortion model if applicable. The presence of a regional 2D structure is judged from vanishing ellipticities of the telluric vectors representing the polarization state of the principal electric field, and the presence of galvanic distortion is inferred from the orientation of ellipses representing the telluric vectors. Based upon the ellipse parameterization, multi-site multi-period strike and dimensionality analysis is easily implemented and proved to be stable even when using noisy data.

During a MT field experiment in the Gaxun-Nur basin in NW-China, performed in conjunction with geological field investigations and satellite remote sensing data interpretation, broad-band MT-data were collected at 36 sites. Impedance data were subjected to dimensionality, distortion and strike analysis using the novel ellipticity analysis and to 1D and 2D inversion where adequate. 3D modeling could explain 3D effects of vertical magnetic transfer functions at intermediate periods, but fails to fit impedance data in the same period range. The final conductivity models of the upper crust suggest, that the Gaxun-Nur basin occupies a Mesozoic extensional region, where tectonic basins have evolved and Mesozoic sediments are trapped in structures more than $1300\,\mathrm{m}$ deep. This scenario fits into a regional extensional event reported from other regions of central Asia. Cenozoic extension and related deformation is aligned along reactivated $SW-NE-$trending Mesozoic fault zones or along synthetically arranged $N-S-$ trending faults. The latter appear to be active in the southeastern part of the Gaxun-Nur basin, and influence present sedimentation and the hydrogeological situation.

# Contents

# 1. Introduction

Structural information about the subsurface may be obtained from Magnetotelluric (MT) data, if structures are differentiable in their electrical conductivity. The MT method, which uses natural electromagnetic waves as energy source, allows for a remote sensing of the underground for a great range of depths, depending on the frequency of the time-varying inducing electromagnetic field. The physical process behind the MT-Method is described by Maxwell's laws in the quasi-static approximation, where displacement currents are neglected. The propagation of the electromagnetic field in the conducting earth may then be considered as a diffusive energy transport, which rapidly is attenuated due to electromagnetic induction within the conductor (Skin-effect). Such energy diffusion is a dispersive process, and signals of low frequencies can effectively penetrate the earth much deeper than faster oscillating signals (high frequencies). The frequency range spanned by natural sources of different types, which is exploited in the scope of MT experiments, lies within $10^3 - 10^{-4}\,\mathrm{Hz}$. Man-made signals are used to broaden the frequency range to even higher frequencies up to $10^5\,\mathrm{Hz}$ (in the VLF and RMT method). Signals of higher frequencies than $10^5\,\mathrm{Hz}$ are not used for MT measurements, since displacement currents may no longer be neglected, and the propagation of electromagnetic fields has to be treated as wave propagation instead of a diffusive process.

The total current density and henceforth the total electric and magnetic fields within and above the conducting earth are functions of the extrinsic source fields, the conductivity distribution, and the point of observation with respect to the source and the geoelectric structure. Fortunately, the source field may be formally treated as a vertically incident plane wave (Schmucker and Weidelt, 1975), permitting the determination of transfer functions, which are independent of the geometry and polarization of the source field (Berdichevsky and Zhdanov, 1984).

MT Transfer functions are determined from measured magnetotelluric variational fields. These transfer functions are only a function of the conductivity distribution and the frequency. Important steps in MT interpretation comprise the analysis of transfer functions with respect to the principal polarization states of fields, and subsequent modeling and inversion of data to obtain conductivity models producing equal transfer functions as being measured. The conductivity model is then supposed to represent true geoelectric structures, at least to some extent, since spatial resolution of MT data is limited due to the diffusive nature of energy transport. Moreover, in practice only a limited number of measurement points is available with noisy transfer functions estimated in a limited period range. Therefore, in the scope of inverse calculations constraints have to be put on the model to remove the indeterminacy resulting from insufficient data and physical limitations with respect to structural resolution.

Once a geoelectric model has been accepted and its uncertainties identified, it has to be converted to a geological model or to be considered as a constraint on a geological model, e.g. with respect to groundwater questions (upper crust), to the lithology of sediments and basement rocks (upper to lower crust) including of natural resource exploration, to the existence of partial melts (middle to lower crust) and to the depth of the asthenosphere. Numerous more examples could be given here.

In the present work, I treat a number of methodological and practical questions, which arose during MT transfer function analysis and interpretation. Fundamental to the MT work is the mode decomposition, which in conjunction with spatial field relations suggests a systematic investigation of spatial relations of transfer functions. After a brief introduction to the basic theory of electromagnetic modes and to MT transfer functions in Chapter 2, I summarize these spatial relations in Chapter 3. This work was initiated by the "Transformation of VLF-anomaly maps into apparent resistivities and phases" (Becken and Pedersen, 2003), where we used purely TE-mode magnetic transfer functions and converted them into corresponding electric fields and finally into apparent resistivity maps. The transformation demonstrates the capability of utilizing spatial relations in order to represent data in a different way, which might be easier to understand. The data, which we (Becken and Pedersen) used, were in some respect extraordinary compared to common MT data, since a very good spatial coverage was obtained using an airborne VLF measurement system, and spatial relations were most easily programmed in wavenumber domain.

The major goal beyond the relations and examples given in Chapter 3 is the separation of TE- and TM-mode constitutes (Tangential-Electric and Tangential-Magnetic with respect to the surface $z = 0$) of the measured electromagnetic field respectively of MT transfer functions. (Here, the modes are referred to as the actual modes of the electromagnetic field, as they are obtained from toroidal and poloidal field components derived from scalar Debye potentials (cf. for example Weidelt, 1975). Most MT practitioners use the modes to describe E- and B-Polarization, which can lead to confusion about terms.) Once the goal of mode separation would have been achieved, the very different characteristics of the two modes could be taken much better into account than using mixed-mode transfer functions as is common practice in case of the MT impedance tensor. Mode separation promises therefore a better understanding of data, and in its consequence, simplified model construction and verification. However, no MT data set is currently available with the spatial coverage required for such a mode separation, and therefore, no application to field data can be added besides the VLF example shown in Becken and Pedersen (2003).

A particular way of mode separation of the single-site impedance tensor is performed during so-called galvanic distortion analysis, though usually not treated in terms of modes. Galvanic distortion is a limiting case of galvanic charge accumulations at small-scale inhomogeneities near to the surface. The case of galvanic distortion is met, when the size of the near-surface inhomogeneity is small compared to the skin-depth of the electromagnetic field within such that no anomalous magnetic fields arise. In case of galvanic distortion, charges accumulate independent of period and cause a purely TM-mode secondary electric field oscillating in-phase with the current density, which would penetrate the domain in absence of the distorter. The secondary distorting electric field cannot be separated from the regional one, but the phase information is retained and can be retrieved in case of a regional two-dimensional structure using classical approaches (Bahr, 1988; Groom and Bailey, 1989; Smith, 1995, among other authors) or by means of the phase tensor of Caldwell et al. (2004) for arbitrary conductivity structures. Implicitly, the aim of removing the effects of galvanic distorter is a subtle way of mode separation, where of course only the distorting TM-mode electric field should be separated from the regional electric field, having regional TE and TM parts.

Therefore, I don't treat the galvanic distortion problem from the viewpoint of modes and mode separation, but from the viewpoint of polarization states of principal electric and magnetic field vectors. The suggested approach is more general than previous decomposition schemes, because the MT tensor is parameterized using eight parameters and therefore covering all degrees of freedom inherent in the impedance tensor in the general case. This approach follows a different

philosophy than the popular Groom-Bailey decomposition (Groom and Bailey, 1989). While the Groom-Bailey approach tries to give a physical meaning to the distortion parameters, I exploit the physical properties of the regional fields, which are the quantities of interest.

Although a great number of impedance tensor analysis schemes are already available and the physical problem of galvanic distortion is well understood, the issue is still a matter of debate between MT practitioners. This is in particular the case since Caldwell et al. (2004) published their views on galvanic distortion and introduced the phase tensor. They claim, that their elements of the phase tensor are the only distortion-free quantities, which may be retrieved from the impedance tensor. The phase tensor has been adopted by other authors to investigate its properties further (for example by Weaver and Agarwal, 2004), while some people do not accept it as a superior representation compared to traditional decomposition schemes (Jones, personal communication). Similar to the approach described in Chapter 4 and in Becken and Burkhardt (2004), the phase tensor elements are also interpreted in terms of field polarization states. Additionally, no a priori 2D assumption for the regional structures is required for both the phase tensor method and the ellipticity criterion suggested in this work. However, in contrast to the phase tensor I do not entirely disregard the absolute values of impedances, and the determination of the strike direction of the regional structure using my approach is both phase- and amplitude-sensitive. The latter accounts for the fact, that large absolute values of the impedance tensor correspond to large electric field amplitudes, which may be measured with higher accuracy.

In the course of MT data interpretation, numerical modeling and inversion is the most time-consuming computational task. Current research on this issue concentrates on the development of 3D modeling codes and inversion algorithms (Avdeev et al., 1997; Farquharson et al., 2002; Haber et al., 2004; Siripunvaraporn et al., 2004; Zhdanov and Hursan, 2000; Zhdanov and Tolstaya, 2004) . Great success has been achieved during the last years in the field of 3D inversion, but most of the codes are not yet available or they require enormous computational resources making the programs impractical to ordinary users. Most codes rely on a finite difference or finite element approximation of the electromagnetic fields. The integral equation method (Hohmann, 1975; Wannamaker, 1991; Weidelt, 1975) is considered to be less flexible in terms of conductivity distributions than finite difference and in particular finite element representations. On the other hand, integral equation approaches are still very attractive, since the method is relatively fast and accurate.

In Appendix B, I describe a solution strategy for the integral equation using a wavelet representation for both the electromagnetic field and the conductivity distribution. The present formulation is restricted to 2D structures and the E-Polarization case, but the idea is believed to be applicable also to 3D modeling issues. Further development is however needed and the numerical implementation has to be improved compared to the current state. For these reasons, the description of wavelet based solutions to the electromagnetic integral equation is placed in the appendix. The basic idea in the new formulation is to overcome standard discretization of conductivities and of the electric field vector, as is currently used in the solution to the integral equation, by implementing a flexible representation of the incorporated quantities in a wavelet basis. Wavelets are most flexible function spaces, where smooth functions can be represented with smooth basis functions, while spiky functions with spiky wavelets. For example, when searching for an inverse model, a smoothness constraint is most commonly imposed on the model to regularize the solution. This means, that a smooth function is sought, and it appears to be more efficient to represent the function in a smooth basis instead of using a (highly discontinuous) regular grid. In particular, smooth conductivities produce smooth fields, and therefore the fields could also be solved for using

a smooth function space.

Probably the most difficult interpretation step of MT data is the final geological interpretation of the geoelectrical model. In Chapter 5 of this work, I describe the MT results from the investigation of a medium-scale basin structure in NW China. The geophysical and collateral geological investigations are a joint effort of the working groups at the Technical and Free University Berlin and the Lanzhou University (China), and comprise a wide spectrum of methods. MT data have been collected, analyzed using the methods described in Chapter 4, modeled and finally interpreted in terms of a geological model, which fits into the background of the regional geology. There remain, however, unresolved issues arising form the discussed data set. Open questions are related to possibly anisotropic conductivities of crustal rocks as well as some of the 3D effects in data, which cannot be sufficiently explained. Finally, the geological interpretation is made in absence of rock dating, and therefore remains speculative. It becomes evident in the present study, that geophysical data deliver valuable constraints on the geological model, but a decisive geological description requires an interdisciplinary approach.

# 2. Basic theory

## 2.1. Vector-analytic properties and mode decomposition

I use right-handed cartesian coordinates $(x, y, z)$ with unit vectors $\widehat{\mathbf{x}}$, $\widehat{\mathbf{y}}$ and $\widehat{\mathbf{z}}$, where $z$ is positive downward. The electric and magnetic fields are given with a time dependency $\{\mathbf{E}, \mathbf{H}\} \sim e^{i\omega t}$, where $\omega$ is the angular frequency. The magnetic permeability is assumed to be the vacuum permeability $\mu_0$ everywhere following e.g. Vozoff (1991), which gives the choice of either working with the magnetic field or the magnetic flux density $\mathbf{B} = \mu_0\mathbf{H}$. The field relations in regions of constant conductivity $\sigma$ are described by Ampere's and Faraday's law

$$\nabla \times \mathbf{H} = \mathbf{J} \quad , \quad \nabla \times \mathbf{E} = -i\omega\mu_0\mathbf{H} \ , \tag{2.1}$$

respectively, where displacement currents are neglected in the quasi-static approximation, and the current density is given by Ohm's law $\mathbf{J} = \sigma\mathbf{E}$.

Let me first summarize the vector analytic properties of the electromagnetic fields in homogeneous regions and in the insulating air half-space in particular and introduce the fundamental mode decomposition. The magnetic flux and electric current density $\mathbf{B}$ and $\mathbf{J}$ (away from sources) are divergence-free and may be decomposed into toroidal and poloidal parts (Berdichevsky and Zhdanov, 1984; McKirdy et al., 1985; Schmucker and Weidelt, 1975; Vasseur and Weidelt, 1977; Weidelt, 1975). The constitutive relations yield the corresponding decompositions for the magnetic and the electric field. Here, I denote the fields connected to toroidal currents by subscript $E$ and those related to poloidal currents by subscript $M$. Thus, the toroidal vectors $\mathbf{J}_E$, $\mathbf{E}_E$ and $\mathbf{B}_M$, $\mathbf{H}_M$ have no vertical components and are tangential to the earth's surface. They are considered as Tangential-Electric (TE-mode) and Tangential-Magnetic (TM-mode) systems following Schmucker and Weidelt (1975). The poloidal vectors $\mathbf{B}_E$, $\mathbf{H}_E$ complete the TE-mode and $\mathbf{J}_M$, $\mathbf{E}_M$ the TM-mode, respectively. In insulating media $\mathbf{H}_E$ and $\mathbf{E}_M$ are potential fields (Rokityanski, 1982; Reitz et al., 1993). Thus,

$$\begin{aligned} \nabla \times \mathbf{H}_E = \mathbf{0} \quad , \quad \nabla \times \mathbf{E}_M = \mathbf{0} \\ \nabla \cdot \mathbf{H}_E = 0 \quad , \quad \nabla \cdot \mathbf{E}_M = 0 \end{aligned} \tag{2.2}$$

and Faraday's law yields $\mathbf{H}_M = \mathbf{0}$ here. In addition, the horizontal divergence of the toroidal electric field vanishes, e.g.

$$\nabla_h \cdot \mathbf{E}_E = 0 \ , \tag{2.3}$$

where $\mathbf{E}_E$ is a horizontal vector. Expressions (2.2) have the consequence, that an inductively coupled source field has only a poloidal magnetic field (Berdichevsky and Zhdanov, 1984) and that poloidal currents in the earth can not produce a toroidal magnetic field at the earth's surface. Due to the total reflection of the extrinsic TM-mode electric field governed by extinguishing horizontal components, only the TE-mode magnetic source field drives the secondary currents within the earth. Anomalous TE- and TM-mode fields are then excited in anomalous conductivity

domains and decouple away from lateral conductivity gradients or contrasts. Anomalous TE-mode fields are purely inductive, while TM-mode fields are associated with the deflection of currents in vertical direction due to charge accumulations, where the current has a component parallel to a conductivity contrast or gradient. Therefore, TE-mode is also referred to as inductive mode and TM-mode to galvanic mode, respectively (Rokityanski, 1982).

The usage of the terms TE- and TM-mode is obviously not standardized in geophysical literature. In magnetotellurics in particular, the TE-mode is often used synonymously to E-Polarization (electric field tangential to strike) and TM-mode to B-Polarization (magnetic field tangential to strike), respectively. This notation is restricted to 2-dimensional conductivity structures. Here, I shall use the general definition of modes given above, which comprises the latter in the 2-dimensional case; e.g. $\mathbf{H}_M = \mathbf{0}$ states, that no anomalous magnetic fields can be observed in B-Polarization and the magnetic field is both tangential to the surface and to strike direction (see also Ward and Hohmann, 1988).

In most geophysical applications the electromagnetic fields are either measured in the homogeneous air half-space with conductivity $\sigma = 0$ or at the surface $z = 0$. Besides the vertical electric field, which is usually not measured, all components of the electric field $\mathbf{E}$ and the magnetic field $\mathbf{H}$ are continuous across the surface and can be considered as being measured in the air half-space at $z = -0$. Under these circumstances, the measured magnetic field is purely poloidal and thus of TE-mode, the vertical electric field is also purely poloidal (i.e. of TM-mode) and the horizontal electric field components are a superposition of both modes.[1]

## 2.2. Transfer functions

In the MT-method, the recorded electric and magnetic field components $E_x$, $E_y$, $H_x$, $H_y$, $H_z$ may be regarded as a superposition of the (presumably plane-wave) TE-mode source field and the reflected field at the surface of an inhomogeneous earth. Processing of the data lies in spectral analysis of temporal variations and determination of local or inter-station transfer functions relating the field components to each other.

The concept of transfer functions in electromagnetics has been adopted from linear system theory. In this frame, the conducting earth serves as an invariant linear system, and the field components are input and output functions. The transfer functions derived are invariant under field and reflect only the electrical properties of the earth (Berdichevsky and Zhdanov, 1984). It is not trivial to construct such transfer functions, since in general it may not be assumed that a linear relation between field components exists independent of the source geometry. Berdichevsky and Zhdanov (1984) described a generalized approach giving a profound theoretical basis for the use of transfer functions.

In the scope of this work, I will throughout deal with uniform external fields, which in synthetic studies are incorporated in terms of two principal horizontal magnetic field vectors $\mathbf{h}_1 = \begin{bmatrix} 1 & 0 \end{bmatrix}^T$ and $\mathbf{h}_2 = \begin{bmatrix} 0 & 1 \end{bmatrix}^T$, oscillating in time with angular frequency $\omega$. These fields are referred to as the normal magnetic field and would be observed in the absence of conductivity anomalies.

[1] In borehole and sea-floor applications, the situation is completely different, since in both cases measurements are carried out within a conductor and the toroidal magnetic field does not vanish. In such environments, however, it should be much more simple to measure the vertical electric field component. As far as I know, this opportunity has not been exploited so far.

The induced principal electric fields above such a normal conductivity structure are given by $\mathbf{e}_1 = Z^n \widehat{\mathbf{z}} \times \mathbf{h}_1$ and $\mathbf{e}_2 = Z^n \widehat{\mathbf{z}} \times \mathbf{h}_2$, where $Z^n$ is the normal impedance.

Anomalous fields $\left\{\mathbf{E}^a_{1,2}, \mathbf{H}^a_{1,2}\right\}$ arise due to conductivity anomalies and affect the total fields $\{\mathbf{E}_{1,2}, \mathbf{H}_{1,2}\} = \{\mathbf{e}_{1,2}, \mathbf{h}_{1,2}\} + \left\{\mathbf{E}^a_{1,2}, \mathbf{H}^a_{1,2}\right\}$ at some point $\mathbf{r}$ on or above the surface. Taking the anomalous fields as output and the normal magnetic fields as input functions, the vectors are connected via a transfer function in matrix form. In particular, the anomalous magnetic field vectors are linearly related to the normal magnetic field via the $3 \times 2$ magnetic perturbation matrix $\mathbf{W}$ as

$$\left[\begin{array}{cc} \mathbf{H}^a_1 & \mathbf{H}^a_2 \end{array}\right](\mathbf{r}) = \mathbf{W}(\mathbf{r}) \left[\begin{array}{cc} \mathbf{h}_1 & \mathbf{h}_2 \end{array}\right] = \mathbf{W}(\mathbf{r}) \quad , \tag{2.4}$$

since $\mathbf{I} = \left[\begin{array}{cc} \mathbf{h}_1 & \mathbf{h}_2 \end{array}\right]$ is the $2 \times 2$ unit matrix. Similarly, I can define an electric perturbation matrix $\mathbf{U}$ as

$$\left[\begin{array}{cc} \mathbf{E}^a_1 & \mathbf{E}^a_2 \end{array}\right](\mathbf{r}) = \mathbf{U}(\mathbf{r}) \left[\begin{array}{cc} \mathbf{h}_1 & \mathbf{h}_2 \end{array}\right] = \mathbf{U}(\mathbf{r}) \quad , \tag{2.5}$$

$E_z$ has been incorporated in equation (2.5), although it is usually not considered in applications. The estimation of the perturbation matrices requires simultaneous measurements of the local magnetic and electric field vectors and the normal magnetic field. The latter will in practice be difficult, since one will only in very rare cases find a point, which is sufficiently far away from conductivity anomalies.

However, one can relate the field vectors at point $\mathbf{r}$ to the horizontal magnetic field observations at point $\mathbf{r}_0$ via matrices $\mathbf{P}$ and $\mathbf{Q}$ as

$$\left[\begin{array}{cc} \mathbf{H}_1 & \mathbf{H}_2 \end{array}\right](\mathbf{r}) = \mathbf{P}(\mathbf{r}, \mathbf{r}_0) \left[\begin{array}{cc} \mathbf{H}_{h,1} & \mathbf{H}_{h,2} \end{array}\right](\mathbf{r}_0) \tag{2.6}$$

$$\left[\begin{array}{cc} \mathbf{E}_1 & \mathbf{E}_2 \end{array}\right](\mathbf{r}) = \mathbf{Q}(\mathbf{r}, \mathbf{r}_0) \left[\begin{array}{cc} \mathbf{H}_{h,1} & \mathbf{H}_{h,2} \end{array}\right](\mathbf{r}_0) \quad , \tag{2.7}$$

which, when inserting definition (2.4), virtually combines $\mathbf{W}(\mathbf{r})$ and $\mathbf{U}(\mathbf{r})$ with $\mathbf{W}_h(\mathbf{r}_0)$, respectively, and is thereby justified. Here, subscript $h$ denotes the first two rows of the $3 \times 2$ matrix $\mathbf{W}$. $\mathbf{P}$ and $\mathbf{Q}$ are so-called inter-station transfer functions.

If $\mathbf{r} = \mathbf{r}_0$, $\mathbf{P}$ maps each of the horizontal components into itself, i.e. $\mathbf{P}_h(\mathbf{r} = \mathbf{r}_0) = \mathbf{I}$ is the unit matrix, but establishes a linear relation with the local vertical magnetic field as

$$\left[\begin{array}{cc} H_{z,1} & H_{z,2} \end{array}\right](\mathbf{r}) = \mathbf{T}(\mathbf{r}) \left[\begin{array}{cc} \mathbf{H}_{h,1} & \mathbf{H}_{h,2} \end{array}\right](\mathbf{r}) \quad , \tag{2.8}$$

where $\mathbf{T}(\mathbf{r}) = \mathbf{P}_z(\mathbf{r} = \mathbf{r}_0)$ is the local vertical magnetic transfer function. The horizontal electric fields $\mathbf{E}_{h,1,2}$ are obtained from

$$\left[\begin{array}{cc} \mathbf{E}_{h,1} & \mathbf{E}_{h,2} \end{array}\right](\mathbf{r}) = \mathbf{Z}(\mathbf{r}) \left[\begin{array}{cc} \mathbf{H}_{h,1} & \mathbf{H}_{h,2} \end{array}\right](\mathbf{r}) \tag{2.9}$$

which defines the local magnetotelluric $2 \times 2$ impedance tensor as $\mathbf{Z} = \mathbf{Q}_h(\mathbf{r} = \mathbf{r}_0)$. In addition, I introduce a vertical electric transfer function $\mathbf{S} = \mathbf{Q}_z(\mathbf{r} = \mathbf{r}_0)$, which maps the horizontal magnetic field vector into the entirely anomalous vertical electric field.

While the impedance tensor $\mathbf{Z}$ and the vertical magnetic transfer function $\mathbf{T}$ are obtained from single-site observations, Matrices $\mathbf{P}$ and $\mathbf{Q}$ maybe estimated from array observations. In particular, the determination of $\mathbf{Z}$ is the objective of the **m**agneto-**t**elluric method (MT), $\mathbf{T}$ is the transfer function aimed in **g**eomagnetic **d**epth **s**ounding (GDS), and $\mathbf{P}$ is determined using geomagnetic arrays. It is not common practice to consider the matrix $\mathbf{Q}$, and the vertical electric transfer function $\mathbf{S}$ cannot be determined due to a number of problems associated with the measurement of the anomalous vertical electric field. It is however constructive to look at the vertical electric

field in the scope of model studies and it is an issue to determine the vertical electric field by other means, as we shall see in section 3.2.2.

The transfer functions in plane-wave electromagnetics may be decomposed into modes like the fields themselves. The magnetic transfer functions $\mathbf{W}$, $\mathbf{T}$, $\mathbf{P}$ are entirely of TE-mode, since only poloidal magnetic fields are involved. The impedance tensor $\mathbf{Z} = \mathbf{Z}_E + \mathbf{Z}_M$ relates the horizontal poloidal magnetic field to the toroidal and poloidal horizontal electric fields via the transfer functions $\mathbf{Z}_E$ and $\mathbf{Z}_M$, respectively. $\mathbf{Z}_E$, which involves only TE-mode fields, and $\mathbf{Z}_M$ which relates normal and anomalous TE-mode magnetic fields to anomalous TM-mode fields, cannot be obtained separately from single-site measurements. The matrix $\mathbf{U}$ is similarly decomposed into TE- and TM-modes $\mathbf{U}_E$ and $\mathbf{U}_M$, where $\mathbf{U}_{E,z} = \mathbf{0}$ , since the TE-mode electric field has no vertical component. Consequently, $\mathbf{U}_z = \mathbf{U}_{M,z}$ is entirely of TM-Mode and reflects the vertical electric field.

# 3. Spatial relations of transfer functions

Transfer functions estimated from actual measurements reflect the conductivity distribution below and in the vicinity of the measurement point. Most commonly, the single-site impedance tensor $\mathbf{Z}$ and the local vertical magnetic transfer function $\mathbf{T}$ are estimated from measured data. The latter is graphically depicted in terms of real and imaginary induction arrows. Real induction arrows are supposed to point away from the axis of elongated conductors, and imaginary induction arrows point parallel or anti-parallel, depending on the period with respect to the depth of the anomaly. The impedance tensor is usually looked at in terms of apparent resistivities and phases as a function of period. Structural information is obtained from the impedance tensor by investigation of its rotational properties.

$\mathbf{T}$ is calculated from magnetic fields solely and therefore is a measure of inductive TE-mode currents. In contrast, $\mathbf{Z}$ involves the electric field, which constitutes of both TE- and TM-modes and therefore carries in addition information about galvanic currents, i.e. charge accumulations associated with currents in parallel to conductivity gradients. It is therefore easily understood that structural information deduced from $\mathbf{T}$ and $\mathbf{Z}$ are occasionally different and only coincide in perfect 1D or 2D environments. When analyzing the impedance tensor, it must therefore be taken into account that anomalous fields are of two-fold origin with different physical background and do not necessarily reflect the same anomaly at a certain period.

In comparison with the vertical magnetic transfer function, the vertical electric transfer functions $\mathbf{S}$ or $\mathbf{U}_z$ would be a suitable measure of galvanic currents, i.e. of TM-mode. Then, vertical magnetic and electric transfer functions can be depicted to separately display anomalous TE- and TM-mode currents, respectively. However, $\mathbf{S}$ or $\mathbf{U}_z$ cannot be determined from measurements directly.

In what is to follow, I will reconstruct the entire electromagnetic field separated into TE- and TM-modes from given local vertical magnetic and impedance tensor transfer functions. The mode separated fields and transfer functions may then be studied for 3D models, and their contribution to the local transfer functions may be quantified. For the purpose of mode separation, I employ the vector-analytic properties of the em-field and spatial relations given by Maxwell's equations as also demonstrated in Becken and Pedersen (2003).

To apply spatial relations, it is demanded that local transfer functions are available on the earth's surface with a sufficient spatial sampling, covering the whole anomalous region. The derivation consists of several steps. In the first step, vertical magnetic transfer functions given on an infinitely extended plane are decomposed into two magnetic field vectors constituting the magnetic perturbation tensor $\mathbf{W}(\mathbf{r})$. In a second step, Faraday's law is solved for the anomalous toroidal electric field, enabling a TE-mode impedance determination in conjunction with the magnetic fields. Thirdly, from given impedances and calculated TE-mode impedances, the TM-mode impedance and corresponding TM-mode horizontal electric field is derived. Finally, from the horizontal TM-mode electric field, its vertical component may be calculated and the vertical electric transfer functions derived.

The derivation is more convenient in wavenumber space. The spatial Fourier transform of a

function $f(\mathbf{r})$ is denoted by $\widetilde{f}(\boldsymbol{\kappa})$, where $\mathbf{r} = (x, y)^T$ is the horizontal space vector and $\boldsymbol{\kappa} = (\kappa_x, \kappa_y)^T$ is the wavenumber vector. Then

$$\widetilde{f}(\boldsymbol{\kappa}) = \mathcal{F}\{f(\mathbf{r})\} = \frac{1}{2\pi}\int_{-\infty}^{\infty}\int_{-\infty}^{\infty} f(\mathbf{r}) e^{-i\boldsymbol{\kappa}\cdot\mathbf{r}} d\mathbf{r} \ , \tag{3.1}$$

and the inverse Fourier transform is given by

$$f(\mathbf{r}) = \mathcal{F}^{-1}\{f(\boldsymbol{\kappa})\} = \frac{1}{2\pi}\int_{-\infty}^{\infty}\int_{-\infty}^{\infty} \widetilde{f}(\boldsymbol{\kappa}) e^{i\boldsymbol{\kappa}\cdot\mathbf{r}} d\boldsymbol{\kappa} \ . \tag{3.2}$$

Derivative operators in space domain correspond to multiplication in wavenumber domain obtained from

$$\mathcal{F}\{\partial/\partial x\,[f(\mathbf{r})]\} = i\kappa_x \widetilde{f}(\boldsymbol{\kappa}) \quad , \quad \mathcal{F}\{\partial/\partial y\,[f(\mathbf{r})]\} = i\kappa_y \widetilde{f}(\boldsymbol{\kappa}) \tag{3.3}$$

which is used later.

## 3.1. TE-Mode transfer functions

### 3.1.1. Decomposition of the vertical magnetic transfer function

Since the measured magnetic field is a potential field (Rokityanski, 1982; Reitz et al., 1993), its dependent components constitute a Hilbert transform pair. Consequently, knowledge of the vertical component on a infinitely extended surface $z = z_0$ is sufficient to calculate the two remaining horizontal field components. This potential field property in conjunction with the definition of the vertical magnetic transfer function (2.8) can be employed to determine uniquely $H_z(\mathbf{r})$ for given $\mathbf{T}(\mathbf{r})$ and hypothetic normal magnetic fields $\mathbf{h}_{1,2}$ of a incident plane wave.

The Hilbert transformation of a potential vector field $\mathbf{V}(\mathbf{r}, z)$ given on the infinitely extended plane $z = z_0$ is transformed to wavenumber domain (Pedersen, 1989) as

$$\widetilde{\mathbf{V}}_h(\boldsymbol{\kappa}, z_0) = \frac{i\boldsymbol{\kappa}}{\kappa}\widetilde{V}_z(\boldsymbol{\kappa}, z_0) \ , \tag{3.4}$$

where $\kappa$ denotes the absolute value of the wavenumber vector. For ease of notation, I subsequently drop the fixed variable $z_0$. The Hilbert transform (3.4) must be satisfied by the anomalous magnetic field, if all field inhomogeneities are of internal origin. Substituting the vertical component in expression (3.4) with equation (2.8) transformed to Fourier domain, the total horizontal magnetic field including inhomogeneities due to conductivity anomalies in the earth is given by

$$\begin{bmatrix} \widetilde{\mathbf{H}}_{h,1} & \widetilde{\mathbf{H}}_{h,2} \end{bmatrix}(\boldsymbol{\kappa}) = \begin{bmatrix} \mathbf{h}_1 & \mathbf{h}_2 \end{bmatrix}\delta(\boldsymbol{\kappa}) + \frac{i\boldsymbol{\kappa}}{\kappa}\left\{\widetilde{\mathbf{T}}(\boldsymbol{\kappa}) * \begin{bmatrix} \widetilde{\mathbf{H}}_{h,1} & \widetilde{\mathbf{H}}_{h,2} \end{bmatrix}(\boldsymbol{\kappa})\right\} \ . \tag{3.5}$$

The star denotes the convolution operator, and $\delta(\boldsymbol{\kappa})$ is the Dirac delta impulse. Equation (3.5) is the wavenumber domain representation of a Fredholm integral equation of second kind. A suitable and fast method for solving such systems is the method of successive approximation, which when switching between space and wavenumber domain can be performed as follows: a first approximation $H_z^0$ of the (anomalous) vertical field component is obtained according to $\begin{bmatrix} H_{z,1}^0 & H_{z,2}^0 \end{bmatrix}(\boldsymbol{r}) = \mathbf{T}(\boldsymbol{r})\begin{bmatrix} \mathbf{h}_1 & \mathbf{h}_2 \end{bmatrix}$. Fourier transformation to wavenumber domain permits a first estimation of the anomalous horizontal field using equation (3.5). Adding the derived

horizontal anomalous part to the normal field enables a new estimation of the vertical component. Hence, a number of iterations $j$ are performed following the procedure

$$\begin{aligned}
\left[\begin{array}{cc} H_{z,1}^{j+1} & H_{z,2}^{j+1} \end{array}\right](\boldsymbol{r}) &= \mathbf{T}(\boldsymbol{r})\left[\begin{array}{cc} \mathbf{H}_{h,1}^{j} & \mathbf{H}_{h,2}^{j} \end{array}\right](\boldsymbol{r}) \ , \\
\left[\begin{array}{cc} \widetilde{\mathbf{H}}_{h,1}^{a,j+1} & \widetilde{\mathbf{H}}_{h,2}^{a,j+1} \end{array}\right](\boldsymbol{\kappa}) &= \frac{i\boldsymbol{\kappa}}{\kappa}\left[\begin{array}{cc} \widetilde{H}_{z,1}^{j+1} & \widetilde{H}_{z,2}^{j+1} \end{array}\right](\boldsymbol{\kappa}) \ , \\
\left[\begin{array}{cc} \mathbf{H}_{h,1}^{j+1} & \mathbf{H}_{h,2}^{j+1} \end{array}\right](\boldsymbol{r}) &= \left[\begin{array}{cc} \mathbf{H}_{h,1}^{a,j+1} & \mathbf{H}_{h,2}^{a,j+1} \end{array}\right](\boldsymbol{r}) + \left[\begin{array}{cc} \mathbf{h}_1 & \mathbf{h}_2 \end{array}\right] \ . \qquad (3.6)
\end{aligned}$$

A criterion to stop the iterative process is required. Here, I use that the maximum difference of the vertical component between the present and the previous iteration $\left|H_z^j(\mathbf{r}_m) - H_z^{j-1}(\mathbf{r}_m)\right|$ at the point $\mathbf{r}_m$ should be less than some $\delta H_z$.

### 3.1.2. Perturbation tensor

The above procedure will be performed for two independent normal magnetic fields $\mathbf{h}_{1,2}$ and yields two magnetic field functionals $\mathbf{H}_{1,2}(\mathbf{r})$. As it is deduced from expression (2.4), the perturbation tensor is readily determined as

$$\mathbf{W}(\mathbf{r}) = \left[\begin{array}{cc} \mathbf{H}_1 & \mathbf{H}_2 \end{array}\right](\mathbf{r}) - \left[\begin{array}{cc} \mathbf{h}_1 & \mathbf{h}_2 \end{array}\right] \ . \qquad (3.7)$$

This result is remarkable, since the perturbation tensor may be obtained solely from single-site vertical magnetic transfer functions employing potential field properties of the magnetic field. Simultaneous observations and knowledge about the normal structure and conductivity anomalies are not required.

### 3.1.3. TE-mode impedance tensor

Next, from the vertical magnetic field components, the toroidal electric fields are derived from Faraday's law (2.1): taking $\mathbf{E}_E(\mathbf{r}) = \mathbf{E}_E^n + \mathbf{E}_E^a(\mathbf{r})$, the anomalous toroidal electric fields are given in wavenumber domain by

$$\widehat{\mathbf{z}} \times \left[\begin{array}{cc} \widetilde{\mathbf{E}}_{E,1}^{a} & \widetilde{\mathbf{E}}_{E,2}^{a} \end{array}\right](\boldsymbol{\kappa}) = \frac{\omega\mu_0\boldsymbol{\kappa}}{\kappa^2}\left[\begin{array}{cc} \widetilde{H}_{z,1} & \widetilde{H}_{z,2} \end{array}\right](\boldsymbol{\kappa}) \ , \qquad (3.8)$$

where the vanishing horizontal divergence

$$i\boldsymbol{\kappa} \cdot \widetilde{\mathbf{E}}_E^a(\boldsymbol{\kappa}) = 0 \qquad (3.9)$$

was applied in wavenumber domain (remember that the toroidal electric field has no vertical component). Division by $\kappa^2$ is required in equation (3.8), which causes indeterminacy at $\boldsymbol{\kappa} = \mathbf{0}$. Anyway, the Fourier coefficient at the singular point in wavenumber domain is equivalent to a shift in space domain by the average anomalous field. For energy conservation reasons, the anomalous fields must vanish towards infinity and is therefore uniquely constrained. Thus, the unknown shift can be easily corrected for.

Having determined the anomalous toroidal electric field, the TE-mode part $\mathbf{U}_E$ of $\mathbf{U}$ defined in equation (2.5) is given by $\mathbf{U}_E = \left[\begin{array}{cc} \mathbf{E}_{E,1}^a & \mathbf{E}_{E,2}^a \end{array}\right]$. Incorporating the normal electric field $\left[\begin{array}{cc} \mathbf{e}_1 & \mathbf{e}_2 \end{array}\right] = \mathbf{Z}^n$, which is presumed to be known, yields for the total local toroidal electric field

$\left[\begin{array}{cc} \mathbf{E}_{E,1} & \mathbf{E}_{E,2} \end{array}\right] = \mathbf{Z}^n + \mathbf{U}_E$, which in turn is related to the local magnetic field via the local TE-mode impedance tensor $\mathbf{Z}_E$ according to expression (2.9). Substituting the anomalous magnetic field with the horizontal magnetic perturbation matrix $\mathbf{W}_h$ and representing the normal magnetic fields in terms of the unit matrix $\mathbf{I}$ leads to

$$\mathbf{Z}^n + \mathbf{U}_E(\boldsymbol{r}) = \mathbf{Z}_E(\boldsymbol{r})\left(\mathbf{W}_h(\boldsymbol{r}) + \mathbf{I}\right) \quad . \tag{3.10}$$

The inverse of equation (3.10) yields the local TE-mode impedance tensor, i.e.

$$\mathbf{Z}_E(\boldsymbol{r}) = \left(\mathbf{Z}^n + \mathbf{U}_E(\boldsymbol{r})\right)\left(\mathbf{W}_h(\boldsymbol{r}) + \mathbf{I}\right)^{-1} \quad , \tag{3.11}$$

provided the inverse of $\mathbf{W}_h + \mathbf{I}$ in equation (3.11) exists.

## 3.2. TM-Mode transfer functions

### 3.2.1. TM-mode impedance tensor

From given $\mathbf{Z}$ and calculated $\mathbf{Z}_E$, the TM-mode impedance tensor is obtained from

$$\mathbf{Z}_M(\boldsymbol{r}) = \mathbf{Z}(\boldsymbol{r}) - \mathbf{Z}_E(\boldsymbol{r}) \quad . \tag{3.12}$$

Since the TM-mode horizontal electric field is purely anomalous, its horizontal components are

$$\left[\begin{array}{cc} \mathbf{E}^a_{M,h,1} & \mathbf{E}^a_{M,h,2} \end{array}\right](\boldsymbol{r}) = \mathbf{Z}_M(\boldsymbol{r})\left(\mathbf{W}_h(\boldsymbol{r}) + \mathbf{I}\right) = \mathbf{U}_{M,h}(\boldsymbol{r}) \quad . \tag{3.13}$$

Thus, $\mathbf{U}_{M,h}$ is also determined.

### 3.2.2. Vertical electric transfer function

It remains to calculate the vertical electric field of internal origin, which can be obtained from the potential field properties of the TM-mode electric field in the air half-space. Hence, switching to wavenumber domain and using the Hilbert-transform (3.4),

$$\widetilde{\mathbf{U}}_{M,z}(\boldsymbol{\kappa}) = \left[\begin{array}{cc} \widetilde{E}_{z,1}(\boldsymbol{\kappa}) & \widetilde{E}_{z,2}(\boldsymbol{\kappa}) \end{array}\right] = -\frac{i\boldsymbol{\kappa}}{\kappa}\left[\begin{array}{cc} \widetilde{\mathbf{E}}^a_{h,1} & \widetilde{\mathbf{E}}^a_{h,2} \end{array}\right](\boldsymbol{\kappa}) = -\frac{i\boldsymbol{\kappa}}{\kappa}\widetilde{\mathbf{U}}_{M,h}(\boldsymbol{\kappa}) \tag{3.14}$$

which when transformed back to space domain completes the TM-Mode. Finally, I calculate the local vertical electric transfer function $\mathbf{S}$ from

$$\mathbf{S}(\boldsymbol{r}) = \mathbf{U}_{M,z}(\boldsymbol{r})\left(\mathbf{W}_h(\boldsymbol{r}) + \mathbf{I}\right)^{-1} \quad . \tag{3.15}$$

## 3.3. Graphical presentation of transfer functions

It is a somewhat awkward procedure to graphically depict all types of transfer functions. However, as shown in the previous sections, many of the transfer functions are linked to each other. Basically, the total information is given by the normal impedance representing the normal structure, the vertical magnetic field representing anomalous TE-mode fields and the vertical electric field representing the anomalous TM-mode field. In this sense $\mathbf{Z}^n$, $\mathbf{W}_z(\boldsymbol{r})$ and $\mathbf{U}_z(\boldsymbol{r})$ are the most

important transfer functions. Vertical transfer functions may be displayed in terms of arrow plots. Arrows are constructed from real and imaginary parts separately in such a way that the real arrows point away from conductive anomalies as suggested for the vertical magnetic transfer functions by Wiese (1962) for $\mathbf{T}$ and Schmucker (1970) for $\mathbf{W}_z$. In analogy to the vertical magnetic transfer functions, the vertical electric transfer function $\mathbf{U}_z$ is conceived as a two-component vector and depictable in terms of arrows. However, $\mathbf{U}_z$ has to be rotated counterclockwise by $\pi/2$ such that constructed arrows point away from anomalies. Since $\mathbf{U}_z(\boldsymbol{r})$ has the dimension of an impedance and intrinsically depends on period, it is reasonable to normalize the vertical electric transfer function by the normal impedance for plotting purposes.

Horizontal transfer functions $\mathbf{W}_h$ and $\mathbf{U}_h$ may also be depicted in terms of arrow plots. Magnetic perturbation vectors $\mathbf{p}$ and $\mathbf{q}$ are defined here from $\pi/2$ counterclockwise rotated columns of $\mathbf{W}_h$, i.e. the anomalous horizontal magnetic fields $\mathbf{H}^a_{h,1}$ and $\mathbf{H}^a_{h,2}$ due to unit normal magnetic fields $\mathbf{h}_1$ and $\mathbf{h}_2$ in $\widehat{\mathbf{x}}$ and $\widehat{\mathbf{y}}$ direction, respectively, as

$$\mathbf{p} = \widehat{\mathbf{z}} \times \mathbf{H}^a_{h,1}, \;\; \mathbf{q} = \widehat{\mathbf{z}} \times \mathbf{H}^a_{h,2} \;\; . \tag{3.16}$$

Then, $\mathbf{p}$ and $\mathbf{q}$ are perpendicular to the magnetic fields and maybe conceived as equivalent anomalous TE-mode current density (Berdichevsky and Zhdanov, 1984). Magnetic perturbation arrows clearly exhibit the effect of current concentration in highly conducting zones. Analogically, vectors

$$\mathbf{u} = \mathbf{E}^a_{M,1} \quad , \quad \mathbf{v} = \mathbf{E}^a_{M,2} \tag{3.17}$$

representing the columns of $\mathbf{U}_h$ exhibit the effect of charge accumulations at conductivity gradients and are here denoted as electric perturbation vectors. They point in direction of the anomalous electric field arising from such charges. Perturbation vectors are variant under rotation, i.e. they depend on the direction of the inducing field.

Transfer functions involving the electric field are usually presented in terms of apparent resistivities and phases. For this purpose, I define TE-mode apparent resistivities $\rho_E$ and phases $\phi_E$ solely based on the TE-mode impedance tensor $\mathbf{Z}_E$ according to Cagniard (1953) as element-wise mappings as

$$\boldsymbol{\rho}_E \;\; = \;\; \frac{1}{\omega\mu_0} \left|\mathbf{Z}_E\right|^2, \;\; \boldsymbol{\phi}_E = \arg\left\{\mathbf{Z}_E\right\} \;\; , \tag{3.18}$$

The remainder $\mathbf{Z}_M$ of the full impedance tensor $\mathbf{Z}$ comprises a mixture of anomalous magnetic TE- and electric TM mode fields (cf. equation 3.13) and is therefore not suitable to demonstrate mode separated responses. Instead, I use TM-mode apparent resistivities $\rho_M$ and phases $\phi_M$ calculated from $\mathbf{Z}_n + \mathbf{U}_{M,h}$, which have purely anomalous TM-mode fields. Here, I add the normal impedance in order to obtain true apparent resistivities and phases away from anomalies. Hence,

$$\boldsymbol{\rho}_M \;\; = \;\; \frac{1}{\omega\mu_0} \left|\mathbf{Z}_n + \mathbf{U}_{M,h}\right|^2, \;\; \boldsymbol{\phi}_M = \arg\left\{\mathbf{Z}_n + \mathbf{U}_{M,h}\right\} \tag{3.19}$$

is used to display the TM-mode apparent resistivities and phases. In general, anomalous parts of impedances are distributed over all elements of the tensor and are variant under coordinate rotation. For visualizing structures, a rotationally invariant is more suitable. For this purpose, the determinants $\|\mathbf{Z}_E\|$ and $\|\mathbf{Z}_n + \mathbf{U}_{M,h}\|$ are calculated and determinant apparent resistivities and phases are used instead for graphical presentation.

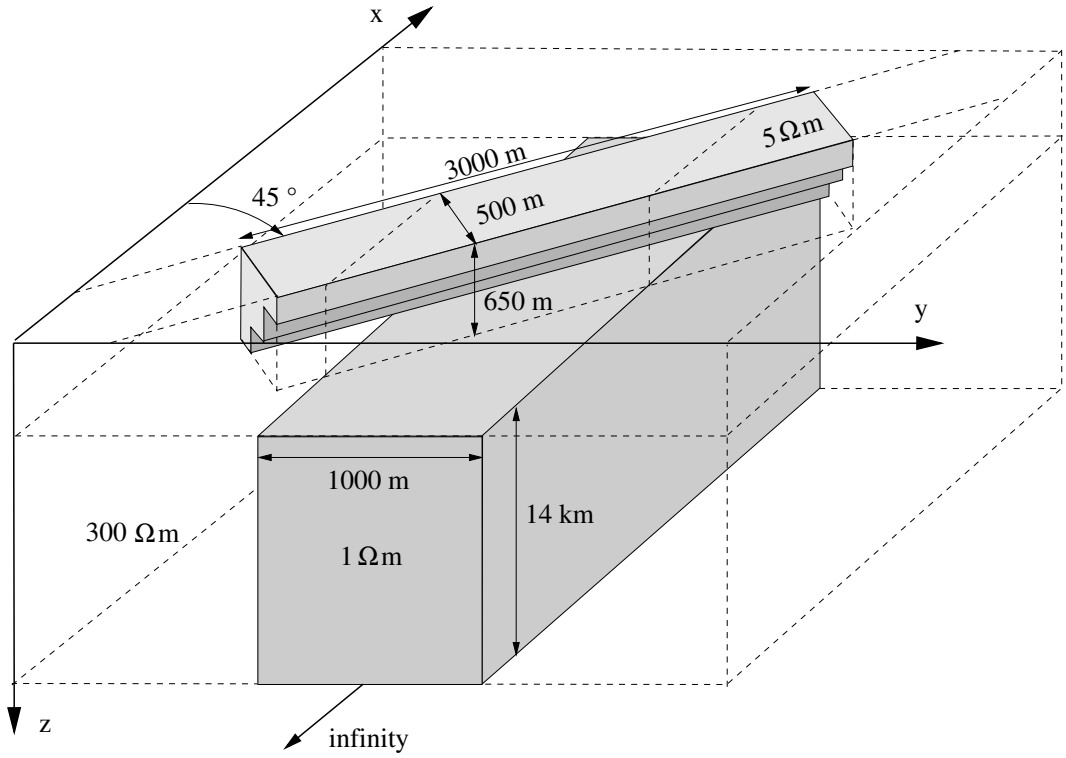


**Figure 3.1.:** Sketch of 3D model. Two elongated, electrically decoupled conductors with a relative orientation of 45° are embedded in a resistive half-space of 300 Ωm. The model is designed to demonstrate the behavior of surface anomalous TE- and TM-mode fields arising from conductors situated in different depths.

## 3.4. A synthetic model study

To demonstrate the properties and information carried in the above treated transfer functions, I show the results of a synthetic model study. The model, sketched in Figure 3.1, combines two elongated conductive anomalies embedded in a $300\,\Omega\mathrm{m}$ half-space. The upper conductor represents the $5\,\Omega\mathrm{m}$ sedimentary filling of a medium-scale, $45°$ clockwise striking half-Graben. Being $500\,\mathrm{m}$ wide and $3000\,\mathrm{m}$ long, it extends to the depth of $650\,\mathrm{m}$ at its left boundary. The lower conductor is electrically coupled with the Graben sediments. It extends between the depth interval from $650\,\mathrm{m}$ to $14\,\mathrm{km}$, is $1000\,\mathrm{m}$ wide and extends to infinity in $\pm x-$direction. Its strike direction is $45°$ counterclockwise with respect to the surface conductor. Such a structure may, for example, be attributed to a fault zone with fluid-filled fractures giving rise to the conductivity of $1\,\Omega\mathrm{m}$.

The model core has been discretized with $70\times70\times30$ cells in $x-$, $y-$ and $z-$direction, respectively. The smallest cell size is $50\,\mathrm{m} \times 50\,\mathrm{m} \times 25\,\mathrm{m}$, progressively being increased to depth and, when sufficiently far away from the boundaries of the surface conductor, in horizontal directions. The local impedance tensor and vertical magnetic transfer function have been calculated for periods between $0.001 - 100\,\mathrm{s}$ using a 3D finite difference modeling program (Mackie et al., 1994). The model responses have then been decomposed into TE- and TM-modes using the formulas of

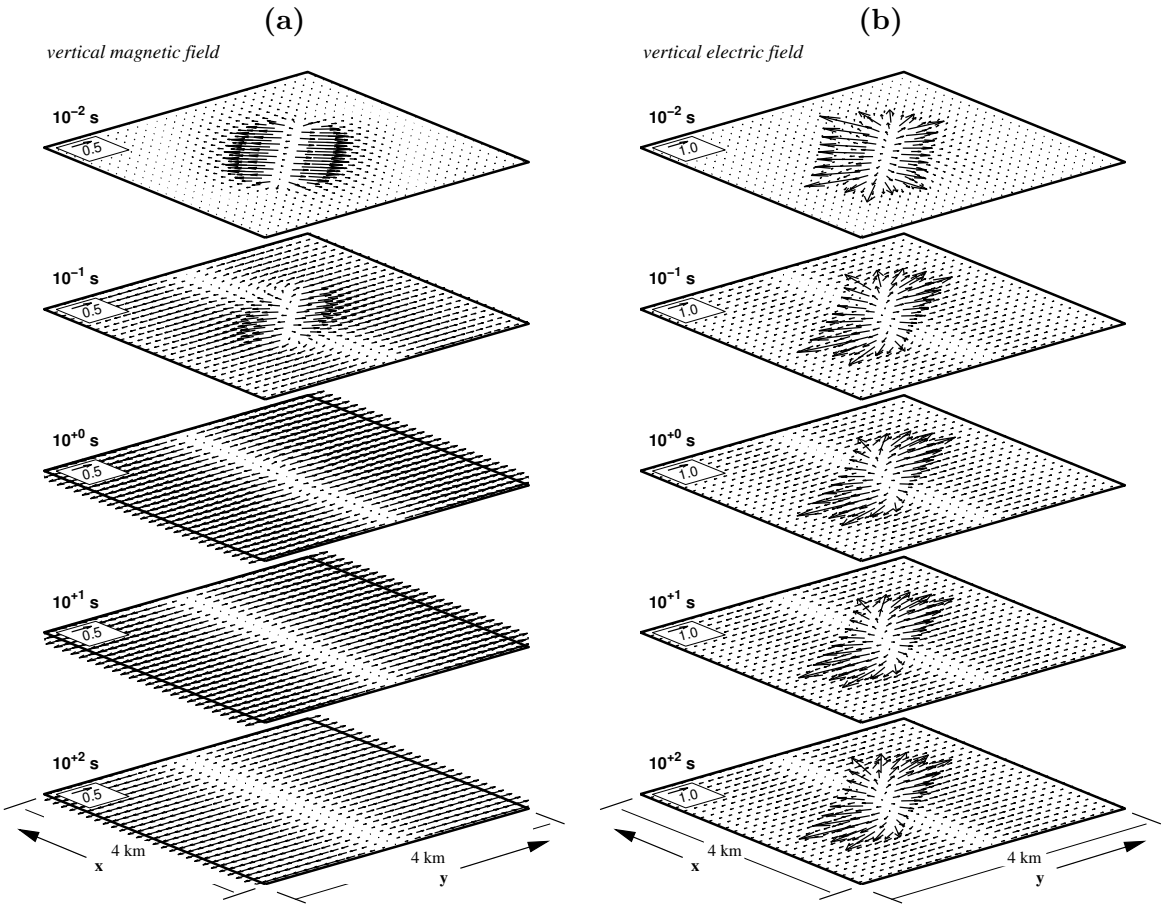


**Figure 3.2.:** Induction arrows and galvanic arrows representing **a)** the vertical magnetic transfer function $\mathbf{W}_z$ and **b)** the vertical electric transfer function $\mathbf{U}_z$, derived for the 3D model shown in Figure 3.1. Only real arrows are shown here, depicted for five periods $T = 10^{-2}$, ..., $10^2$ s from top to bottom. At short periods, the vertical magnetic field is primarily sensitive to the shallow conductor. With longer periods, the deeper conductor becomes more important, and the influence of the surface structure becomes neglectable. In contrast, the vertical electric field indicates the presence of the shallow conductor at all periods, and the effect of the deeper structure is small though visible.

chapter 3.1 and 3.2 and are graphically depicted in Figures 3.2, 3.3, 3.4, 3.5 and 3.6.

Figures 3.2a and b show the spatial distribution of real arrows derived from vertical magnetic and electric transfer functions $\mathbf{W}_z$ and $\mathbf{U}_z$, respectively, for five periods $T = 10^{-2}$, ..., $10^2$ s from top to bottom. Imaginary arrows have been omitted to reduce the number of plots. Arrows shown in Figure 3.2 are representative for inductive (Fig. 3.2a) and galvanic (3.2b) anomalous currents, i.e. for TE- and TM-mode, and are therefore denoted as induction and galvanic arrows.

Real induction arrows are basically pointing away from the axis of the shallow conductor at short periods ($10^{-2}$ s). With increasing period, the deeper conductor becomes more important and both the shallow and the deep conductors act as inductive anomalies. Induced anomalous currents within are coupled, and the surface response is affected by both anomalies. At long periods ($> 10^0$ s), only the deep anomaly is indicated by induction arrows pointing parallel to the $y-$axis. Distortion

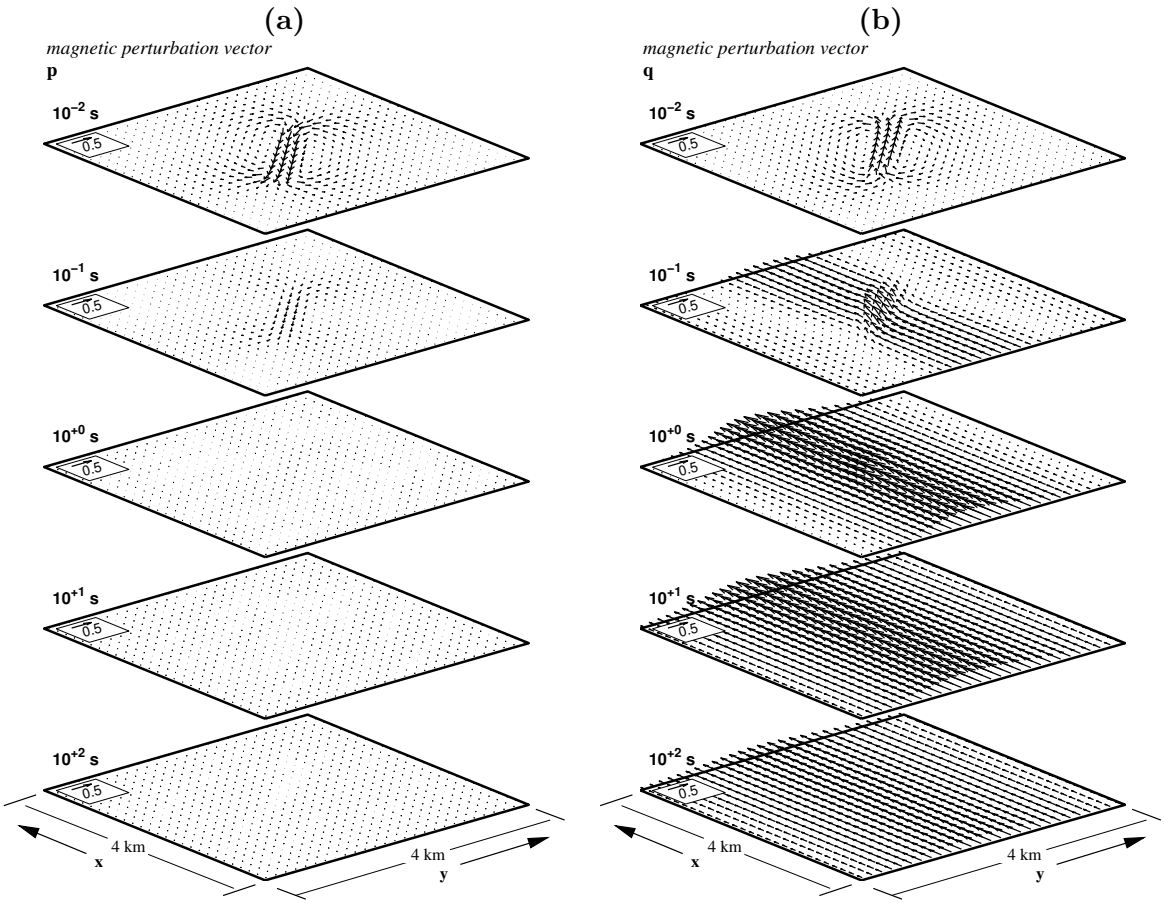


**Figure 3.3.:** TE-mode response: Magnetic perturbation vectors **p** and **q** for the model shown in Figure 3.1. Responses are shown for five periods $T = 10^{-2}$, ..., $10^{2}$ s from top to bottom. **a)** real part of magnetic perturbation vector **p** indicating the zones of current concentration and the direction of anomalous inductive currents due to a magnetic excitation in $x-$direction and **b)** real part of magnetic perturbation vector **q** representing inductive currents due to an excitation in $y-$direction, respectively. At short periods, anomalous currents are induced within the shallow conductor, and at long periods, the anomalous response is mostly contained in **q**, indicating 2D conditions and E-Polarization.

of long-period induction arrows due to the presence of the shallow anomaly cannot be observed.

Real galvanic arrows, indicating the vertical electric field distribution normalized by the normal horizontal electric field, are plotted in Figure 3.2b. Vertical electric fields arise due to charges accumulating at interfaces such that the currents are deflected in vertical direction. This effect is observed relatively independently of period and is even known from DC-currents. Thus, the shallow conductor is clearly indicated at all periods depicted in Figure 3.2b. Vertical electric field anomalies decay much faster in space than vertical magnetic field anomalies. Therefore, surface structures are primarily reflected in the vertical electric field, and the effect of charges accumulating at greater depths is of minor importance though clearly visible. Attributing the properties of the vertical transfer functions to the modes, TE-mode reflects anomalies at greater depths, while shallow anomalies control the surface TM-mode response.

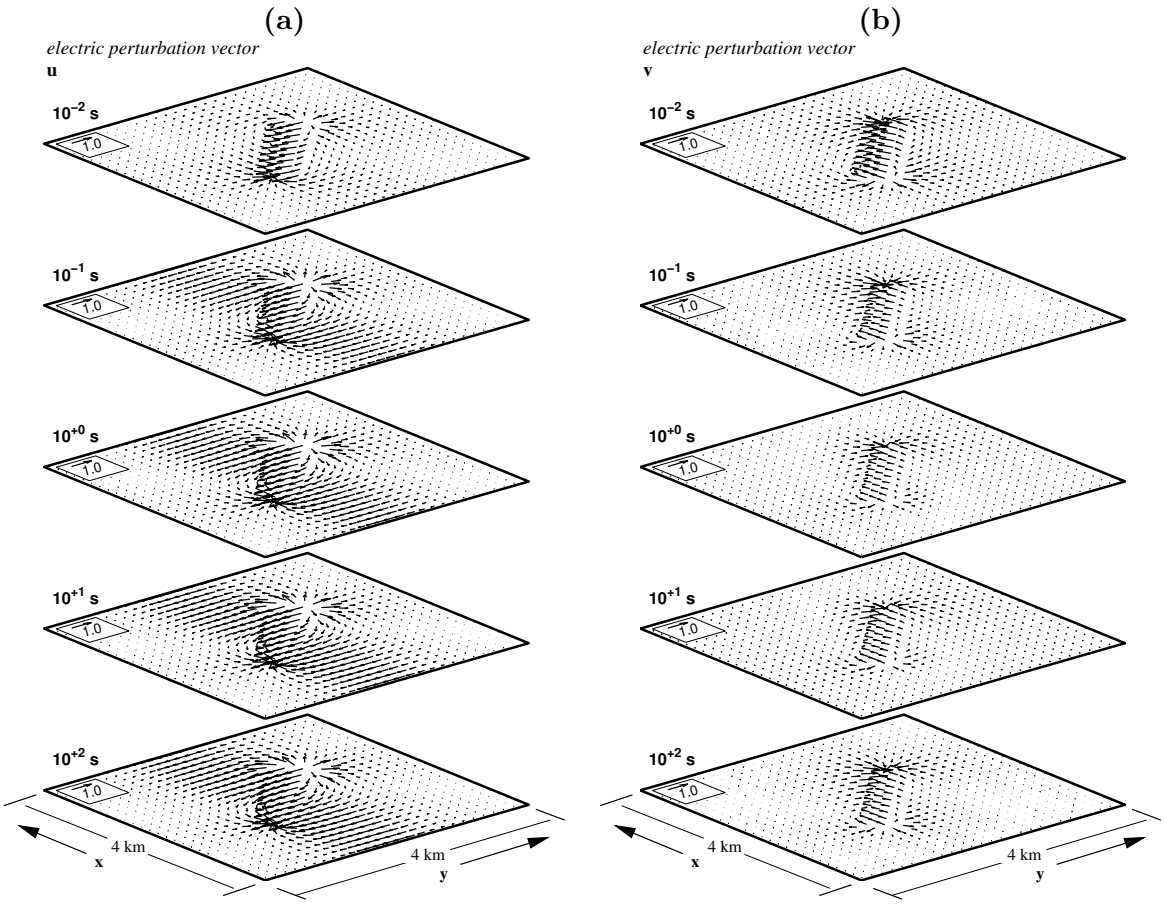


**Figure 3.4.:** TM-mode response: TM-mode electric perturbation vectors $\mathbf{u}$ and $\mathbf{v}$ for the model shown in Figure 3.1. Responses are shown for five periods $T = 10^{-2}$, ..., $10^{2}$ s from top to bottom. **a)** real part of electric perturbation vector $\mathbf{u}$ indicating the zones of charge accumulations and the direction of anomalous galvanic currents due to a magnetic excitation in $x-$direction and **b)** real part of electric perturbation vector $\mathbf{v}$ representing galvanic currents due to an excitation in $y-$direction, respectively. At short and long periods, the galvanic currents within the shallow conductor dominate the TM-mode response at the surface. The deeper conductor is only visible aside from the shallow conductor and if currents flow perpendicular to it as can be seen from $\mathbf{u}$ in the left panel.

It is instructive to look at magnetic perturbation vectors $\mathbf{p}$ and $\mathbf{q}$ as defined in equation (3.16) and depicted as real arrows in Figure 3.3. Anomalous inductive currents due to a source field in $x-$direction as shown in Figure 3.3a are restricted to the shallow conductor. They occur only at short periods, when the dimensions of the anomaly are of the same order than the skin-depth of the fields within. At longer periods, currents are concentrated within the deeper conductor and oriented in $x-$direction. They are excited by a source field in $y-$direction and are shown in Figure 3.3b. For periods longer than $10^{0}$ s, the effect of the shallow conductor becomes small, and the problem is basically that of the 2D E-Polarization case.

In comparison with magnetic perturbation vectors, electric perturbation vectors constructed from equation (3.17) exhibit a different signature. Real parts of $\mathbf{u}$ and $\mathbf{v}$, representing the anomalous

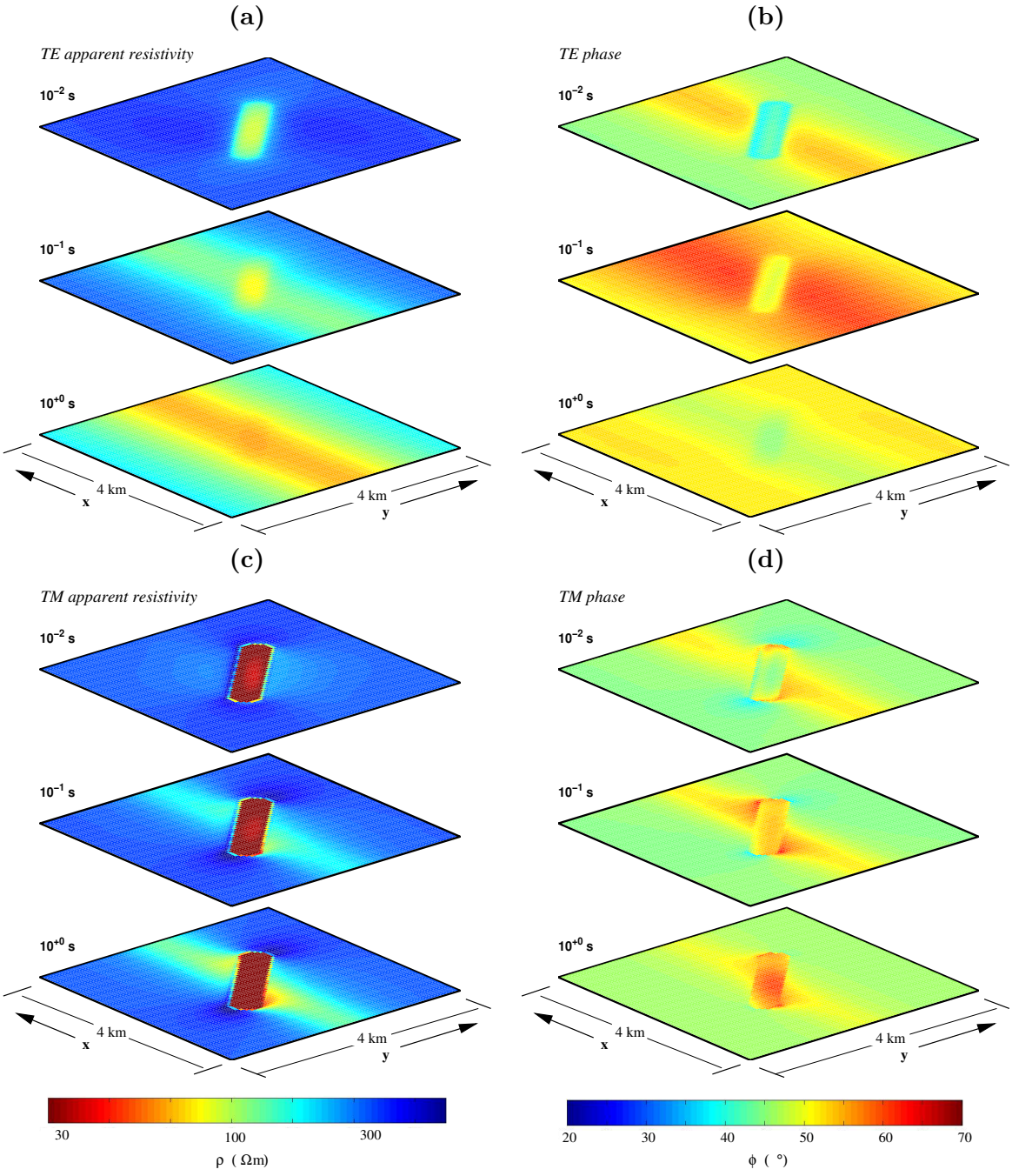


**Figure 3.5.:** Mode separated impedances $\mathbf{Z}_E$ and $\mathbf{U}_{M,h} + \mathbf{Z}_n$. **a)** and **c)** Determinant apparent resistivities and and **b)** and **d)** phases for three periods $T = 10^{-2}$, $10^{-1}$, $10^{0}s$, separated into TE- and TM-mode contributions. TE-mode quantities are shown in panels **a)** and **b)** and are derived from the determinant of $\mathbf{Z}_E$. Corresponding TM-mode contributions are depicted in panels **c)** and **d)** and are calculated from the determinant of $\mathbf{U}_{M,h} + \mathbf{Z}_n$.

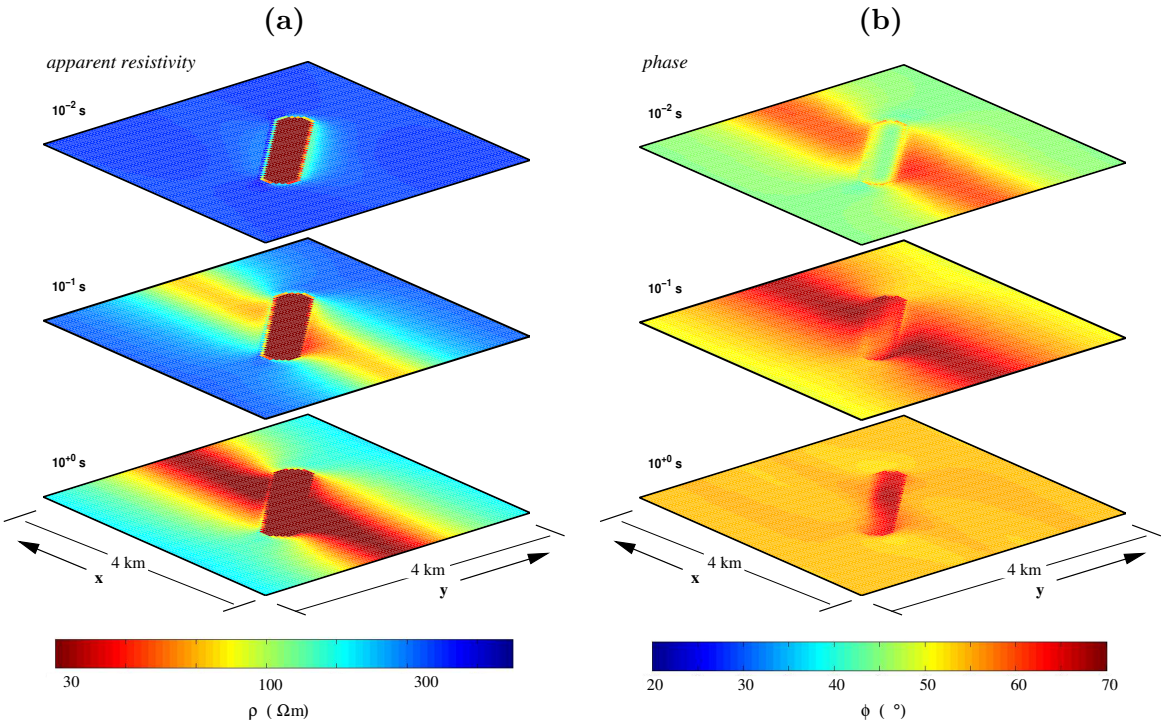


**Figure 3.6.:** Impedance tensor $\mathbf{Z}$. **a)** Determinant apparent resistivities and **b)** phases of the single site impedance tensor $\mathbf{Z}$ for three periods $T = 10^{-2}, 10^{-1}, 10^{0}s$. Apparent resistivities and phases can be conceived as a mixture of TE- and TM-mode quantities depicted in Figure 3.5. The TM-mode contribution from the shallow conductor causes serious distortion of the impedance response at longer periods.

horizontal electric field due to magnetic source fields polarized in $x-$ and $y-$direction, respectively, are shown in Figure 3.4. As can be deduced from non-vanishing arrows, anomalous TM-mode currents arise within the surface anomaly at all periods. This is in agreement with the vertical electric transfer function shown in Figure 3.2b. With increasing period, normal currents penetrate to the depth of the deeper conductor, and galvanic excess currents are excited in direction perpendicular to its strike. Again, the anomalies are much more focused in the TM-mode, but the contribution of the shallow conductor distorts the electric field even at long periods.

Mode separated apparent resistivities and phases calculated from the determinant of TE- and TM-mode impedances (cf. equations 3.18 and 3.19) are shown as color coded surface plots in Figure 3.5 for three periods $T = 10^{-2}, 10^{-1}, 10^{0}$ s from top to bottom. In the upper panels (3.5a and b) TE-mode apparent resistivities and phases are depicted, and in the lower panels (3.5c and d), corresponding TM-mode parameters are shown, respectively, using the same color scale as for TE-mode quantities. They may be compared with apparent resistivities and phases in Figure 3.6 representing the determinant of the full impedance tensor $\mathbf{Z}$, i.e. the impedance which would actually be derived from measurements. Again, it may be stated that TE- and TM-mode apparent resistivities and phases differ with respect to the depth of origin of anomalous field contributions at the surface. While pure TE-mode fields are not shadowed by the surface conductor at long period, the TM-mode and therefore also the full impedance tensor are severely effected in its vicinity.

It is evident from the results of the mode decomposition that - when analyzing single site impedances tensors - different types of information from different depth ranges are contained in the full impedance tensor. This effect has consequences on 2D inversion of MT impedance data, in particular if they are affected by 3D effects and/or galvanic distortion. Galvanic distortion is a special limiting case of 3D effects, and is discussed in detail in Chapter 4. Ordinary 3D effects lead to a fully occupied impedance tensor, where each of its element comprises a mixture of modes. When applying 2D inversion on 3D data, E- and B-Polarization have to be assigned to the off-diagonal elements of the tensor while neglecting the main-diagonal elements. Although each of the tensor elements contains both modes, anomalous fields assigned to E-Polarization are assumed to be purely of TE-mode and those assigned to B-Polarization are assumed to be purely of TM-mode. Hence, the 2D inversion code attempts to reproduce mode-mixed responses with either pure TE-mode or TM-mode in case of E-Polarization or B-Polarization, respectively. While supposed B-Polarization data will be fittable in most of the cases by introducing shallow anomalies into the subsurface, galvanic effects (TM-mode) polluting the supposed E-Polarization response are hardly reproduced permitting solely inductive (TE-mode) anomalous currents. Therefore, a higher misfit on E-Polarization data may be expected. Both cases are problematic. B-Polarization inversion does not promise to provide resolution a greater depths, as also reported by Ledo et al. (2002) from synthetic model studies. E-Polarization inversion occasionally will produce deep phantom structures in order to reproduce anomalous TM-mode effects at long periods due to shallow anomalies. Joint inversion of E- and B-Polarization data might improve the results, but no control is given about the reliability of the obtained resistivity model.

Although Ledo et al. (2002) recover to some extent the cross-section of their original 3D model using 2D inversion, I believe from the results suggested by mode separated responses that their results may not be generalized. In particular, their original model did not have any shallow 3D anomalies, but consisted only of structures at roughly one scale. Moreover, the galvanic distortion they artificially applied to their data in order to simulate the effect of small-scale anomalies, already in the limit of static distortion, did have shift factors fixed to unity. Hence, their model does not meet realistic cases of 3D effects resulting from shallow anomalies, but only includes regional 3D effects.

Without having conducted detailed tests using 3D data and 2D inversion codes, it can be stated that from the viewpoint of modes the most suitable responses for 2D inversion of 3D data are the induction arrows, since they are only of TE-mode and will be inverted as E-Polarization response function, which also has only TE-mode anomalous fields. As shown in (Pedersen and Becken, 2005) for a VLF example, the vertical magnetic field transfer function carries information about both anomalous currents and the background resistivity structure. The first is expressed in the strength of anomalous fields and the latter in terms of the spatial decay of anomalous fields. In MT applications, however, spatial coverage is often not good along the profile and the spatial decay of vertical magnetic field anomalies anomalies is not well defined. Therefore, it might be necessary to include presumed B-Polarization data into a joint inversion with induction arrows to improve control about the absolute values of resistivities. Static shift does not pose a problem in this case, since the inversion code can simulate static shift by placing shallow anomalies close to the surface.

## 3.5. An application to airborne tensor-VLF data

In Sweden, **v**ery-**l**ow-**f**requency (VLF) three-component magnetic data in the frequency range $14\text{-}25\,\mathrm{kHz}$ covering areas of several tens of thousand square kilometers have been collected by the Geological Survey of Sweden (SGU) during the last decade. By introducing the "tensor-VLF" concept in analogy to magnetotellurics, Pedersen et al. (1994) derived local vertical magnetic transfer functions for each measurement point. The Swedish data provide in both horizontal coordinates $(x, y)$ spatially well sampled magnetic transfer functions and are a suitable field data set to apply the spatial relations for the TE-mode as described in Chapter 3.1. The aim of this application was to construct images of the resistivity distribution, which provide a better structural insight into the earth compared to vertical magnetic transfer functions.

For this purpose, we (Becken and Pedersen, 2003) calculated TE-mode apparent resistivities and phases from local vertical magnetic transfer functions $\mathbf{T}(\mathbf{r})$. To obtain apparent resistivities and phases, which represent the conductivity structures very closely, we manipulated the determinant in such a way, that it closest resembles true apparent resistivities. Using the determinant of $\mathbf{Z}_E$ directly, anomalies are always underestimated. This can be anticipated from the 2D form of the TE-mode impedance tensor

$$\mathbf{Z}_E = \begin{pmatrix} 0 & Z_n + Z^a_{E,xy} \\ -Z_n & 0 \end{pmatrix} \ . \tag{3.20}$$

Taking the determinant of equation (3.20) is actually the geometric mean of the E-polarization impedance $Z_{E,2d} = Z_n + Z^a_{E,xy}$ and the normal impedance, respectively. Thus, apparent resistivities are biased by the normal structure, though the structure itself remains resolved. An alternative rotationally invariant of the impedance tensor can be used to overcome this problem. From equation (3.20), we can express the E-Polarization impedance $Z_{E,2d}$ via the determinant independent of the measurement coordinate system according to

$$Z_{E,2d} = \frac{\|\mathbf{Z}_E\|}{Z_n} \ , \tag{3.21}$$

since only rotationally invariants are involved. For 3D impedances, equation (3.21), which is a simple manipulation of the determinant, can be used as an optimal approximation to E-polarization. Note, that $Z_{E,2d}$ can be obtained without the critical step of rotation angle determination.

Synthetic examples as well as an application to field airborne data from Sweden are given in Becken and Pedersen (2003). The maps of TE-mode apparent resistivities and phases, which we produced from magnetic data only, show remarkable agreement with geological maps and are interpreted much more intuitively than magnetic transfer function alone.

# 4. Analysis of the single-site magnetotelluric impedance tensor

The aim of practical work in broad-band magnetotellurics (MT) is primarily to obtain high-quality sounding curves as a function of frequency, which demands relatively long recording times for subsequent spectral analysis. Typical frequency tables in MT range from $1\,\mathrm{kHz}$ to $1\,\mathrm{mHz}$, requiring recording times of at least $48\,\mathrm{h}$ at each point. Thus, the number of points to be measured during one campaign is limited, in particular if only few instruments are in use, and the spatial relations from the preceeding chapter are hardly applicable. The focus of MT-practitioners is instead basically on estimation, analysis and inversion of single-site transfer functions, i.e., the MT impedance tensor and vertical magnetic transfer functions. In fact, a number of conclusions may be drawn about the type of conductivity structure even from single-site transfer functions. Namely, the dimensionality and - in case of a 2D structure - the strike direction of the underlying geoelectrical structure may be inferred from both local vertical magnetic transfer functions and local impedance tensors.

Here, I will focus on the analysis of the local impedance tensor $\mathbf{Z}$ as obtained from single-site measurements. The magnetotelluric impedance tensor, which is estimated from magnetic *and* electric measurements, is complicated by the fact, that both TE and TM mode electric fields enter the transfer function. From a physical point of the view, TM mode electric fields substantially differ from TE-mode fields, since they reflect charge accumulations at lateral conductivity gradients, resulting in secondary electric fields, which can be of the same order as the primary electric field (Price, 1973). Neglecting displacement currents, charges accumulate, if $\mathbf{E}$ has a component parallel to the conductivity gradient. Then, they cause secondary electric fields due to Coulomb's law. If the anomalous domain $\nabla\sigma \neq \mathbf{0}$ becomes small compared to the skin-depth of the electromagnetic field in the surrounding medium, induction effects within become negligible, and the body acts as a so-called galvanic distorter. The local secondary electric fields $\mathbf{E}^l$ in the vicinity of a galvanic distorter becomes frequency-independent proportional to the undisturbed regional electric field $\mathbf{E}^r$ and oscillates in-phase. The total electric field, i.e. the superposition of regional and local constitutes, is a deflected and amplified version of the regional field. These effects may already be deduced from the results of the previously discussed mode decomposition of the electromagnetic field. There, it was observed, that shallow anomalies are evident in the TM-mode electric field components, even if the period corresponds to a much larger skin-depth than the dimensions of the anomalous body. The case of galvanic distortion can be conceived as the limiting case for long periods, when the anomalous TM-mode fields due to the distorting body oscillate in phase with the undistorted electric field.

This in-phase distortion is mathematically incorporated in terms of real matrices acting on the regional field and accounting for field rotations and amplifications while retaining the phase. Since by definition of galvanic distortion no secondary magnetic fields are to be observed, $\nabla \times \mathbf{E}^l = \mathbf{0}$ at the surface states that the observed local contribution to the electric field is curl-free and thus purely of TM-mode. This argument can be anticipated also from the results of the mode

decomposition illustrated in Figures 3.2 and 3.4, where no magnetic but only TM mode electric effects due to the shallow conductor are present at long periods. If such galvanic distortion affects the data, the regional response, which only is of interest, is partly hidden and interpretation of data is hampered.

Since spatial relations can in general not be applied to MT field data in order to separate the modes and in particular to separate 'regional induction and local distortion' (Bahr, 1988), other analysis schemes have been developed (Bahr, 1988; Groom and Bailey, 1989; Smith, 1995). These 'physical decompositions' (Groom and Bahr, 1992) may account for galvanic distortion and extract parameters of the regional impedance tensor as long as the regional structure is 2D. However, the absolute value of the impedance tensor elements may only be determined beside a shift factor, which is independent of frequency. The number of parameters, i.e. the number of degrees of freedom, which describe the impedance tensor under these circumstances is seven among which only three, namely the phases and the strike directions, are purely of regional cause.

In a new approach, Caldwell et al. (2004) introduced the so-called phase tensor, which is free of distortion even in presence of a 3D regional structure. They show, that their phase tensor elements contains all the information about the regional structure, which is not affected by galvanic distortion. The phase tensor has four degrees of freedom, while the impedance tensor has eight in the 3D case. Thus, half of the degrees of freedom is lost or hidden by galvanic distortion.

Alternatively to the galvanic distortion model, a mathematical decomposition is often used by MT practitioners in order to resolve characteristic properties of a 3D impedance tensor: LaTorraca et al. (1986) introduced a modified singular value decomposition (SVD), which is reformulated in terms of the canonical decomposition in Yee and Paulson (1987). These mathematical decompositions are attractive, since the tensor is fully parameterized with eight parameters and no a priori assumptions are required. Therefore, in contrast to the distortion analysis, the SVD never fails (at least theoretically). On the other hand, it may be considered a drawback of the method, that it is not directly related to any simplifying model, such as a locally distorted regional 2D structure. In practice, the SVD cannot recover the general distortion model with seven degrees of freedom. This is a consequence of the orthogonality restriction, which is pairwise imposed on the singular vectors, i.e., the principal components of the local electric and magnetic field. In case of six degrees of freedom, however, the SVD yields the same results as the distortion analysis.

We (Becken and Burkhardt, 2004) introduce an alternative physical parameterization, which combines the SVD approach and the distortion analysis. In contrast to the SVD, we permit a non-orthogonal basis for the electric polarization states, which is required to adequately account for a general type of galvanic distortion. When such a distortion model fits the data, one or two of the parameters automatically vanish in the regional coordinate system, while the other parameters are directly related to the regional impedances and local distortion parameters. It is shown, that the regional coordinate system is identified from vanishing ellipticities of the columns of the impedance tensor, i.e., the telluric vectors. Based upon our parameterization, an algorithm for simultaneously analyzing data at different stations and periods is proposed. Its implementation is very simple and yields stable results. In contrast to standard single site galvanic distortion analyses or the multi-site version of McNeice and Jones (2001), we search directly for the regional coordinate system by minimizing the ellipticities of the telluric vectors instead of fitting the distortion model to data. In regional coordinates, the distortion parameters including their error bars are then analytically determined.

If the impedance tensor represents a strong 3D structure with 3D inductive effects, our analysis does not fail, however the result may no longer be interpreted in terms of galvanic distortion. In

this case, one or both of the telluric vectors are elliptically polarized in any coordinate system. If one of the telluric vectors is found to be linearly polarized at a broad range of periods for one rotation angle, it may physically be connected to a linear polarization state of a electric field. Depending on the position with respect to a shallow conductor, this electric field is then either related to a magnetic source field polarized tangential or perpendicular to the conductor. I observe such cases in our synthetic model studies as well as in field data.

## 4.1. Theory

I start the magnetotelluric impedance tensor analysis in the following section by briefly revisiting the galvanic distortion model and its relation to the SVD. The ellipticity parameterization of the impedance tensor, which is the goal of this derivation, is then a straightforward task.

### 4.1.1. Galvanic distortion

Following Smith (1995), I assume that the measured local electric field $\mathbf{E}^l$ deviates from a regional electric $\mathbf{E}^r$ field due to local galvanic distortion according to the model $\mathbf{E}^l = \mathbf{D}\mathbf{E}^r$, where $\mathbf{D}$ is a real and frequency-independent electric distortion matrix. In absence of distortion, $\mathbf{D}$ is the identity matrix. Bahr's parameterization (Bahr, 1988)

$$\mathbf{D} = \begin{bmatrix} g_x \begin{pmatrix} \cos\beta_x \\ \sin\beta_x \end{pmatrix} & g_y \begin{pmatrix} -\sin\beta_y \\ \cos\beta_y \end{pmatrix} \end{bmatrix} \tag{4.1}$$

has a very intuitive meaning: Here, the gain factors $g_x$ and $g_y$ are the (static) shifts, amplifying the regional electric fields in the $x-$ and the $y-$directions, respectively. The real quantities $\beta_x$ and $\beta_y$ are the clockwise rotation angles of the regional $x-$ and $y-$field components. The measured (distorted) electric fields give rise to a distorted magnetotelluric impedance estimate $\mathbf{Z}^l$, which is related to the undistorted regional impedance $\mathbf{Z}^r$ as

$$\mathbf{Z}^l = \mathbf{D}\mathbf{Z}^r \ . \tag{4.2}$$

In general, none of the distortion parameters nor the elements of the regional impedance tensor can be deduced from (4.2) without further assumptions. Therefore, assuming that $\mathbf{Z}^r$ represents the response of a regional 2D structure, equation (4.2) reads in regional coordinates as

$$\mathbf{Z}^l = \begin{bmatrix} \cos\beta_x & -\sin\beta_y \\ \sin\beta_x & \cos\beta_y \end{bmatrix} \begin{bmatrix} 0 & g_y Z^r_{xy} \\ g_x Z^r_{yx} & 0 \end{bmatrix} \ . \tag{4.3}$$

In measurement coordinates (rotated clockwise with respect to regional coordinates), equation (4.3) reads as

$$\mathbf{Z}^{l'} = \mathbf{R}\mathbf{D}\mathbf{Z}^r\mathbf{R}^T \ , \tag{4.4}$$

where $\mathbf{R}$ is a clockwise rotation matrix, the superscript $T$ denotes matrix transpose, and the prime denotes the rotated matrix. From equation (4.3), it is seen, that in and only in regional coordinates do the elements of each column of $\mathbf{Z}^{l'}$ have a common phase. This criterion is employed to detect the regional coordinate system, in which the regional impedance tensor and the distortion matrix are uniquely separated aside from the gain factors $g_x$ and $g_y$.

Distortion analysis has become a standard tool of magnetotelluric tensor analysis and is applied to determine an appropriate rotation angle for 2D data analysis and occasionally to separate distortion from the regional signature. Successful examples of galvanic distortion analysis have been reported by many authors, of which a list can be found in McNeice and Jones (2001). Sometimes, however, distortion analysis does not provide a consistent picture. This is the case in the presence of strong 3D inductive effects.

### 4.1.2. SVD

The SVD of LaTorraca et al. (1986) of the $2\mathrm{x}2-$matrix $\mathbf{Z}$ yields two pairs of normalized complex right- and left-singular vectors $\mathbf{h}_i$ and $\mathbf{e}_i$, respectively, where $i = 1, 2$. Each pair forms an orthonormal basis in the sense

$$\begin{aligned} \mathbf{h}_i^* \cdot \mathbf{h}_j &= \delta_{ij} \\ \mathbf{e}_i^* \cdot \mathbf{e}_j &= \delta_{ij} \end{aligned} \tag{4.5}$$

such that

$$\begin{aligned} \mathbf{Z}\mathbf{h}_i &= r_i \mathbf{e}_i \\ \widetilde{\mathbf{Z}}\mathbf{e}_i &= r_i \mathbf{h}_i \end{aligned} \tag{4.6}$$

where the superscript * denotes complex conjugate, $\widetilde{\mathbf{Z}}$ is the hermitian transpose of $\mathbf{Z}$, $r_1 \geq r_2 \geq 0$ are the real singular values and $\delta_{ij}$ is the Kronecker delta. With the ellipse representation of a complex two-component vector described in Appendix A, the singular vectors can be uniquely rewritten in terms of ellipse parameters as

$$\mathbf{v} = e^{i\zeta} \left( a\widehat{\mathbf{a}} + ic\widehat{\mathbf{c}} \right) \tag{4.7}$$

with real major and minor axes $a$ and $c$ pointing into the directions of the unit vectors $\widehat{\mathbf{a}}$ and $\widehat{\mathbf{c}}$, respectively, where $\widehat{\mathbf{c}} = \widehat{\mathbf{z}} \times \widehat{\mathbf{a}}$, and an initial phase $\zeta$. Note, that my ellipse definition slightly deviates from that of LaTorraca et al. (1986). As shown in the following paragraph, using equation (4.7) leads immediately to the complex 'characteristic values' $\mu_i$ - the modified singular values suggested by LaTorraca et al. (1986) - which may physically be interpreted in terms of electromagnetic impedances.

I modify the singular vectors $\mathbf{e}_i$ and $\mathbf{h}_i$, defined from the SVD of an impedance tensor $\mathbf{Z}$ as

$$\mathbf{Z} = \left[ \begin{array}{cc} \mathbf{e}_1 & \mathbf{e}_2 \end{array} \right] \mathbf{Z}^r \left[ \begin{array}{cc} \mathbf{h}_1 & \mathbf{h}_2 \end{array} \right] \ , \tag{4.8}$$

using equation (A.4) as

$$\mathbf{e}_i' = \mathbf{e}_i e^{-i\zeta_{e,i}} = (a_{e,i}\widehat{\mathbf{a}}_{e,i} + ic_{e,i}\widehat{\mathbf{c}}_{e,i}) \tag{4.9}$$

and

$$\mathbf{h}_i' = \mathbf{h}_i e^{-i\zeta_{h,i}} = (a_{h,i}\widehat{\mathbf{a}}_{h,i} + ic_{h,i}\widehat{\mathbf{c}}_{h,i}) \ . \tag{4.10}$$

The modified SVD parameterization as suggested in LaTorraca et al. (1986) reads as

$$\mathbf{Z} = \mathbf{U}_e \mathbf{M} \widetilde{\mathbf{U}}_h \ . \tag{4.11}$$

where the phase modified singular vectors $\mathbf{e}_i'$ and $\mathbf{h}_i'$ are used as the columns of the matrices $\mathbf{U}_e$ and $\mathbf{U}_h$, respectively, instead of the singular vectors themselves. Expanding equation (4.11) yields directly for the elements of $\mathbf{M} = \mathrm{diag}\,(\mu_1, \mu_2)$

$$\mu_i = r_i e^{i(\zeta_{e,i} - \zeta_{h,i})} \quad . \tag{4.12}$$

Thus, the appropriate phase factors as defined in Appendix B in the paper of LaTorraca et al. (1986) are identified as the initial phases of the ellipse representation (A.4).

The orthogonality (4.5) of the singular vectors $(\mathbf{h}_i,\, \mathbf{h}_j)$ or $(\mathbf{e}_i,\, \mathbf{e}_j)$ is an important constraint on the analysis. It is given in terms of the ellipse parameterization (4.7) by

$$e^{i(\zeta_i - \zeta_j)}\,[a_i \widehat{\mathbf{a}}_i - i c_i \widehat{\mathbf{c}}_i] \cdot [a_j \widehat{\mathbf{a}}_j + i c_j \widehat{\mathbf{c}}_j] = \delta_{ij} \tag{4.13}$$

which states the normalization

$$a_i^2 + c_i^2 = 1 \tag{4.14}$$

for $i = j$ and the orthogonality

$$\widehat{\mathbf{a}}_i \cdot \widehat{\mathbf{a}}_j = 0 \;\;,\;\; \widehat{\mathbf{c}}_i \cdot \widehat{\mathbf{c}}_j = 0 \;\; (i \neq j) \tag{4.15}$$

of the ellipse axes except for circular polarization. Since $\widehat{\mathbf{a}}_i \cdot \widehat{\mathbf{c}}_i = 0$, it follows from condition (4.15), that $\widehat{\mathbf{a}}_i \cdot \widehat{\mathbf{c}}_j = \pm 1$, which can only be true from equation (4.13) if the ellipticities $|\epsilon_i| = |c_i/a_i|$ are the same for $i$ and $j$. Thus, non-orthogonal linear polarization states of some principal electric and/or magnetic field vectors are represented in orthogonal but elliptical polarization states. Therefore, the SVD of LaTorraca et al. (1986) is not suitable to describe the situation of galvanic distortion of regional 2D fields as defined in expressions (4.3) and (4.4), where the distorted electric field components constitute a non-orthogonal basis.

The modified SVD-parameterization of the impedance tensor reads in matrix notation as

$$\mathbf{Z} = \mathbf{U}_e \mathbf{M} \widetilde{\mathbf{U}}_h \;\;, \tag{4.16}$$

where the columns of the unitary matrices $\mathbf{U}_e$ and $\mathbf{U}_h$ are phase modified singular vectors $\mathbf{e}_i e^{-i\zeta_{e,i}}$ and $\mathbf{h}_i e^{-i\zeta_{h,i}}$, respectively, and $\mathbf{M} = \mathrm{diag}(\mu_1, \mu_2)$.

Theses characteristic impedances $\mu_i$ as well as the direction of singular vectors are supposed to give a better insight into the 3D conductivity distribution than the impedance tensor itself LaTorraca et al. (1986). However, the method was not designed with the background of a particular physical model as for instance the distortion model (4.2) is. It is therefore not surprising, that the modified SVD of a galvanically distorted 2D impedance of the form (4.3) generally does not yield the regional impedances nor the distortion parameters nor the regional strike direction, as reported for instance in Groom and Bailey (1991). The reason is given in terms of the orthogonality imposed on the singular vectors, while the distorted horizontal components of the regional electric field are at most incidentally orthogonal in the regional coordinate system. There are however some indications deducible from the outcome of the SVD, which point towards the existence of a (distorted) regional 2D structure. They have partly been reported in Groom and Bailey (1991) and are summarized and proven below.

### 4.1.3. The ellipticity of telluric vectors

Let us assume for simplicity, that according to equation (4.7) the local horizontal magnetic field

$$\mathbf{B} = e^{i\zeta_B} a_B \widehat{\mathbf{a}}_B \tag{4.17}$$

is linearly polarized with phase $\zeta_B$, amplitude $a_B$ and direction $\widehat{\mathbf{a}}_B$. The horizontal electric field $\mathbf{E} = \mathbf{ZB}$ is in general elliptically polarized and represented in the form

$$\mathbf{E} = e^{i\zeta_E} \left( a_E \widehat{\mathbf{a}}_E + i c_E \widehat{\mathbf{c}}_E \right). \tag{4.18}$$

Further assume a coordinate system, in which the magnetic field $\mathbf{B}_1$ is given with direction $\widehat{\mathbf{a}}_{B,1} = (1,\, 0)^T$ and the corresponding electric field $\mathbf{E}_1 = \mathbf{ZB}_1$ with $\widehat{\mathbf{a}}_{E,1} = (\cos\alpha_{E,1},\, \sin\alpha_{E,1})^T$ and $\widehat{\mathbf{c}}_{E,1} = (-\sin\alpha_{E,1},\, \cos\alpha_{E,1})^T$. Combining equations (4.17) and (4.18) with the impedance relation yields after rearrangement for the column vector $\mathbf{e}_x = (Z_{xx},\, Z_{yx})^T$

$$\mathbf{e}_x = e^{i\zeta_x} \left( a_x \widehat{\mathbf{a}}_{E,1} + i c_x \widehat{\mathbf{c}}_{E,1} \right) \quad , \tag{4.19}$$

where $a_x = a_{E,1}/a_{B,1}$ , $c_x = c_{E,1}/a_{B,1}$ , $\zeta_x = \zeta_{E,1} - \zeta_{B,1}$. The same parameterization applies to $\mathbf{e}_y = (Z_{xy},\, Z_{yy})^T$ for the magnetic field $\mathbf{B}_2$ with direction $\widehat{\mathbf{a}}_{B,2} = (0,\, 1)^T$ and the electric field $\mathbf{E}_2$ with $\widehat{\mathbf{a}}_{E,2} = (\cos\alpha_{E,2},\, \sin\alpha_{E,2})^T$ and $\widehat{\mathbf{c}}_{E,2} = (-\sin\alpha_{E,2},\, \cos\alpha_{E,2})^T$ yielding

$$\mathbf{e}_y = e^{i\zeta_y} \left( a_y \widehat{\mathbf{a}}_{E,2} + i c_y \widehat{\mathbf{c}}_{E,2} \right) \quad , \tag{4.20}$$

where $a_y = a_{E,2}/a_{B,2}$ , $c_y = c_{E,2}/a_{B,2}$ , $\zeta_y = \zeta_{E,2} - \zeta_{B,2}$. Following Bahr (1988), the columns of $\mathbf{Z}$ are referred to as telluric vectors. They obey the same polarization state as the input electric fields $\mathbf{E}_1$ and $\mathbf{E}_2$, i.e. they are oriented in the same direction and have the same ellipticity. Thus, the ellipse representation of electric and magnetic fields yields a parameterization of the impedance tensor in terms of elliptically polarized telluric vectors $\mathbf{e}_i$. Observe, that the normalized versions of $\mathbf{B}_1$ and $\mathbf{B}_2$ satisfy the orthogonality criterion (4.5) while $\mathbf{E}_1$ and $\mathbf{E}_2$ are not orthogonal.

Expanding expressions (4.19) and (4.20) for $\mathbf{Z}$ and substituting for notational simplicity $\alpha_x = \alpha_{E,1}$ and $\alpha_y = \alpha_{E,2}$ yields

$$\begin{aligned} \mathbf{Z} \;=\; & \begin{bmatrix} \cos\alpha_y & \cos\alpha_x \\ \sin\alpha_y & \sin\alpha_x \end{bmatrix} \begin{bmatrix} 0 & a_y e^{i\zeta_y} \\ a_x e^{i\zeta_x} & 0 \end{bmatrix} + \\ & \begin{bmatrix} -i\sin\alpha_y & -i\sin\alpha_x \\ i\cos\alpha_y & i\cos\alpha_x \end{bmatrix} \begin{bmatrix} 0 & c_y e^{i\zeta_y} \\ c_x e^{i\zeta_x} & 0 \end{bmatrix} \end{aligned} \tag{4.21}$$

Introducing the ellipticity $\epsilon_i = c_i/a_i$, equation (4.21) maybe rewritten as

$$\mathbf{Z} = \mathbf{C}\mathbf{Z}^{\mathbf{r}} \tag{4.22}$$

where

$$\mathbf{C} = \begin{bmatrix} \cos\alpha_y & \cos\alpha_x \\ \sin\alpha_y & \sin\alpha_x \end{bmatrix} + i \begin{bmatrix} -\epsilon_y \sin\alpha_y & -\epsilon_x \sin\alpha_x \\ \epsilon_y \cos\alpha_y & \epsilon_x \cos\alpha_x \end{bmatrix}$$

and

$$\mathbf{Z}^r = \begin{bmatrix} 0 & a_y e^{i\zeta_y} \\ a_x e^{i\zeta_x} & 0 \end{bmatrix}$$

Thus, the impedance tensor $\mathbf{Z}$ can be represented by an anti-diagonal 'characteristic impedance tensor' $\mathbf{Z}^r$ and a complex-valued matrix $\mathbf{C}$, describing the polarization characteristics.

The decomposition (4.22) of the impedance tensor is a full parameterization requiring eight degrees of freedom. Using elliptically polarized magnetic *and* electric fields at the same time yields indistinguishable parameterizations but with the loss of their simple interpretability in terms of field polarization ellipses. The parameters in expression (4.22) will rather be an algebraic mixture of the fields of both polarizations, as will be shown in section 4.1.3.2.

#### 4.1.3.1. Galvanic distortion model

Since the parameterization (4.22) covers all possible degrees of freedom in the given coordinate system, any rotation into another coordinate system, where the rotation angle is an additional parameter, introduces a dependency. Thus, two rotation angles $\delta_x$ and $\delta_y$ must exist, where one of the ellipticities $\epsilon_x$ and $\epsilon_y$ vanishes. If, in addition, $\delta_x = \delta_\mathrm{y}$, the number of degrees of freedom of the tensor drops to seven. In this case, the second addend of $\mathbf{C}$ in equation (4.22) vanishes and $\mathbf{C}$ becomes real. This states, with the review of equations (4.19) and (4.20), that the telluric vectors are linearly polarized while no restrictions are imposed on $\alpha_x$ and $\alpha_y$, i.e., the directions of the (now linearly) polarized electric field.

Physically, vanishing ellipticities of both telluric vectors in the same coordinate system may be interpreted in terms of linear polarization states of pairs of electric and magnetic fields, as can be deduced from equation (4.21) with $c_{x,y} = 0$. Such polarization states, if occurring independent of period, may only be observed in presence of a 1D earth or a 2D conductivity distribution, where in the latter case, the fields must be oscillating in the principal directions of the 2D structure. Otherwise, or in presence of a (strong) 3D distribution, the electromagnetic fields will generally be elliptically polarized. Galvanic distortion of the electric fields due to small inhomogeneities does not change their polarization states, but may alter their directions of oscillation. Therefore, $\alpha_{x,y}$ do only coincide with the coordinate axes in the absence of galvanic distortion.

By comparison of parameterizations (4.3) and (4.22) with $\epsilon_i = 0$,

$$g_x Z^r_{yx} = a_x e^{i\zeta_x} \ , \ g_y Z^r_{xy} = a_y e^{i\zeta_y} \ , \tag{4.23}$$

are identified as the regional impedances and

$$\alpha_x = \beta_y + \frac{\pi}{2} \ , \ \alpha_y = \beta_x \ , \tag{4.24}$$

are related to the distortion angles.

Therefore, I conclude, that if a coordinate system exists, in which the ellipticities of the telluric vectors $\mathbf{e}_x$ and $\mathbf{e}_y$ vanish, i.e., $\epsilon_x = \epsilon_y = 0$ for $\delta_x = \delta_y$, then the galvanic distortion model is satisfied, the underlying magnetic states are linear and orthogonal, and the electric states are linear but not necessarily orthogonal. This opens a strategy for seeking the regional coordinate system, which is formulated in section 4.1.4 in terms of an optimization problem.

If no such coordinate system exists, the tensor represents a strong 3D structure with eight degrees of freedom. Though the impedances in representation (4.22) can be considered as some type of characteristic impedances following LaTorraca et al. (1986), I can not connect them to a physical model simpler than a 3D model. Occasionally, the ellipse parameters might give better insight into the nature of the 3D problem than the pure impedance elements (apparent resistivities and phase) do. Such a case is discussed in the sequel and illustrated in section 4.2.2.2.

#### 4.1.3.2. 3D-effects

As I mentioned in the previous section, there always exists one rotation angle for each period, for which one of the ellipticities $\epsilon_x$ or $\epsilon_y$ must vanish. This rotation angle has not necessarily a physical relevance in terms of the polarization states of the horizontal electromagnetic field components, since it may be determined for any combination of elliptically polarized electric and magnetic fields.

However, due to different boundary conditions for the perpendicular and tangential components of the electric field at lateral contrasts, the polarization state of one of the telluric vectors will often be dominated by the corresponding horizontal electric field. This can be shown as follows: Assume two orthogonal normal magnetic fields $\mathbf{B}_{1,n} = B_n\widehat{\mathbf{x}}$ and $\mathbf{B}_{2,n} = B_n\widehat{\mathbf{y}}$, oscillating collinear with the coordinate axes. The total magnetic fields are then given by $\mathbf{B}_{1,2} = \mathbf{B}_{1,2,n} + \mathbf{B}_{1,2,a}$, where $\mathbf{B}_a$ denotes the anomalous fields, and are connected to the electric fields via the local impedance $\mathbf{Z}$ as $\mathbf{E}_{1,2} = \mathbf{Z}\mathbf{B}_{1,2}$. Following e.g. Zonge and Hughes (1991), the first column of the impedance tensor, i.e., the telluric vector $\mathbf{e}_x$ is given by

$$\mathbf{e}_x = \mathbf{E}_1 cB_{y,2} - \mathbf{E}_2 cB_{y,1} \ , \tag{4.25}$$

where $c = B_{x1}B_{y2} - B_{x2}B_{y1}$ may be regarded as a complex constant. Each of the electric field vectors may be rewritten in terms of the ellipse parameterization (4.18) yielding

$$\mathbf{e}_x = ca_{E,1}B_{y,2}\widetilde{\mathbf{e}}_{E,1} - ca_{e,2}B_{y,1}\widetilde{\mathbf{e}}_{E,2} \ , \tag{4.26}$$

where $\widetilde{\mathbf{e}}_{E,1,2}$ are the electric field ellipses normalized by their major axes $a_{E,1,2}$, i.e., by the amplitude of the electric field vector. A similar parameterization applies to $\mathbf{e}_y$:

$$\mathbf{e}_y = -ca_{E,1}B_{x,2}\widetilde{\mathbf{e}}_{E,1} + ca_{e,2}B_{x,1}\widetilde{\mathbf{e}}_{E,2} \ . \tag{4.27}$$

Thus, the telluric vector $\mathbf{e}_x$ ($\mathbf{e}_y$) is generally the superposition of the normalized electric fields scaled by their amplitudes $a_E$ and the amplitude of the magnetic field components in $y-$direction ($x-$direction). In the 2D case (including galvanic distortion), equations (4.26) and (4.27) reduce to equations (4.19) and (4.20) with $c_{x,y} = 0$, respectively, since $B_{y,1}$ and $B_{x,2}$ vanish identically in a coordinate system aligned with the strike direction.

Let me now consider a 3D conductivity distribution with a conductive surface anomaly, and let the $x-$axis be tangential to the shallow conductivity contrast. Then, the fields $\mathbf{B}_1, \mathbf{E}_1$ may be considered as 'local' B-Polarization (i.e., the normal part of $\mathbf{E}_1$ is oriented normal to the contrast), while $\mathbf{B}_2, \mathbf{E}_2$ are in 'local' E-Polarization (normal part of $\mathbf{E}_2$ tangential to the contrast). In the vicinity of the lateral contrast, but on the resistive side, the electric field in local B-Polarization (more precisely: the component normal to the contrast) is amplified due to the galvanic-like charge accumulation at the discontinuity, while the electric field in local E-Polarization is attenuated. Hence, $a_{E,1} > a_{E,2}$. Moreover, $|B_{y,2}| = |B_n + B_{a,y,2}| > |B_{y,1}| = |B_{a,y,1}|$, since the anomalous magnetic field is usually smaller than the normal magnetic field. Combining the two inequalities yields for many cases a domination of the corresponding telluric vector by the local B-Polarization electric field on the resistive side of the conductivity contrast (even in the presence of 3D effects) due to $|a_{E,1}B_{y,2}| >> |a_{E,2}B_{y,1}|$, i.e.,

$$\mathbf{e}_x \simeq ca_{E,1}B_{y,2}\widetilde{\mathbf{e}}_{E,1} \ . \tag{4.28}$$

On the other hand, $|B_{x,1}| = |B_n + B_{a,x,1}| > |B_{x,2}| = |B_{a,x,2}|$, which means, that in review of equation (4.27) the contribution of the strong local B-Polarization electric field $\mathbf{E}_1$ to the telluric

vector $\mathbf{e}_y$ is scaled down (but may not be neglected in the 3D case), while the weaker local E-Polarization electric field $\mathbf{E}_2$ becomes more important. Thus, an approximate interpretation of $\mathbf{e}_y$ in terms of the polarization of the electric field is in this coordinate system not possible. It will rather reflect the 3D response.

On the conductive side of the contrast, the situation is different. Here, the local B-Polarization electric field is strongly attenuated due to the charge accumulation. Thus, $a_{E,1} < a_{E,2}$, which gives in conjunction with the inequalities for the magnetic field, that

$$\mathbf{e}_y \simeq -ca_{E,2}B_{x,1}\mathbf{e}_{E,2} \ . \tag{4.29}$$

For $\mathbf{e}_x$ no simplifying approximation applies.

Therefore, I conclude, that, in the given coordinate system, one of the telluric vectors ($\mathbf{e}_x$ on the resistive side and $\mathbf{e}_y$ on the conductive side) basically represents the polarization state of one electric field vector ($\mathbf{E}_1$ and $\mathbf{E}_2$, respectively).

Assume now further, that for some reason these electric fields are predominantly linearly polarized and aligned with the coordinate axes, i.e., that $\mathbf{E}_1 \simeq E_n\widehat{\mathbf{y}} + E_{y,1,a}\widehat{\mathbf{y}}$ on the resistive side and $\mathbf{E}_2 \simeq E_n\widehat{\mathbf{x}} + E_{x,2,a}\widehat{\mathbf{y}}$ on the conductive side, which is in agreement with the previous approximations. This has the consequence, that on the resistive side of the shallow anomaly, the amplitude of $Z_{xx}$ is small and those of $Z_{xy}$, $Z_{yx}$ and $Z_{yy}$ can be strong, while on the conductive side, the amplitude of $Z_{yy}$ is small and those of $Z_{xx}$, $Z_{xy}$ and $Z_{yx}$ can be strong. Thus, an explanation could be given for the observation, that in a particular coordinate system, i.e. the local coordinate system, the tensor is often composed of three large and one small element. If, additionally, galvanic distortion is present, all four elements might be large, but the ellipticity of the linearly polarized telluric vector remains unchanged, i.e., linear, as can be easily seen from equation (4.2) with either $Z^r_{xx} = 0$ or $Z^r_{yy} = 0$.

The validity of the approximations given here may not be generalized, but depends on the particular conductivity model. However, in the later discussed synthetic example 2, I recover the above described properties of the impedance tensor, and I am also aware of many field data showing such a behavior.

### 4.1.4. Minimization of ellipticities by rotation

I have shown in section 4.1.3.1 that a solution to the galvanic distortion problem can be obtained in terms of vanishing ellipticities of the telluric vectors. For a numerical treatment, the optimization problem is formulated as follows: find the coordinate system $\delta$, in which the ellipticities of the telluric vectors are minimal. Thus,

$$F(\mathbf{R}(\delta)\mathbf{Z}\mathbf{R}(\delta)^{-1}) = \min! \ , \tag{4.30}$$

where $\mathbf{F}(\delta)$ is a function yielding the sum of squared ellipticities $\epsilon_i^2(\mathbf{e}_i)$ in the rotated coordinate system, e.g.

$$F(\delta) = \sum_{i=1}^{2} \epsilon_i^2(\mathbf{e}_i) \ . \tag{4.31}$$

The ellipticities are analytically calculated with formulas (A.7) (Appendix A) from rotated impedances. In the case of real data, the derived ellipticities contain errors and a weighting is required when

simultaneously considering both vectors. Letting $\sigma_{\epsilon_i}$ be the standard deviation of $\epsilon_i(\mathbf{e}_i)$, the optimization problem is weighted according to

$$F(\delta) = \sum_{i=1}^{2} \left(\epsilon_i^2(\mathbf{e}_i)/\sigma_{\epsilon_i}^2\right) \quad . \tag{4.32}$$

In order to stabilize the problem, one might want to include several periods $p = 1, \ldots, P$ and sites $k = 1, \ldots, K$ as suggested by McNeice and Jones (2001). This is easily accomplished by expanding expression (4.32) to

$$F(\delta) = \sum_{k=1}^{K} \sum_{p=1}^{P} \sum_{i=1}^{2} \left(\epsilon_{i,k,p}^2(\mathbf{e}_{i,k,p})/\sigma_{\epsilon_{i,k,p}}^2\right) \quad . \tag{4.33}$$

As $F(\delta)$ is a scalar function dependent on only one variable, minimization is quite simple. Here, I use a combination of golden section search and parabolic interpolation, an algorithm, found in many mathematical computer packages (e.g. Matlab). Alternatively, following Zhang et al. (1987) one can rotate stepwise through the interval $0 < \delta \leq \pi/2$, determining the strike angle as that angle which yields a minimum $F(\delta)$ .

Having found an appropriate rotation angle $\delta$, all parameters ($a_x$, $a_y$, $c_x$, $c_y$, $\zeta_x$, $\zeta_y$, $\alpha_x$, $\alpha_y$) for each site and period may be derived analytically from the rotated impedance tensor $\mathbf{Z}^l$. Moreover, the associated error bars are calculated by linear error propagation using the equations of Appendix A. For ideal regional 2D data, all $c_i = 0$, but in practice, this will not hold true when a broad period band and site range are simultaneously minimized.

The local strike direction, introduced in section 4.1.3.2, may be determined by minimizing the ellipticity of only one telluric vector, say $\mathbf{e}_y$ for a number of periods simultaneously. It does not make sense to permit for a multiple site analysis, since the local strike may change form site to site. Therefore, I define the solution $\delta_y$ of

$$F(\delta) = \sum_{p=1}^{P} \left(\epsilon_{y,p}^2/\sigma_{\epsilon_{y,p}}^2\right) = \min! \ , \tag{4.34}$$

as the 'local strike'. Note, that in contrast to the regional strike direction, $\delta_y$ has an ambiguity of $180°$.

## 4.2. Synthetic examples

### 4.2.1. Example 1 - Galvanic distortion analysis

To illustrate the performance of the optimization routine proposed above, I consider a synthetic data example with defined statistical parameters. Here, I take a 2D regional apparent resistivity tensor with strike direction $\delta = 0\,°$ and off-diagonal apparent resistivities and phases $\rho_{xy} = 300\,\Omega\mathrm{m}$, $\rho_{yx} = 150\,\Omega\mathrm{m}$, $\phi_{xy} = 30\,°$ and $\phi_{xy} = 41\,°$, respectively. From these data, 31 regional impedance tensors have been constructed for the period range from $0.001 - 100\,\mathrm{s}$. Galvanic distortion of the impedances is generated using equation (4.3) with $g_x = g_y = 1$, $\beta_x = 23\,°$ and $\beta_y = -27\,°$. To produce noisy realizations, Gaussian noise with a standard deviation of $5\,\%$ of the largest impedance magnitude and modified with a random phase between $0\,°$ and

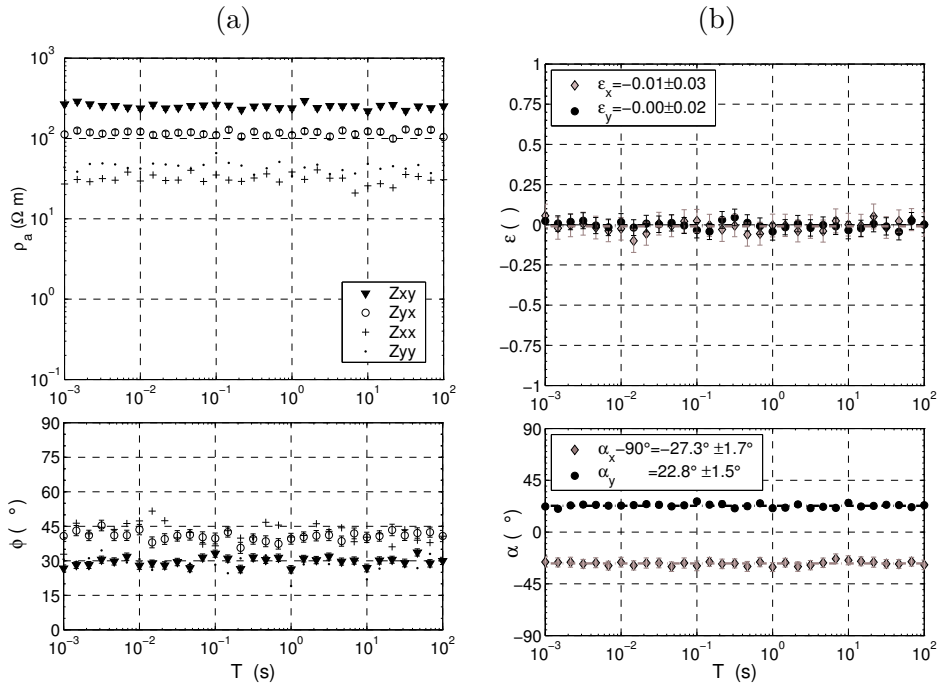


**Figure 4.1.:** Example 1: a) 31 Noisy and distorted realizations of apparent resistivities and phases for testing the performance of the minimization routine. The distortion matrix is constructed with distortion angles $\beta_x = 23°$ and $\beta_y = -27°$ and unity gain factors. b) Ellipticities $\epsilon_x$ and $\epsilon_x$ and related directions of major axes $\alpha_x$ and $\alpha_y$ determined from joint optimization of 31 periods. Symbols indicate individual estimates in the regional coordinate system, dash-dotted lines denote their weighted means.

$360\,°$ was added to the distorted tensor at each period. These data, shown in Figure 4.1a, are comparable to those from the first example of McNeice and Jones (2001), since the ratio of apparent resistivities, the phases, distortion parameters and noise level are similar. However, in contrast to McNeice and Jones (2001), I take into account the period dependence inherent in the impedances, which should cancel out in the ellipticities of the telluric vectors.

Minimizing equation (4.33) yields a regional strike direction $\delta^o = -0.3\,°$, which is close to the true strike. Here, the superscript $o$ denotes the optimal estimates. In this coordinate system, ellipticities and distortion angles have been calculated with the formulas (A.8) and (A.10) of Appendix A1 and their associated standard deviations from the variances given in Appendix A3 and A4. They are depicted in Figure 4.1. Open circles and triangles correspond to parameters derived from the first ($\mathbf{e}_x$) and second column ($\mathbf{e}_y$) of the tensor, respectively. Dash-dotted lines in Figure 4.1b indicate the weighted means of the related parameter distributions. A quality criterion of the optimization is given in terms of weighted mean ellipticities and the standard deviation of the individual estimates from their mean.

For this example, $\overline{\epsilon}^o_x(\mathbf{e}_x) = -0.01 \pm 0.03$ and $\overline{\epsilon}^o_y(\mathbf{e}_y) = 0.00 \pm 0.02$, indicating a correct determination of the regional coordinate system. Distortion angles are constant with respect to frequency and recovered with mean values $\overline{\alpha}^o_x - 90\,° = -27.3 \pm 1.7\,°$ and $\overline{\alpha}^o_y = 22.8 \pm 1.5\,°$, close to the true values of $\beta_y$ and $\beta_x$. Major axes $a^o_x$ and $a^o_y$ of the telluric vectors are related to the regional apparent resistivities $\rho^o_{yx}$ and $\rho^o_{xy}$, and their phases $\phi^o_{yx}$ and $\phi^o_{xy}$ are given by the

initial phases $\zeta_x^o$ and $\zeta_y^o$, respectively. Their mean values are recovered to $\overline{\rho}_{xy}^o = 300.1 \pm 13.6\,\Omega\mathrm{m}$, $\overline{\rho}_{yx}^o = 152.9 \pm 9.3\,\Omega\mathrm{m}$ and $\overline{\phi}_{xy}^o = 29.9 \pm 1.2\,^\circ$, $\overline{\phi}_{yx}^o = 42.0 \pm 1.8\,^\circ$, which is again close to the true values. Note, that the standard deviation of the individual estimates is of the order of the noise level added to the data previously. This verifies, that the propagation of errors does not introduce severe bias in error levels.

Alternatively, the regional impedances may be obtained from inversion of equation (4.3), if the distortion parameters are determined. Here, I used the mean of the distortion angles $\overline{\alpha}_x^o - 90\,^\circ$ and $\overline{\alpha}_y^o$ in order to construct the inverse of the distortion matrix $\mathbf{D}^{-1}$ and derived an estimate of the regional impedance in rotated coordinates with $\mathbf{Z}^r = \mathbf{D}^{-1}\mathbf{Z}$. This leads to regional apparent resistivities and phases $\overline{\rho}_{xy}^o = 292.2 \pm 18.5\,\Omega\mathrm{m}$ , $\overline{\rho}_{yx}^o = 154.7 \pm 15.6\,\Omega\mathrm{m}$, $\overline{\phi}_{xy}^o = 30.3 \pm 1.9\,^\circ$ and $\overline{\phi}_{yx}^o = 41.6 \pm 2.9\,^\circ$, respectively. These results are slightly less accurate than those obtained from the ellipse parameters. I do not generalize this, because the generation of synthetic noise and error bars might not meet real conditions exactly. Furthermore, real data are never exactly 2D such that the main-diagonal elements of the impedance tensor vanish exactly as assumed when interpreting the ellipse major axes as regional impedance magnitudes. Nevertheless, this somewhat unrealistic example demonstrates, that our algorithm produces statistically reasonable and reproducible results with an accuracy similar to that reported in McNeice and Jones (2001).

### 4.2.2. Example 2 - A 3D model

The same 3D model as in Chapter 3 is used for a more realistic model study, and schematically illustrated in Figure 3.1. As the model has been designed, it does not only produce distorted 2D fields, but also generates strong 3D-effects within the modeled period range. Therefore, the model is suitable to demonstrate both the distortion analysis and the parameterization of a 3D-impedance.

The data at seven locations s01 - s07 along a profile perpendicular to the regional (lower) conductor and with a site separation of $100\,\mathrm{m}$ (Figure 4.2) are first considered in this model study. They have been contaminated with $5\%$ Gaussian noise as in the previous example. All sites exhibit 3D effects between $0.1 - 100\,\mathrm{s}$. Upon inspection, the data can be classified into three subsets: the short-period part ($\sim 0.001 - 0.005\,\mathrm{s}$ for stations s01-s04, located outside of the surface conductor, and $\sim 0.001 - 0.025\,\mathrm{s}$ for stations s05-s07, placed on the top of the surface anomaly) is predominantly sensitive to the shallow conductor. Between $\sim 0.01 - 1\,\mathrm{s}$, depending on the station, data are strongly 3D, since the fields are sensitive to both the shallow and the deep conductor. For periods longer than a few seconds, the skin-depth exceeds several kilometers and currents are predominantly induced in the deeper, regional structure. However, the surface conductor continues to act on the regional electric fields as a galvanic distorter even when the anomalous magnetic fields induced within become negligible. Thus, 3D-effects should be explained with a distortion model.

#### 4.2.2.1. Strike detection and galvanic distortion analysis

The period subsets defined above span a range of periods, because their sensitivities to the conductors vary between stations depending on the distance to them. For the short-period part, I have grouped and simultaneously analyzed stations s01-s04 and s05-s07 in the period ranges given above, respectively. In the long-period section, all stations have been grouped together for the purpose of a multi-site and multi-period regional strike detection. All sites in each group are

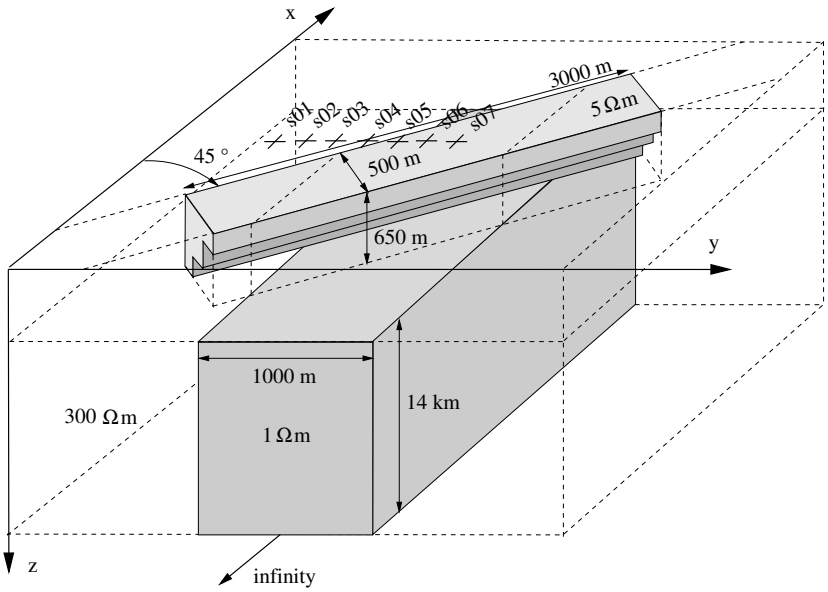


**Figure 4.2.:** Example 2: Sketch of the 3D-model (cf. Figure 3.1). The model attempts to represent a combination of 2D, strong 3D and regional 2D-structure with local distortion for small, medium and large skin-depths, respectively. It serves here to illustrate the ellipticity analysis, which has been applied to synthetic impedance tensors, generated with a 3D modeling program. A profile with seven stations s01-s07 is indicated, for which a of set of noise contaminated impedance tensors has been created. They were subjected to the multi-site multi-period optimization routine in order to determine the geoelectric strike direction.

treated equally for simplicity. The period range, for which the retrieved strike direction is actually valid, may be determined later by inspecting the ellipticities at each site individually.

In Table 4.2.2.1, the results of a joint analysis are listed for all sites. Within the short-period band, the first group recovers a strike direction of $\delta^o = 46.3\,^\circ$, while the second group yields $\delta^o = 46.9\,^\circ$; both close to the true direction of $\delta = 45.0\,^\circ$. In both groups, mean ellipticities (here: root mean square of $\overline{\epsilon}_x^o$ and $\overline{\epsilon}_y^o$) and distortion angles $\overline{\beta}_x^o$ and $\overline{\beta}_y^o$ nearly vanish, as can be seen in Table 4.2.2.1a and b. Thus, the 2D surface structure is clearly expressed in the ellipse parameters.

In the long period band (Table 4.2.2.1c), $\delta^o = -0.6\,^\circ$ was found to be the optimal regional strike angle. In this coordinate system, both ellipticities again vanish, indicating the existence of a regional 2D structure at long periods. However, the orientation of ellipse axes $\alpha_x^o$ and $\alpha_y^o$ deviate strongly from the regional coordinate system. This effect is the result of local distortion due to the surface anomaly. According to the distortion angles $\overline{\beta}_x^o$ and $\overline{\beta}_y^o$, the sites may again be classified into two groups. Sites s01-s04, having positive $\overline{\beta}_y^o$ and negative $\overline{\beta}_x^o$, are located adjacent to the shallow conductor. In contrast, the distortion angles at stations s05-s07 located above the conductor have opposite sign. Effectively, the rotation of the regional field components adjacent to the surface conductor is less severe than above the conductor. In particular, at stations s05-s07, the regional $E_x^r$ component (in the $-0.6$ rotated coordinate system) is rotated clockwise into the strike direction of the surface structure, while $E_y^r$ is rotated counterclockwise due to distortion. Thus, the surface electric field is strongly polarized in the direction of the local structure. In real measurements, such a case will result in poor correlation between the local magnetic and electric

Example 2: Ellipse parameters from joint minimization.

| Site | $\overline{\epsilon}^o = \sqrt{\overline{\epsilon}_x^{o2} + \overline{\epsilon}_y^{o2}}$ | $\overline{\alpha}_x^o - 90\,^\circ = \overline{\beta}_y^o$ | $\overline{\alpha}_y^o = \overline{\beta}_x^o$ |
|---|---|---|---|
| **a)** | $0.001 - 0.006\,s$ | $\delta^o = 46.3\,^\circ$ | s01-s04 |
| s01 | $0.01 \pm 0.04$ | $0.9 \pm 0.6$ | $0.2 \pm 2.4$ |
| s02 | $0.03 \pm 0.04$ | $0.0 \pm 0.9$ | $0.5 \pm 2.5$ |
| s03 | $0.01 \pm 0.04$ | $0.6 \pm 1.4$ | $1.3 \pm 2.0$ |
| s04 | $0.05 \pm 0.05$ | $1.3 \pm 0.8$ | $0.6 \pm 3.7$ |
| **b)** | $0.001 - 0.025\,s$ | $\delta^o = 46.9\,^\circ$ | s05-s07 |
| s05 | $0.01 \pm 0.04$ | $0.8 \pm 3.3$ | $-1.2 \pm 0.7$ |
| s06 | $0.01 \pm 0.05$ | $-0.8 \pm 2.0$ | $0.4 \pm 0.9$ |
| s07 | $0.02 \pm 0.06$ | $-0.2 \pm 1.3$ | $-0.4 \pm 1.7$ |
| **c)** | $4\,s - 100\,s$ | $\delta^o = -0.6\,^\circ$ | s01-s07 |
| s01 | $0.00 \pm 0.04$ | $10.5 \pm 1.2$ | $-18.5 \pm 2.2$ |
| s02 | $0.01 \pm 0.03$ | $16.1 \pm 1.4$ | $-20.1 \pm 1.9$ |
| s03 | $0.02 \pm 0.03$ | $23.5 \pm 1.1$ | $-19.6 \pm 1.2$ |
| s04 | $0.03 \pm 0.04$ | $23.7 \pm 1.5$ | $-10.1 \pm 2.4$ |
| s05 | $0.02 \pm 0.02$ | $-37.7 \pm 1.2$ | $41.6 \pm 1.2$ |
| s06 | $0.03 \pm 0.03$ | $-35.3 \pm 1.3$ | $41.0 \pm 1.5$ |
| s07 | $0.03 \pm 0.04$ | $-35.4 \pm 1.6$ | $41.0 \pm 1.4$ |

Root mean square ellipticities $\overline{\epsilon}^o$ and mean distortion angles $\overline{\beta}_x^o$, $\overline{\beta}_y^o$ in the optimal coordinate system $\delta^o$ estimated by multi-site multi-period analysis. **a)** Results for group s01-s04 and periods $0.001 - 0.006\,s$. **b)** Results for group s05-s07 and periods $0.001 - 0.025\,s$. **c)** Results for group s01-s07 and periods $1 - 100\,s$. The given standard deviation of the parameters from their weighted mean indicates the consistency of the parameters with respect to the frequency band.

components parallel and perpendicular to the local structure, respectively, due to strong current channeling in the direction of the surface anomaly.

The above stated results are illustrated as a top view map in Figure 4.3 for the period $T = 100\,\mathrm{s}$ using stations covering the whole model area. Telluric vectors $\mathbf{e}_x$ (gray) and $\mathbf{e}_y$ (black) are plotted as ellipses (normalized by their major axes) after rotation of the impedance tensor into the regional coordinate system (which coincides in this model study with the measurement coordinate system). The position of the regional conductor is indicated by the dash-dotted lines, the solid lines mark the boundary and strike direction of the local structure. In the absence of distortion, the regional vector $\mathbf{e}_x^r = \left(0,\, Z_{yx}^r\right)^T$ would be linearly polarized and oriented perpendicular to the regional strike, i.e., to the dashed line, while $\mathbf{e}_y^r = \left(Z_{xy}^r,\, 0\right)^T$ would be parallel. Rotation of the telluric vectors is observed due to the presence of the surface anomaly, however they remain linearly polarized. Thus, the case of galvanic distortion is met. Outside of the surface anomaly, the $E_y^r-$component ($\mathbf{e}_x^r$) is rotated clockwise pointing towards the local conductor, while the $E_x^r-$component ($\mathbf{e}_y^r$), is slightly rotated counterclockwise. Above the local conductor (in between the solid lines), the rotation of the regional fields is more dramatic. Because of distortion, both telluric vectors and thus both regional electric field components are rotated into the direction of the surface conductor, being almost parallel to each other.

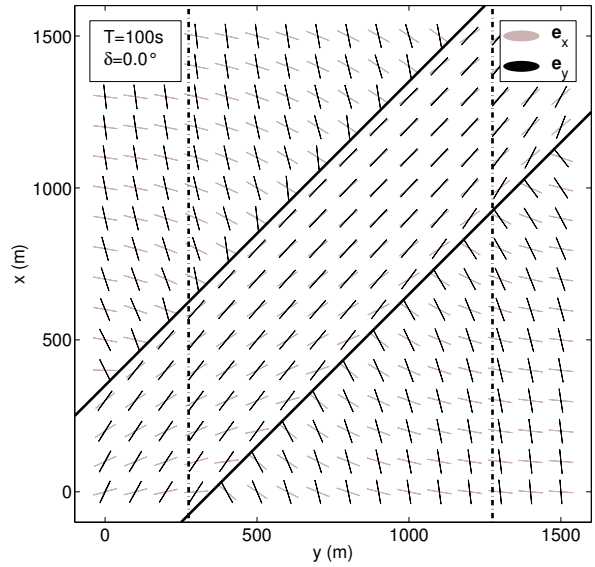


**Figure 4.3.:** Example 2: Ellipses (normalized by the length of their major axes), calculated for the period $T = 100\,\mathrm{s}$ in the regional coordinate system ($0\,^\circ$), representing the polarization state of telluric vectors. Dash-dotted and solid lines indicate strike direction and boundaries of the regional and local structure, respectively. The telluric vectors are linearly polarized and rotated out off the regional coordinate system. Hence, they indicate a regional 2D structure with strong galvanic distortion effects.

Hence, the results given Table 4.2.2.1c, where the regional strike and galvanic distortion parameters were calculated from stations s01 - s07 in the period range $4 - 100\,\mathrm{s}$, are representative for the whole model area. I may therefore conclude, that the 3D-effects observed in the long period band are consistently identified as galvanic effects from the shallow distorter, and the regional coordinate system is determined with satisfying accuracy by multi-site multi-period minimization of the ellipticities of the telluric vectors.

#### 4.2.2.2. 3D-effects

At medium skin-depths, both subsurface anomalies contribute to the observed response. The tensor is strongly 3D and no coordinate system is found, in which both telluric vectors are linearly polarized for a range of periods. Thus, galvanic distortion models assuming a regional 2D structure cannot adequately represent the tensor. However, using the approximations of section 4.1.3.2, I can understand some of the information contained in the 3D response.

In Figure 4.4a and 4.4b, I have plotted the ellipticities and angles of major axes vs. period for the sites s03 adjacent to and s06 above the surface conductor (compare Figure 4.2, where the location of the stations is indicated) in a fixed $45\,^\circ$ rotated frame, i.e., with the $x-$axes in strike direction of the local structure. Ellipse parameters of $\mathbf{e}_x$ and $\mathbf{e}_y$ are depicted in gray filled diamonds and black filled circles, respectively. The ellipticity of the telluric vector $\mathbf{e}_x$ at s03 is approximately zero for all periods ($\overline{\epsilon}_x = -0.01 \pm 0.04$), while $\overline{\epsilon}_y = 0.00 \pm 0.21$ depends on period, which is expressed in a large standard deviation. Above the conductor (site s06), $\overline{\epsilon}_y = 0.00 \pm 0.02$ vanishes, while $\overline{\epsilon}_x = 0.04 \pm 0.26$ is a function of period, respectively. Note also, that in coincidence with the corresponding ellipticity, the orientation of ellipses is either stable ($\overline{\alpha}_x = -1.0^\circ \pm 2.4^\circ$ at site s03

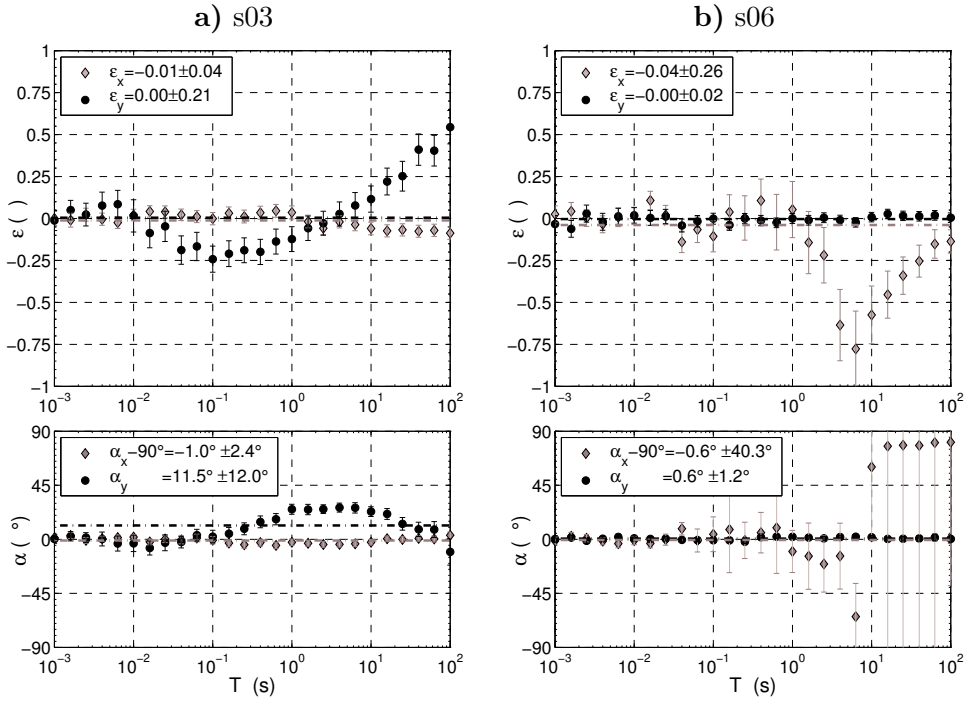


**Figure 4.4.:** Example 2: Ellipse parameters of telluric vectors in the local coordinate system $\delta = 45\,^\circ$. Ellipticities $\epsilon_{x,y}$ and direction of major axes of ellipses $\alpha_{x,y}$ for **a)** station s03 adjacent and **b)** station s06 above of the local conductor. Weighted means of parameters are indicated by dash-dotted lines. One of the telluric vectors is approximately linearly polarized at all periods and indicates local B-Polarization (s03) and local E-Polarization (s06), respectively.

and $\overline{\alpha}_y = 0.6^\circ \pm 1.2^\circ$ at site s06) or a function of period ($\overline{\alpha}_y = 11.5^\circ \pm 12.0^\circ$ at site s03 and $\overline{\alpha}_x = -0.6^\circ \pm 0.26^\circ$ at site s06), respectively.

Suppose now, that the approximations (4.28) and (4.29) are valid. Then, for the present example, the polarization state of $\mathbf{e}_x$ at site s03 and $\mathbf{e}_y$ at site s06 approximately corresponds to the electric field associated with a normal magnetic field tangential and normal to the local anomaly, respectively. Here, I observe, that these telluric vectors and therefore the corresponding electric fields are predominantly linearly polarized over the whole period range, which was already anticipated previously. For an explanation, take into account that (a) the electric field of local B-Polarization adjacent to the contact dips in $(y, z)$-plane due to vertical current flow, but its projection into the horizontal plane is again dominated by the charge accumulation at the shallow lateral interface even in the presence of 3D effects and that (b) within the surface anomaly, currents are strongly channeled, which in particular applies to those currents with the normal part in strike direction of the channel. Thus, the electric field in local B-Polarization adjacent to the contact and in local E-Polarization above the conductor exhibit approximately a linear polarization state, which is reflected in vanishing ellipticities of the telluric vectors in Figure 4.4a and b, respectively.

By using the optimization scheme given in expression (4.34), I may estimate for each site the coordinate system, in which one of the telluric vectors (here: $\mathbf{e}_y$) has minimal ellipticity for a range of periods. This coordinate system was referred to as local strike. Since at sites s03 and

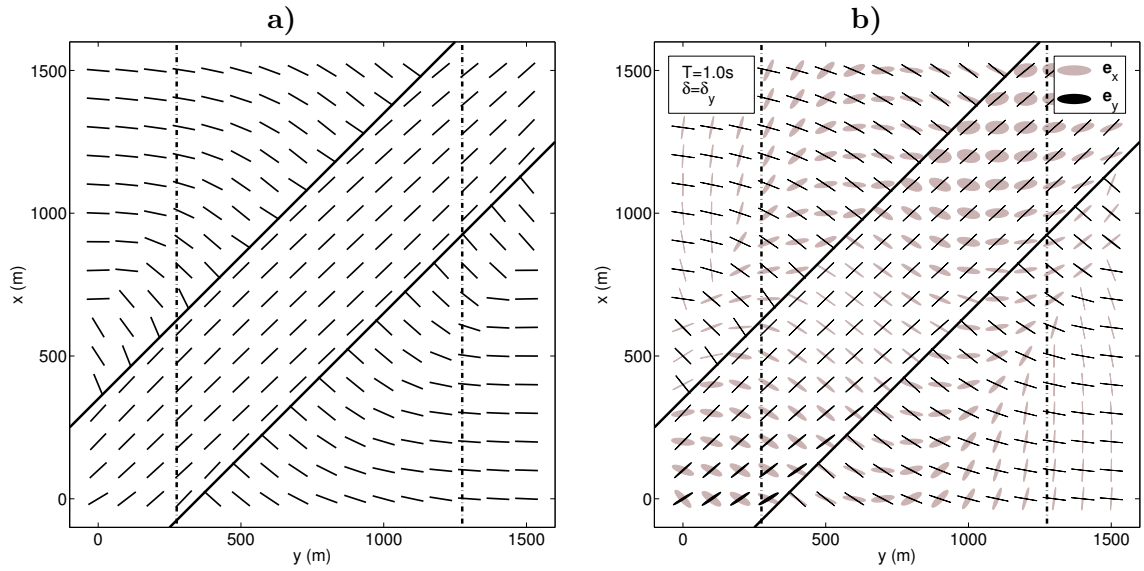


**Figure 4.5.:** Example 2: 'Local' coordinate system. **a)** Local strike direction obtained from minimization of only one telluric vector (here: $\mathbf{e}_y$) for the period range $0.001 - 100\,\mathrm{s}$. Note, that the local coordinate system has an ambiguity of $180\,^\circ$. **b)** Telluric vectors for the period $T = 1.0s$ plotted as ellipses after rotation of the impedance tensor to the directions shown in a). The vector $\mathbf{e}_y$ is approximately linearly polarized at all points, while $\mathbf{e}_x$ has a strong ellipticity in particular above the surface conductor and in the vicinity of the crossover points of the shallow and deep conductor.

s06, the same coordinate system applies to the whole period range, I use all periods between $0.001 - 100\,\mathrm{s}$ in order to determine the local strike.

The estimated local strike directions for the model shown in Figure 4.2 are plotted as top view maps in Figure 4.5a, the corresponding telluric vectors in Figure 4.5b for the period $T = 1s$, for which the coupling of induction effects in the shallow and the deep conductor is evident. As it can be deduced from Figure 4.5b, the ellipticities of $\mathbf{e}_y$ vanish almost exactly in the appropriate coordinate system, while $\epsilon_x \neq 0$ for most sites. This corresponds to the results for s06 (Figure 4.4b), where $\epsilon_y \simeq 0$, and to s03 (Figure 4.4a), but in a $180\,^\circ$ rotated frame, since $\epsilon_y$ had been minimized. Thus, adjacent to the local conductor, the electric field in local B-Polarization and on top of the surface anomaly, the local E-Polarization electric field are predominantly linearly polarized.

It is obvious from Figure 4.5a, that the local strike directions have a distinct meaning above and in the vicinity of the shallow conductor. Above the surface anomaly, they directly give the strike direction of the local anomaly, while adjacent but close to the surface anomaly, they point perpendicular to the local strike. Further away from the distorting anomaly, the strike direction is a mixture of regional and local strike or indicates the regional strike, if the influence of the local anomaly is small.

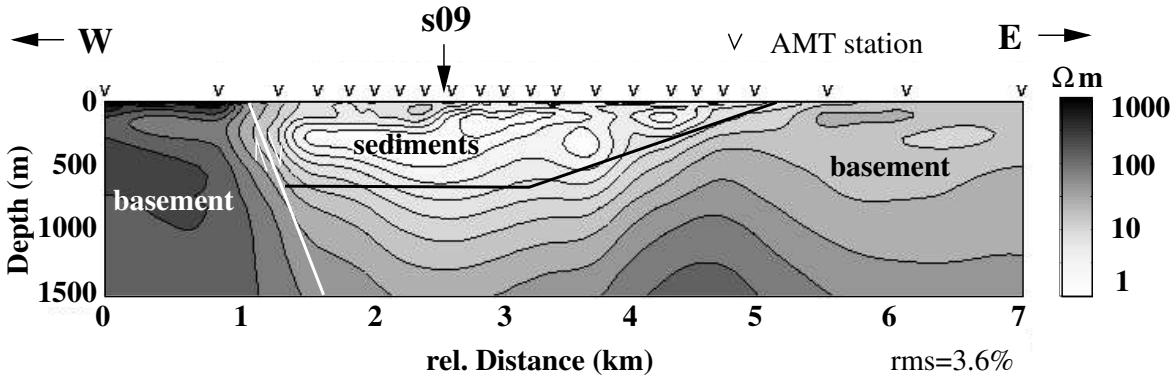


**Figure 4.6.:** Field data example: 2D-joint inversion of E-and B-Polarization apparent resistivities and phases for the period range $(0.001 - 0.1\,\mathrm{s})$ from 22 stations indicated by triangles at the surface. Strike direction is approximately $N$. The highly conducting body is suspected to act as a distorter at long periods by effectively channeling currents.

## 4.3. An application to MT data from NW-China

The previously described model study has been motivated by AMT/MT data in the period range $0.001 - 100\,\mathrm{s}$, which we measured in Gaxun-Nur Basin, an intra-continental basin structure in the Inner Mongolia province of the PR China. This basin is of key interest for geoscientists, because its sediments are presumed to be a valuable archive for climatic and environmental signals from the past million years (Wünnemann and Hartmann, 2002). Today, the basin is partially covered by sand dunes due to the hyper-arid climate of the Gobi desert. Within the frame of a multidisciplinary investigation of this basin, electromagnetic measurements (TEM,AMT/MT) were carried out across a $4\,\mathrm{km}$ wide northward striking wadi, a potential drainage channel in which material is discharged from the Gobi-Altay mountain range into the Gaxun-Nur Basin. A detailed description of the Gaxun-Nur basin and of some of the measurements we made at this location follows in Chapter 5.

A 2D joint inversion (Siripunvaraporn and Egbert, 2000) of E- and B-Polarization apparent resistivities and phases for the upper period range of the AMT-data $(0.001 - 0.1\,\mathrm{s})$ yields the resistivity model shown in Figure 4.6, many features of which have also been recovered by 1D-inversion of TEM data. Thus, the model is well constrained. The section is divided into two different resistive crystalline rock units (black and gray) and a highly conducting body (white) corresponding to sediments in the wadi. Crystalline rocks, exposed to the east and west of the wadi, are clearly differentiable into an eastern and a western block both geologically as well as from their different resistivities. The sediments of the wadi reach a thickness of around $500\,\mathrm{m}$ in the western part and a width of approximately $4\,\mathrm{km}$ along the section. The total length of the structure is approximately $20\,\mathrm{km}$, bounded to the north by metamorphic rocks, and disappearing to the south under lake sediments and dunes. The low resistivity (less than $1\,\Omega\mathrm{m}$) of the sedimentary infill must be explained by a high concentration of dissolved salt in the pores of the sediments, which is reasonable given the background of high evaporation rates exceeding the precipitation by the order of several magnitudes.

A $500\,\mathrm{m}$ deep section of conducting sediments above more resistive layers is considered as a large

scale structure with respect to the shortest period of $0.001\,\mathrm{s}$ (skin-depth $\sim 15\,\mathrm{m}$), but it appears as a small scale inhomogeneity for periods of $100\,\mathrm{s}$ (skin-depth $> 10\,\mathrm{km}$). Thus, we may expect serious distortion effects for long periods, caused by the structure well resolved at short periods.

In Figure 4.7, data from MT site $s09$, indicated in Figure 4.6, are shown as an illustrating example. Rotated to the strike direction of the wadi ($-12°$, counterclockwise), determined from the minimization of ellipticities of both telluric vectors within the first two period decades, apparent resistivities and phases (Figure 4.7a) indicate a 1D increase in conductivity with depth at the shortest periods. With increasing period, the sounding curves split, as the margins of the Graben become included in the inductive volume.

For periods longer than $\sim 0.1\,\mathrm{s}$, the diagonal impedance elements become increasingly important, approaching the amplitudes of the off-diagonal elements between $1 - 100\,\mathrm{s}$. Therefore the period range for the 2D-inversion was restricted to the shortest periods.

The response characteristics are equivalently reflected in the elliptical parameters shown in Figure 4.7b: vanishing ellipticities with weighted means $\overline{\epsilon}_x = 0.00 \pm 0.00$ and $\overline{\epsilon}_y = 0.01 \pm 0.01$ of the telluric vectors $\mathbf{e}_x$ and $\mathbf{e}_y$ within the first two decades indicate 1D or 2D conditions, the latter in principal coordinates. Accordingly, distortion angles in this period range are constant and, moreover, vanish, indicating the absence of galvanic distortion. A sharp increase of $\epsilon_x$ at $0.1\,\mathrm{s}$ rising to a maximum at $1\,\mathrm{s}$ and slowly decaying at longer periods coincides with non-vanishing main-diagonal elements. Thus, 3D effects are evident in the data, being either the result of strong 3D-structure, the distorted response of a 2D regional structure, or a combination of both.

Application of the minimization routine (4.34) to the lowest decade from $10\,\mathrm{s}$ to $100\,\mathrm{s}$ leads to the results shown in Figures 4.7c and d. Vanishing ellipticities with $\overline{\epsilon}_x = 0.01 \pm 0.07$ and $\overline{\epsilon}_y = 0.01 \pm 0.00$ indicate linear polarization of the telluric vectors, which point towards a deep 2D conductivity distribution, striking at $36.8°$ clockwise. Distortion angles are constant over nearly two decades from $1 - 100\,\mathrm{s}$ approaching almost $\pm 45°$. Note, that at long periods, phases of the off-diagonal elements and the corresponding main-diagonal elements are the same and related apparent resistivity curve are parallel in the double-logarithmic scale (Figure 4.7c). Thus, strong distortion effects the long period data, where the distorter has previously been postulated as the sedimentary filling of the Graben shown in Figure 4.6.

From these results, which are similarly observed at other stations, the following interpretation is established to explain the data: (1) The short-period band of the sounding curve reflects the 2D Graben structure. Its strike direction is $16°E$. (2) A deep conductor/resistor, which is also 2D, is resolved by long periods. It is oriented $37°W$, thus deviating from the surface strike by about $53°$. This is also supported by the high distortion angles. (3) At intermediate periods currents are induced in both the shallow surface conductor and the deep anomaly giving rise to strong 3D effects.

The survey discussed above was designed for rather shallow investigations. Therefore, the distribution of stations is not suitable for a 2D-inversion of undistorted long-period data nor for a 3D modeling in order to verify the outcome of the distortion analysis. It should also be noted, that magnetic transfer functions, which were also measured, do not strictly support the results stated above for long periods. However, the orientation of real and imaginary induction arrows in presence of 3D-structures is not well understood and often deviates from directions suggested by impedance tensor analysis.

Let me finally utilize this sounding curve to exemplarily study the 3D characteristics of the magnetotelluric impedance tensor. The measurement point is located above a conductive channel,

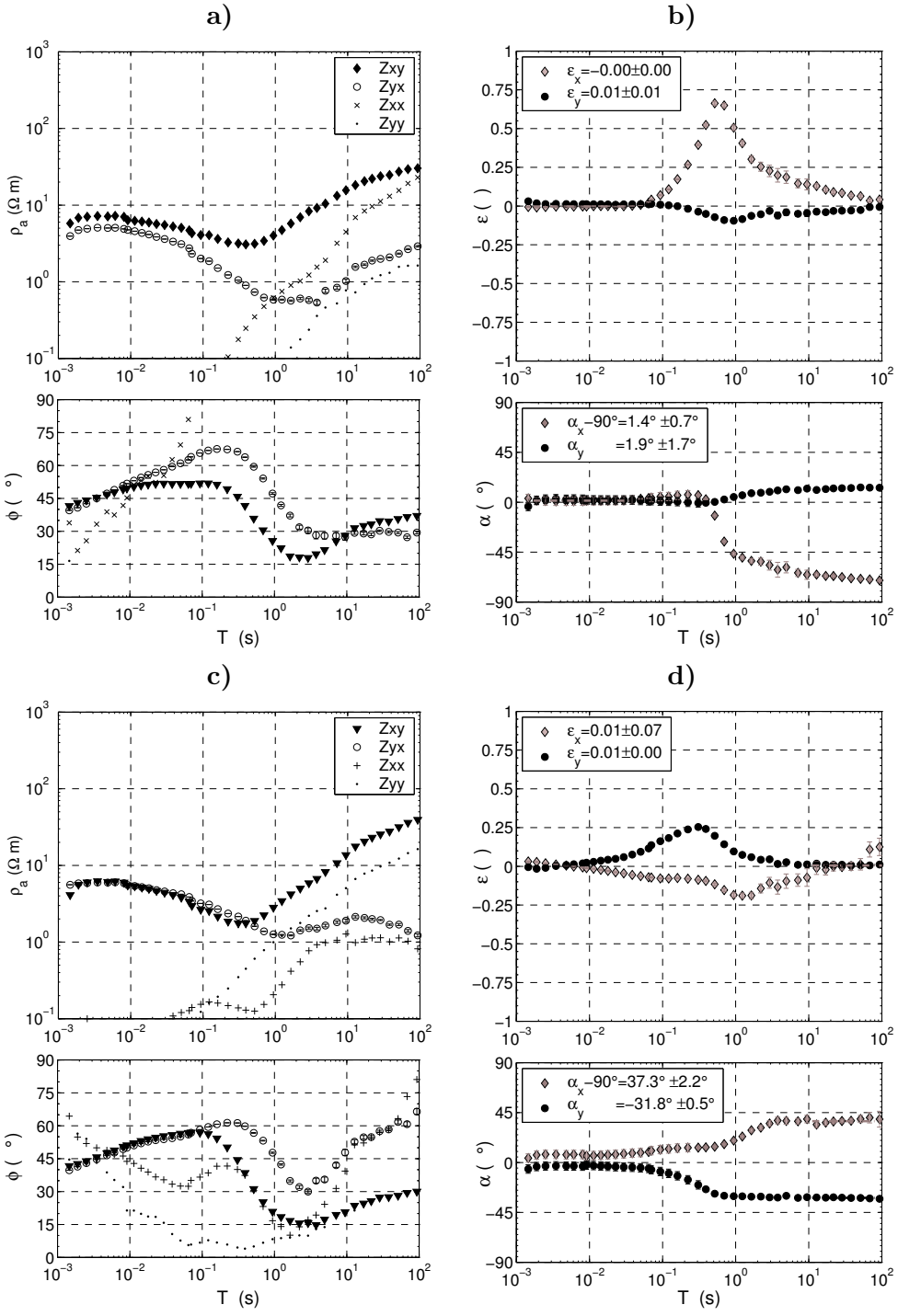


**Figure 4.7.:** continued on next page.

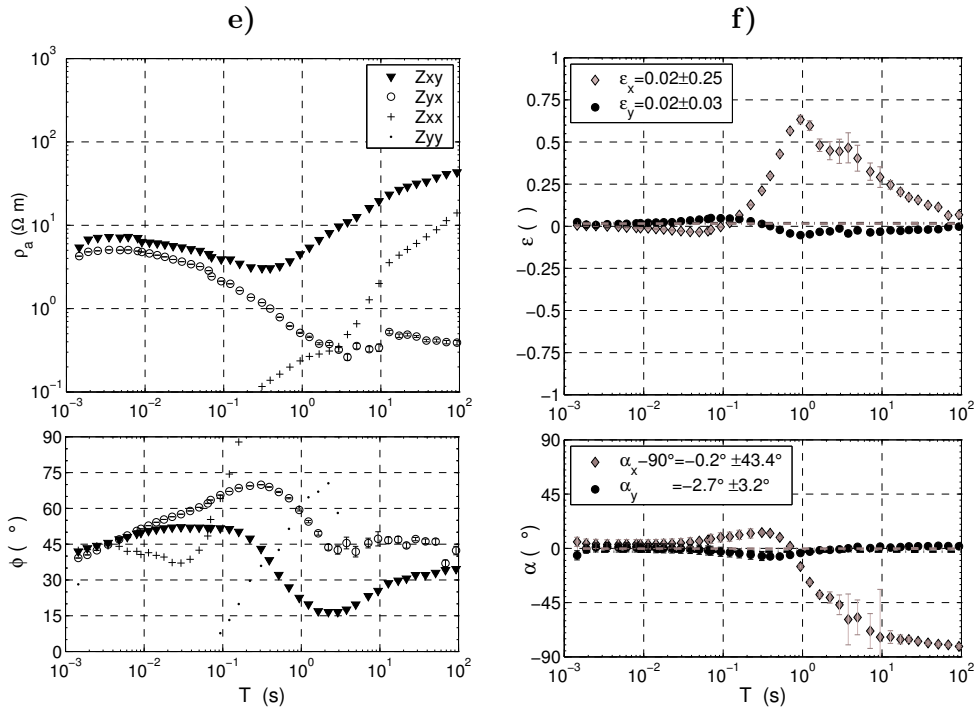


**Figure 4.7.:** (continued) Field data example: Site s09. **a)** Apparent resistivities and phases rotated $-12°$ (counterclockwise) into the strike direction of the shallow conductor depicted in Figure 4.6. **b)** Elliptical parameters of telluric vectors in the same coordinate system. **c)**, **d)** and **e)**, **f)**: Same as **a)**, **b)** but rotated 36.8° and 0.5° clockwise, where the first is interpreted as the regional coordinate system and the latter is the estimated 'local coordinate system'. (See text for detailed discussion.)

which is - comparable to example 2 - embedded in a more complicated 3D structure. I claimed, that in such a case, there often exists a coordinate system, in which the telluric vector $\mathbf{e}_y$ vanishes approximately, if rotated to the local strike direction. The rotation angle was determined in this case to $0.5°W$ by jointly minimizing $\epsilon_y$ for all periods, and is close to but not exactly the strike direction used for the 2D inversion of the short period band. In this coordinate system, the apparent resistivities and phases are shown in Figure 4.7e, the related ellipse parameters are depicted in Figure 4.7f. Note, that $\overline{\epsilon}_y = 0.02 \pm 0.03$ approximately vanishes for the whole period range, while $\epsilon_x \neq 0$ and depends on period. Similarly, the orientation of $\mathbf{e}_y$ is stable and aligned with the local strike direction ($\overline{\alpha}_y = -2.7° \pm 3.2°$), while that of $\mathbf{e}_x$ changes with period. It is therefore reasonable to assume, that the polarization state of $\mathbf{e}_y$ represents that of the linearly polarized electric field in local E-Polarization. The apparent resistivities in this coordinate system are composed of three elements ($\rho_{xx}$, $\rho_{xy}$ and $\rho_{yx}$) with large amplitudes and $\rho_{yy}$, which has a small amplitude. This is in coincidence with our assumptions about the impedance tensor, measured above a shallow conductive anomaly.

Thus, I recover the 3D effects inherent in the impedance tensor due to the presence of a local conductor also on field data.

# 5. Magnetotelluric studies in the Gaxun-Nur basin, NW-China

## 5.1. Introduction

In the scope of a DFG-funded interdisciplinary bundle project, the working group of the Technical University Berlin carried out electromagnetic measurements in combination with geological investigations in the Gaxun-Nur basin, located in the northern foreland of the Tibetan plateau in the Inner Mongolia province of China (Figure 5.1) . The Gaxun-Nur basin is considered as a geoarchive, bearing information about the climate and climatic changes of the past. The components of the archive, from which conclusions about the paleo-environment may be drawn, are its sediments, the fossil flora and fauna within, the structure of these sediments, and present landform, which witness ancient conditions. Of particular interest in the on-going investigations are climatic and environmental changes since late Pleistocene (40 ka).

The Gaxun-Nur basin (mong.: Nur = lake), named after the endorheic Gaxun-Nur lake in the far north of the basin, is situated between $100°\mathrm{E}$ and $102°\mathrm{E}$ longitude and $40°\mathrm{N}$ and $43°\mathrm{N}$ latitude (Figure 5.4). The altitude within the basin ranges from $1300\,\mathrm{m}$ a.s.l in the south to $900\,\mathrm{m}$ a.s.l. in the north. The local administrative center is the oasis Ejina Qi approximately $60\,\mathrm{km}$ south of the border between China and Mongolia. The Gaxun-Nur basin is bounded by northern ranges of the Qilian-Shan (chin.: Shan = mountain) with maximum altitudes of $5300\,\mathrm{m}$ a.s.l. in the south, the Bai-Shan $(1500\,\mathrm{m})$ in the west, the Gobi-Altay $(2800\,\mathrm{m})$ in the north and the Yabrai-Shan $(1900\,\mathrm{m})$ in the east. The Yabrai-Shan separates the Badain-Jaran-Shamo and the Tengger-Shamo (chin.: Shamo = desert). The sand dune field of the Badain-Jaran-Shamo bears the largest sand dunes of the world with dune heights up to $400\,\mathrm{m}$ and lies adjacent to and partly covers the southern and eastern part of the Gaxun-Nur basin. The locations of these major units as well as the basin itself are indicated in the regional map shown in Figure 5.3 and, in greater detail, in Figure 5.4.

Today, the largest part of the Gaxun-Nur area is composed of Gobi planes; in the east and south the dune field of the Badain-Sharan-Shamo covers sediments and basement rocks. The Gobi planes of the Gaxun-Nur basin are alluvial fan deposits of the Ruoshui river system, forming one of the largest endorheic deltas of the world, covering an area of $130000\,\mathrm{km}^2$. At the northern rim of the delta, the distal terminal lakes Gaxun-Nur (name-giving), Sogo-Nur and Yuanze are remainders of the paleo-Gaxun-Nur lake. The terminal-lakes, which are indicated in Figure 5.4, form a lake archipelago covering an area of about $3600\,\mathrm{km}^2$, in size comparable to the largest lake on the Tibetan plateau (Qinghai-Hu).

Due to recent precipitation of less than $40\,\mathrm{mm/a}$ with potential rates of evaporation of about $2600\,\mathrm{mm/a}$ and the diminishing flow of water from the south, the terminal lakes are rarely filled with water and dried out most of the time. One major reason for the declining flow of water is the inclining need of water for expanding agriculture in the Hexi corridor in the south (Province Gansu), a cause for major political disputes in the region. Within large parts of the Gaxun-Nur

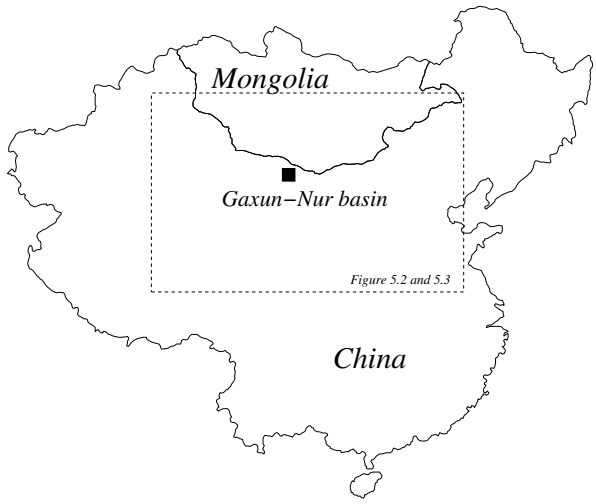


**Figure 5.1.:** Location of area of investigation. The Gaxun-Nur basin, located in the Inner Mongolia Province of China close to the border to Mongolia, is indicated with a filled square. Approximate position of Figures 5.2 and 5.3 is indicated by a dashed rectangle.

basin, desertification endangers vegetation and infrastructure. So far, there has been no evidence for modern climatic changes to be the reason in this context; instead it seems that human factors like overgrazing, intensive water management and farming are major causes (Wünnemann, 1999). For the near future it is likely, that the declining influx of water from the Ruoshui and the therefore also declining recharge of ground water will endanger the oasis Ejina Qi altogether even though it is not clear yet, to what extent.

The Gaxun-Nur basin is of key interest for the purpose of paleo-environmental studies, since it is located between different wind system (monsoon, westerlies), being enclosed by the Tibetan Plateau in the south and the Gobi-Altay in the north. These wind systems were initiated during the uplift of the Tibetan plateau since late Cretaceous and in particular within the Cenozoic and underwent several dislocations with consequences for global climate. Rapid climatic changes of regional and global dimensions are also documented in the archive, since change of precipitation and of glaciation due to shifting wind systems and temperature variability yield a great variability of environmental conditions of the catchment areas of northward discharging river system feeding the main sedimentation in the Tibetan foreland. In the northern part of the Gaxun-Nur basin, southward discharging river systems originating in the Gobi-Altay mountains have an influence on sedimentation as well. Additionally, local changes resulting from adjustment of the monsoonal system can cause dramatic environmental changes in the nowadays hyper-arid region, even on small spatial scales.

On the other hand, undisturbed and continuous sedimentological records are not granted due to the active tectonic deformation taking place in the northern foreland of the Tibetan plateau. This intra-plate deformation is due to the southerly continent-continent collision of the Indian sub-continent and the Eurasian platform. For the purpose of paleo-environmental reconstruction, an estimate of recent tectonic activities within the area of investigation is required. For instance, Wünnemann and Hartmann (2002) estimated the fluctuations of the Gaxun-Nur paleo-lake levels and dimensions based upon topographic correlation of dated paleo-beach ridges and small-scale

sedimentary sections. Such an estimate might be biased due to tectonic deformation if not taken into account and might lead to false conclusions about the environment in the past. To address the problem of paleo-environmental analysis in a comprehensive way such that all factors having an influence on the geoarchive maybe identified and occasionally quantified, a multidisciplinary approach was taken.

In the scope of the Project "Geophysical investigations of the sedimentary inventory of the Badain Jaran Shamo, Inner Mongolia, NW-China", we carried out electromagnetic and geoelectric measurements in three different parts of the Gaxun-Nur basin. The purpose of geophysical measurements was accordingly to investigate the structural setting, to provide information about the thickness of sedimentary layers and the depth of the crystalline basement, to detect lateral discontinuities in the subsurface attributable to tectonic deformation and to identify fault zones. To achieve these goals, we employed a spectrum of methods, covering several spatial ranges in resolution. From the largest scale to smallest, the methods in use were the Magnetotelluric method (MT), the transient electromagnetic method (TEM), DC-geoelectrics (DC). I have been working with the MT-method, and I will concentrate on this method and only mention the results of TEM and DC where they give additional valuable information to understand the image retrieved from MT.

## 5.2. Geological background

### 5.2.1. Regional geology and tectonics of central Asia

The continent-continent collision of the Indian sub-continent with the Eurasian mega-continent induces a NNE oriented principal stress due to the northward motion of India and resulted in the formation of the Himalayan mountain ranges, the uprise, movement and rotation of the Tibetan plateau, the over-thrusting, faulting and folding of crustal rocks in the Qilian-Shan at the northern rim of the Tibetan plateau and a lateral, basically $ENE-WSW$ oriented displacement of crustal masses along shear zones. Compressional deformation is accompanied by extensional forces oriented in direction of the smallest stress and leads to the formation of basin and Graben structures at intra-continental locations. Intra-plate deformation is observed more than $2500\,\mathrm{km}$ north of the collision zone reaching as far as the Gobi-Altay mountain and has formed and still forms the shape of the central Asian crust and controls the spatial distribution and setting of sedimentation and denudation areas.

The Ala-Shan block and the Bai-Shan fold belt compose the basement in the area of investigation. They are connected to the North-China para-platform (Hongzhen, 1985; Jiang, 1996) and form together with the Tarim-, Yangtze- and Songpan-Ganzo complex the continental basement of North China as indicated in the sketch shown in Figure 5.2, which is reprinted after Lamb et al. (1999). These continental nuclei were consolidated during at least 8 Precambrian orogenies (Qianxi, Fuping, Wutai, Zhongtiao, Wuling, Sibao, Jinning and Chengjiang orogeny), which culminated during the Sinian (800-600 Ma) with the final aggregation of the above mentioned platforms (Jiqing, 1979; Meyerhoff et al., 1991). During these tectonic stages, weak zones were implemented in the continental crust, which were poly-cyclically reactivated in geological history. They determine in particular the extent of the present-day active Altyn-Tagh fault zone and the Qilian-Shan fold- and thrust-belt in the south as well as the Tian-Shan-Gobi-Altay fault zone in the north of the Gaxun-Nur basin.

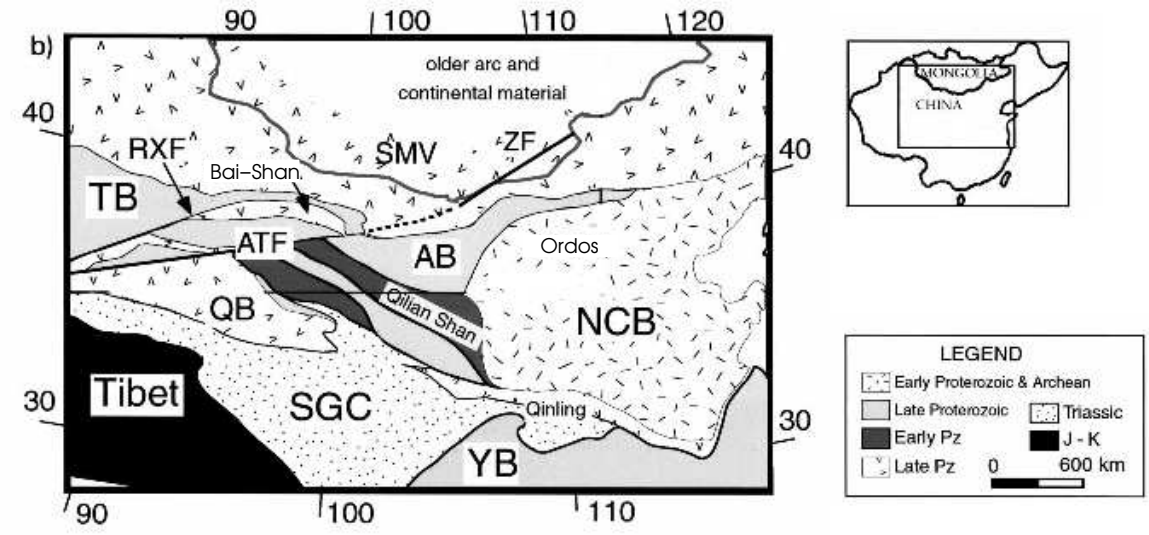


**Figure 5.2.:** Map of major blocks and terranes in central Asia, modified after Lamb et al. (1999). AB = Ala Shan block; ATF = Altyn Tagh fault system; NCB = North-China block; QB = Qaidam basin; RXF = Ruoqiang Xingxinxia fault system; SGC = Songpan-Ganzo complex; SMV = southern Mongolia Paleozoic volcanic arcs; TB = Tarim block; YB = Yangtze (South China) block; ZF = Zuunbayan fault.

A first reactivation occurred during an early-Palaeozoic transtensional phase, when epi-continental basins (NW-China basin or Tien-Shan-Hinggan trough in the north of the North-China platform, Kunlun-Qilian-Qinling in the south, Bai-Shan in the west) with shallow marine facies evolved at the position of the Precambrian suture zones. This extensional strain was accompanied by submarine mafic to intermediate volcanism. Ophiolites in the present Qilian-Shan document the existence of oceanic crust due to rifting within the Kunlun-Qilian-Qinling basin (Zhigao, 1980). This process of reorganization of the North-Chinese continent was reversed during the Caledonian orogeny, and in the Devonian the northern part of China was stabilized along a stripe between $35°N$ and $41°N$ (Jiang, 1996), and finally terminated with the collision of the Tarim and North-China platforms with Siberia in the scope of the Variscian orogeny. During the Variscian orogeny (Carboniferous, Perm), the formerly extensional continental and oceanic basins were inverted and intensively folded, the oceanic crust in the Kunlun-Qilian-Qinling basin was sub- and partly obducted (Xiao et al., 2002). The Paleo-Qilian Shan evolved at the location of the modern Qilian Shan and the fold belts of the Bai-Shan and Tien-Shan originate from the Variscian orogeny. The Suture zone between North-China and Siberia is believed to be the EW oriented Ebinur-Yuanze zone, which crosses the working area at 42° latitude (Jiqing, 1979, cited after Wünnemann, 1999).

After the final stage of the Variscian deformation phases, the Siberian platform, the North-China/Tarim/Qaidam platform and the Yangtze platform were part of the Eurasian mega-continent. However, the amalgamization of the sub-continents to a mega-continent did not result in a stable block. Instead, the Mesozoic era was dominated by a continously acting compressive stress due to successive aggregation of terranes to the Chinese platform in the Tibetan area, leading to intra-continental deformation in central Asia. In the frame of this northward oriented compression, the Paleo-Qilian-Shan (already of Caledonian age) as well as the northward located mountain ranges of the Heli-Shan, Longshou-Shan and Beida-Shan, separated from the Qilian-Shan by the

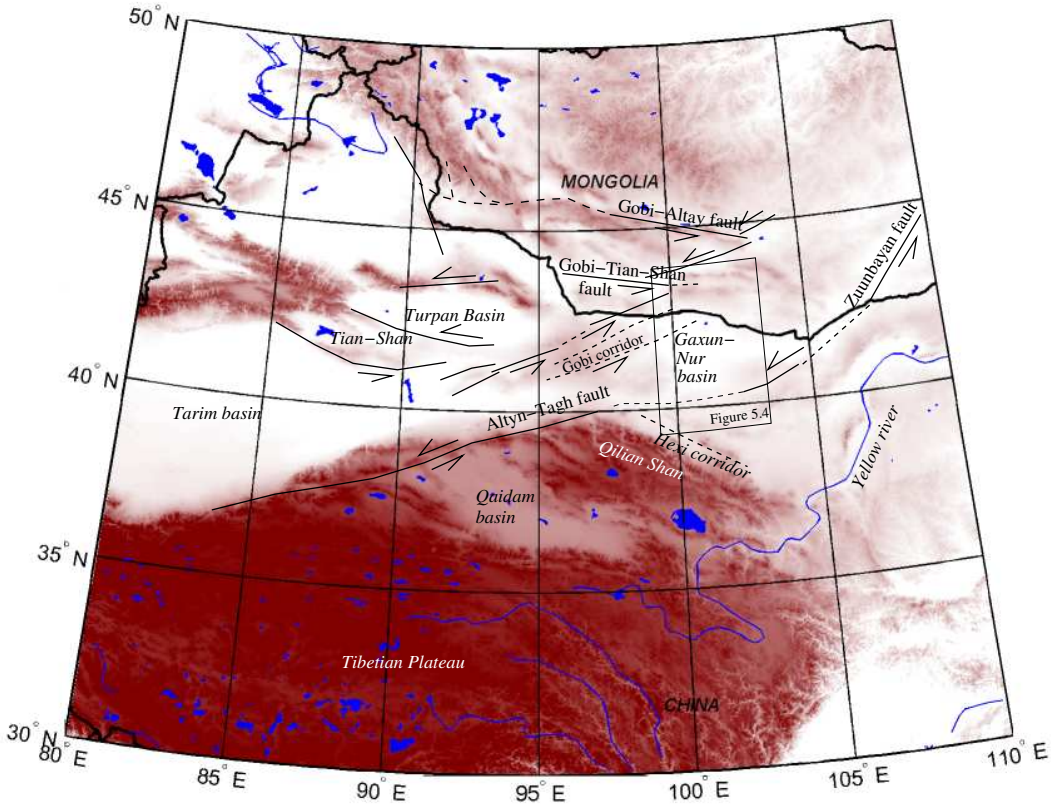


**Figure 5.3.:** Major geographical units and tectonic faults, plotted on a relief map of the Asia topography (gtopo30). Faults are reprinted after Lamb et al. (1999); Cunningham et al. (1996). The Gaxun-Nur area is indicated by a black rectangle. It is bounded by several left-lateral faults in the north, west and south.

$NW - SE$ trending Hexi-corridor, grew to mountain ranges of considerable dimensions. The Qinling trough south of the Qilian-Shan was inverted and folded, yielding an uprise of the Paleo-Qinling mountains. While molasse sediments were deposed in the Hexi corridor, the Triassic area of sedimentation further to the north in the Bai-Shan area and in the Ordos Plateau was dominated by fluvio-lacustrine deposits, which nowadays bear coal seams. In between the Bai-Shan and the Ordos Plateau, the latter located on the North-China platform (cf. Figure 5.2), large parts of the Ala-Shan Plateau remained erosion area. The Yan-Shan phase of deformation in Jurassic lead to an uprise of the NS oriented Helan-Shan at the eastern bound of the Tengger desert and the evolution of NS-oriented Graben- and Horst- structures at the eastern margin of the Ordos Plateau (Xingyuan et al., 1982), accompanied by relative subsidence of the Ala-Shan Plateau and onset of sedimentation with continuous deposition of fine clastic sediments, where embedded coal beds developed in a fluvio-lacustrine environment. North and northeast of the Ala-Shan plateau, Lamb et al. (1999) describe the evolution of northeastward elongated tectonic basins along the left-laterally displacing Zuunbayan fault (cf. Figures 5.2 and 5.3). The major activity of displacement is supposed to take place in late Mesozoic times (Cretaceous), but is still a matter of debate (Graham et al., 2001; Johnson, 2004; Lamb et al., 1999; Suvorov, 1982).

The convergence of the Indian sub-continent and Eurasia and the continuous subduction of the Tethys ocean since late Cretaceous lead to continental collision in the Eocene (Himalayan or Alpine Orogeny). This resulted in an enlarged northeastward oriented transpressional stress and the beginning uplift of the Tibetan plateau. Since the time of collision of India and Eurasia, Molnar and Tapponier (1975) have estimated the total crustal shortening to 1500 km with a mean relative plate convergence of 50 mm/a. The consequences of the shortening are expressed in the growth of the Himalaya mountains, the progressive lifting of the Tibetan plateau, a fast lifting of the Qilian-Shan, the Tian-Shan and the Gobi-Altay north of the Tibetan plateau. Left-lateral slip movements along the major central Asian strike-slip shear zones, in particular the Altyn-Tagh, which with a total length of 1600 km is the largest shear zone of Asia (Gouyu et al., 2004), the Gobi-Tian-Shan and the North-Gobi-Altay fault system (Cunningham et al., 1996) compensate the crustal shortening in a transpressive stress regime. Eastward extrusion of central Asian crust takes place in conjuction with a continuative formation of NS-trending Graben structures and counterclockwise block-rotation of Precambrian platforms, as reported for the Ordos block by Zhang et al. (1995) and Xingyuan et al. (1982).

Active, transpressional, intra-continental mountain building and strike-slip faulting is observed in the Gobi-Altay far to the north of the Tibetan plateau (Cunningham et al., 1996). The total displacement along the presently active Gobi-Altay and Gobi-Tian-Shan fault systems (Figure 5.3) is unknown but according to Cunningham et al. (1996) a major player in accommodation of intra-continental stress due to the Indian-Eurasian collision. Of particular interest seems to be the so far not further investigated Gobi corridor of Altyn-Tagh parallel left-lateral strike-slip faults across the Bai-Shan (Cunningham et al., 1996) and thereby linking the Altyn-Tagh zone and its derivates and the Gobi-Tian-Shan deformation zones in the west and northwest of the Gaxun-Nur basin. Fault zones of the Gobi corridor are traced from Landsat satellite imagery and disappear to the east below the sediments of the Gaxun-Nur basin. A connection of left-lateral strike-slip along the Zuunbayaan fault, which has been investigated by Lamb et al. (1999) within Mongolia (Figure 5.3), is also suspected to transfer stress from the Altyn-Tagh zone to the north. The extension of the Zuunbayan fault into China and its position is not clear and matter of debates between different authors. Lamb et al. (1999) suggest that the southward extension of the Zuunbayan fault runs through the southern part of the Gaxun Nur basin (which they do not denote explicitly), where it is hidden under the dunes of the Badain-Jaran-Shamo east of the Gaxun-Nur. Although Lamb et al. postulate major activity of the Zuunbayan fault during Cretaceous, they do not exclude Cenozoic reactivation.

According to Wang et al. (2001), strike-slip displacement along the above mentioned fault zones and crustal shortening in the mountain ranges accommodate 90% of the northward penetration of India into the Eurasian continent. In addition, in the foreland of the easternmost Qilian Shan, a counterclockwise rotation of the Ordos block results in NW-SE oriented crustal extrusion since Late Pliocene and was accompanied by the formation of the NS-trending Yinchuan and Shanxi Graben (Zhang et al., 1995). Counterclockwise rotation of the Ala-Shan plateau in conjunction with the development of normal faults is also mentioned in Guo et al. (2000), but without further explanation or citation. Following Wang et al. (2001), east-southeastward directed crustal extrusion amounts to 2-8 mm for the North-China platform with respect to the stable Eurasia.

### 5.2.2. Geology of the Gaxun-Nur basin

The oldest sediments, which outcrop widespread in the Gaxun-Nur basin are of Jurassic age, and consist of reddish fluvio-lacustrine and limnic sediments. Cretaceous sediments can be found in similar facies in the working area and indicate comparable sedimentation environments. Patches of these late Mesozoic sediments are exposed in depression within the basement dominated border areas of the Gaxun-Nur basin. It may be anticipated, that the basal sediments of the Gaxun-Nur basin over crystalline basement are also of Jurassic and/or Cretaceous age, and according to our own investigations in the central area of the Gaxun-Nur basin reach thicknesses of more than $800\,\mathrm{m}$.

Sedimentation of terrigenous sediments in a continental environment continued throughout Tertiary. Tertiary sediments in the greater area often carry gypsum and are described in the western part of the Badain-Jaran-Shamo by Hedin (1943) who found ostrich eggs at the base of Quarternary sediments (Mischke, 1996). Consolidated Tertiary sand and gravel deposits are indicated in the geological map (Gansu Province) in the northern part of the Tengger-Shamo east of the Badain-Jaran-Shamo. Large exposures of Tertiary sediments are not known in the Gaxun-Nur area.

Tertiary strata are covered by Quaternary limnic and eolian deposits, which reach a thickness of more than $300\,\mathrm{m}$ in the distal areas of the alluvial fan of the Ruoshui river (Zhang et al., 1990, cited after Wünnemann, 1999). Quaternary sediments are described in great detail by Wünnemann and Hartmann (2002), who analyzed sediment cores from a $230\,\mathrm{m}$ deep drill-hole penetrating the entire Quaternary. The age of basal sediments is not clear according to Wünnemann (1999) and is either Tertiary or Jurassic. In any case an early Quaternary Hiatus may be deduced, since the onset of Quaternary sedimentation at the drill-hole location is dated to 1 Ma.

Little is published about the structural setting of the Gaxun-Nur basin and its tectonic evolution. According to Lamb et al. (1999), Graham et al. (2001) and Johnson (2004), late Mesozoic extensional deformation along the Zuunbayan fault and other nearby faults in southern Mongolia lead to the evolution of basin and Graben structures, which nowadays bear late Mesozoic sediments of up to $2\,\mathrm{km}$ thickness. This extensional phase was followed by contraction leading to basin inversion in early to late Cretaceous, which is related to the southerly collision of India and Eurasia. Late subsidence in the southern part of Mongolia is documented by widespread late-Cretaceous sedimentation. Cunningham et al. (1997) describe late Jurassic and early Cretaceous continental clastic and locally volcanic rocks deposited in eastern Gobi-Altay region during an intra-plate extensional phase, which were peneplaned during latest Cretaceous and early Tertiary, i.e. they also assume a poly-phase evolution of Mesozoic basins structures. It is therefore likely to assume a similar setting for the Gaxun-Nur basin located in between and south of the locations described by Lamb et al. (1999), Graham et al. (2001) Johnson (2004) and that by Cunningham et al. (1997).

Therefore, I assume that documented onset of Jurassic sedimentation is related to extensional or transtensional stress along the major faults in northern China and southern Mongolia and lasted as long as Cretaceous. A subsequent compressional phase in early to late Cretaceous presumably lead to the dissection of the basin into several swells and to the evolution of ridges and depressions. Previously described exposed patches of jurassic sediments, unconformly lying on basement rocks, document pre- or syn-tectonic sedimentation. Within depressions, Mesozoic sediments are partly preserved and exposed or covered by younger sediments.

A small scale $2\,\mathrm{km}$ wide Graben (Jingshutu depression), which extends from the Yuanze lake northward into the northerly exposed Paleozoic and Precambrian basement (location indicated in

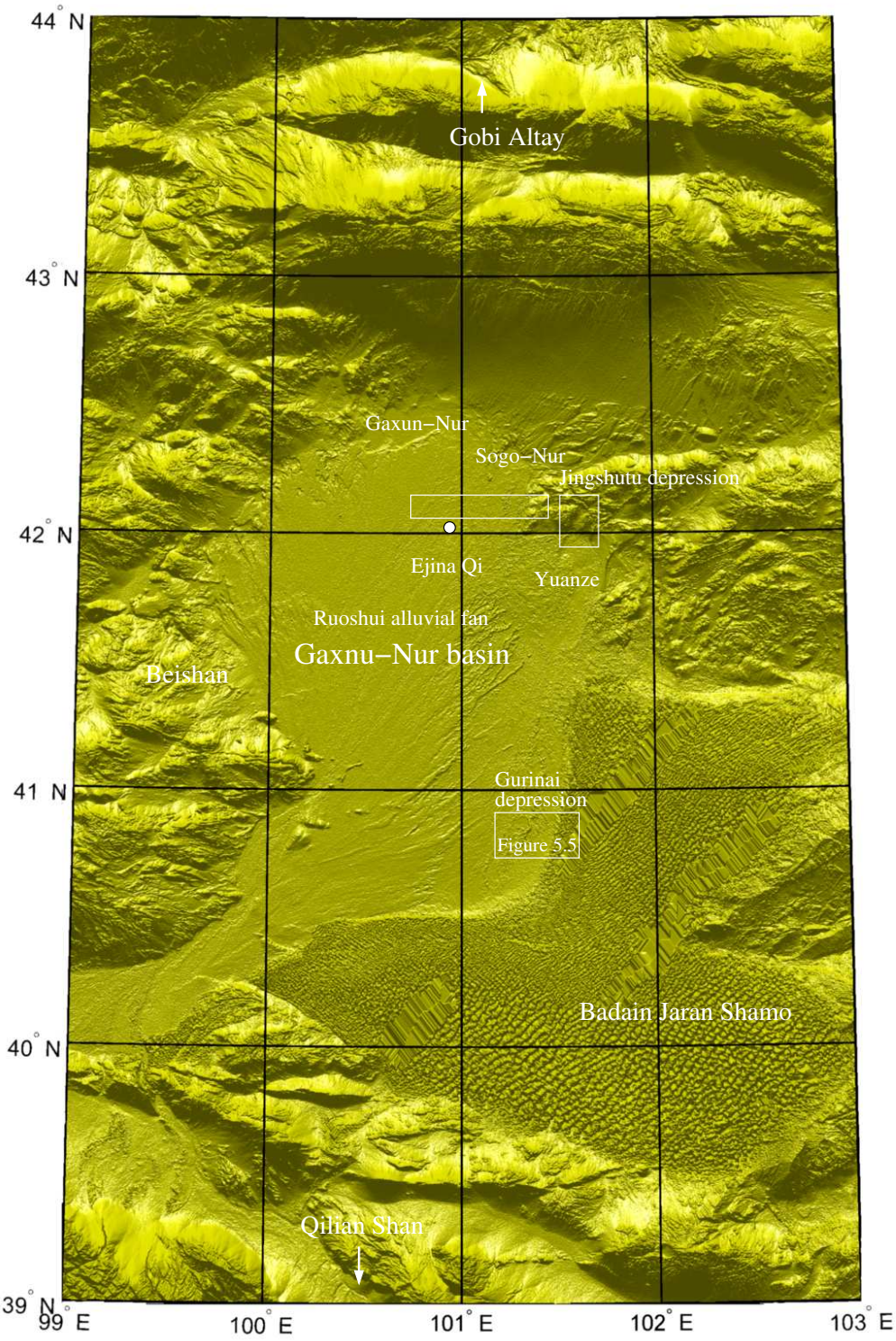


**Figure 5.4.:** Shaded relief topographic map of Gaxun-Nur basin and adjacent mountainous regions based upon satellite SRTM data. The location of the Oasis Ejina Qi, the terminal lakes (Gaxun-Nur, Sogo-Nur and Yuanze) at the northern rim of the Ruoshui alluvial fan, the Gurinai depression in the east of the fan and the adjacent dune field of the Badain-Jaran-Shamo are indicated. Previous geophysical investigation areas are indicated by white boxes in the north part.

Figure 5.4 by a rectangle), has been investigated by us with geophysical methods. We found, that the sedimentary filling has a thickness of up to $500\,\mathrm{m}$ and is largely composed of deformed, terrigenous sediments of pre-Quaternary, possibly jurassic age. The Jingshutu depression has the shape of a half-Graben and is bounded by a NS-striking sub-vertical fault at its western margin. Along the margin, rhyolitic rocks are exposed and according to geophysical data interpretation overly Jurassic sediments. In the regional context, this structure is supposed to represent a relict of a Mesozoic sedimentation area, which underwent later inversion and dissection as described above, where in the Jingshutu depression Mesozoic sediments are preserved. Aside of the Jingshutu depression, sediments have been eroded and old basement rocks are nowadays exposed and form topographic highs. Rhyolitic rocks overlying a sequence of Jurassic sediments as at the western margin fault of the Jingshutu depression point towards rifting processes. Age determination of Rhyolites is however required to justify speculative syn-rifting volcanic activity.

Similarly, within the Gaxun-Nur basin Jurassic sediments exist and have presumably been preserved on a larger scale. They are nowadays covered by Cenozoic and likely also late Cretaceous sediments. A Hiatus between Jurassic and Cretaceous sediments or within the Cretaceous may be anticipated due to regional uplift during the compressional phase in late to early Cretaceous, but cannot be proven. Our own geophysical measurements at the northeastern rim of the Gaxun-Nur basin revealed a sequence of NS-striking normal faults with a cumulative vertical offset of more than $800\,\mathrm{m}$, which was interpreted in terms of syn- or post-sedimentary pre-Quaternary extension and fits into the regional context of late Jurassic extension and later inversion.

Cenozoic or at least Quaternary extension and relative subsidence must be assumed for the Gaxun Nur basin, such that the region remained an area of sedimentation. Little is also documented about Cenozoic and in particular Quaternary tectonic deformation within the Gaxun Nur basin, which is of particular interest in the project, to which this work is related. Active faulting occurs along the margins of the Tibetan plateau to the south (Gouyu et al., 2004) and the northerly Gobi-Altay mountains and fault zones (Cunningham et al., 1996, 1997). The Gobi-corridor (Bai-Shan area) and also the Zuunbayan fault is assumed to transfer stress from the Altyn-Tagh fault zone to the North. Graham et al. (2001) indicate a connection of both the Zuunbayan and the Gobi corridor via a detachment fault passing at the northern boundary of the Gaxun-Nur basin. Hartmann (2004) interpretes Quaternary tectonic deformation from satellite imagery at several locations within the Gaxun-Nur-basin, in particular at the northern terminal lakes and the Gurinai-depression in the south-east. From statistical analysis of SRTM topography data (Figure 5.4), Hölz and Burkhardt (2004) detected a lineament across the entire Gaxun-Nur basin linking the Gurinai-depression and the Gaxun-Nur terminal lake. Our geophysical measurements, which revealed pre-Quarternary normal faulting along $N-S-$trending faults at the northeastern margin of the Gaxun-Nur basin show variation in thickness of Quarternary sediments across the Mesozoic faults. Resolution is, however, not sufficient to prove neo-tectonic deformation here.

### 5.2.3. The Gurinai depression

In the year 2004, a number of geophysical and geological investigations has been carried out in the southeastern part of the Gaxun-Nur basin, adjacent to the sand dune field of the Badain-Jaran-Shamo. This area is assumed to play a key role in understanding the Cenozoic tectonic settings of the whole Gaxun-Nur basin. The location of the measurement area is indicated in the SRTM image in Figure 5.4 and in greater detail shown in a Landsat TM sub-scene in Figure 5.5. It occupies the transition from the alluvial fan of the Ruoshui to the west and the sand dune field of the Badain

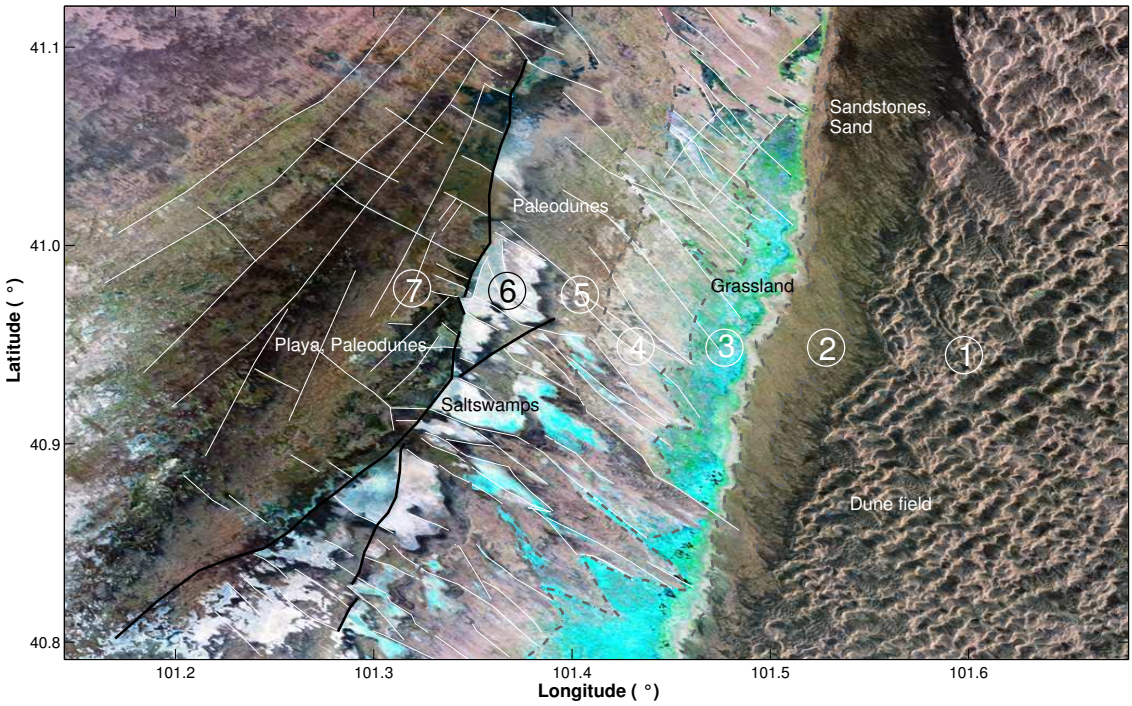


**Figure 5.5.:** Landsat TM subset of the area of investigation. The major geographical units and lineaments are indicated by number and lines. (1) Badain-Jaran-Shamo Dune field (2) Paleo-dunes, partly composed of consolidated sandstone layers (3) Grassland, turquoise colors indicate vegetation, dark spots indicate small lakes (4) Grassland with less vegetation (5) Paleo-dunes (6) Salt swamp (7) Playa planes, transition to Ruoshui fan. Western boundary of the Gurinai structure (3-6) is depicted by black solid lines. Black dashed lines indicate changes in morphology. White lines indicate lineaments identified from satellite interpretation and partly from field observations. Within the Gurinai structure, white lines correspond to topographical depressions.

Jaran Shamo to the east and is enclosed by two parallel, 12 km separated lineaments, striking in northern direction and indicated by color and texture changes in the satellite image (Figure 5.5). The structure within the lineaments is hereafter referred to as the Gurinai depression, named after the small Gurinai settlement in the southern part of the structure. It should already be mentioned, that the western lineament coincides with an only small topographic effect deducible from satellite SRTM data (Figure 5.4), but with a change of sedimentary deposits, while the eastern lineament, which is on a small scale more diffuse, is basically highlighted in the Landsat scene due to sand coverage in the east. However, at the latter boundary, a stronger relief change is observed.

**Geomorphology:** The area of investigation comprises the Gurinai depression and extends across the previously mentioned lineaments some kilometers to the west into the southeastern branches of the Ruoshui fan and to the east as far as to the dune field. It may be roughly divided into seven NS-striking stripes, where each stripe coincides with a particular geomorphological setting. In the following paragraphs, I describe and partly interprete the geomorphological and sedimentological features from east to west, labeled with numbers 1-7 in Figure 5.5.

The sand dunes of the Badain Jaran Shamo, numbered as stripe 1 in Figure 5.5 and illustrated in

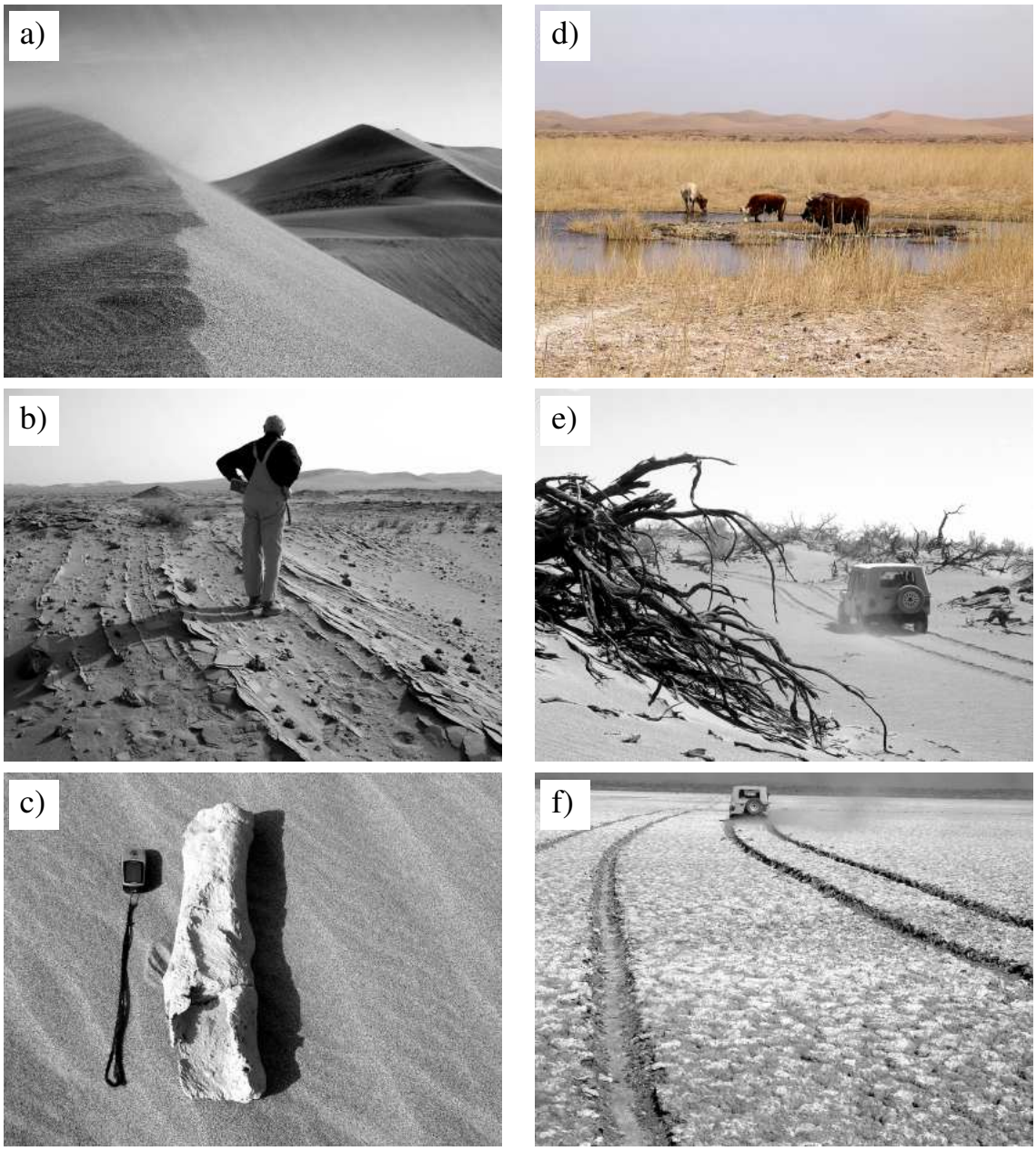


**Figure 5.6.:** **a)** Sand dune in the Badain Sharan Shamo with a height of approximately 40 m. The dunes can be conceived as fresh water reservoirs. **b)** Dipping layers of consolidated sandstones, interbedded with sand. **c)** Fossilized root, probably of a tamarisk plant. **d)** Cows resting at a small pool in the Gurinai grassland. **e)** Tamarisk trees growing in the paleo-dunes with dune sand accumulated within complicate the accessibility of some regions. **f)** Salt marshes in the western part of the Gurinai depression. Deep lane groves are due to wet, plastic clay in the subsurface.

Figure 5.6a, form the eastern boundary of the investigated area. Here, dunes reach relative heights of $40-60\,\mathrm{m}$, intersected by app. $N45°E$ and $N45°W$ striking valleys, which form a chessboard-like pattern. In these valleys, fine to coarse grained sediments (consolidated sandstones interbedded with loose sand layers) are exposed, which are similar to the sediments found west of the dunes. It is remarkable, that the dune sands at the basis and slopes of the dunes are wet in depths not more than one meter.

Terraces at different, from east to west successively decreasing altitudes with a total relief change of approximately $30\,\mathrm{m}$, represent area 2 in Figure 5.5 and separate the dune field from the Gurinai grassland (area 3 and 4) to west. These terraces consist of consolidated sandstones of different thicknesses ranging from centimeters to more than half a meter (Figure 5.6b), with loose sand layers interbedded. These layers dip in various directions with slopes from $0° - 30°$ and partly intersect each other. Such sedimentary structures are most frequently observed in sand dunes. The cement, which preserves the layered structure, is calcium carbonate and originates either from evaporation of groundwater or surface water, the latter provided by strong precipitation events during summer monsoon. First datings indicate an age of $30\,\mathrm{ka}$ for one cementation phase (pers. communication, Z. Hucai).

Yang (2000) describes similar dune forms in the southeastern part of the Badain-Jaran-Shamo. He assumes, that the four cementation phases he has identified and dated within $2 - 32\,\mathrm{ka}$, represent moisture conditions due to increased local precipitation. For our area of investigation, the possibility of periodical flooding of the area due to an increased discharge from the Ruoshui river should also be taken into account. A great number of fossil roots and plants is found (Figure 5.6) on top of some of the terraces only. This is a hint for several environmental changes during the sedimentation history. At the foot of the terraced stripe, an increasing number of tamarisk trees grow, partly forming an impenetrable coppice.

The Gurinai grassland or wetland, which is represented by turquoise colors in the Landsat subscene in Figure 5.5, is nowadays used by several farmers for animal husbandry. The implementation of agriculture farming in the 1970-ties proved to be an ineffective trial and was given up in the 1980-ties. Fresh water required for livestock farming is supplied from groundwater wells, with groundwater levels at $1 - 3\,\mathrm{m}$. Small pools, depicted in Figure 5.6d, with upcoming groundwater and surface areas of typically not more than $100\,\mathrm{m}^2$ exist. These pools are arranged in $N - S$ direction along the eastern margin of the Gurinai depression. Some of them are covered with crystalline salt crusts, others contain fresh water (Figure 5.6d). The lakes demonstrate the water richness in the Gurinai area, which can be considered as a peculiarity of this hyper-arid area and poses the question after the origin of groundwater.

Further to the west, a decrease in grass vegetation causes a color change between stripe 3 and 4 in Figure 5.5. In stripe 4, the groundwater becomes progressively more brackish to salty and thereby restricts the area being suitable for settlements. Salinisated depressions, mostly elongated in $N45°W$ directions, illuminate the outflow of salty, near-surface groundwater. The sediments close to the surface within the wetland area range from clays to fine sand with a high lateral variablity, indicating locally different energetic conditions during sedimentation.

Approximately in the center of the Gurinai depression, the occurrence of paleo-dunes, densely overgrown by tamarisk, mark an abrupt change in landform (Figure 5.6e). The paleo-dune field, denoted as stripe 5, is intersected by approximately $N45°W$ striking valleys, where mainly silt and clay in conjunction with salt is exposed. Huge salt-swamps (area 6 in Figure 5.5) are found in the western part of the Gurinai depression, apparently cut-off at the lineament mentioned previously. The occurrence of crystalline salt at the surface as shown in Figure 5.6f causes white to light

blue colors in the Landsat scene. Plastic clays and silts are the dominating sediments within the swamps. The color change in the satellite image is also observable in the field and coincides with the disappearance of crystalline salt and a stepwise topographic rise to the west. The total relief increase is, however not more than $2\,\mathrm{m}$ across the lineament and distributed over three steps with distances of approximately $100\,\mathrm{m}$.

The westernmost stripe considered here is again occupied by sand covered ridges with loose coverage of tamarisk. The ridges are separated by depressions, in which playa sediments comprise clay to silt deposits in conjunction with crystalline gypsum. Gravels with grain sizes of several mm to cm together with the high content of gypsum make a distinct difference to the sediments within the Gurinai depression and the adjacent eastern dune field.

Unfortunately, no datings of sedimentary samples are readily available. For later interpretation, I therefore assume, that the Gurinai depression is presently a sedimentation area (i.e. Holocene sediments), while at its shoulder aside, sediments are considerably older (according to reports of the Department of water management in Ejina Qi, middle to old Pleistocene ages have to be assumed here), and partly covered by modern eolian sediments.

**Tectonic lineaments and fractures:** Since Quaternary sediments are exposed throughout, lineaments related to tectonic processes can be put into the frame of Cenozoic deformation. The most pronounced structures identified from the satellite image are the lineaments enclosing the Gurinai depression, which extent more than $60\,\mathrm{km}$ along the $N-S-$direction. From SRTM data follows that the western lineament is in many areas governed by a few hundred meters wide and few meters deep depression with a relative uplift of the western block. Therefore it may be conceived as a fault zone with a normal component of displacement. The eastern boundary of the Gurinai depression is governed by a step-like increase in altitude to the east.

The landform described in the previous section, also exhibit a $N-$strike, but with diffuse boundaries. In addition, within the Gurinai depression, small scale depressions striking approximately $N45°W$ maybe attributed to tectonic deformation. The direction of depressions coincides with the major wind direction of the winter monsoon. Therefore, it may be anticipated, that eolian denudation is particularly effective along the presumed tectonic lineaments and emphasizes their appearance. The occurrence of salt pans is connected to these depressions and can be explained by upcoming and evaporating brackish or salty groundwater. The pathways for the groundwater flow are thus assumed to be related to fault zones of neotectonic origin. These depressions extend across the whole Gurinai depression and can be related to valleys in the terraced transition zone to the Badain-Jaran-Shamo (stripe 2 in Figure 5.5). In contrast, west of the Gurinai depression, the dominant direction of lineaments is $N30° - 50°E$, being almost perpendicular to the ones previously described. Both groups of lineations are feather-like arranged with respect to the central $N-$striking fault and have been interpreted by Hartmann (2004) in terms of Duplex structures originating from two deformation phases of different ages. The older deformation phase is supposed to be characterized by transpressional stress, leading to the evolution of restraining belts at the western flank of the sinistral $N-$striking fault. The younger phase leads to extensional fractures in a transtensional stress regime at the eastern flank. In fact, assuming the $N45°W$ striking depressions within the Gurinai depression to represent extensional fractures related to a shear motion at the $N-$striking fault, the latter must be interpreted as an oblique shear zone. Although well-defined lateral displacements have not been identified, the orientation of shear motion in this context is due to the mutual orientation of extensional fractures and driving shear deformation assumed to be sinistral and therefore synthetic with the major left-lateral shear zones

**Figure 5.7.:** Fractures in consolidated sandstone in a conjugate relation, observed in stripe 2 of Figure 5.5.

of regional extent (Altyn-Tagh and Gobi-Altay). An older, transpressive phase as interpreted by Hartmann (2004) due to the texture west of the western lineament remains questionable, i.e, no further indication from field investigations can be added to support his hypothesis.

Naturally, it is difficult to identify deformation in unconsolidated sediments; the deformation will rather result in diffuse effects due to the plastic reaction of the wet and soft material. However, in the consolidated sandstones in the east we found many fractures, mainly with strike in $N90°E$ or $N30° - 45°E$ and sometimes arranged like conjugate shear fractures (see Figure 5.7). From some of these fractures, a sinistral sense of deformation may be deduced and coincides with the major regional shear sense of the Altyn-Tagh and Gobi-Altay left-lateral shear zones.

From these observations, we conclude that the local geological and hydrogeological situation must to some extent be controlled by active tectonic deformation and/or older tectonic deformation processes, which sustainably influenced the younger sedimentation and the hydrogeology. To get a deeper insight into the structural setting and the distribution of sediments within the Gurinai area, we conducted a number of geophysical measurements. The electrical conductivity is at first a measure of the amount and the salinity of fluids in rocks and sediments. Only in a second step can the electrical conductivity model be converted to a geological model, employing all available boundary conditions of geological and hydrological type.

## 5.3. Magnetotelluric data

### 5.3.1. Recordings and transfer function estimation

Broad-band MT data were collected in 2004 at 36 stations in the Gurinai-depression operating four GPS-synchronized ADU06 Metronix systems and one Spam MkIII instrument simultaneously. The latter was installed as base station for the whole period of measurements in order to serve as a remote reference for latter time-series processing. The total recording time at each point was between 36 and 48 hours. For the short period band (AMT range), the instruments were programmed to sample 3 min at 4 kHz and 20 min at 512 Hz during sun-set. In the early morning between 4 and 9 o'clock, data were recorded at 64Hz, and the remainder of the day and night,

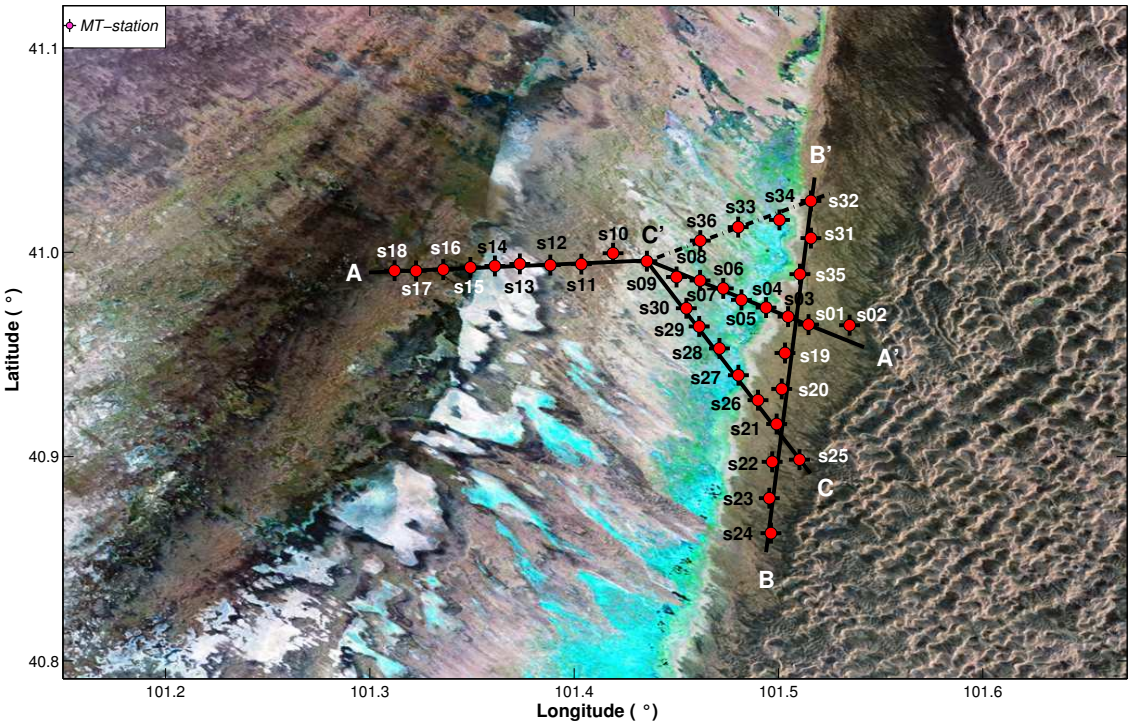


**Figure 5.8.:** Location of sites MT array, plotted on a Landsat sub-scene. Profiles $\overline{AA'}$ in $E-W$ direction, $\overline{BB'}$ in $S-N-$direction and supplementary profiles $\overline{CC'}$ and $\overline{B'C'}$ are indicated with black lines.

we sampled at 2Hz. Using this recording scheme, we were able to estimate transfer functions of reasonable quality for the period range from $1\,\mathrm{ms} - 1000\,\mathrm{s}$ using a robust bivariate time-series processing scheme (Egbert, 1997). The remote reference method was incorporated in processing, if an improvement of estimates could be achieved. However, the noise level is typically small in the measurement area, and the data are of high quality.

The location of sites is depicted in Figure 5.8. The MT array is composed of two main profiles $\overline{AA'}$ and $\overline{BB'}$ in $E-W-$ and $N-S-$ direction, respectively. Supplementary connective profiles are denoted with $\overline{CC'}$ and $\overline{B'C'}$ oriented in $SE-NW-$ and $NE-SW-$direction. The total length of profiles $\overline{AA'}$ and $\overline{BB'}$ is $21\,\mathrm{km}$ and $19\,\mathrm{km}$ with approximate site-spacings of $1\,\mathrm{km}$ and $2\,\mathrm{km}$, respectively.

### 5.3.2. Data analysis

The transfer functions, which could be estimated over six period decades, bear information about the conductivity distribution in the subsurface at scales ranging from tens of meters to tens of kilometers, covering roughly three spatial decades of increasing inductive volume but decreasing resolution. It is therefore advisable to divide the data set into period ranges, where each range may be understood in terms of structures at roughly one scale. The choice of period ranges is dictated by the data themselves and depends on the complexity and overlap of geological and related geoelectrical structures.

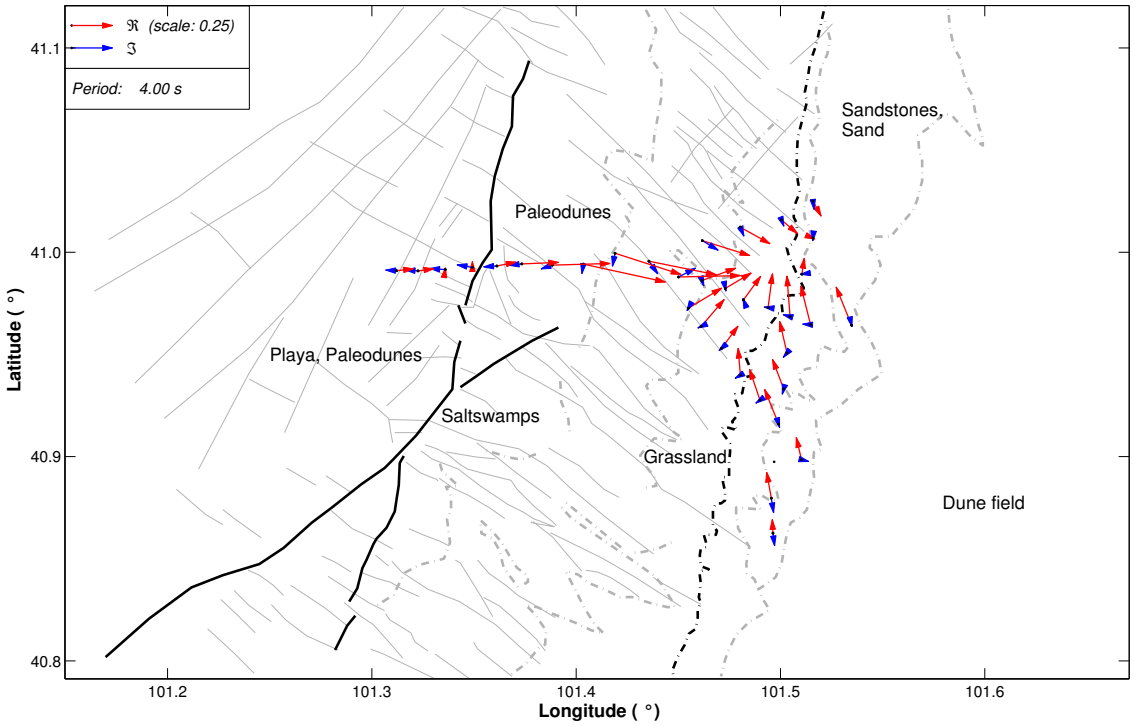


**Figure 5.9.:** Induction arrows for the period $4s$, plotted in Wiese convention. Red arrows indicate real and blue arrows imaginary induction arrows, respectively. At around this period, the real induction arrows at all sites exhibit maximum length.

**Induction arrows:** Induction arrows are generally of high quality in the whole period range from $10^{-3} - 10^{3}\,\mathrm{s}$. Their amplitudes are typically close to zero in the short-period range from $10^{-3} - 10^{-1}\,\mathrm{s}$ and the long-period range from $10^{2} - 10^{3}\,\mathrm{s}$. In between, they have maximum lengths of not more than $0.4$ and are typically changing their direction with increasing period.

An example of induction arrows is given in Figure 5.9, plotted as real and imaginary arrows in red and blue in Wiese convention (real induction arrow pointing away from a conductor) for the period of $4.0\,\mathrm{s}$. Roughly at this period, real induction arrows exhibit maximum length, while imaginary induction arrows have approximately zero length. It is seen from Figure 5.9 that at stations located in the western part of the measurement area, real arrows point basically in eastern direction with increasing length towards the center of the NS trending Gurinai structure. Further to the east, the arrows rotate, pointing to northern directions in the south and southeastern directions in the north. Thus, it is evident that the induction arrows at intermediate periods reflect the response from a 3D conductivity structure and simple interpretation in terms of a previously expected NS strike is not feasible, at least in the eastern part of the area adjacent to the Badain-Jaran-Shamo dune field.

A preliminary interpretation based upon 2D properties of real induction arrows is as follows: the subsurface in the western part of the array, i.e. stripe 5 and 6 in Figure 5.5 is occupied by a $N-S$ trending conductor causing anomalous currents along its axes at a depth corresponding to a few periods. Another conductive body of similar depth extent (assuming comparable conductivities), roughly striking $ENE-WSW$ is found in the southern part of the array, where induction arrows

point northward. Along the $S-N-$oriented profile $\overline{BB'}$, induction arrows decrease in length and turn by $180^\circ$ towards southern direction. Thus, it may be assumed, that a relative resistive body with axes at the turn-over point of induction arrows (which is equivalent to two conductive feature to the North and South, respectively) is crossed by the profile in the north. Different strike directions of conductive/resistive features can cause the irregular behavior of induction arrows in the center of the array. 3D modeling is, however, required to fully understand the behavior of induction arrows.

**Impedance tensor:** I used the impedance tensor analysis scheme described in Chapter 4 and in Becken and Burkhardt (2004) to determine the dimensionality and the regional geoelectric strike direction where a regional 2D assumption is adequate. After close inspection of the impedance tensors and ellipse parameters from the data set discussed here, three period ranges have been discriminated, comprising the AMT range from approximately $10^{-3}-1\,\mathrm{s}$ with 1D and 2D properties, an intermediate period range with 3D effects, and a long period range from approximately $64-10^3\,\mathrm{s}$, where 3D effects in the data are explainable by a 2D model with galvanic distortion. However, these data are more noisy than at short or intermediate periods and correspondingly error bars of ellipticities are large. Therefore, a regional 2D assumption with galvanic distortion is only valid within the error bars and not clearly distinguishable from induction in a 3D structure producing ellipticities in the order of their error bars. Therefore, care must be taken when attempting to explain long-period data with a 2D model, since the 2D assumption cannot be granted .

**Short period band:** In the short period band (AMT period range from $10^{-3}-1\,\mathrm{s}$), the tensor is 1D or 2D, the latter indicated by splitting sounding curves $Z_{xy}$ and $Z_{yx}$ but with neglectable main-diagonal elements $Z_{xx}$ and $Z_{yy}$ in rotated coordinates. These properties are already deducible from the sounding curves, which are shown in Figure 5.10. The range of periods, which yields vanishing ellipticities of the telluric vectors, i.e. permits a regional 2D interpretation, differs from site to site, in particular due to locally varying conductivities of the upper layers and consequently varying skin depths at a certain period. Careful selection of period bands for each site individually leads to the strike estimates, plotted as cumulative directions in the rose diagram in Figure 5.11a and as red arrows on the the map in Figure 5.12. Five sites had to be excluded from the strike analysis, since they either show a 1D behavior at shortest periods and immediately indicate 3D conditions with increasing period or data quality is not sufficient to estimate the dimensionality. The number of strike estimates, i.e. sites, which fall within a $10^\circ$ segment of a quadrant, have been counted and the number of counts determines the length of the segment in the rose diagram. (Due to the $90^\circ-$ambiguity of the strike estimate, each quadrant contains ambivalent information.) From the polar representation, a dominant strike direction of $N10^\circ W$ or $N80^\circ E$ can be deduced for the shallow structures. Only few stations yield strike estimates deviating from these directions. In conjunction with the induction arrows shown in Figure 5.9, it is obvious that in the western part of the station array, a $N-S-$strike can be concluded, and in the eastern part an EW strike will be the correct choice. Interpreting the AMT strike estimates in this way, they are plotted as red arrows in the map shown in Figure 5.12a. Here, we see a consistent representation of the geoelectric strike, which changes direction from $N-S$ in the west to $E-W$ in the east. Only at sites s22 and s25, directions of $N50^\circ E$ were obtained, which deviates from the previously described consistent image.

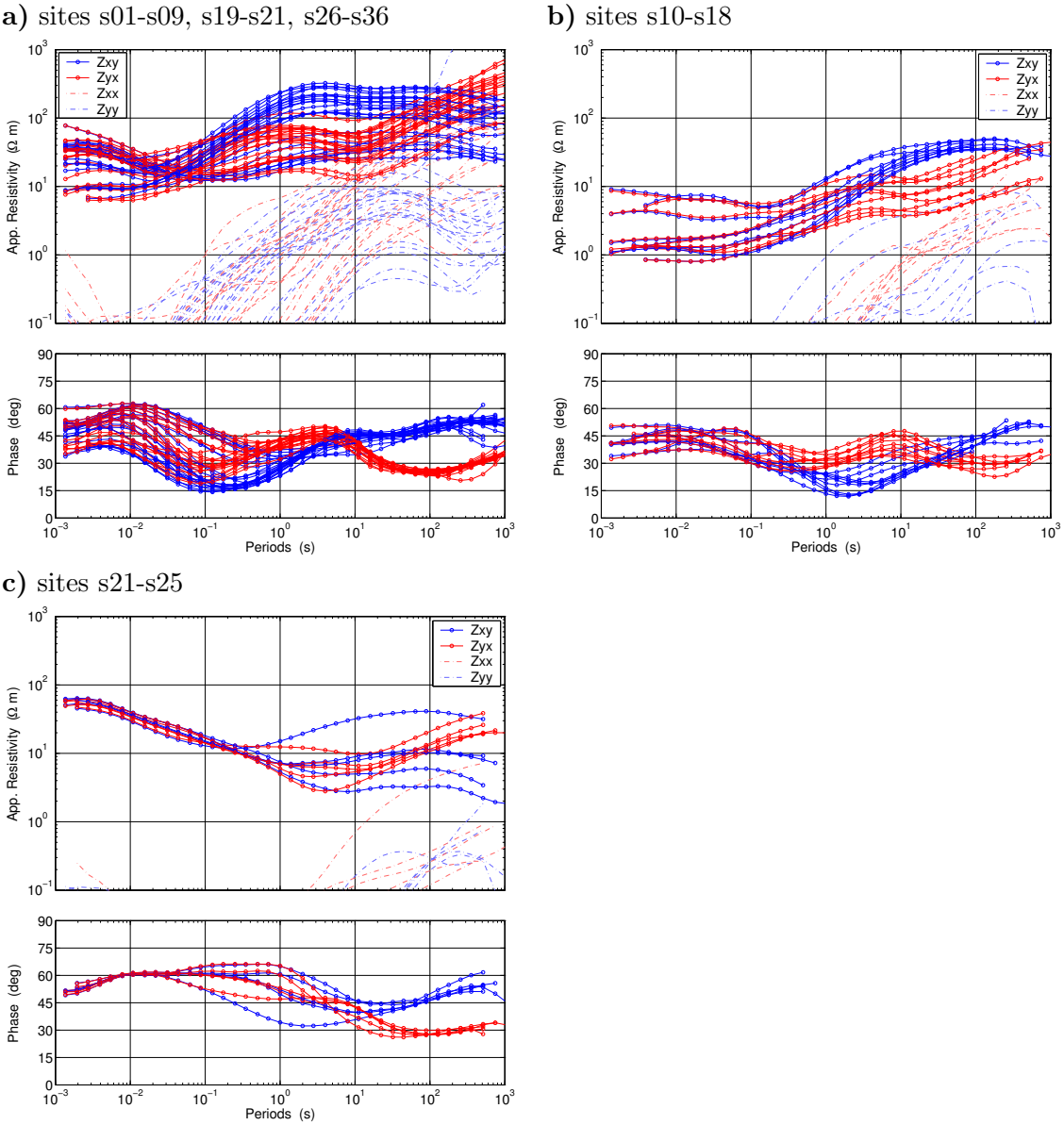


**Figure 5.10.:** $D^+$−smoothed apparent resistivities and phases of $Z_{xy}$ (blue) and $Z_{yx}$ (red), roughly separated into groups of similar characteristics. Smooth diagonal elements $Z_{xx}$ (light red) and $Z_{yy}$ (light blue) become important for periods longer than $0.1 - 10\,\mathrm{s}$ depending on site. **a)** Sites in the NE-area of measurements are characterized by a sequence of resistor-conductor-resistor. **b)** Sites in the western part of the Gurinai structure. **c)** Sites in the southern part of the measurement area.

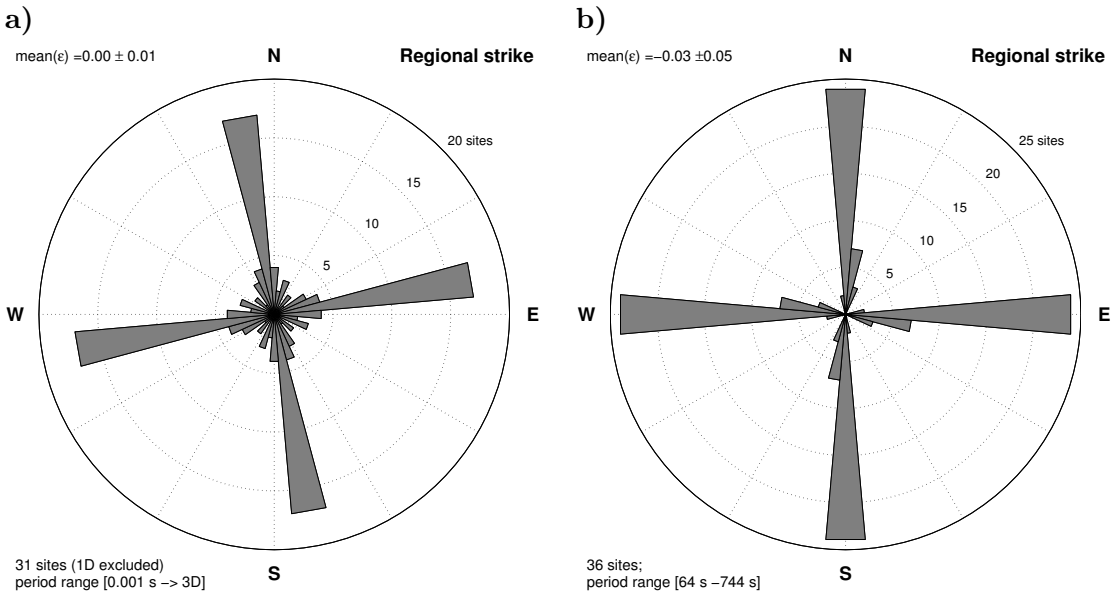


**Figure 5.11.:** Rose diagram of cumulative strike directions obtained from ellipticity analysis of the impedance tensor. **a)** Regional strike direction in the short period band from 0.001 s to several seconds. The period band was chosen for each site individually in such a way that the dimensionality is 1D/2D over the selected period range. The shallow strike direction is either $N10°W$ or $N80°E$. **b)** Regional strike direction in the long period band from $64 - 744$ s. The data are consistently explained with a 2D strike of $N0°$ respectively $N90°E$ direction, but galvanic distortion must be considered to explain the 3D effects inherent in the MT tensor.

**Long period band:** In the longest period decade, i.e., from $64 - 10^3$ s, approximately vanishing ellipticities of the telluric vectors in rotated coordinates again suggest a 2D distribution, but distortion of the electric field plays a considerable role and must be taken into account, and the 2D characteristic is not rigorously justified due to error bars of impedance data. Assuming a regional 2D structure, the results of multi-period single-site strike analysis at long periods are shown in Figure 5.11b as a rose diagram and in the map in Figure 5.12b. Inherent in the data is a predominant strike direction of large scale structures of $N0°$ or $N90°E$. Due to the large inductive volume, which is of the order of more than 10 km, I assume that only one of the directions is valid. In general, the induction arrows are small in the long period range, which contradicts the characteristics of the impedance tensor at a first glance, exhibiting a large phase split at long periods. Therefore, it is not possible to constrain the impedance strike by means of the induction arrows as in the AMT-period range, and the directions shown in Figure 5.12b are only one of two possible strike directions.

**Intermediate periods:** At periods within the range $1 - 64$ s , the off-diagonal elements $Z_{xx}$ and $Z_{yy}$ become increasingly important. Here, no coordinate can be found, in which the ellipticities of both telluric vectors vanish and the tensor represents induction in a 3D structure, which was for the same period range already deduced from induction arrows.

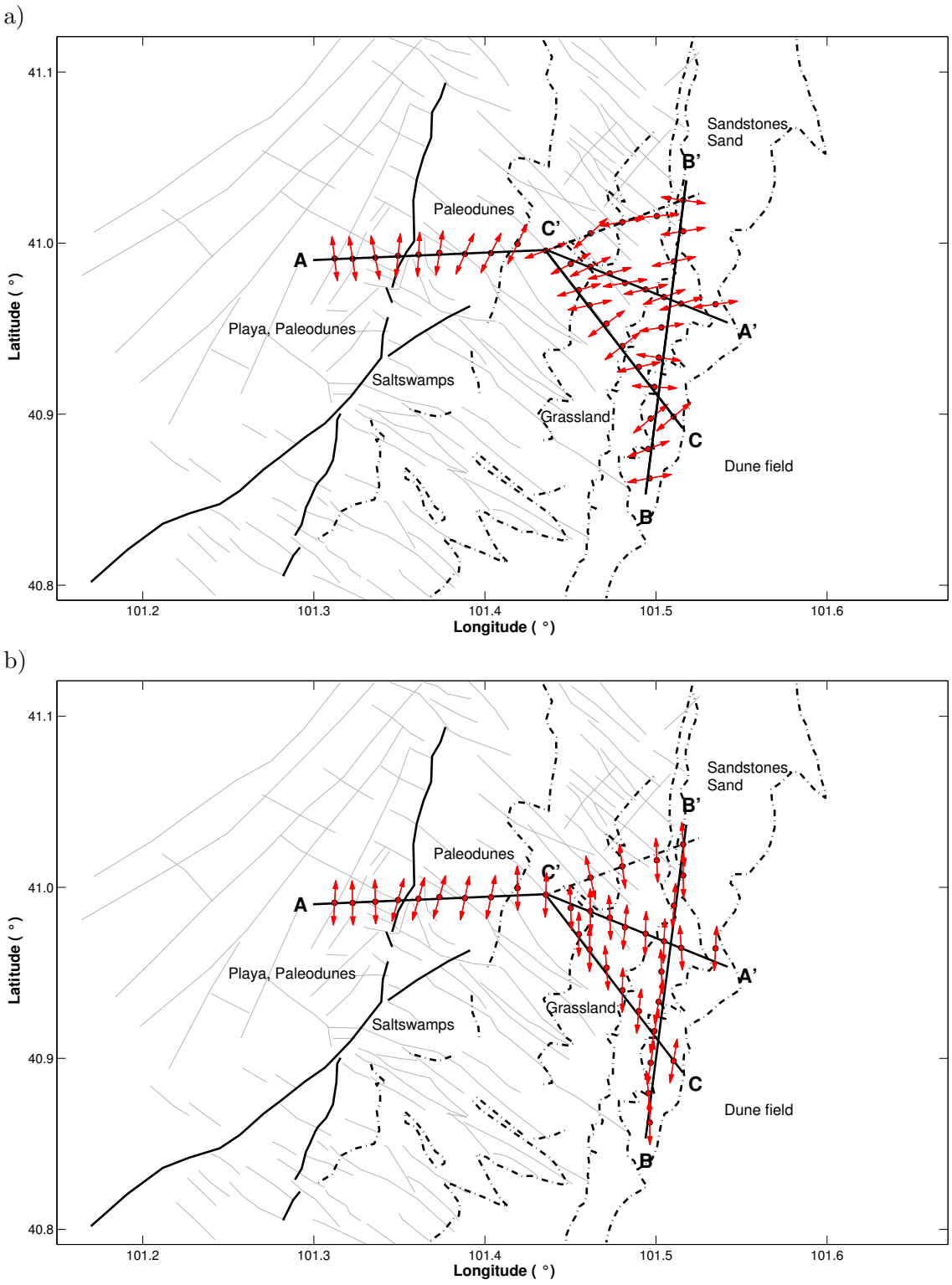


**Figure 5.12.: a)** Site-by-site estimated strike directions in the short period band $10^{-3} - 1\,\mathrm{s}$ and **b)** in the long period band $64 - 10^{3}\,\mathrm{s}$. At short periods (a), the $90°-$ambiguity of geoelectric strike determination from the impedance tensor alone has been removed in agreement with the orientation of real induction arrows. At long periods, perpendicular strike to the $N - S-$directions shown in b) are also possible.

## 5.4. Resistivity models

### 5.4.1. 1D Resistivity models

At most stations of the MT array, data show 1D behavior ($Z_{xy} = -Z_{yx}$, $Z_{xx} = Z_{yy} \simeq 0$) in the shortest period range, typically for periods smaller than $10^{-1}\,\mathrm{s}$. A 1D inversion at shortest periods (using the determinant of the impedance tensor as observed data) at each site is thus appropriate to construct a first set of resistivity models, assuming a layered earth and using a block inversion. Performing blocky 1D inversion is to some extent subjective, since the number of layers must be specified, if a layered model is sought, and secondly a number of equivalent models fits erroneous data with equal quality. On the other hand, blocky models are more illustrative in terms of layer boundaries and thicknesses and can help to connect model parameters with geological layers.

**1D Inversion:** Constraints partly removing model equivalences can be put on the model, when data from different methods are used, owing to their different sensitivities to model parameters. Removal of model ambiguity employing a joint inversion requires naturally, that data have an overlap in depth of penetration. Therefore, at most MT-sites on profile $\overline{AA'}$, we have measured DC-geoelectrical data using a Schlumberger layout with maximum current electrode separations of $574\,\mathrm{m}$ ($L/2 = 237\,\mathrm{m}$) yielding depths of penetrations of $250\,\mathrm{m}$ at maximum. Joint inversion of short-period MT data and DC soundings is therefore feasible in order to obtain high-resolution models for the uppermost section of the subsurface.

In general, MT and DC apparent resistivities are not directly comparable owing to the influence of static shift of the electric field measurements in both methods and, if present, to transversal anisotropy within the subsurface. Transversal (macro-)anisotropy is frequently observed in case of rhythmic stratification of sedimentary packages, composed of, say, clay and sand layers differing in their resistivity. Telluric currents excited by an external plane wave flow in horizontal directions, and the effective MT resistivity may be conceived as shunt circuit of individual layer resistivities. In DC, where currents are galvanically injected into the subsurface, both vertical and horizontal currents arise and consequently series and parallel connexions of layer resistivities contribute to the electric potential difference observed at the surface. The effective resistivity for DC currents is therefore determined by the geometric mean of series and parallel resistivities (Mundry, 1985), and differs from the effective MT resistivity.

The detection of transversal anisotropy using joint inversion is obscured by unknown static shifts of measured electric fields yielding shifted apparent resistivities, while MT phases are not affected. Thus, in addition to the resistivity model, two static shift factors and a transversal anisotropy coefficient are to be determined in the inverse calculations. To reduce ambiguity, DC static shift has been fixed to unity, and in a first step DC and MT apparent resistivities and phases were jointly inverted using an isotropic model, while static shift of MT data was permitted. In a second step, which was only applied if data fit was not acceptable, anisotropy was permitted, but the anisotropy model was only accepted, if data fit could be improved. This was not the case for any of the measurement points, and therefore only isotropic models have been produced. For joint inversion, we used a simulated annealing code of the class of random search algorithms (Kroupa, 2001), where inversion was run several times for each data set in order to produce equivalent models or to detect local minima in the objective function, i.e. the function which is sought to be minimized in inversion.

At MT points, where no DC data were available, individual MT 1D block inversion was conducted.

Equivalent models were disqualified by comparison with models at adjacent measurement points in order to produce a high semblance of 1D models. However, in some parts of the profiles, considerable differences in the characteristics of the short period sounding curves have to be noticed, indicating lateral variability on a larger scale than the penetrated depth and consequently leading to different 1D model types.

For an interpretation of 1D-models, conductivities within sediments are basically to be explained by the salinity of the pore fluid, fully saturating the porous medium, which is composed of sand, silt or clay or a small-scale stratification or mixture of both or all of them. The resistivity of basement rocks is not safely determined from our data using 1D inversion, since the MT-sounding curves split up when penetrating the basement. On the other hand, this effect suggests the interpretation in terms of metamorphic and crystalline basement rocks with either undulating topography or directional dependency of conductivities due to intrinsic or macroscopic anisotropy or due to both. In the present case, we therefore determined the basement resistivity using 1D inversion from the determinant of the impedance tensor, producing a sort of mean value of resistivities. Note, that from resistivity values alone, it is sometimes difficult to decide whether basement rocks or sediments are present, since - as we found from measurements in other parts of the Gaxun-Nur area directly above out-cropping basement - basement resistivities can be as low as $20\,\Omega\mathrm{m}$. Then, such resistivities typically represent highly fractured or weathered, water saturated metamorphic rocks.

The results of 1D inversion at all MT sites are perspectively depicted in Figure 5.13 as colored columns with a vertical exaggeration of factor 4. Superimposed on the plot are the profile lines (solid grey) and the boundaries of the Gurinai depression separating stripes 2 and 3 in the east and 6 and 7 in the west, respectively (compare with Figure 5.5). The same models are plotted in Figure 5.14 as sections along profiles $\overline{AA'}$, $\overline{BB'}$ and $\overline{CC'}$, where a interpretation in terms of layer boundaries, faults and lithology has already been added and is discussed in section 5.5. Resistivity models may basically be classified into three groups corresponding to the grouping of impedance transfer function shown in Figure 5.10. They comprise layer sequences of types conductor/resistor in the western part of the array, resistor/conductor/resistor in the eastern part and resistor/conductor in the southern part. Let me describe the models briefly following the profile traces.

**Profile $\overline{AA'}$:** The geoelectric section along Profile $\overline{AA'}$, shown in Figure 5.14a, is composed of various low resistive ($1\,\Omega\mathrm{m}$) to intermediate resistive ($30\,\Omega\mathrm{m}$), discontinuous sedimentary layers ranging in cumulative thickness between $200\,\mathrm{m}$ and $600\,\mathrm{m}$, which are based by rocks of intermediate ($30\,\Omega\mathrm{m}$) to high resistivities ($> 500\,\Omega\mathrm{m}$). Basement rocks may itself be discriminated into different types according to their resistivities and are hereafter denoted as crystalline (label C in Figure 5.14a) and metamorphic basement (P), representing high resistivities and intermediate resistivities, respectively. Interpretation of basement in depths of several hundred meters is only granted for the highly resistive block due to the absence of highly resistive sedimentary layers in the Gaxun-Nur basin, as deduced from our previous measurements. The assumption of metamorphic rocks is also justified by previous measurements above exposed basement rocks in the Jingshutu area and at the northeastern margin of the Gaxun-Nur basin (cf. Figure 5.4), where crystalline and metamorphic rocks occur closely assembled and the latter had resistivities of the order of $20\,\Omega\mathrm{m}$. If, in spite, resistivities of $30\,\Omega\mathrm{m}$ below $600\,\mathrm{m}$ depth in Figures 5.13 and 5.14 were interpreted in terms of sediments, enormous vertical displacements along the boundaries of the crystalline block had to be assumed, which cannot be justified.

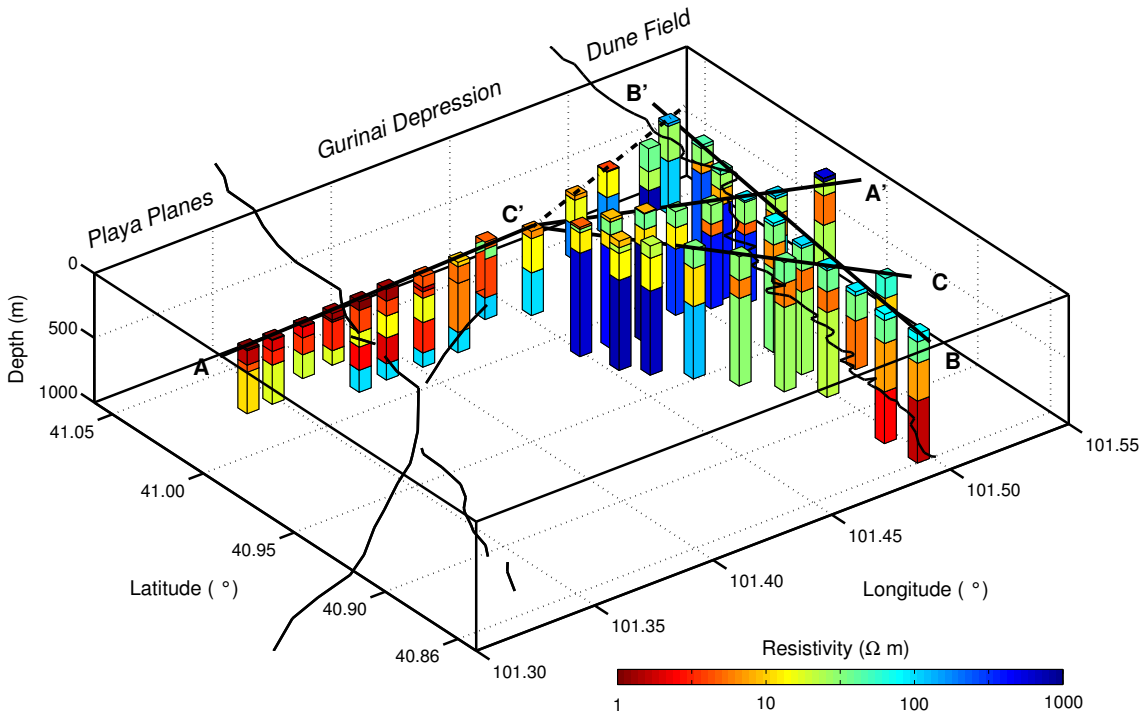


**Figure 5.13.:** 1D inversion results. Colored columns indicate resistivity section as obtained from 1D block inversion of determinant of the impedance tensor. Profile lines are depicted in black and boundaries of the Gurinai depression in black lines. Vertical exaggeration of resistivity sections is at factor 4.

A laterally inhomogeneous basement with laterally varying topography is therefore interpreted from Figure 5.14a. From east to west, a successive decrease in basement depth from $400\,\mathrm{m}$ to $200\,\mathrm{m}$ is observed between sites s02-s08. Further to the west, a basement depression is found east of site s08 and west of site s15, with a maximum basement depth of approximately $600\,\mathrm{m}$ at site s12. The depth of the basement cannot be reliably determined from 1D-inversion at the westernmost stations. Along the profile, basement resistivities correlate with its topography, i.e. lowest basement depths of $200-300\,\mathrm{m}$ are found for the resistive, crystalline block (C), while the depression in the central part of the profile and the basement in the eastern part of the profile part are considerably deeper ($300-600\,\mathrm{m}$) and based by metamorphic rocks (P,P'). The westernmost basement (P") is presumably also composed of metamorphic rocks due to low resistivities.

Resistivities of sediments indicate a heterogeneous composition of sedimentary strata pointing towards locally varying sediment types or locally changing salinity of pore fluids or both. Generalizing the uppermost resistivity section, an increase of resistivities from west to east across the Gurinai depression is found. In particular, near-surface sediments ($< 300\,\mathrm{m}$ depth, $\mathrm{Q}^l$) in the western part of the profile $\overline{AA'}$ are composed of highly conducting layers ($1\,\Omega m$, red colors in Figure 5.14a) and, in conjunction with the salt swamps found at the surface east of site s15 and the playa sediments west of s15, are interpreted as material saturated with salt water and having a large content of clay. While the type of rocks (basement or sediments) deeper than $200-300\,\mathrm{m}$ west of s15 is unclear, a conductive sedimentary layer (M') is found east of s15 at depths between

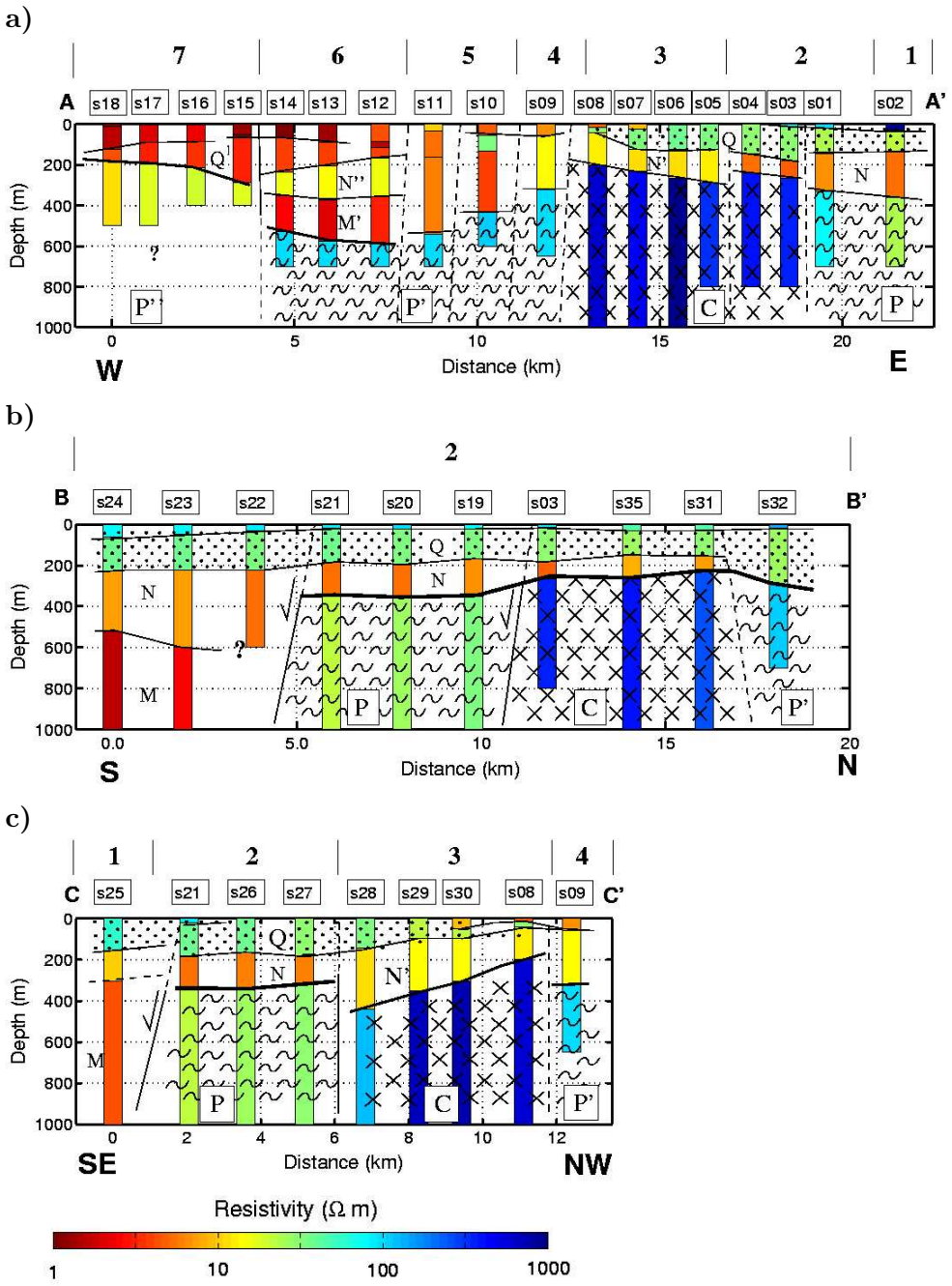


**Figure 5.14.:** 1D model section. **a)** Profile $\overline{AA'}$ across the Gurinai structure from west (left) to east (right). **b)** Profile $\overline{BB'}$ along the eastern margin of the Gurinai structure from south (left) to north (right). **c)** Diagonal $\overline{CC'}$ from southeast (left) to northwest (right). Profiles $\overline{AA'}$ and $\overline{BB'}$ intersect each other at sit s03, profiles $\overline{BB'}$ and $\overline{CC'}$ have the common site s21 and $\overline{AA'}$ and $\overline{CC'}$ site s09. Numbers 1-7 indicate stripes defined in Figure 5.5. Resistivities are color-coded using the same scale as in Figure 5.13. Resistivity boundaries are interconnected where appropriate and layers are partly assigned a signature indicating the lithology. Supposed traces of faults are indicated. Green, dotted areas correspond presumably to fresh-water bearing sand layers with moderate resistivities ( $50\,\Omega$m), crosses indicate resistive basement (dark blue colors,$> 300\,\Omega$m), and tildes are connected to metamorphic basement. Red and yellow colors indicating high conductivities ($1 - 15\,\Omega$m) correspond to salt- or brine-water layers. Labels Q,N,M,C,P are referred to in the text.

$400\,\mathrm{m}$ and $600\,\mathrm{m}$, overlain by a moderately resistive layer (N") of $200\,\mathrm{m}$ thickness, which cannot be traced further to the east than site s12. Note that the deep conductor (M') east of s15 is significantly absent west of s15.

While no layering can be interpolated within the central part of the profile (s11-s09), sediments in the eastern segment of the profile are differentiable into two layers. The shallow layer ($30\,\Omega m$, dotted green in Figure 5.14a, label Q), thinning out to the west, is composed of fresh-water bearing sandy material, which follows from surface observations. It is underlain by a conductor ($5-12\,\Omega\mathrm{m}$, N' and N) with decreased resistivity (N) in the east and thickness between $100\,-300\mathrm{m}$. A thin surface resistor ($90\,\Omega\mathrm{m}$) east of s03 corresponds to not fully satisfied sand/sandstone, which are exposed here.

It is remarkable, that lateral conductivity changes clearly coincide with geomorphological transitions as follows: the western termination of the layer sequence N" and M' and the basement transition from P' to P" corresponds to the western boundary of the Gurinai depression, i.e. the transition between stripes 7 and 6 in Figure 5.5; the extent of layers N" and M' corresponds to the extent of the salt swamp (stripe 6); the irregular domain in the central part of the profile corresponds to the paleo-dunes (stripe 5). The freshwater layer Q reaches as far to the west as to the boundary between stripes 3 and 4 coinciding with a change in vegetation; the resistivity of conductor N' drops across the eastern boundary of the Gurinai depression, i.e. between stripe 2 and 3; a surface resistor is only observed within stripes 1 and 2.

**Profile $\overline{BB'}$:** Parallel to the eastern margin along the Gurinai-depression, i.e., along profile $\overline{BB'}$ shown in Figure 5.14b, undisturbed sediments of $200\,\mathrm{m}$ thickness (dotted, green area, Label Q) are found, indicating fresh-water as a pore fluid due to resistivities of $30\,\Omega\mathrm{m}$ and corresponding to the layer Q identified in the eastern part of profile $\overline{AA'}$. A thin surface layer of higher resistivities corresponds to out-cropping sandstone-sand bedding, which are presumably not fully saturated with fluids and therefore more resistive than the underlying layer. Conductive sediments (N, $5\,\Omega\mathrm{m}$, orange colors) below the fresh-water layer (Q) extend over a depth range from $200\,\mathrm{m}$ to $400\,m$ in the central and northern part of profile $\overline{BB'}$, where they are based by metamorphic (P, P') and crystalline (C) rocks. In the southern part of the profile, i.e, south of site s21, conducting layers (N,M) attributed to sedimentary strata saturated with salt-water giving rise to resistivities of $1-5\,\Omega\mathrm{m}$ are found down to a depth of at least $1300\,\mathrm{m}$. Depth of layer N in the southern part is not clearly determinable due to low resistivities of both layers N and M, but apparently, the thickness of layer N increase towards the south.

Basement rocks may again be differentiated into metamorphic and crystalline rocks, corresponding to profile $\overline{AA'}$. A significant increase of basement depth coinciding with the increased thickness of sediments (N,M) exists in southward direction.

**Profile $\overline{CC'}$:** 1D-models of the diagonal profile $\overline{CC'}$ are shown in Figure 5.14c. The same units (Q,N,N',M related to sedimentary strata and P,C related to basement) as on profiles $\overline{AA'}$ and $\overline{BB'}$ are easily identified, and not further described here.

### 5.4.2. 2D Resistivity models

For periods longer than $10^{-1}-1\,\mathrm{s}$, impedance sounding curves split and induction arrows become increasingly important, both indicating the presence of anomalous conductivity structures in the

subsurface. For periods not longer than $1 - 10\,\mathrm{s}$ depending upon site, the impedance tensor analysis suggests anomalous features with a 2D character and the strike directions depicted in Figure 5.12a.

In conjuction with the results of 1D-inversion (Figure 5.14), the cause of anomalous fields may hypothetically be attributed to structures within the basement and to a change of basement depth, which are assigned a strike direction as an outcome from strike analysis. In particular, three main anomalies are deduced from 1D models.

- Across the western lineament (cf. Figure 5.5), a roughly $N - S-$striking trough of highly conducting sediments (Q,N",M') with maximum depths of app. $600\,\mathrm{m}$ is detected. The depth of the sedimentary trough decreases to $200\,\mathrm{m}$ towards the center of the Gurinai depression. Such a structure causes anomalous currents along its axes producing induction arrows pointing away from the conductor, i.e. pointing in eastern direction east of its axes, as also observed in measured data.
- The basement is not homogeneous, but composed of blocks with different resistivities (C,P). In particular, a resistive, presumably crystalline block (Figures 5.13 and 5.14), embedded in rocks of moderate resistivities, is evident from 1D inversion and found below the measurement points in the northeastern part of the MT-array. Results of strike analysis as well as the results from 1D inversion suggest a strike direction of $N80°E$.
- Thirdly, in the south of profile $\overline{BB'}$, the thickness of highly conductive, presumably sedimentary layers (N,M) increases from $350\,\mathrm{m}$ to more than $1300\,\mathrm{m}$. The strike directions estimated from impedance tensor analysis in the vicinity of this structure (s25 and s22) are $N50°E$.

2D inversion is performed to test the preceeding interpretation of 1D models with respect to basement topography and basement composition, to add or delete anomalies where required, and to add information at greater depths.

**2D Inversion:** Most 2D MT inversion codes employ a linearized finite difference forward modeling operator, where the conductivity distribution is represented in terms a number of cells with constant conductivity, and the electromagnetic field is solved for iteratively. The electromagnetic field is numerically evaluated on the same grid and for an accurate solution, a great number of grid cells has to be used. Since the number of cells greatly exceeds the number of data (i.e. the surface transfer functions as a function of profile distance and period), there exists no unique solution of the inverse problem, and a regularization is required. In most of the cases, a smoothing operator is introduced, which minimizes a norm of the conductivity gradients, while fitting the data. The model roughness as well as the data fit enter the objective function, which is sought to be minimized. The relative weight of data fitting and smoothing is controlled by the regularization parameter $\tau$, which has to be determined for each problem individually. There is no safe way to determine $\tau$, because the conductivity distribution is unknown a priori. It should, however be chosen large enough to eliminate spurious features in the solution, e.g. vertical features occurring within neighboring sites.

In addition to the smoothness constraint, it can be demanded that the solution deviates minimally from a given a priori model, which has been constructed by other means. I found this feature to be useful in particular when the site spacing is large compared to the skin-depth and the overlap

of induction volumes of neighboring sites is small. Then, an a priori model can be constructed from 1D models, and 2D inversion can be employed to add anomalies or to delete features of the a priori model, which do not agree with 2D data.

A critical point in the inversion is the relative weighting of apparent resistivities and phases of E- and B-Polarization, respectively, and of the induction arrows. In general, each datum is weighted with its inverse variance, such that good estimates of transfer functions have a higher influence on the inverse model than weak estimates. However, error bars of MT transfer functions are often not well determined, e.g. coherent noise does not produce error bars but does lead to erroneous transfer functions estimates, and in addition geological noise like galvanic distortion is not incorporated. To account for galvanic distortion, it can be advantageous to emphasize phases and induction arrows, which are free of galvanic effects and to downweight apparent resistivities, which still might be shifted due to unresolvable static shift. The latter applies in particular to E-Polarization apparent resistivities. Due to the 2D restriction of conductivity models, E-Polarization apparent resistivities with static shift cannot not be simulated and have to be accounted for by other means, e.g. by putting large error bars on data or by inverting for shift factors also. For B-Polarization apparent resistivities, static shift can be produced by the model itself, if shallow anomalies are placed at the surface.

A number of tests has been performed with respect to the choice of the regularization parameter and the value of floor error bars imposed on data. Due to generally high conductivities of the upper few hundred meters of the section and a site spacing of $1-2\,\mathrm{km}$, high regularization has to be used. Here, I use $\tau = 30,\ \ ,100$ and relatively small error bars ($0.05$ of apparent resistivities, $0.02$ of phases, and $0.01$ on induction arrows) if no galvanic distortion is evident, otherwise, I increase the error bar on E-Polarization apparent resistivities up to a level of $0.5$.

**Short-period range:** Where the 2D assumption holds and where the strike direction is not aligned with the profile, short-period data are subjected to a 2D inversion. The latter criterion demands exclusion of the eastern part of profile $\overline{AA'}$ from 2D inversion, since the strike direction of the resistive basement block is subparallel to profile direction. For the purpose of 2D inversion, impedance tensor data have been rotated to the directions indicated in Figure 5.12a, and apparent resistivities and phases and induction arrows have jointly been inverted using small error floor.

Two types of models have been produced for profiles $\overline{AC'}$, $\overline{BC'}$ and $\overline{CC'}$ from short period data and are depicted in Figures 5.15-5.17. Firstly, I calculated smooth models starting from homogeneous half-space of $20\,\Omega\mathrm{m}$. Secondly, I constructed 2D a priori models by inter- and extrapolating 1D resistivity profiles and performed regularized inversion with a priori information. A priori models and results of inverse modeling incorporating a priori models are shown in Figures 5.15-5.17a and b, respectively. The smooth models are shown in Figures 5.15-5.17c, respectively. The same color scale as for the 1D models in Figures 5.13 and 5.14 has been used to display the 2D resistivity sections. For inverse calculations, the codes of Mackie et al. (1997) and of Siripunvaraporn and Egbert (2000) have been used. Since both codes lead to similar results, I only show the models calculated with Mackie's code.

**Profile $\overline{AC'}$:** The mean rotation angle along the sub-profile $\overline{AC'}$ is approximately $N0°$, i.e. data have already been measured in strike coordinates. Data fit, which can be achieved for short period data along profile $\overline{AC'}$ is in the order of 2.5 for the models shown Figure 5.15b and c. These models can be conceived as spanning a range of possible solutions within blocky models

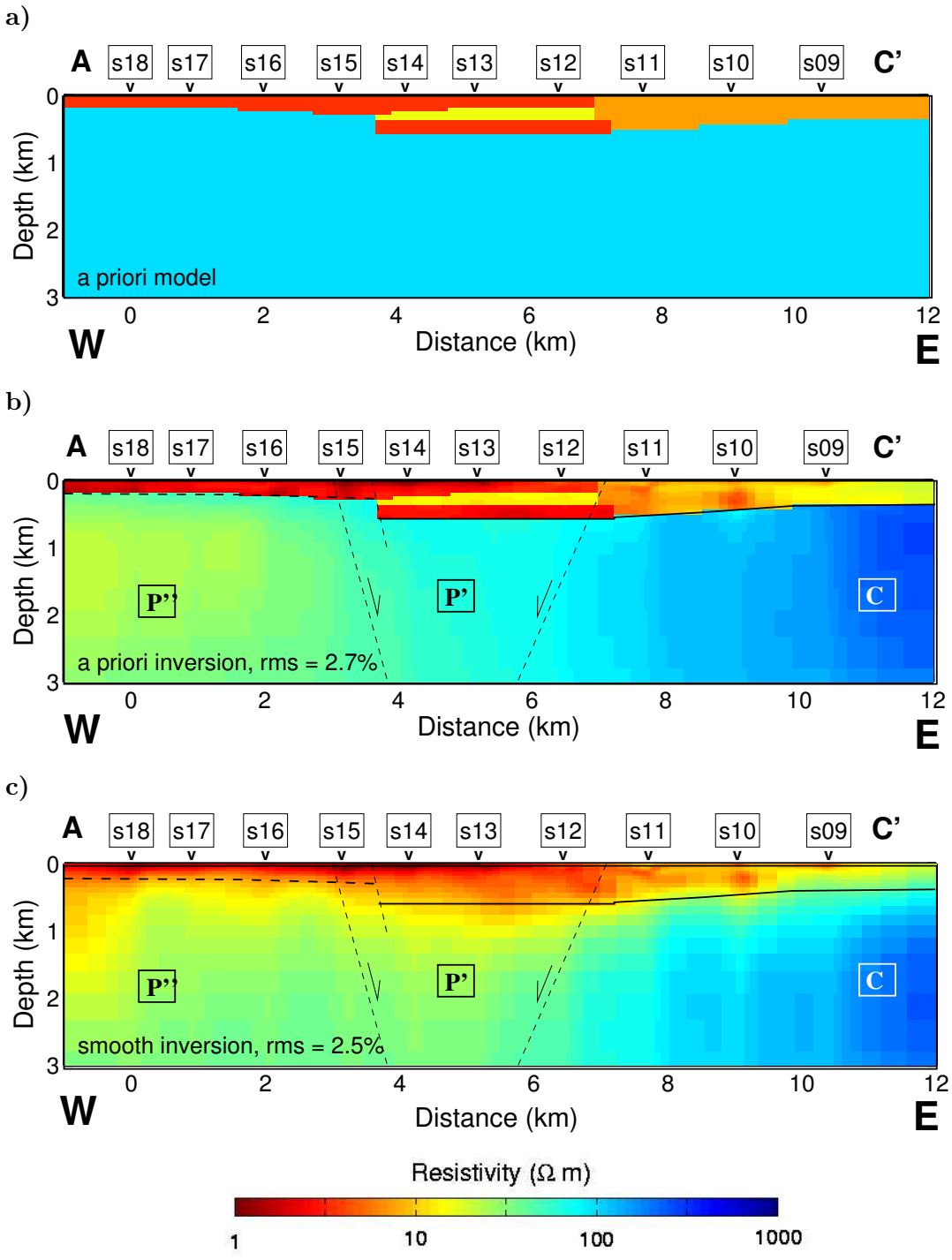


**Figure 5.15.:** Profile $\overline{AC'}$: 2D joint inversion of E- and B-polarization apparent resistivities and phases and induction arrows in the periods range $10^{-3} - 10^{1}$ s. **a)** A priori resistivity model constructed from 1D inversion results. **b)** Inversion result closest to the a priori model while fitting the data with RMS=2.7. **c)** Smooth Inversion result (RMS=2.5) using a homogeneous half-space of $20\Omega m$ as starting model.

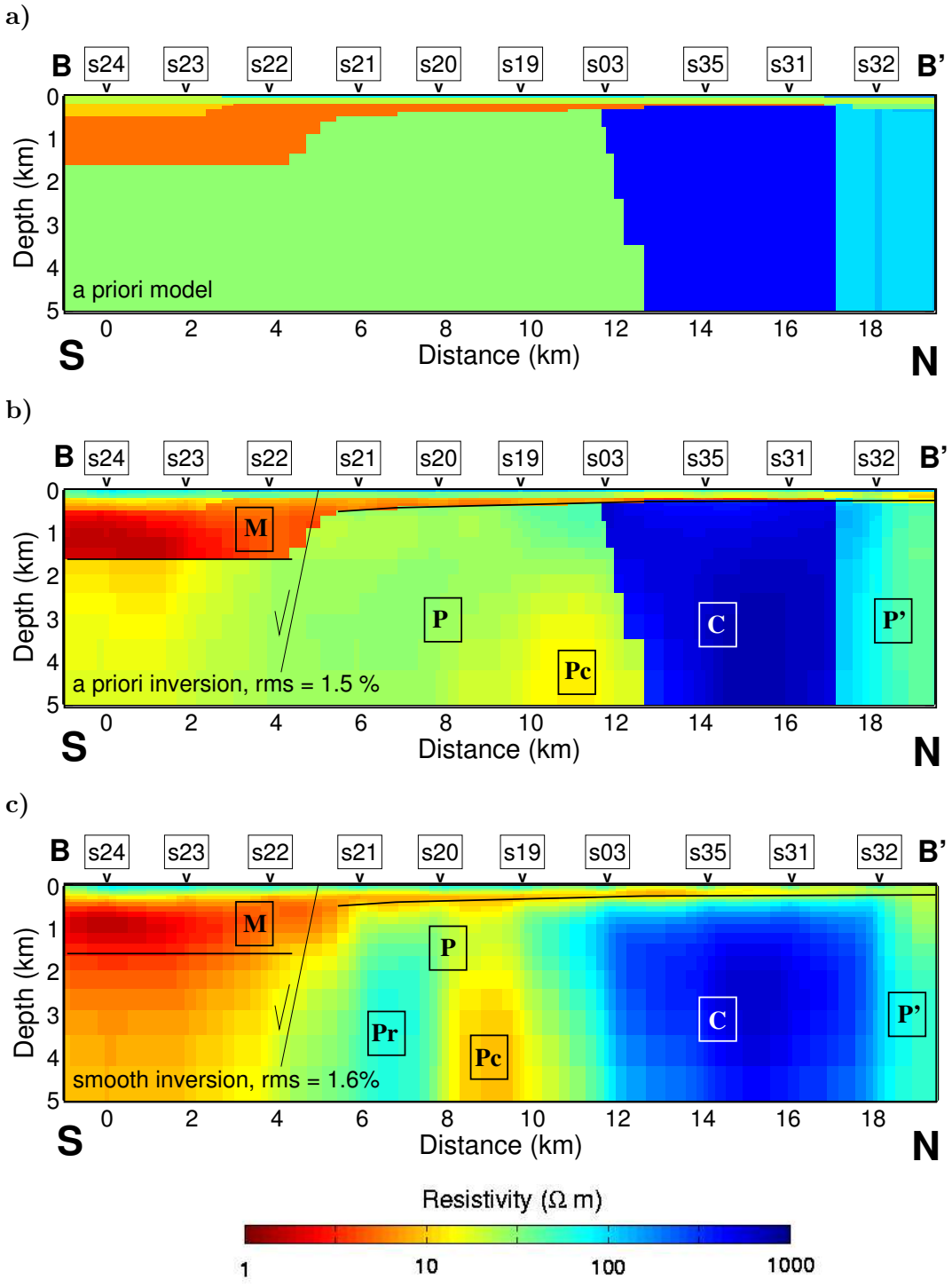


**Figure 5.16.:** Profile $\overline{BB'}$: 2D joint inversion of E- and B-polarization apparent resistivities and phases. **a)** A priori resistivity model constructed from 1D inversion results. **b)** Inversion result closest to the a priori model while fitting the data with RMS=1.5. **c)** Smooth Inversion result (RMS=1.6) using a homogeneous half-space of $20\Omega m$ as starting model.

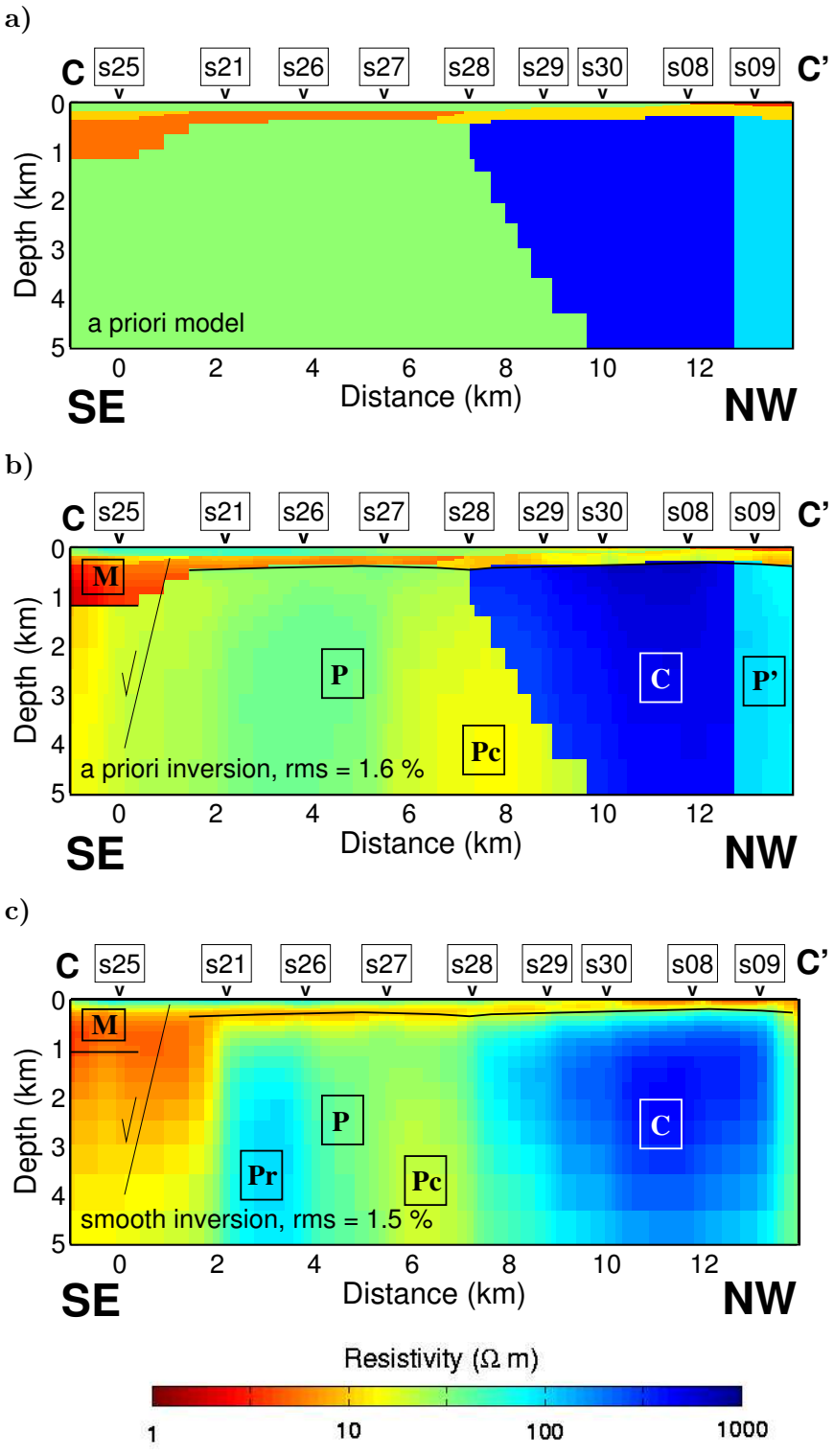


**Figure 5.17.:** Profile $\overline{CC'}$: 2D joint inversion of E- and B-polarization apparent resistivities and phases. **a)** A priori resistivity model constructed from 1D inversion results. **b)** Inversion result closest to the a priori model while fitting the data with RMS=1.7. **c)** Smooth Inversion result (RMS=1.5) using a homogeneous half-space of $20\Omega m$ as starting model.

and smooth models, respectively. The blocky model is the outcome of an a priori inversion using the a priori model shown in Figure 5.15a, which approximately represents the 1D section of Figure 5.14a. As stated previously, the depth of the basement in the westernmost part of profile $\overline{AA'}$ could not be determined by means of 1D inversion. Therefore, I assumed for the construction of the a priori model, that the basement type is the same throughout the whole profile, and that its depth west of site s15 corresponds to the maximum resolved depth of shallow conductive layers.

Note, that most of the features of the a priori model are retained in the final inversion result. In particular, it was not necessary to change the depth of the basement, imposed as an a priori information, in order to fit the data. This does, however, not imply that the basement depth is verified but rather demonstrates, that the MT transfer functions are not sensitive to resistors. In spite, the resistivity distribution within the conductive layers and the basement has slightly been modified during inversion. In particular, west of site s15, resistivities below $300\,\mathrm{m}$ were decreased such that a sub-vertical transition (P'',P') within the basement is indicated below the surface trace of the western lineament (cf. Figure 5.5) at site s15. In order to test if this effect is significant, I repeated the inversion while fixing the basement resistivity to $50\,\Omega\mathrm{m}$ west of site s15. As a result, it turned out that the misfit at stations s15 to s18 significantly increased by a factor of approximately 2. Therefore, a small but significant change of resistivity in the basement has to be noticed here, with resistivities of not more than $20\,\Omega\mathrm{m}$ west of site s15.

The smooth model is shown in Figure 5.15c. Due to the large site spacing compared with the small skin-depth within the highly conducting sediments, the lateral resolution is poor. Additionally, the small resistive inclusion below site s12-s14 at a depth of $300\,\mathrm{m}$ is not reproduced owing to the insensitivity of the electromagnetic fields to resistive features. However, it is also evident from smooth inversion, that the thickness of sediments changes along profile with a maximum at site s13, and the basement depth equals to some extent that deduced from 1D and 2D a priori inversion. Additionally, it may be concluded from the result of smooth inversion, that the basement resistivity increases from west to east, which is in agreement with the results of the a priori inversion.

**Profile $\overline{BB'}$:** The same inversion procedure has been applied to short-period data along profile $\overline{BB'}$, with the results being depicted in Figure 5.16. The mean rotation angle at sites is $N15°W$, i.e. the projected profile lies between the actual profiles $\overline{BB'}$ and $\overline{CC'}$. The data fit, which could be achieved after convergence of the inverse procedure lies at 1.5 and 1.6 and indicates with respect to the small floor errors being used a nearly perfect representation of data. In order to obtain this data fit in the a priori inversion, the basement resistivities in southern part, i.e. below the $1.5\,\mathrm{km}$ thick sedimentary conductor (labeled with M in Figure 5.16), and north of the resistive body (C) were adjusted. A very similar model is found from smooth inversion, starting with a homogeneous half-space of $30\,\Omega\mathrm{m}$. The shallow conductor along the whole profile, which was already known from 1D inversion models, as well as the southern conductor (M) and the northern resistor (C) are nicely reproduced without providing a priori information. Note, that smooth inversion also adds a conductive column (Pc) and a resistive column (Pr) in the central part of the profile, which are less pronounced in the result of the a priori inversion. Tests with different a priori models have shown, that an a priori given dip of the southern margin of the resistor C controls the extent of the conductive region Pc in the inversion result, which is most prominent when using a vertical boundary and less pronounced using the dip shown in Figure 5.16. These class of models equivalently well explain data at the surface, but it is easier to explain a dipping contact within the basement than a vertical conductor with resistivities of $10\,\Omega\mathrm{m}$ or less at depths below $3\,\mathrm{km}$.

However, the conductor Pc cannot be disregarded completely. To test its significance, I ran several smooth inversions with the area comprising features Pc and Pr fixed to resistivities within the range between $10 - 30\,\Omega\mathrm{m}$ but none of the results yields acceptable data fit. Therefore, a homogeneous basement in the central part of the profile is rejected by data.

Thus, besides conductor Pc and resistor Pr, the models shown in Figure 5.16b and c are similar and well constrained with respect to the main features M,N,Q,P, and C.

**Profile $\overline{CC'}$:** The mean rotation angle for stations along profile $\overline{CC'}$ is again $N15°W$, equal to profile $\overline{BB'}$. Thus, for 2D inversion, profiles $\overline{CC'}$ and $\overline{BB'}$ are projected onto each other. The inversion results for profile $\overline{CC'}$ shown in Figure 5.17 are consequently very similar to those of $\overline{BB'}$ and only differ with respect to near surface features in the northwestern part of the profile. On the upper crustal scale, the same features M,N,Q,P, and C are recovered. The same argumentation as for profile $\overline{BB'}$ holds here with respect to the column-like anomalies Pc and Pr.

**Long-period range:** As an outcome of impedance tensor analysis, impedance data at long periods exhibit a regional 2D character with a consistent strike direction of either $N - S$ or $E - W$. Since galvanic distortion is evident, data have to be decomposed prior to 2D-inversion. The galvanic distortion is supposed to be due to the conductivity anomalies resolved at short periods and described in the previous paragraphs.

At periods longer than $64\,\mathrm{s}$, the skin-depth exceeds $10\,\mathrm{km}$, assuming a mean resistivity of $10\,\Omega\mathrm{m}$ or higher, and is of the order of the length of profiles or longer. Thus, 2D inversion tends to place anomalies away from the profile, which are no longer reliable. In addition, as can be seen from Figure 5.10, all sounding curves exhibit the same phase split at long periods, i.e. no lateral variations along the profiles are evident from the data, although the phase split itself indicates 2D conditions. Induction arrows are small at long periods with maximum length of approximately $0.1$ at $100\,\mathrm{s}$ contradicting the assumption of lateral changes being the major cause of the observed phase split. These observations do not suggest an ordinary 2D inversion. Instead, anisotropic conductivities in the middle and lower crust can serve as an explanation of laterally constant phase splitting in conjunction without a vertical magnetic field anomaly, i.e small induction arrows.

### 5.4.3. 3D Resistivity model

In the previous section, I constructed and described 1D and 2D conductivity models from short-period data only. At all sites, data exhibit 3D characteristic at intermediate periods, and the simplifying 1D and 2D approaches are not feasible. In the long period range, 2D inversion neither seems to be appropriate as discussed above. Either full 3D modeling or 2D modeling incorporating anisotropy are required to explain data at intermediate and long periods, respectively. For both classes of models, no practical inversion codes are available and the interpreter is restricted to trial-and-error forward modeling. Both model types have been considered in this study, and the results of 3D modeling are briefly described.

**3D modeling:** To contribute to the issue of 3D numerical forward modeling and inversion, I suggest a novel solution of the electromagnetic integral equation, which is based upon a wavelet decomposition (Daubechies, 1992) of the electric field and the conductivity structure. The current formulation, outlined in Appendix B, is restricted to the 2D E-Polarization case, but is also

promising with respect to 3D problems. The latter were not solved so far, and therefore I used a readily available code for 3D modeling.

Here, I employed the finite difference code of Mackie and Madden (1993); Mackie et al. (1993). The forward modeling procedure consists of the construction of the model, the definition of the finite difference grid, the discretization of the model, i.e., its projection onto the grid, the modeling itself, and finally an adjustment of the model as deduced from comparison of modeled data with measured data.

In the way I have used the program, the model is constructed from a plane layered background earth, into which a number of homogeneous bodies are placed. In order to define the background structure and the bodies, I considered the conductivity models described earlier as slices within the 3D volume. From these slices, blocks of constant conductivity were abstracted and extrapolated in strike direction. Additional information was imposed from satellite image interpretation (cf. Figure 5.5) and from the comparison of surface features interpreted from satellite data with the conductivity anomalies derived from 2D inversion and strike analysis.

Each body has been defined via its vertices (at least eight) in geographical coordinates and depth, and later on interpolated onto a metric grid, which is used in numerical modeling. For this purpose, the center point of the numerical grid is assigned a geographical coordinate corresponding to the center of the desired modeling volume. This means that body coordinates are defined absolutely, and the numerical grid has only relative coordinates.

Once all bodies, the background structure and the grid are defined, the conductivity model has to be projected onto the grid. For this purpose, the body vertices are converted from geographical to metric coordinates with respect to the geographical center of the grid. Then, an interpolation scheme is applied, which assigns the body resistivity to the cell resistivity, if the center of mass of the cell lies within the body, i.e. beyond the faces spanned by the body vertices. Shifting the grid in order to focus on a particular region of the measurement area means in this context, that only the geographical center of the grid has to be re-defined. Similarly, when testing for different grid layouts and cell sizes, the conductivity model does not have to be specified again. This procedure simplifies the model generation enormously.

The finite difference grid I used in model calculation consists of $70 \times 70 \times 35$ cells in the 3D domain, where bodies are cut off outside a core of $50 \times 50 \times 25$ cells such that all anomalies are embedded in a plane layered outer ring. Within the core, a constant side-length of $250\,\mathrm{m}$ ($500\,\mathrm{m}$) in horizontal direction is used for cells, and their depth extent progressively increases from $30\,\mathrm{m}$ at the surface by a factor of 1.18. Away from the central core, cell sizes are expanded in horizontal direction by a factor of 1.4. Using this grid, a total volume of $61\,\mathrm{km} \times 61\,\mathrm{km} \times 50\,\mathrm{km}$ ($122\,\mathrm{km} \times 122\,\mathrm{km} \times 50\,\mathrm{km}$) is considered, and the core covers $12.5\,\mathrm{km} \times 12.5\,\mathrm{km}$ ($25\,\mathrm{km} \times 25\,\mathrm{km}$) in horizontal directions. Since the whole measurement area covers approximately $20\,\mathrm{km} \times 20\,\mathrm{km}$, and moreover, anomalous bodies do exceed the measurement area, the grid has to be shifted four times (two times) and several modeling tasks have to be carried out. The resulting model responses are then merged together. Using this grid, forward calculations were carried out in the period range $T = 0.2\,, \ldots, 5\,s$ ($T = 5\,, \ldots, 50\,s$), and thereby covering only a small fraction of the measured period range. Computation of shorter periods would require a finer discretization and longer periods would require a larger core volume in order to obtain reliable results. The intermediate period range considered here is, however, of particular interest for 3D modeling of the data set, since no 2D assumption is valid here, as seen from dimensionality analysis and also from the behavior of induction arrows as depicted in Figure 5.9.

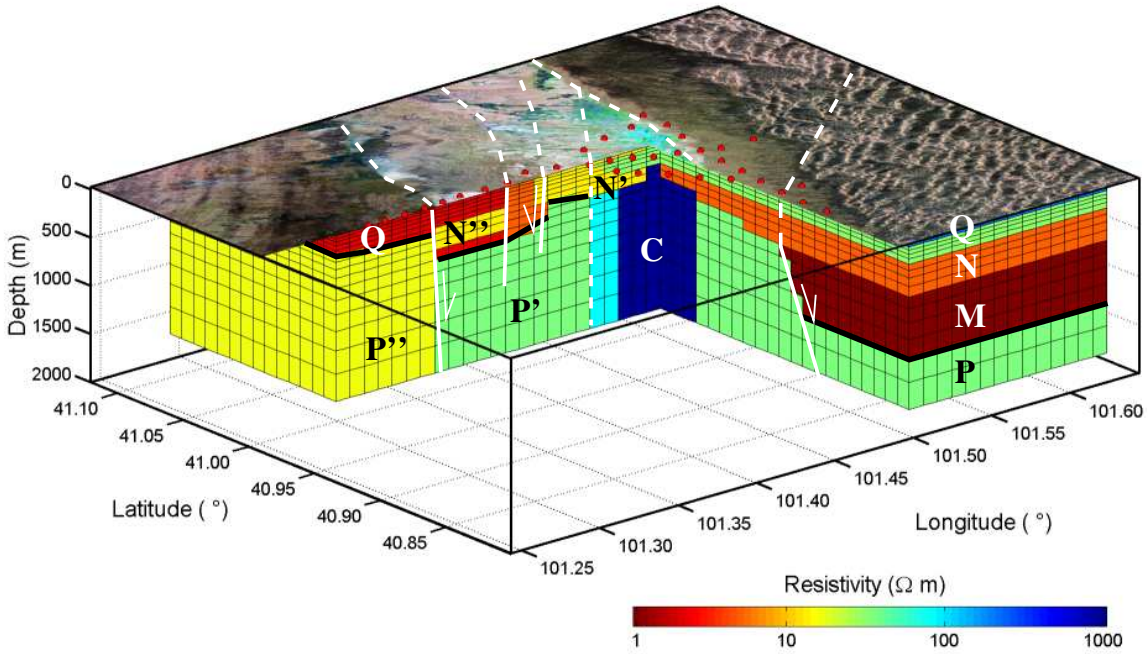


**Figure 5.18.:** 3D resistivity model. Color coded resistivity model used for final 3D modeling. Vertical and horizontal black lines indicate a 1 km × 1 km discretization, which is only used for plotting purposes. Main anomalous features are the conductors M and N,N',N" with resistivities of less than 5 Ωm corresponding to sediments and the resistor C representing crystalline basement (1000 Ωm). Green and yellow colors (15 – 30 Ωm) in the deeper subsurface are interpreted as metamorphic basement. A green layer (30 Ωm) below the dune field extending into the Gurinai depression indicates a fresh-water reservoir. It is underlain by a salty groundwater layer having considerably lower resistivities (5 Ωm). Interpreted faults and their surface traces are indicated by white lines.

**3D Model:** The final 3D model is graphically depicted in Figures 5.18 and 5.19. To ease orientation with respect to the surface features, the Landsat TM sub-scene is overlaid on top of the perspective view of the 3D model in Figure 5.18. The extent and strike direction of anomalies can be taken from depth slices at $z = 100, 250, 600, 3000\,\mathrm{m}$ in Figure 5.19. Only for plotting purposes, the model is discretized in horizontal directions with cell sizes of $1\,\mathrm{km} \times 1\,\mathrm{km}$, indicated by black solid mesh lines. The color scale used for resistivity coding is the same as has been used to display 1D and 2D resistivity models in Figures 5.13-5.17. Let me first describe the model and later on compare the model responses with measured data.

The model has been constructed from 19 bodies, having 12 different resistivities and aims to represent the 1D/2D inversion results as closely as possible along the profiles. However, some features were eliminated for 3D modeling in order to simplify the final model. This applies in particular to the vertical conductor Pc and resistor and Pr along profiles $\overline{BB'}$ and $\overline{CC'}$ (cf. Figures 5.16 and 5.17). The nature of these anomalies and their significance is not clear from 2D inversion, and therefore they have been omitted here for simplicity. Moreover, small scale variations in the upper conductive layers could not be adequately reproduced here in all cases. Therefore, a shift in apparent resistivities may be expected in some cases and will also be accepted

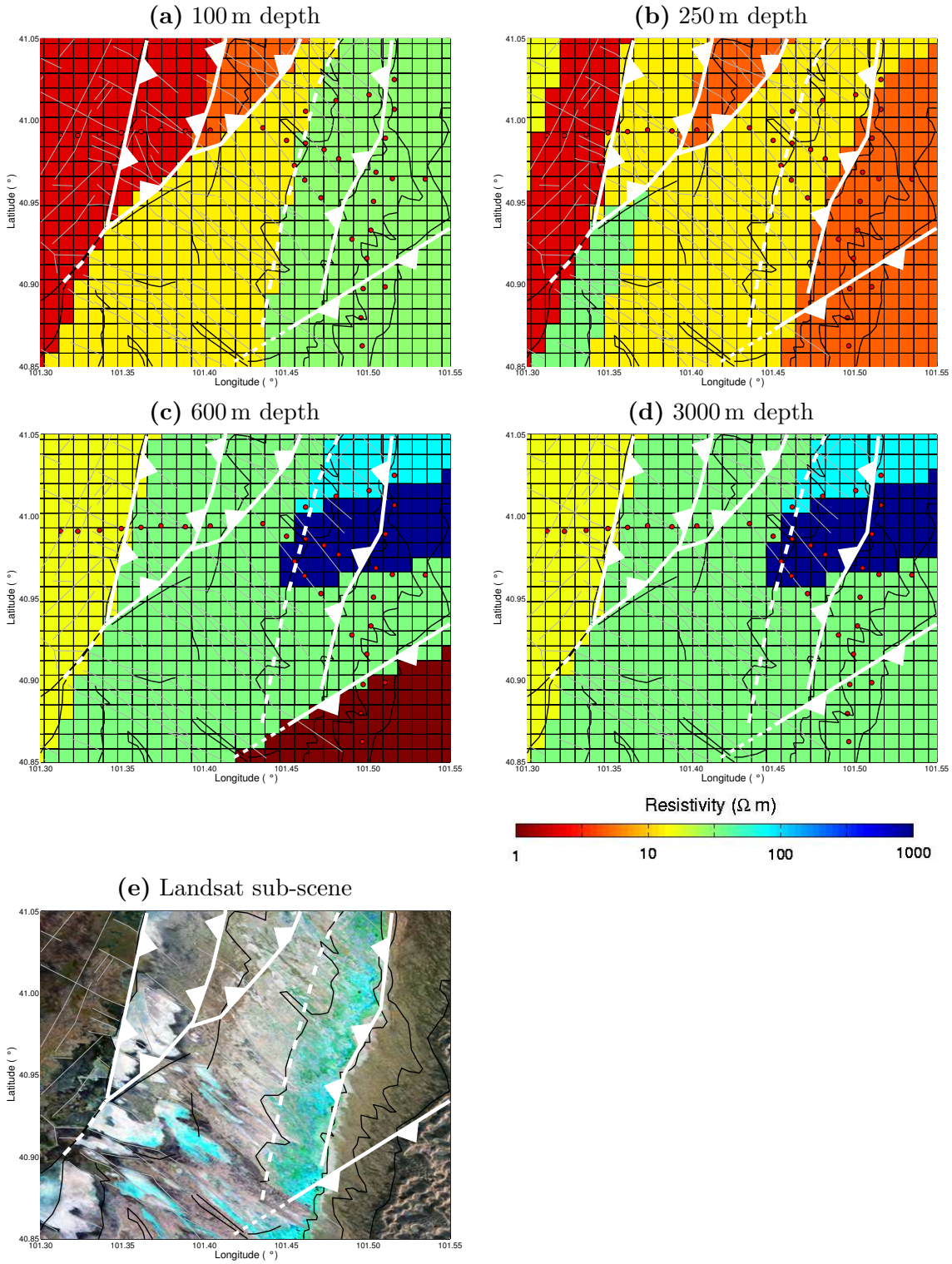


**Figure 5.19.:** 3D resistivity model. Depth slices of resistivities at **a)** 100 m **b)** 250 m **c)** 600 m and **d)** 3000 m are shown in comparison to **e)** the Landsat TM sub-scene. See text on pp. 78-81 for description. Major boundaries and tectonic lines are indicated by white lines. Red dots indicate MT stations. Black lines indicate discretization of 1 km × 1 km in horizontal directions, which is used for plotting only.

as long as the shape of sounding curves and in particular the phases are reproduced.

The main focus was however on the explanation of induction arrows, which are smooth functions in space and not affected by small scale surface anomalies. There are three main anomalies in the model, which are required to explain the induction arrows. These are the $1500\,\mathrm{m}$ deep conductive layer (labeled with M in Figure 5.18) in the south of profile $\overline{BB'}$, the resistive basement block (C) in the central part of the array, and in addition the conductive trough (N") above and east of the western boundary of the Gurinai depression, i.e. east of site s15. The conductor M with a resistivity of $1\,\Omega\mathrm{m}$, given a strike direction of $N50°E$ and extended over the southeastern edge of the central modeling core, produces northwestward pointing real induction arrows having maximum length at a period of few seconds. Due to the abrupt increase of thickness of sediments here, a normal fault is assumed and indicated in Figures 5.18 and 5.19.

In turn, the conductive trough (N") causes induction arrows pointing in eastward direction as observed at site s08-s10. The western boundary of the trough coincides with the western lineament bounding the Gurinai depression, as shown in Figure 5.19a and b in comparison with the satellite image in Figure 5.19c. The eastern rim of the sedimentary trough strikes in NNE direction across the profile, following the transition of stripes 4 and 5 in Figure 5.5. In addition, an internal dissection of the trough is inferred mainly from 1D models, and can be traced at the surface along the transition of stripe 5 and 6. Due to the basement topography, normal faults are deduced and indicated in Figure 5.19. The southward extension of the trough is not clear. Following the satellite image interpretation, I bounded the trough to the south along the eastern branch of the western lineament indicated, which coincides with the southern boundary of the salt-swamp.

The major cause of irregularly distributed induction arrows is the resistor C, which is embedded in a host rock (P) of moderate resistivities between $25 - 100\,\Omega\mathrm{m}$. It was found from 3D modeling, that the resistor, with its long axis being oriented $N80°E$, is necessarily bounded to the west in order to reproduce the spatial pattern of induction arrows shown in Figure 5.9. In the final model, it extends to $101.45°$ Longitude to the west, and is unlimited to the east within the central modeling core. In presence of the resistor C, modeled induction arrows in the south, west and north of the resistor basically point towards a singular point on top of the resistor, where they exhibit zero length and a turn-over in direction. The westward extension of the resistor has strong influence on the position of the singular point, which moves eastward with the resistor's length being limited to the west. The singular point of the induction anomaly is well determined by measured data and lies in the vicinity of site s31. Thereby, and by the length of induction arrows along profile $\overline{CC'}$, the extent of the resistor is well determined.

In addition to these main features, the 3D model contains a previously discussed but poorly determined transition within the basement across the westerly margin fault of the Gurinai depression, where the western basement is more conductive ($12\,\Omega\mathrm{m}$) than the eastern basement ($30\,\Omega\mathrm{m}$) . Both are supposed to represent metamorphic rocks. Also poorly determined in resistivity and geometry is the basement to the north, of which its western boundary was assumed to coincide with the western boundary of the resistor C. Extent and resistivity are mostly speculative, but a higher resistivity than for the southern basement is required here. The southern basement, which occupies most of the deeper sub-surface of the 3D model, is well determined in its resistivity of $30\,\Omega\mathrm{m}$ equal to the basement below the western part of the Gurinai depression.

Well known from 1D and 2D modeling is a conductive layer (N) of $5\,\Omega\mathrm{m}$, which occupies basement and deeper sediments (M). Its eastern boundary is fairly well known and coincides with the transition from stripe 2 and 3 in Figure 5.5, i.e. with the eastern margin of the Gurinai depression. This conductor is overlain by a more resistive layer (Q) of $30\,\Omega\mathrm{m}$, which extends further to

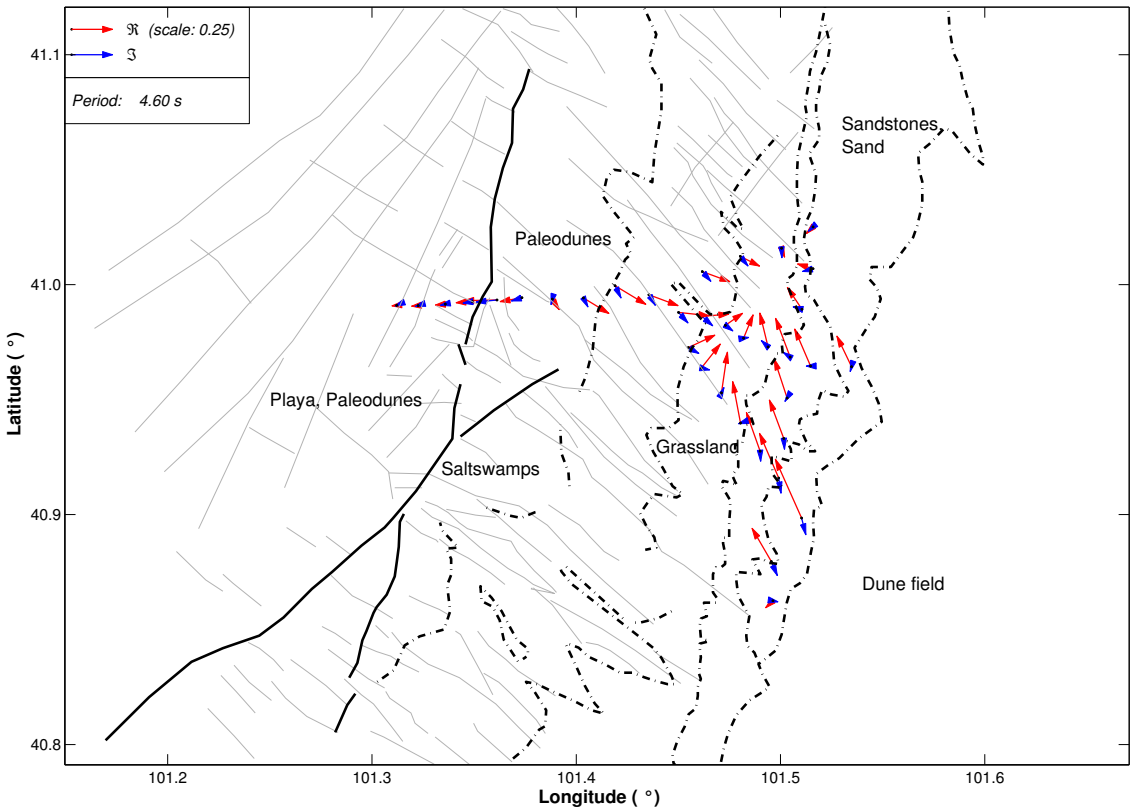


**Figure 5.20.:** Model response. Induction arrows for the period 4.6 s. The spatial pattern of measured induction arrows shown in Figure 5.9 can be simulated with 3D model calculations.

the east where it thins out at the transition between stripes 3 and 4. This layer with maximum thicknesses of 200 m most likely represents the fresh water reservoir of the Gurinai area, and is obviously connected to the Badain-Jaran-Shamo sand sea.

**Comparison of modeled and measured data:** A comparison of the model response with measured data is obtained from modeled induction arrows shown in Figure 5.20 and measured induction arrows shown in Figure 5.9 for the period $T = 4\,\mathrm{s}$. Both maps of arrows show the same characteristics, i.e. real arrows apparently point towards one point in the vicinity of site s31 and imaginary arrows are small at this period. Measured and modeled induction arrows as a function of period for each site individually also show a principal coincidence of model response and data (not shown here). Note, that the model was abstracted from 1D/2D inversion results using the short-period band only and can serve to explain the 3D characteristics of induction arrows at intermediate periods. Therefore, it is assumed, that the most important anomalies within the shallow crust have been identified and the 3D model roughly represents the actual conductivity distribution, with the uncertainties discussed above.

However, the impedance tensor cannot be appropriately be fitted with the 3D model shown here. Therefore, I do not show impedance responses of the model in comparison with the measured impedances. Three reasons might be supposed to explain insufficient fit of impedance data. Firstly,

the 3D model is wrong, i.e. important anomalies have not been considered, wrong anomalous resistivities have been chosen, or the geometry of anomalies is incorrect. Secondly, small inhomogeneities within the sedimentary layers have not been sufficiently abstracted, and the electric field is therefore not adequately modeled. Thirdly, the model assumption was wrong or insufficient, leading to the issue of anisotropic modeling.

With the review of the mode separated responses of Chapter 3, it is evident that in complicated 3D environments, TE- and TM-mode fields can reflect different anomalies at different depths. In the present case, TE-mode response functions are to some extent reproduced with the model, while impedances - being a mixture of TE and TM mode fields - are not well explained, and consequently, the TM-mode electric field is insufficiently modeled. Since TE responses are pre-dominantly sensitive to regional structures while TM can severely be affected by shallow structures (cf. for instance Figures 3.5 and 3.6) it may be anticipated, that the regional structure is correctly modeled (at least to some extent), while shallow structures are badly represented in the 3D (regional) model. Finally, an influence of anisotropy can not be refused and needs further investigation.

### 5.4.4. Comment on anisotropic resistivity modeling

During data analysis and modeling, a number of hints were collected which point towards an directional dependency, i.e. anisotropy, of the conductivity of basement rocks at greater depths. Anisotropy may be inferred from constant phase splittings at periods longer than $100\,s$, observed over the whole measurement area, which occur in absence of a significant inductive anomaly and consequently small induction arrows, as described previously. The first indicate significant directional dependency of the electric field, the latter are zero in case of a homogeneous or plane layered anisotropic earth. Strike analysis retrieves equal strike directions at all sites at long periods, which is in agreement with the phase characteristics. Differences occur in apparent resistivities sounding curves due to the inhomogeneously composed upper crust, but are absorbed in the distortion parameters during decomposition of the tensor. Distortion parameters are therefore reflecting shallow anomalies at long periods.

In addition to the characteristics of the data themselves, further implications for the existence of anisotropy are inferred from modeling results. Column-like conductivity anomalies (Pc and Pr in Figures 5.16 and 5.17), as found within the basement at a depth of $3-4\,\mathrm{km}$ along Profiles $\overline{BB'}$ and $\overline{CC'}$ can occur, if responses of an anisotropic earth are inverted using a 2D inversion scheme excluding anisotropy (Heise and Pous, 2001). In this case, however, these anomalies are hardly separated from normal 2D or 3D effects due to insufficient spatial resolution in data and the presence of lateral anomalies in the vicinity of the presumably anisotropic basement.

Additionally, the 3D model discussed in the previous section nicely reproduces the basic characteristics of the induction arrows at intermediate periods, but fails to explain the impedance tensor in many cases. As possible explanations, an insufficient conductivity model or an insufficient model assumption can be considered. In the first case, the model would have to be adjusted in such a way, that only impedances are affected while preserving the general behavior of induction arrows. The latter case would again suggest to include anisotropy instead of using isotropic models.

Finally, there is geological evidence for the presence of macro-anisotropy in terms of highly fractured crystalline basement rocks and foliated metamorphic rocks and meta-sediments, which outcrop approximately $80\,\mathrm{km}$ to the north in the Jingshutu area (cf. Figure 5.4). If fractures are filled with saline pore fluid, a possible cause of anisotropy is given. However, geological field studies have shown, that fractures are found with orientation in several directions forbidding the prediction of

anisotropy axes. Furthermore, the out-cropping basement is highly heterogeneous and composed of a mélange of different lithologies. This is comparable to the basement in the measurement area, where crystalline rocks have been attributed high resistivities and metamorphic rocks intermediate resistivities. Hence, representing such a basement composite including anisotropy would require full 3D anisotropic modeling in the present case, which is beyond the scope of this study.

2D anisotropic forward modeling has been carried out on the profile $\overline{BB'}$, but is not shown here, since it is not clear at the current stage of interpretation, whether 2D anisotropy is really suitable to explain data, as pointed out above.

## 5.5. Interpretation

The conductivity model derived from MT data shows lateral and vertical changes at different depths scales from tens of meters to several kilometers. Interpretation of the conductivity models derived in section 5.4 in terms of lithology, stratigraphy and tectonic history is not unique and requires incorporation of geological background information given in section 5.2. The following interpretation is to some extent speculative, since datings of sediments are not yet available.

### 5.5.1. Interpretation of sediments and structures

Late Quaternary (Holocene) sediments are supposed to be deposited in the center of the Gurinai depression while at its shoulders an early Quaternary age is assumed for the uppermost sediments. This assumption is mainly inferred from sections shown in the report of the Water Department of Ejina Qi (Xiou, 1990). From groundwater exploration boreholes distributed over the whole Gaxun-Nur basin, the total thickness of Quaternary sediments is in the range of $100 - 300\,\mathrm{m}$. This coincides with layer thickness of layers Q and Q' (cf. for example Figure 5.14) outside of the Gurinai depression adjacent to the Badain-Jaran-Shamo in the east and the Ruoshui fan in the west, respectively. Therefore, Q and Q' are assumed to represent early-Quaternary (Pleistocene) sediments. Resistivities of Q and Q' substantially differ and represent both different salinity of pore fluid as well as different sedimentological composition. In the east, Q is assumed to represent early Quaternary eolian sand deposits (dune sands) in comparison with exposed sequences of sediments in the benchland area in stripes 1 and 2 (cf. Figure 5.5). With resistivities of $30\,\Omega\mathrm{m}$, fresh water can be assumed as pore fluid. The sand sea of the Badain-Jaran-Shamo is conceived as the source of fresh water, being recharged by precipitation events during the summer monsoon. In contrast, highly conducting sediments Q' in the west of the Gurinai depression (stripe 6 and 7) have a high content of clay, and are saturated with saline pore water as also deduced from surface observations.

According to the geological sections shown in (Xiou, 1990), Pleistocene sediments are underlain by late Tertiary (Neogene) strata close to and within the Badain-Jaran-Shamo and outcrop further to the east as also described by Mischke (1996) and other authors. Therefore, layer N, indicated in resistivity models shown in Figure 5.14 and 5.18, presumably corresponds to Neogene sediments. Note, that layer N can be traced in the eastern part of the array in the $N-S-$direction, i.e. along the Profile $\overline{BB'}$, where it appears electrically homogeneous with $5\,\Omega\mathrm{m}$. In the $E-W$ direction, layer N is discontinuous and exhibits a change in conductivity (N-N') across the eastern margin of the Gurinai depression. It cannot be traced west of site s09. A resistive intersection N" has been identified between s12 and s14. It is speculative to assume Tertiary strata here.

Mesozoic sediments occur at greater depths $> 400\,m$ in the southern part of the measurement area

(label M in Figures 5.14 - 5.18), and - purely speculative - also within the Gurinai-depression (M' in Figure 5.14). A similarity of M and M' is given in terms of resistivities of $1\,\Omega\mathrm{m}$ pointing again towards a high clay content and saline pore fluid. Mesozoic sediments in the south are trapped in a more than $1.3\,\mathrm{km}$ deep tectonic Graben. The strike direction of the detected northern peripheral fault is $N40°W$ and runs sub-parallel to the hypothetic southward branch of the Zuunbayan fault in the greater area (cf. Figure 5.3), discussed in Lamb et al. (1999) and other authors, which exhibited major activity in late Mesozoic time. Therefore, I suggest that the southerly detected fault is of similar transtensional setting as the Zuunbayan fault (sinistral and normal displacement) or even a branch of the Zuunbayan fault zone and had a normal component of displacement when active. From this argument, the sedimentary filling is presumably of late Jurassic and/or early Cretaceous age. The evolution of $N-S$ oriented Graben structures in the same period of time is also documented in literature, such that a tectonic-based scenario for the speculative Mesozoic sediments M' in the center of Gurinai depressions is also available.

A number of tectonic elements has been imposed on conductivity models. They are mainly inferred from basement topography, transitions within the basement and from correlation of discontinuities of sediments, surface observations and satellite interpretation. Roughly $N-S$ striking faults as indicated in Figure 5.19 are interpreted at the western and eastern margin of the Gurinai depression and in between, based on satellite image interpretation and supported by both basement and sediment structures. The western margin fault coincide with a resistivity change within the metamorphic basement (P'-P'' in Figures 5.14a, 5.15 and 5.18) as well as with the absence of the conductive layer M' west of the surface trace of the fault. Normal faulting with relative subsidence of the eastern block is assumed due to increased thickness of sediments within the Gurinai depression. If the age of basal sediments M' is Mesozoic, syn-tectonic or pre-tectonic Mesozoic sedimentation and consequently Mesozoic or older implementation of the fault system may be assumed. In any case, the fault seems to be active recently due to its clear, linear surface trace, although only small vertical displacements are assumed due to relatively continuous layering of shallow sediments deformed at the fault. Left-lateral strike-slip is inferred from $N45°W$ oriented elongated depressions east of the lineament, when interpreting these depressions as extensional fractures. The overall recent activity along the fault seems to be of small amplitude. The western extent of the fresh-water reservoir Q coincides with the western extent of the basement block C. An old fault within the basement is necessary here, which might have undergone reactivation in the Cenozoic such that a horst-like, east-ward dipping uprise of the crystalline basement has evolved. Hartmann (2004) suggested en-echelon-like normal faulting for the Gaxun-Nur basin, which might also be the case here on a small scale, causing eastward dipping of sediments accompanied by eastward retro-grading erosion and thinning of layer Q towards the west. In such a way, a causal relation between a basement fault and the extent of the freshwater reservoir could be established. More substantial uplift is assumed for the eastern shoulder of the Gurinai-depression, where the relief progressively increases towards the east, supporting the hypothesis of retro-grading erosion of early Quaternary sediments forming the bench land. It should be noted, that a resistivity change of presumably Tertiary sediments N and N' across the eastern margin fault is significant. Assuming the fault to be a pathway for fluids, small lakes arranged in the $N-S$ direction parallel to the eastern margin of the Gurinai-depression, are connected to groundwater at depth. Fresh water pools as shown in Figure 5.6d are related to the fresh-water aquifer Q, while salt-lakes are connected to aquifer N. This implies strained groundwater conditions such that fluids come to the surface.

### 5.5.2. Geological evolution of the Gurinai depression

A widespread extensional tectonic regime in late Mesozoic times as documented for basins in southern Mongolia (Cunningham et al., 1997; Graham et al., 2001; Johnson, 2004; Lamb et al., 1999) may also be assumed for parts of the Gaxun Nur basin, as discussed above. Subsequent uplift due to regional compression as reported for southern Mongolia in late to early Cretaceous cannot be derived from geophysical models, but can neither be denied. Assuming a regional uplift event in a compressional stress regime, sedimentation would terminate, Graben sediments would be folded and peneplaned, but grossly preserved in depressions. Re-onset of sedimentation within the Cretaceous or the Tertiary in relatively low-lying areas unconformly covers both peneplaned Jurassic sediments and basement rocks. The thickness of Tertiary and/or late Cretaceous sediments depend on rates of subsidence and on later erosion, if any.

Continuity of sedimentation since late Cretaceous or early Tertiary cannot be assumed within the entire Gaxun-Nur basin due to a Hiatus at the base of Quaternary sediments deduced from the D100 drilling core of Wünnemann and Hartmann (2002). It is likely to assume locally differing sedimentation and denudation areas within an overall continental environment. The nset of Quaternary sedimentation is dated to $1\,\mathrm{Ma}$ in the northern central part (Wünnemann and Hartmann, 2002) with the steady and widespread deposition of limnic sediments though fluctuations of the Paleo-Gaxun-Nur lake level is assumed. Wünnemann and Hartmann (2002) do not suggest that the Paleo-Gaxun-Nur extended as far to the southeast as the Gurinai area. Instead, they see the possibility of isolated lake systems of smaller dimensions in the Gurinai area. I assume a playa-like environment here, not excluding episodically flooding and fluviatile sedimentation justified by occurrence of playa-like sediments and gravels west of the Gurinai depression. This environment is isolated from the already existing or evolving Badain-Jaran sand sea by the subsiding Gurinai-depression, where pre-Quarternary and Quaternary sediments are deposited and covered by younger sediments. Whether subsidence has to be taken into account throughout the whole Quaternary, can only be judged upon reliable stratigraphy of sediments, which is currently not available.

In any case, within the Quaternary, the course of the Ruoshui river and consequently the sedimentation areas shift consecutively towards the west, as may be deduced from paleo-channels of the Ruoshui river described in Hartmann (2004) as well as from the sedimentological map shown in Wünnemann and Hartmann (2002) (their Figure 3). Hartmann attributes the shifting of deposition centers to a westward dipping of the whole Gaxun-Nur area, which is also mentioned in Guo et al. (2000). However, the Gurinai-depression remains relatively subsident and therefore a deposition area.

The $N-S$ trending Graben margins are synthetically arranged with respect to the left-lateral Zuunbayan fault or its previously suggested Gurinai-branch. The amount of Cenozoic displacement is not quantified for the Zuunbayan fault but in a regional context its sense should be sinistral. Therefore sinistral slip is also assumed along the $N-S$ directed faults at the margins and within the Gurinai depression. This interpretation is in agreement with extensional fractures oriented in the $NW-SE$ direction, which where described in Hartmann (2004) and interpreted in terms of releasing bends of a Duplex structure with its left axis at the western margin of the depression. However, the major component of faulting appears to be normal, since the sedimentary filling of the Gurinai depression composed of quarternary and pre-quarternary sediments reaches a maximum thickness of $600\,\mathrm{m}$.

# 6. Conclusions

I have treated a range of different aspects related to the theory of the Magnetotelluric method as well as to its application in a geological environment with the aim of an actual geological interpretation. For conciseness the main methodological findings and the results of an application of the MT method in the Gaxun-Nur basin (NW China) are separately summarized below.

**Methods:** Exploiting spatial relations of the electromagnetic field is of two-fold usefulness. Firstly, application of a simple spatial decomposition and transformation scheme to vertical magnetic transfer functions yields apparent resistivity and phase maps, and thereby gives a different point of view on solely magnetic induction fields. The developed scheme is now routinely applied by the Geological Survey of Sweden as a tool in airborne VLF data interpretation. Further relations concerning the electric field have been established and summarized. They cannot be directly applied so far, since the collection of electric field data with sufficient spatial resolution is very difficult and has not been achieved so far.

Secondly, in synthetic models studies, mode separated responses can be constructed using spatial relations. Then, TE- and TM-mode fields and related transfer functions can be separately studied. The model I show in this work consists of two elongated conductors at different depths with a relative orientation of $45^\circ$ degrees such that responses from shallow and deep structures including 3D effects at intermediate periods and galvanic distortion effects at very long periods arise. Mode separated responses for this model show, that the TE-mode fields, most comprehensively depicted in vertical magnetic transfer functions, reflects the response of the shallow structure at short periods, a coupled response at intermediate periods, and solely the response from the deep structure at long periods. In contrast, the TM-mode fields, which can be depicted in terms of the vertical electric field transfer function, are primarily sensitive to the shallow structure, even at long periods. In the limit of galvanic distortion, TM-mode electric fields oscillate in-phase with the regional electric field, but primarily are an indicator of the shallow structure.

This leads to the conclusion, that inversion of TM-mode data only (or B-Polarization in the 2D case) is not an adequate approach to recover deep anomalous structures, since it will in most cases be possible to produce equivalent models with a number of shallow anomalies. TE-mode fields have therefore to be incorporated, preferably magnetic transfer functions, since they are definitely free of distorting TM-mode fields (including galvanic distortion). E-Polarization apparent resistivities will always be polluted by TM-mode parts arising from 3D effects in a realistic earth.

Galvanic distortion itself can also be analyzed for single site impedance tensors. I suggest a new decomposition scheme of the impedance tensor, which relies on the polarization states of the regional electric field. Thus, not the physical properties of distorting fields are aimed at as in the decomposition scheme of Groom and Bailey (1989) but the resolvable parts of the regional field. Moreover, the novel approach uses eight parameters to describe the tensor instead of seven as in classical distortion schemes, and thereby covers all degrees of freedom inherent in the tensor in a general 3D environment. If a simplifying 2D regional structure with or without distortion is present, the number of non-vanishing parameters drops to seven (galvanic distortion affects data)

or five (pure 2D structure) and is directly related to the parameters of the Smith's decomposition (Smith, 1995).

As an appendix to methodological work, I added a generalized solution scheme of the electromagnetic integral equation using a wavelet multi-resolution analysis. Although this work has not been finalized in the scope of this work, the new approach is promising with respect to a more flexible discretization of the model and the electromagnetic field compared to the standard integral equation solution. Future research will have to address a proper numerical implementation in order to demonstrate, that the wavelet based solution is an valuable contribution to numerical electromagnetic modeling and inversion issues.

**Magnetotelluric studies in the Gaxun-Nur basin, NW-China:** The Magnetotelluric method has proven to be an effective and valuable tool for the investigation of a complex geological structure in the southeastern part of the Gaxun-Nur basin. Little has been known about the geology of this area before, and an integrated approach including geophysical measurements, geological field investigations and satellite interpretation had to be taken. The geological model, which has been established in the scope of this study, relies on the subsurface geoelectric structure, which was derived from broad-band Magnetotelluric data.

Dimensionality, distortion and strike analysis of MT transfer functions in the period range from $10^{-3}\,\mathrm{s}$ to $10^{3}\,\mathrm{s}$ reveals 1D characteristics, 2D effects with and without galvanic distortion as well as general 3D effects inherent in the data, depending upon period range and location of sites.

For the construction of resistivity models, 1D and 2D inversion codes as well as 3D forward modeling codes were comprehensively employed, and the model results are reliable down to depths of several kilometers. However, for long periods, no acceptable data fit could be achieved in the scope of this study. Further work including anisotropic modeling is suggested, based on the hints pointing towards the existence of anisotropic conductivity structures in the middle and lower crust.

Geophysical investigations in the southeastern part of the Gaxun-Nur basin (Gurinai-depression) showed, that the Gurinai is a medium-scale $N-S-$trending depression, bearing more than $600\,\mathrm{m}$ thick sediments. It can be conceived as a tectonic Graben linked to Mesozoic tectonic basin structures, the latter having evolved during a regional extensional stress regime prior to the continent-continent collision of India and Eurasia. A relict of more than $1300\,\mathrm{m}$ deep Mesozoic basin sediments was found in the subsurface in the southern part of the Gurinai structure, bounded to the north by a $SW-NE$ oriented normal fault, which is seen in context with the Zuunbayan fault, one of the major Mesozoic fault zones in central Asia (Graham et al., 2001; Johnson, 2004; Lamb et al., 1999). It is therefore denoted as the Gurinai-branch of the Zuunbayan fault zone, although a direct connection to the Zuunbayan fault cannot be proven.

During reactivation of the Gurinai-branch in late Mesozoic or Cenozoic times, $N-S-$oriented secondary faults, likely along pre-existing basement structures, became active, and nowadays enclose the Gurinai-Graben. It cannot be denied, that the Gurinai-depression was already active in the context of Mesozoic extension. However, major activity is assumed to be in Cenozoic times. From geophysical models and collected geological data, it can neither be verified nor rejected, that the Gurinai structure was subjected to a transpressive stress regime as assumed by Hartmann (2004), which was later reversed into a transtensional stress regime. However, transtensional stress seems to be likely in youngest times due to the subsident character of the depression itself, and also serves as an explanation of feather-like arranged extensional depressions identified from satellite image interpretations and field observations. In this context, the Gurinai margin faults

undergo an oblique deformation with a left-lateral component of shear. Then, the Gurinai faults are synthetically arranged with the major left-lateral Asian shear zones (Molnar and Tapponier, 1975; Cunningham et al., 1996, 1997; Gouyu et al., 2004), and in particular with the reactivated Gurinai-branch of the Zuunbayan fault zone. Therefore, it can be deduced, that stress is accommodated within the Gurinai-structures, which might either result from a block-rotation of the whole Gaxun-Nur system as suggested by Hartmann (2004), or that stress is transferred to the north, and the Gurinai-structures serves as a step over structure between left-lateral, $SW - NE$ oriented shear zones. The overall deformation is, however, small compared to large scale basin and Graben structures in central Asia, which might serve as an explanation, that the Ala-Shan region is considered as a stable platform during Cenozoic times. On the other hand, Hartmann (2004) has shown that the present landform is sustainably influenced by tectonic deformation in many parts of the Gaxun-Nur basin. From geophysical models and geological field investigations, we have shown, that present and ancient sedimentation and denudation in the Gurinai-area is strongly affected by tectonic movements. This applies also to the extent and distribution of groundwater, which is only in a very limited area suitable for housing and agriculture.

# 7. Acknowledgement

Indirect and direct support and contributions to this work came from many different people. In particular I am grateful to Prof. H. Burkhardt, who supervised my phd-work and encouraged me to work on a broad range of topics while providing the freedom to pursue my own ideas. He also strongly supported my work at the Department of Applied Geophysics at the Technical University of Berlin, which was not related to my phd-thesis. For the latter reasons, Prof. U. Yaramanci is also acknowledged. Both teachers provided perfect working conditions.

I am very grateful to Prof. L. B. Pedersen, who contributed a lot to my understanding of electromagnetic problems. I would like to express my hope to keep close contact to him in order to continue some joint work in future. He has also taken over the job to review my phd-thesis as an external reviewer.

During my employment at the Technical University Berlin, I had the chance to participate in three field campaigns in the Gobi desert in China. The geophysical working group members are or were R. Fiedler-Volmer, S. Hölz, D. Polag, H. Brasse, A. Pfaffhuber, A. Schenk, T. Hiller, M. Kroupa. All members had their individual contribution to the successful realization of these expeditions. In particular, I would like to thank R. Fiedler-Volmer for the geological discussion in the field and also during the interpretation of geophysical data. The same applies with respect to geophysical problems in particular to S. Hölz and D. Polag. Furthermore, I would like to mention B. Wünnemann and K. Hartmann from the geographical working group as well as members of other working groups related to the China project for valuable support during field work and interpretation. The Chinese colleagues have contributed a lot to successful field work. In particular, Prof. Zhang Hucai and his students Fan Hongfang, Ding Hu and others as well as Prof. Gu Wei-zu participated in the campaign documented in this work.

People in the geophysics department of the Technical University and of the MT working group have been available for discussions and provided help in technical problems. Here, I would like to emphasize my student- and phd-co-worker M. Hertrich, also M. Müller, the technical staff (U. Töpper, U. Schenkluhn, M. Schmarsow, U. Diefenbach-Moschick), the MT working group leader O. Ritter and H. Brasse and many others.

Beyond geophysics, I enjoyed support of manifold type and also interest in my work from my parents and the rest of my family for the whole period of studies and during the phd-time.

Finally, Katja had uncomplainingly accepted, that I have been in the field for several times, each time several weeks or even months. This cannot be taken for granted in a relationship, and therefore, I am deeply grateful to her.

# Bibliography


Avdeev, D. B., Kuvshinov, A. V., Pankratov, O. V., Newman, G. A., 1997. High-performance three-dimensional electromagnetic modelling using modified Neumann series. Wideband numerical solution and examples. J. Geomag. Geoelectr. 49, 1519–1539.

Bahr, K., 1988. Interpretation of the magnetotelluric impedance tensor: regional induction and local telluric distortion. J. Geophys. 62, 119–127.

Becken, M., Burkhardt, H., 2004. An ellipticity criterion in magnetotelluric tensor analysis. Geophys. J. Int. 159, 69–82.

Becken, M., Pedersen, L. B., 2003. Transformation of VLF anomaly maps into apparent resistivities and phases. Geophysics 68, 497–505.

Berdichevsky, M. N., Zhdanov, M. S., 1984. Advanced theory of deep geomagnetic sounding. Elsevier.

Cagniard, L., 1953. Basic theory of the magneto-telluric method of geophysical prospecting. Geophysics 18, 605–635.

Caldwell, T. G., Bibby, H. M., Brown, C., 2004. The magnetotelluric phase tensor. Geophys. J. Int. 158, 457–469.

Cunningham, W. D., Windley, B. F., Dorjnamjaa, D., Badamgarav, J., Saandar, M., 1996. Late Cenozoic transpression in southwestern Mongolia and the Gobi Altai-Tien Shan connection. Earth planet. Sci. Lett. 140, 67–81.

Cunningham, W. D., Windley, B. F., Owen, L. A., Barry, T., Dorjnamjaa, D., Badamgarav, J., 1997. Geometry and style of partitioned deformation within a late Cenozoic transpressional zone in the eastern Gobi Altai Mountains, Mongolia. Tectonophysics 277, 285–306.

Daubechies, I., 1992. Ten lecturs on wavelets. SIAM, Philadelphia.

Egbert, G. D., 1997. Robust multiple-station magnetotelluric data processing. Geophys. J. Int. 130, 475–496.

Farquharson, C., Oldenburg, D., Haber, E., Shekhtman, R., 2002. An algorithm for the three-dimensional inversion of magnetotelluric data. In: 72nd Ann. Internat. Mtg. Soc. of Expl. Geophys., pp. 649–652.

Gouyu, D., Jie, C., Qinjian, T., Xuhui, S., Chengqi, X., Kaibo, W., 2004. Active faults and magnitude of left-lateral displacement along the northern margin of the Tibetian Plateau. Tectonophysics 380, 243–260.

Graham, S. A., Hendrix, M. S., Johnson, C. L., Badamgarav, D., Badarch, G., Amory, J., Porter, M., Barsold, R., Webb, L. E., Hacker, B. R., 2001. Sedimentary record and tectonic implications of Mesozoic rifting in southeast Mongolia. Geol. Soc. Am. Bull. 113, 1560–1579.

Groom, R. W., Bahr, K., 1992. Corrections for near surface effects: decomposition of the magnetotelluric impedance tensor and scaling corrections for regional resistivities: a tutorial. Geophys. Surv. 132, 341–379.

Groom, R. W., Bailey, R. C., 1989. Decomposition of magnetotelluric impedance tensors in the presence of local three-dimensional galvanic distortion. J. geophys. Res. 94, 1913–1925.

Groom, R. W., Bailey, R. C., 1991. Analytic investigation of the effects of near surface 3-d galvanic scatterers on MT tensor decompositions. Geophysics 56, 496–518.

Guo, H., Liu, H., Wang, X., 2000. Subsurface old drainage detection and paleoenvironment analysis using spaceborne radar images in alxa plateau. Science in China (Series D) 43, 439–448.

Haber, E., Ascher, A. M., Oldenburg, D. W., 2004. Inversion of 3D electromagnetic data in frequency and time domain using an inexact all-at-once approach. Geophysics 69, 1216–1228.

Hartmann, K., 2004. Spätpleistozäne und holozäne Morphodynamik im nördlichen Gaxun Nur Becken, Innere Mongolei, NW China. Ph.D. thesis, FU Berlin, (in german).

Hedin, S., 1943. History of the Expedition in Asia 1927-1935, Part I-IV. Stockholm.

Heise, W., Pous, J., 2001. Effects of anisotropy on the two-dimensional inversion procedure. Geophys. J. Int. 147, 610–621.

Hohmann, D. W., 1987. Numerical modeling for electromagnetic methods in geophysics. In: Nabighian, M. N. (Ed.), Electromagnetic Methods in Applied Geophysics. Volume 1, Theory. SEG, Tulsa, pp. 314–362.

Hohmann, G. W., 1975. Three-dimensional induced polarization and electromagnetic modeling. Geophysics 40, 309–324.

Hölz, S., Burkhardt, H., 2004. Topographic Modeling of SRTM-Data Using Matlab. Computers & Geosciences (submitted).

Hongzhen, W., 1985. Atlas of Paleogeography of China. China Cartogr. Publ. House, Beijing.

Jiang, Z., 1996. Atlas of Mineral Resources and Crust Evolution in China. Geol. Publishing Houses, Beijing.

Jiqing, H., 1979. An attempt to the seismological regionalization of china according to the tectonic point of view. Bull. Chin. Acad. Geol. Sci. 1.

Johnson, C. L., 2004. Polyphase evolution of the East Gobi basin: sedimentary and structural records of Mesozoic-Cenozoic intraplate deformation in Mongolia. Basin Research 16, 79–99.

Kroupa, M., 2001. Eindimensionale gemeinsame Inversion von Geoelektrik- und Magnetotellurik-Daten mittels Simulated Annealing unter Berücksichtigung transversaler Anisotropie. Master's thesis, TU Berlin, (in german).

Lamb, M. A., Hanson, A. D., Graham, S. A., Badarch, G., Webb, L. E., 1999. Left-lateral sense offset of Upper Proterozoic to Paleozoic features across the Gobi Onon, Tost, and Zuunbayan faults in southern Mongolia and implications for other central Asian faults. Earth planet. Sci. Lett. 173, 183–194.

LaTorraca, G., Madden, T., Korringa, J., 1986. An analysis of the magnetotelluric impedance tensor for three-dimensional structures. Geophysics 51, 1819–1829.

Ledo, J., Queralt, P., Marti, A., Jones, A. G., 2002. Two-dimensional interpretation of three-dimensional magnetotelluric data: an example of limitations and resolution. Geophys. J. Int. 150, 127–139.

Mackie, R., Rieven, S., Rodi, W., Jul. 1997. Users manual and software documentation for two-dimensional inversion of magnetotelluric data. GSY-USA, Inc., 2261 Market St., Suite 643, San Francisco, CA 94114, User Documentation.

Mackie, R. L., Madden, T. R., 1993. Conjugate direction relaxation solutions for 3-D magnetotelluric modeling. Geophysics 115, 1052–1057, short note.

Mackie, R. L., Madden, T. R., Wannamaker, P. E., 1993. Three-dimensional magnetotelluric modeling using difference equations - theory and comparisons to integral equation solutions. Geophysics 58, 215–226.

Mackie, R. L., Smith, J. T., Madden, T., 1994. Three-dimensional electromagnetic modeling using finite difference equations: The magnetotelluric example. Radio Science 29, 923–936.

McKirdy, D. M., Weaver, J. T., Dawson, T. W., 1985. Induction in a thin sheet of variable conductance at the surface of a stratified earth - II. Three-dimensional theory. Geophys. J. R. astr. Soc. 80, 177–194.

McNeice, G., Jones, A. G., 2001. Multi-site, multi-frequency tensor decomposition of magnetotelluric data. Geophysics 66, 158–173.

Meyerhoff, A. A., Kamen-Kaye, M., Chen, C., Taner, I., 1991. China - Stratigraphy, Paleogeography and Tectonics. Luwer Academic Publisher, Dordrecht/Boston/London.

Mischke, S., 1996. Sedimentologische Untersuchungen zur Landschaftsgenese der nordwestlichen Badain Jaran Shamo (Innere Mongolei, Volksrepublik China). Master's thesis, FU Berlin, (in german).

Molnar, P., Tapponier, P., 1975. Cenozoic tectonics of Asia: effects of a continental collision. Science 189, 350–360.

Mundry, F., 1985. Gleichstromverfahren. In: Bender, F. (Ed.), Angewandte Geowissenschaften. Ferdinand Enke Verlag, Stuttgart.

Pedersen, L. B., 1989. Relations between horizontal and vertical gradients of potential fields (short note). Geophysics 54, 662–663.

Pedersen, L. B., Becken, M., 2005. Equivalent current images derived from filtering of VLF-data along profiles. Geophysics (accepted) .

Pedersen, L. B., Qian, W., Dynesius, L., Zhang, P., 1994. An airborne tensor VLF system, from concept to realization. Geophys. Prosp. 42, 863–883.

Price, A., 1973. The theory of geomagnetic induction. Phys. Earth and Planet. Int. 7, 227–233.

Reitz, J., Milford, F., Christy, R., 1993. Foundations of Electromagnetic Theory. Addison-Wesley.

Rokityanski, I. I., 1982. Geoelectric Investigation of the Earth's Crust and Mantle. Springer.

Schmucker, U., 1970. Anomalies of Geomagnetic Variations in the Southwestern United States. Univ. of California Press, Berkeley.

Schmucker, U., Weidelt, P., 1975. Electromagnetic Induction in the Earth. Lectures Notes, Aarhus, (unpublished).

Siripunvaraporn, W., Egbert, G., 2000. An efficient data-subspace inversion for two-dimensional magnetotelluric data. Geophysics 65, 791–803.

Siripunvaraporn, W., Uyeshima, M., Egbert, G., 2004. Three-dimensional inversion for Network-Magnetotelluric data. Earth planet. Sci. Lett. 56, 893–902.

Smith, J. T., 1995. Understanding telluric distortion matrices. Geophys. J. Int. 122, 219–226.

Stollnitz, E. J., DeRose, T. D., Salesin, D. H., 1996. Wavelets for Computer Graphics. Morgan Kaufman Publishers, Inc., San Francisco.

Suvorov, A. I., 1982. Structural map of western Mongolia. Izv. Akad. Nauk. SSSR Ser. Geol. 6, 122–136, (in Russian).

Vasseur, G., Weidelt, P., 1977. Bimodal electromagnetic induction in non-uniform thin-sheets with an application to the northern Pyrenan anomaly. Geophys. J. R. astr. Soc. 51, 669–690.

Vozoff, K., 1991. The magnetotelluric method. In: Nabighian, M. N. (Ed.), Electromagnetic methods in applied geophysics, Volume 2, Application. SEG, Tulsa, pp. 641–711.

Wang, Q., Zhang, P., Freymueller, J. T., Bilham, R., Larson, K. M., Lai, X., You, Y., Niu, Z., Wu, J., Li, Y., Liu, J., Wang, Z., Chen, Q., 2001. Present-day Crustal Deformation in China Constrained by Global Positioning System Measurements. Science 294, 574–577.

Wannamaker, P. E., 1991. Advances in three-dimensional magnetotelluric modeling using integral equations. Geophysics 56, 1716–1728.

Ward, S. H., Hohmann, G. W., 1988. Electromagnetic theory for geophysical applications. In: Nabighian, M. N. (Ed.), Electromagnetic methods in applied geophysics. Volume 1, Theory. SEG, Tulsa, pp. 131–312.

Weaver, J. T., Agarwal, A. T., 2004. Magnetotelluric invariants and the phase tensor. 17th international workshop on electromagnetic induction, Hyderabad, India.

Weichmann, P. B., Lavely, E. M., Ritzwoller, M. H., 2000. Theory of surface nuclear magnetic resonance with application to geophysical imaging problems. Phys. Rev. E. 62, 1290–1312.

Weidelt, P., 1975. Electromagnetic induction in three-dimensional structures. J. Geophys. 41, 85–109.

Wiese, H., 1962. Geomagnetische Tiefentellurik Teil ii: Die Streichrichtung der Untergrundstrukturen des elektrischen Widerstandes, erschlossen aus geomagnetischen Variationen. Geofis. Pura e Appl. 52, 83–103.

Wünnemann, B., 1999. Untersuchungen zur Paläohydrography der Endseen in Badain Jaran- und Tengger Wüste, Innere Mongolei, Nordwest-China. Habilitationsschrift, Berlin, (in german).

Wünnemann, B., Hartmann, K., 2002. Morphodynamics and paleohydrography of the Gaxun Nur Basin, Inner Mongolia, China. Z. Geomorph. N. F. 126, 147–168.

Xiao, W., Windley, B. F., Hao, J., Li, J., 2002. Arc-ophiolite obduction in the western Kunlun Range (China): implications for the Paleozoic evolution of central asia. Journal of the Geological Society of London 159, 517–528.

Xingyuan, M., Qidong, D., Yipeng, W., Hefu, L., 1982. Cenocoic graben systems in north china. Z. Geomorph. N.F. Suppl. 42, 99–116.

Xiou, G., 1990. Hydrogeolical map (Jiuquan). Tech. rep., Dep. of water management, Ejina QI, PR China, (in chinese).

Yang, X., 2000. Landscape evolution and precipitation changes in the badain jaran desert. Chinese Science Bull. 45, 1042–1047.

Yee, E., Paulson, K. V., 1987. The canonical decomposition and its relationship to other forms of magnetotelluric impedance tensor analysis. J. Geophys. 61, 173–189.

Zhang, P., Roberts, R. G., Pedersen, L. B., 1987. Magnetotelluric strike rules. Geophysics 52, 267–278.

Zhang, Y. Q., Vergely, P., Mercier, J., 1995. Active faulting in and along the Qinling Range (China) inferred from Spot imagery analysis and extrusion tectonics of south China. Tectonophysics 243, 69–95.

Zhang, Z., Zhou, M., Shao, S., 1990. Quaternary Geologic Map of the People's Republic of China and adjacent sea area, 1:250000. Tech. rep., China Cartog. Publishing House, Beijing.

Zhdanov, M., Hursan, G., 2000. 3D electromagnetic inversion based on quasi-analytical approximation. Inverse Problems 60, 1297–1322.

Zhdanov, M., Tolstaya, E., 2004. Minimum support nonlinear parameterization on the solution of a 3D magnetotelluric inverse problem. Inverse Problems 20, 937–952.

Zhigao, S., 1980. Lower paleozoic Spilite-Keratophyre Suite of the Northern Qilian Range (Nan Shan) and its bearing on Ophiolite Suite. Bull. Chin. Acad. Geol. Sci. 1.

Zonge, K. L., Hughes, L. J., 1991. Controlled source audio-frequency magnetotellurics. In: Nabighian, M. N. (Ed.), Electromagnetic Methods in Applied Geophysics. Volume 2, Application. Soc. Expl. Geophys., pp. 713–809.

# A. Ellipticity analysis

## A.1. Representation of elliptical polarisation states

The following ellipse parameterisation has been introduced by Weichmann et al. (2000). It is briefly summarized here. Linear gaussian error propagation is added to Weichmann's formulas.

### A.1.1. Parameterisation:

A monochromatic vector field $\mathbf{v}$ oscillates with angular frequency $\omega_0$ in time domain with

$$\begin{aligned}\mathbf{v}(t) &= \mathbf{A}(\omega_0)\cos(\omega_0 t) + \mathbf{B}(\omega_0)\sin(\omega_0 t) \\ &= \overline{\mathbf{A}}(\omega_0)e^{i\omega_0 t} + \overline{\mathbf{A}}^*(\omega_0)e^{-i\omega_0 t} \ , \end{aligned} \tag{A.1}$$

in which $\overline{\mathbf{A}}(\pm\omega_0) = \mathbf{A}(\omega_0) + i\mathbf{B}(\omega_0) = \overline{\mathbf{A}}^*(\mp\omega_0)$ is the complex field amplitude. In general, $\mathbf{A}$ and $\mathbf{B}$ are non-collinear, corresponding to an elliptically polarised vector field.

Now, let $\mathbf{v}(t) = (v_1,\, v_2)^T$ and consequently $\overline{\mathbf{A}}(\omega_0)$ be a vector lying in the $z = 0$ plane and decompose it in the form

$$\overline{\mathbf{A}}(\omega_0) = e^{i\zeta(\omega_0)}\left(a(\omega_0)\widehat{\mathbf{a}}(\omega_0) + ic(\omega_0)\widehat{\mathbf{c}}(\omega_0)\right) \ , \tag{A.2}$$

where the phase $\zeta$ is chosen in such a way that $a$ and $c$ are real and $a \geq |c| \geq 0$. The unit vectors are given by $\widehat{\mathbf{a}} = (\cos\alpha,\, \sin\alpha)^T$ and $\widehat{\mathbf{c}} = \widehat{\mathbf{z}} \times \widehat{\mathbf{a}}$ . Since $\overline{\mathbf{A}}(-\omega_0) = \overline{\mathbf{A}}^*(\omega_0)$, it follows that $\zeta(\omega_0) = -\zeta(-\omega_0)$ and $c(\omega_0) = -c(-\omega_0)$ are odd functions of frequency and $a(\omega_0) = a(-\omega_0)$ and $\widehat{\mathbf{a}}(\omega_0) = \widehat{\mathbf{a}}(-\omega_0)$ are even functions of frequency.

With this decomposition, we see that the total field may be written in the form

$$\mathbf{v}(t) = a\cos\left(\omega_0 t - \zeta\right)\widehat{\mathbf{a}} + c\sin\left(\omega_0 t - \zeta\right)\widehat{\mathbf{c}} \ . \tag{A.3}$$

The first addend is denoted as the co-rotating part, the second as the counter-rotating part of the elliptically polarised field. The real amplitudes $a$ and $c$ are identified as major and minor axes of the polarisation ellipse, respectively, and the phase $\zeta$ determines the vector at $t = 0$.

For notational simplicity, we rewrite equation (A.2) as

$$\mathbf{v} = e^{i\zeta}\left(a\widehat{\mathbf{a}} + ic\widehat{\mathbf{c}}\right) \ , \tag{A.4}$$

where now $\mathbf{v} = \mathbf{v}(\omega_0)$.

### A.1.2. Calculation of ellipse parameters:

From the combinations

$$\begin{aligned}\mathbf{v}\cdot\mathbf{v} &= \left(a^2 - c^2\right)e^{2i\zeta} \\ \mathbf{v}\cdot\mathbf{v}^* &= a^2 + c^2 \\ \mathbf{v}\times\mathbf{v}^* &= -2iac\widehat{\mathbf{z}} \ , \end{aligned} \tag{A.5}$$

one obtains

$$e^{i\zeta} = \left[\frac{\mathbf{v}^2}{|\mathbf{v}^2|}\right]^{\frac{1}{2}} \tag{A.6}$$

for the phase, and the major and minor axes are given by

$$\begin{aligned} a &= \left[\frac{1}{2}\left(|\mathbf{v}|^2 + |\mathbf{v}^2|\right)\right]^{\frac{1}{2}} \\ c &= \text{sign}(i\widehat{\mathbf{z}} \cdot \mathbf{v} \times \mathbf{v}^*)\left[\frac{1}{2}\left(|\mathbf{v}|^2 - |\mathbf{v}^2|\right)\right]^{\frac{1}{2}} \quad , \end{aligned} \tag{A.7}$$

where $a > 0$ and the sign of $c$ may be positive or negative indicating the sense of rotation in time domain. The ellipticity is then determined from

$$\epsilon = \frac{c}{a} \quad . \tag{A.8}$$

Finally, the unit vector is

$$\widehat{\mathbf{a}} = \frac{1}{a}\Re\left(e^{-i\zeta}\mathbf{v}\right) \quad , \tag{A.9}$$

from which the angle $\alpha$ with the $x-$axis can be derived:

$$\tan\alpha = \frac{1}{a}\frac{a_2\cos\zeta + b_2\sin\zeta}{a_1\cos\zeta + b_1\sin\zeta} \tag{A.10}$$

Here, we denote real and imaginary parts of $v_i$ by $a_i$ and $b_i$, respectively, i.e. $v_i = a_i + ib_i$.

## A.2. Linear error propagation

### A.2.1. Variance of $a$, $c$ and $\epsilon$

Let us denote the variance of $\mathbf{v}$ by $\sigma^2_{\mathbf{v}} = \begin{pmatrix} \sigma^2_{v_1} & \sigma^2_{v_2} \end{pmatrix}^T$, where the same standard deviation is applied to real and imaginary part of each component. Assuming linear error propagation, then the variance of the major axes $a$ is derived from

$$\sigma^2_a = \sum_k \left(\frac{\partial a}{\partial p_k}\right)^2 \sigma^2_{p_i} \quad , \tag{A.11}$$

where $p_k$ denotes the variables of $a$, i.e. $a = a(p_k)$.

Let $v_i = a_i + ib_i$. Differentiating equation (A.7) with respect to one of the parameters $p \doteq p_k \,\epsilon\, \{a_1, b_1, a_2, b_2\}$ yields

$$\frac{\partial a}{\partial p} = \frac{1}{2a}\left[\frac{\partial |\mathbf{v}|^2}{\partial p} + \frac{\partial |\mathbf{v}^2|}{\partial p}\right] \quad , \tag{A.12}$$

where

$$\frac{\partial |\mathbf{v}|^2}{\partial p} = 2p$$

and

$$\begin{aligned}\frac{\partial\left|\mathbf{v}^2\right|}{\partial p} &= \frac{\pm 2p\left(a_1^2-b_1^2+a_2^2-b_2^2\right)}{|\mathbf{v}^2|} \\ &+ \frac{4\left(1+\frac{\partial}{\partial p}\right)\left(a_1b_1+a_2b_2\right)}{|\mathbf{v}^2|} \ ,\end{aligned}$$

where the negative sign is chosen, if $p\,\epsilon\,\{b_1, b_2\}$. The variance of $a$ is summed up to

$$\begin{aligned}\sigma_a^2 &= \left[\left(\frac{\partial a}{\partial a_x}\right)^2+\left(\frac{\partial a}{\partial b_x}\right)^2\right]\sigma_{v_1}^2 \\ &+ \left[\left(\frac{\partial a}{\partial a_y}\right)^2+\left(\frac{\partial a}{\partial b_y}\right)^2\right]\sigma_{v_2}^2 \ . \end{aligned} \tag{A.13}$$

The variance of $c$ differs from that of $a$ only by a sign as can easily be deduced from equation (A.7). The $\mathrm{sign}-$function determines only the sign of $c$ and does not enter the squared partial derivative in the error propagation law.

Having calculated the variances of major and minor axes, the variance for the ellipticity (A.8) is easily obtained by

$$\sigma_\epsilon^2 = \left(\frac{\epsilon}{a}\right)^2\sigma_a^2+\left(\frac{1}{a}\right)^2\sigma_b^2 \tag{A.14}$$

### A.2.2. Variances of phase $\zeta$ and directional parameter $\alpha$

The radical of equation (A.6) is a complex number $|z|\,e^{i\phi}$ where $|z|=1$ since $e^{i\zeta}=\left[|z|\,e^{i\phi}\right]^{\frac{1}{2}}=e^{i\frac{\phi}{2}}$, and $\tan\phi=\Im\left(\mathbf{v}^2\right)/\Re\left(\mathbf{v}^2\right)$, since $\left|\mathbf{v}^2\right|$ is real. Thus,

$$\tan\phi=\frac{2\left(a_1b_1+a_2b_2\right)}{a_1^2+b_1^2+a_2^2+b_2^2} \tag{A.15}$$

and $2\zeta=\phi$. The partial derivative with respect to one of the variable $p$ is given by

$$\frac{\partial\zeta}{\partial p}=\frac{1}{1+\tan^2 2\zeta}\frac{\left(\mathbf{v}\cdot\mathbf{v}^*\frac{\partial}{\partial p}-2p\right)\left(a_1b_1+a_2b_2\right)}{\left(\mathbf{v}\cdot\mathbf{v}^*\right)^2} \ , \tag{A.16}$$

which can be used to estimate the variance of $\zeta$.

Finally, from equation (A.10)

$$\frac{\partial\alpha}{\partial p}=\frac{1}{1+\tan^2\alpha}\frac{\partial}{\partial p}\frac{a_2\cos\zeta+b_2\sin\zeta}{a_1\cos\zeta+b_1\sin\zeta} \ , \tag{A.17}$$

$$\frac{\partial\alpha}{\partial a}=\frac{-\tan\alpha}{1+\tan^2\alpha}\frac{1}{a} \ , \tag{A.18}$$

and

$$\frac{\partial\alpha}{\partial\zeta}=\frac{1}{1+\tan^2\alpha}\frac{a_1b_2-a_2b_1}{\left(a_1\cos\zeta+b_1\sin\zeta\right)^2} \ , \tag{A.19}$$

which yields estimates for the variance of the angle $\alpha$.

## A.3. SVD of a galvanically distorted 2D impedance tensor

In this section, we repeatedly take reference to formulas from LaTorraca et al. (1986), hereafter abbreviated with 'LaTo (equation number)'. The calculations are for simplicity performed in the regional coordinate system. The results, however, apply to any coordinate system.

As observed by Groom and Bailey (1991), the result of the modified SVD for a galvanically distorted impedance tensor of the form (4.3) with $g_x = g_y = 1$

$$\mathbf{Z} = \mathbf{D}\mathbf{Z}^r = \mathbf{U}_e\mathbf{M}\widetilde{\mathbf{U}}_h = \begin{bmatrix} -\sin\beta_y Z^r_{yx} & \cos\beta_x Z^r_{xy} \\ \cos\beta_y Z^r_{yx} & \sin\beta_x Z^r_{xy} \end{bmatrix} \tag{A.20}$$

has the following properties:

- The ellipticities $\epsilon_e$ of the modified left-singular vectors $\mathbf{e}'_i$ vanish exactly.
- The ellipticities $\epsilon_h$ of the modified right-singular vectors $\mathbf{h}'_i$ vanish, if the phases of the regional impedance elements are equal (or if their difference is equal $\pi$).
- The orientations of modified singular vectors do not coincide with any of the directions given by the distortion angles nor the regional coordinate system.

Additionally, we found, that if $\beta_x = \beta_y \doteq \beta$, then

- $\beta$ is the angle, the $\mathbf{e}'_i$ are rotated out of the regional coordinate system
- $\epsilon_h$ vanishes exactly
- $\mathbf{h}'_i$ are linearly polarised and span the regional coordinate system.

These statements are easily proven using the formulas LaTo (26), (27), (32) and (33). Consider first the hermitian matrix $\mathbf{C}_{e,h}$ defined as

$$\mathbf{C}_h = \mathbf{Z}\widetilde{\mathbf{Z}} \ , \tag{A.21}$$

(LaTo (26)) and

$$\mathbf{C}_e = \mathbf{Z}\widetilde{\mathbf{Z}} \ , \tag{A.22}$$

(LaTo (27)) which are expanded to

$$\begin{aligned} C_{h,xx} &= \left|Z^r_{yx}\right|^2 \sin^2\beta_y + \left|Z^r_{xy}\right|^2 \cos^2\beta_y \\ C_{h,xy} &= \cos\beta_y \sin\beta_x Z^r_{xy} Z^{r*}_{yx} - \cos\beta_x \sin\beta_y Z^r_{xy} Z^{r*}_{yx} \\ C_{h,yx} &= \cos\beta_y \sin\beta_x Z^{r*}_{xy} Z^r_{yx} - \cos\beta_x \sin\beta_y Z^{r*}_{xy} Z^r_{yx} \\ C_{h,yy} &= \left|Z^r_{yx}\right|^2 \cos^2\beta_y + \left|Z^r_{xy}\right|^2 \sin^2\beta_y \end{aligned} \tag{A.23}$$

and

$$\begin{aligned} C_{e,xx} &= \left|Z^r_{yx}\right|^2 \sin^2\beta_y + \left|Z^r_{xy}\right|^2 \cos^2\beta_x \\ C_{e,xy} &= \left|Z^r_{xy}\right|^2 \sin\beta_x \cos\beta_x - \left|Z^r_{yx}\right|^2 \sin\beta_y \cos\beta_y \\ C_{e,yx} &= \left|Z^r_{xy}\right|^2 \sin\beta_x \cos\beta_x - \left|Z^r_{yx}\right|^2 \sin\beta_y \cos\beta_y \\ C_{e,yy} &= \left|Z^r_{yx}\right|^2 \cos^2\beta_y + \left|Z^r_{xy}\right|^2 \sin^2\beta_x \ , \end{aligned} \tag{A.24}$$

respectively.

The ellipticities $\epsilon_e = \tan \nu_e$ of the modified electric singular vectors are derived from equation LaTo (33),

$$\sin 2\nu_e = \frac{i\,(C_{e,xy} - C_{e,yx})}{r_1^2 - r_2^2} \ , \tag{A.25}$$

where $r_i$ are the singular values of $\mathbf{Z}$. Since $C_{e,xy} = C_{e,yx}$ as seen from (A.24), the nominator in equation (A.25) vanishes and thus $\nu_e = 0$ and $\epsilon_e = 0$ independent of the singular values. Thus, the left-singular vectors are linearly polarised.

Denote now the angle $\gamma_e$ as the angle of the major axes of $\mathbf{e}_1$ with the x-axes. It is calculated with LaTo (32) as

$$\tan 2\gamma_e = \frac{C_{e,xy} + C_{e,yx}}{C_{e,xx} - C_{e,yy}} \tag{A.26}$$

Expanding as before leads to a mixture of the absolut values of the regional impedances and sines and cosines of the distortion angles, respectively. If, however, $\beta_x = \beta_y = \beta$, equation (A.26) simplifies to $\tan 2\gamma_e = \tan 2\beta$, thus

$$\gamma_e = \beta \ , \tag{A.27}$$

i.e. the direction of the left-singular vectors is determined by the distortion angle $\beta$.

Equation (A.23) shows, that $C_{h,xy} = C^*_{h,yx}$. If $\arg(Z_{xy}) + \pi = \arg(Z_{yx})$, i.e. the regional impedances have the same phase, then $C_{h,xy} = C^*_{h,xy}$ becomes real. Thus, applying formula (A.25) to the right singular vectors $\mathbf{h}_i$, its nominator vanishes. Therefore, the ellipticity

$$\epsilon_h = \tan 2\nu_h \tag{A.28}$$

vanishes, if the impedance elements have the same phase. If $\beta_x = \beta_y = \beta$ again, $C_{h,xy} = C_{h,yx} = 0$ independent of the impedance phases and thus $\epsilon_h = 0$ as well.

Only in the latter case, it can be shown using equation (A.26), that

$$\gamma_h = 0 \ , \tag{A.29}$$

i.e. the direction of right-singular vectors coincides with the regional frame. Otherwise, the direction of $\mathbf{h}_i$ is an algebraic mixture of the regional impedances and the distortion angles.

These results state that the SVD indicates the existence of a regional 2D structure, if the left-singular vectors are linearly polarised. If the right-singular vectors are also linearly polarised, and the phases of the regional impedances are not equal, then the right-singular vectors indicate the regional coordinate system. This is however only the case, if $\beta_x = \beta_y$. Then, the deviation of the left-singular vectors from the regional frame yields the distortion angle. The equality of regional phases may be deduced from equal phases of the characteristic values $\mu_i$.

In a rotated coordinate system, e.g, $\mathbf{Z} = \mathbf{R}\mathbf{D}\mathbf{Z}^r\mathbf{R}^T$, the SVD yields the same polarisation states, but the directions of singular vectors are altered. In analogy to the previous results, it is now a straightforward calculation to show for the case $\beta_x = \beta_y = \beta$ , that

$$\begin{aligned}
\mathbf{R} &= \mathbf{U}_h \begin{bmatrix} 0 & 1 \\ 1 & 0 \end{bmatrix} \\
\mathbf{D} &= \begin{bmatrix} 0 & 1 \\ 1 & 0 \end{bmatrix} \mathbf{U}_h^T \mathbf{U}_e \\
\mathbf{Z}^r &= \begin{bmatrix} -1 & 0 \\ 0 & 1 \end{bmatrix} \mathbf{M} \begin{bmatrix} 0 & 1 \\ 1 & 0 \end{bmatrix} \ ,
\end{aligned} \tag{A.30}$$

where $\mathbf{U}_h$ and $\mathbf{U}_e$ are real. More precisely, $\mathbf{U}_h$ is the mirrored rotation matrix and $\mathbf{U}_e$ is a function of the distortion angle $\beta$, i.e. performs an additional rotation of the regional electric field components out of the regional coordinate system.

In the sequel, we will introduce an alternative approach, which is related to the modified SVD, since it relies on principal vectors, but their orthogonality is removed. By doing so, the general case of galvanic distortion is also covered.

# B. A solution of the electromagnetic integral equation using wavelets

## B.1. Conductivity models and field approximations

For numerical modeling of the electromagnetic field response for a given source $\mathbf{J}^e(\mathbf{r})$ above or within a conducting inhomogeneous earth, the conductivity distribution is usually discretized in terms of small cells, where the conductivity is taken constant within each cell. In general, two classes of conductivity models are used in electromagnetics: blocky models and smooth models, both being computed on a similar numerical grid. Blocky models consist of a small number of anomalous conductors or resistors, each of which are represented by a large number of cells with equal conductivity values. This class of models is most widely used in forward modeling and synthetic model studies. Smooth models are typically retrieved from inversion of measured data. Due to insufficient number of (erroneous) data and a large number of unknown conductivity values, i.e. a large number of cells, a smoothness constraint is imposed on the model demanding so-called minimum structure models while fitting the data. This representation is believed to be objective and therefore to be a reasonable choice of model class if no a priori information is available. Thus, the sought conductivity function is supposed to be a continuous function, but is still represented an a numerical grid with cells of constant conductivity and therefore in fact a discontinuous function.

While the choice of model class and discretization type only determines the representation of the conductivity model, the discrete representation of the electric field controls the accuracy of the solution. It is a common procedure to describe the variation of the electric field within each cell by simple polynomial functions, e.g., constant or linear behavior. In the scope of the solution of the electromagnetic integral equation, it is for instance assumed, that the electric field is constant within each cell, and approaches the true electric field at the center of the cell ((Hohmann, 1987; Weidelt, 1975). This is of course only a rough approximation to the electric field variations in the vicinity of conductivity contrasts, and therefore a relatively fine discretization is required.

Here, I try a more general description of conductivity models and the electric field using a discrete wavelet transformation. Wavelets provide a set of basis functions for function spaces. In contrast to the Fourier transform basis functions, which are perfectly localized in Fourier domain but not compact in space domain, wavelets are both localized in space and Fourier domain. This opens the possibility to use wavelets in order to represent functions that are both localized in space and spatial frequency. In particular, wavelets enable us to represent functions with fewer terms, when the wavelet is chosen in such a way that it resembles the function to be represented. For instance, function with spikes may well be represented using spiky wavelets. Thus, using wavelets as basis functions has obviously advantages in numerical applications, because the computational effort might be reduced due a decreased number of required terms.

Let me very briefly introduce the basic formulation of the wavelet transform and the Multi-resolution analysis, which basically is taken from Daubechies (1992) and Stollnitz et al. (1996).

**The wavelet transform and the MRA:** Assume, that a function is given at discrete samples $k = 0, ..., N-1$ with values $f_k^J$. The discretely sampled function corresponds to a low-pass filtered approximation to the original function $f(x)$. The approximate representation $f_J(x)$ is given in terms of its discrete samples and some basis functions $\phi_{Jk}(x)$, i.e.,

$$f_J(x) = \sum_k f_k^J \phi_{J,k}(x) \ . \tag{B.1}$$

$f_J(x)$ will essentially be smoother then $f(x)$, since the resolved fluctuations are limited by the sampling frequency. The level of approximation is indicated by subscript $J$. In the scope of the wavelet transform, the functions $\phi_{Jk}(x)$ have to satisfy certain restrictions and are in particular orthogonal functions forming the basis of the *approximation space*. In the language of the wavelet transform, $\phi_{Jk}(x)$ is said to be the scaling function at a level $J$ with scale $2^J$. The function $f_J(x)$, i.e. the smooth approximation to the original function $f(x)$, is uniquely described by its approximation coefficients $f_k^J$ and entirely fits into the approximations space $V_J$. The space $V_J$ spanned by $\phi_{Jk}(x)$ is decomposable into orthogonal subspaces $V_{J-1}$ and $W_{J-1}$, where $V_{J-1}$ is an approximation space at lower scale $2^{J-1}$, i.e. contains less details than $V_J$, and the *detail space* $W_{J-1}$ contains the fluctuations of $f_J(x)$. The representation of $f_J(x)$ is then given by

$$f_J(x) = \sum_k f_k^{J-1} \phi_{J-1,k}(x) + \sum_k d_k^{J-1} \psi_{J-1,k}(x) \ . \tag{B.2}$$

The coefficients $d_k^{J-1}$ are denoted as detail coefficients. Equation (B.2) is a wavelet representation of the function $f_J(x)$, the coefficients $f_k^{J-1}$ and $d_k^{J-1}$ are the wavelet transform of $f_k^J$. The wavelet decomposition can be repeatedly applied down to a level $j$ and yields the multi-resolution analysis (MRA) of $f_J(x)$:

$$f_J(x) = \sum_k f_k^j \phi_{j,k}(x) + \sum_j \sum_k d_k^j \psi_{j,k}(x) \tag{B.3}$$

Each step in the MRA can be conceived as a low-pass and high-pass filtering of a signal given in an approximation space, followed by (dyadic) down-sampling. The detail and approximation spaces are constructed from the approximation space of higher level by high-pass and low-pass filtering. Using discrete high- and low-pass filter sequences $h_k$ and $g_k$, respectively, the basis functions at a certain resolution are related to the scaling functions of a higher resolution by convolution-like filter operations. This two-scale relation is the fundamental idea of the wavelet transform and is formulated as

$$\begin{aligned} \phi_{J-1,k}(t) &= \sum_l h_{l-2k} \phi_{J,l}(t) \\ \psi_{J-1,k}(t) &= \sum_l g_{l-2k} \phi_{J,l}(t) \ , \end{aligned} \tag{B.4}$$

The same filter apply to the decomposition of the approximation coefficients $f_k^J$ into approximation and detail coefficients $f_k^{J-1}$, $d_k^{J-1}$ and is given by

$$\begin{aligned} f_k^{J-1} &= \sum_l h_{l-2k} f_l^J \\ d_k^{J-1} &= \sum_l g_{l-2k} f_l^J \ . \end{aligned} \tag{B.5}$$

Expression (B.5) is referred to as the discrete wavelet transform (DWT). The MRA of a signal is obtained by a cascade of discrete wavelet transforms applied to each of the approximation coefficient sequences. Numerically, the MRA can be casted into a matrix equation, where the matrix is basically a convolution matrix containing the filter coefficients of low- and high-pass filter. Then,

$$\mathbf{c} = \begin{bmatrix} \mathbf{f}^j \\ \vdots \\ \mathbf{d}^{J-2} \\ \mathbf{d}^{J-1} \end{bmatrix} = \mathbf{W}\mathbf{f} \ , \tag{B.6}$$

where $\mathbf{f}$ is a data vector with elements $f_n$ and $\mathbf{W}$ is the MRA matrix. To make a wavelet transform practical, perfect reconstruction of the signal from its approximation and detail coefficients is demanded. Thus,

$$\mathbf{f} = \mathbf{R}\mathbf{c} \ , \tag{B.7}$$

where $\mathbf{R}$ is a reconstruction matrix. The reconstruction includes (dyadic) up-sampling followed by high-pass and low-pass filtering of the signals in approximation and detail spaces.

In the following, I will exemplarily demonstrate the DWT using the most simple available wavelet, the Haar wavelet.

**Haar MRA:** Let $V_0$ be the space of functions, that are constant on unit intervals $[k, k+1)$ for integer $k$, and let $V_j$ be the space of functions, which are constant on intervals $[k/2^j, (k+1)/2^j)$. For this set of function spaces, we can choose the scaling function to be the box function

$$\phi(x) = \begin{cases} 1 & \text{for} \quad 0 \le x < 1 \\ 0 & \text{otherwise} \end{cases} \ . \tag{B.8}$$

Clearly, the translates $\phi(x-k)$ are orthogonal functions, since thy do not overlap for different translations. Thus, every piecewise function in space $V_0$ maybe represented in the basis $\phi_{0,k}$. The Haar wavelet function is

$$\psi(x) = \begin{cases} 1 & \text{for} \quad 0 \le x < \frac{1}{2} \\ -1 & \text{for} \quad \frac{1}{2} \le x < 1 \end{cases} \tag{B.9}$$

The function space $W_0$ is orthogonal to $V_0$ since $\int \phi(x-k)\psi(x-l)dx = 0$ for any integer translation. The space $V_J$ maybe decomposed into subspaces $V_{J-1}$ and $W_{J-1}$. The basis functions of these subspaces are obtained from $\phi(x)$ and $\psi(x)$ by scaling operations according to

$$\begin{aligned} \phi_{j,k} &= 2^{j/2}\phi(2^j x - k) \\ \psi_{j,k} &= 2^{j/2}\psi(2^j x - k) \ . \end{aligned} \tag{B.10}$$

Hence, at level $j = -1$, $\phi_{-1,k} = 1/\sqrt{2}\phi(x/2 - k)$ and $\psi_{-1,k} = 1/\sqrt{2}\psi(x/2 - k)$ or for zero translation

$$\begin{aligned} \phi_{-1,0}(x) &= \begin{cases} \frac{1}{\sqrt{2}} & \text{for} \quad 0 \le x < 2 \\ 0 & \text{otherwise} \end{cases} \ , \\ \psi_{-1,0}(x) &= \begin{cases} \frac{1}{\sqrt{2}} & \text{for} \quad 0 \le x < 1 \\ -\frac{1}{\sqrt{2}} & \text{for} \quad 1 \le x < 2 \end{cases} \ . \end{aligned}$$

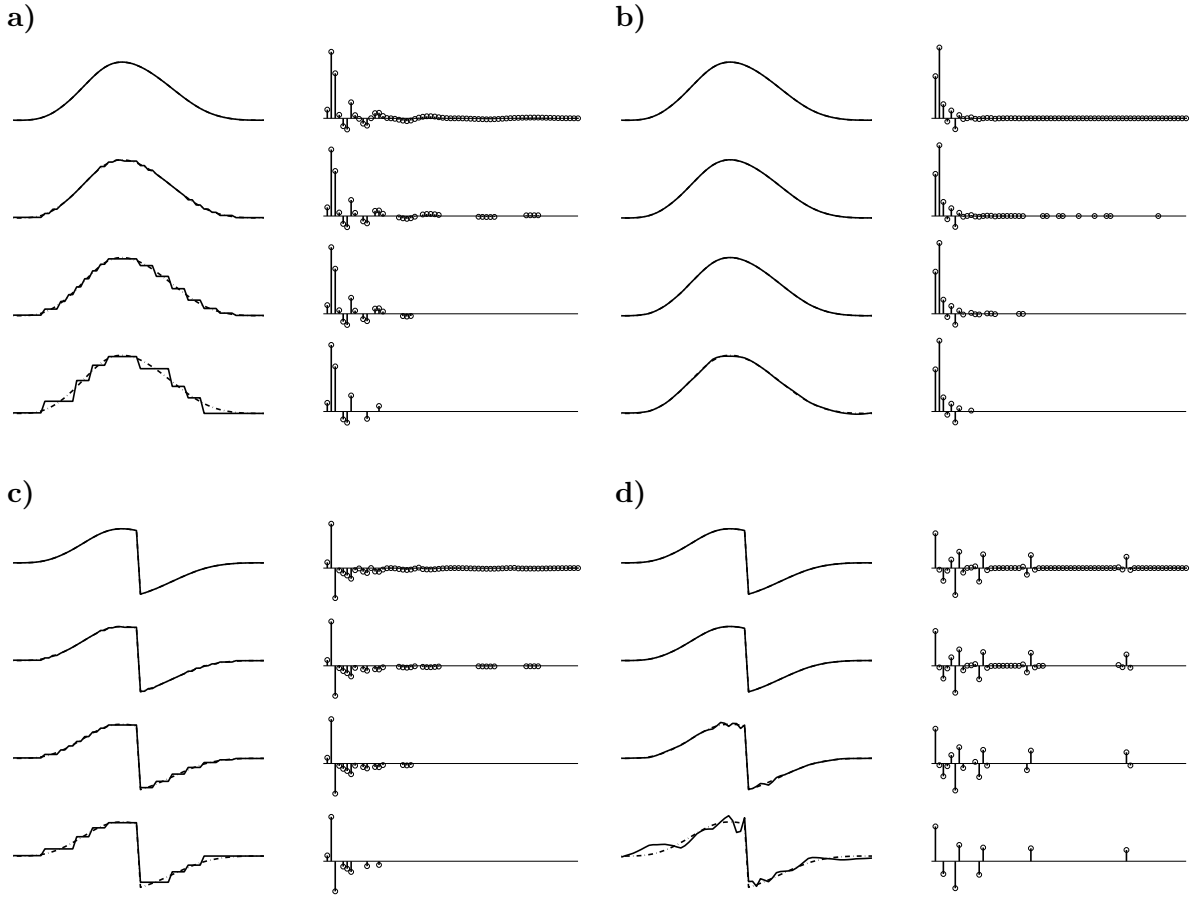


**Figure B.1.:** Representation of a smooth and discontinuous functions in wavelet basis. Left panel shows original function (dashed line, 64 samples) and solid line indicates the reconstructed function using 64, 32, 16 and 8 coefficients (from top to bottom). The coefficients, which are used for reconstruction are displayed in the right panel. Least significant coefficients have been omitted. **a)** Haar wavelet and **b)** Symlet (order 4) multi-resolution analysis and compression of a smooth function and **c)** and **d)** of a discontinuous function, respectively.

The filter coefficients $h_k$ and $g_k$ in expression (B.5) are easily identified as

$$h_k = \left\{ \frac{1}{\sqrt{2}}, \frac{1}{\sqrt{2}} \right\} \quad , \quad g_k = \left\{ \frac{1}{\sqrt{2}}, -\frac{1}{\sqrt{2}} \right\} \quad .$$

Application of the Haar filter to a sequence $f_k^J$ as in equation (B.4) basically yields the mean and the differences of consecutive samples, followed however by dyadic down-sampling, i.e. only every second mean and difference is kept.

The wavelet decomposition is demonstrated using a smooth and a discontinuous function as shown in Figure B.1. Here I decomposed the original function with 64 samples, depicted by a solid black line, using a MRA analysis of degree four, and consecutively deleted the least significant coefficients prior to reconstruction. This has been exemplarily done using the Haar wavelet and a smooth wavelet (symlet, cf. Daubechies, 1992). As can be seen in Figures B.1a and c, the Haar

wavelet is not a suitable choice to represent smooth functions, but it can well be employed to represent discontinuous functions. In both cases, a step-function occurs when deleting coefficients, however, with the discontinuity in Figure B.1c well being reproduced. This simply demonstrates that when using a Haar wavelet, a piecewise constant function is assumed. By decreasing the number of coefficients, the original function is worse recovered, because the length of each step increases.

In contrast, the symlet is a smooth wavelet, and only few coefficients are significant and necessary to represent a function of 64 samples - as long as the function itself is smooth. In Figure B.1b, even eight coefficients might be acceptable when approximating the original function. If the function exhibits a discontinuity, the symlet representation implicitly produces unwanted oscillations in the vicinity of the discontinuity.

This example demonstrates, that the choice of wavelet basis is of importance when treating a specific problem. In the scope of the electromagnetic modeling problem, we might want to choose a Haar wavelet representation when considering blocky models, while a symlet basis might be the better choice to treat smooth models. Note, that different wavelet basis can be chosen for different quantities, i.e. for a blocky conductivity functions we select a Haar representation, while for electric field of E-Polarization, which is always a smooth function, another type of basis functions might be suitable.

## B.2. Integral equation in E-Polarization

Before applying the wavelet decomposition to the electromagnetic integral equation, let me first briefly describe the derivation of integral equation and the standard solution. The derivation follows that given in Schmucker and Weidelt (1975).

In the scope of volume integral equation method, the computation of the electromagnetic field is restricted to an anomalous domain, in which the conductivity function $\sigma = \sigma(x, y, z)$ deviates from the normal distribution $\sigma_n(z)$, where the latter is only dependent on depth. This implies the decomposition of the conductivity into its normal and anomalous part, where the anomalous part is given by

$$\sigma_a = \sigma - \sigma_n \quad . \tag{B.11}$$

With this decomposition,

$$\sigma_a = \begin{cases} \sigma_a(\mathbf{r}) & , \quad \mathbf{r} \in V_a \\ 0 & , \quad \mathbf{r} \notin V_a \end{cases} \tag{B.12}$$

where $\mathbf{r} = (x, y, z)^T$.

Let now the $x-$axis be parallel to the strike direction as indicated in Figure B.2 such that $\sigma = \sigma(y, z)$ and for all field components $F = F(y, z)$ and $\partial F/\partial x = 0$ is demanded. The latter condition requires, that the external $E-$Polarization source field $J_x^e(y, z)$ maybe a function of $(y, z)$ while in $B-$Polarization only a plane $J_y^e(z)$ wave is permitted.

For convenience, I omit the subscripts of the horizontal field components and define $E \equiv E_x$. The quantities in the $E-$Polarization differential

$$\Delta E_x \quad = \quad k^2 E_x + J^e \tag{B.13}$$

are split into their normal and anomalous parts as

$$\begin{aligned} \sigma(\mathbf{r}) &= \sigma_n(z) + \sigma_a(y,z) \\ k^2(\mathbf{r}) &= k_n^2(z) + k_a^2(y,z) \\ E(\mathbf{r}) &= E_n(z) + E_a(y,z) \end{aligned} \tag{B.14}$$

Here, $E_n$ is the solution of

$$\Delta E_n = k_n^2 E_n + i\omega\mu_0 J^e \tag{B.15}$$

In virtue of equations (B.13,B.14 and B.15), the anomalous part $E_a$ satisfies

$$\Delta E_a = k_n^2 E_a + k_a^2 E \ . \tag{B.16}$$

Let $G = G(\mathbf{r}|\mathbf{r}_0)$ be the Greens function for the normal conductivity structure, satisfying

$$\Delta G(\mathbf{r}|\mathbf{r}_0) = k_n^2(\mathbf{r})\, G(\mathbf{r}|\mathbf{r}_0) - \delta(\mathbf{r}|\mathbf{r}_0) \ . \tag{B.17}$$

It can be conceived as the electric field of a unit line source current placed at $\mathbf{r}_0$ and observed at $\mathbf{r}$. Multiplication of equation (B.16) with $G$ and (B.17) with $E_a$, subtracting and integrating with respect to $\mathbf{r}$ over the whole space leads to

$$E_a(\mathbf{r}_0) = -\int_{\mathcal{A}} k_a^2(\mathbf{r})\, E(\mathbf{r})\, G(\mathbf{r}|\mathbf{r}_0)\, d\mathbf{r} + \int_{\mathcal{A}} \left(G(\mathbf{r}|\mathbf{r}_0)\, \Delta E_a(\mathbf{r}) - \Delta G(\mathbf{r}|\mathbf{r}_0)\, E_a(\mathbf{r})\right) d\mathbf{r} \ . \tag{B.18}$$

Greens theorem yields

$$\int_{\mathcal{A}} \left(G\Delta E_a - \Delta G E_a\right) d\mathbf{r} = \oint_{\mathcal{C}} \left(G\frac{\partial}{\partial n}E_a - \frac{\partial}{\partial n}G E_a\right) d\mathbf{s} = 0 \ , \tag{B.19}$$

since $E_a$ and $G$ vanish at infinity. Hence, introducing $E$ instead of $E_a$ in expression (B.18), the integral equation for the electric field is

$$E(\mathbf{r}_0) = E_n(\mathbf{r}_0) - \int_{\mathcal{A}} k_a^2(\mathbf{r})\, E(\mathbf{r})\, G(\mathbf{r}|\mathbf{r}_0)\, d\mathbf{r} \ . \tag{B.20}$$

In equation (B.20), integration is performed with respect to the observation coordinates $\mathbf{r}$. The fundamental reciprocity theorem in electromagnetic states, that source and receiver location are interchangeable, i.e.

$$G(\mathbf{r}|\mathbf{r}_0) = G(\mathbf{r}_0|\mathbf{r}) \ . \tag{B.21}$$

Therefore, the integral in equation (B.20) maybe evaluated over the source coordinates $\mathbf{r}_0$ instead of the observation coordinates $\mathbf{r}$:

$$E(\mathbf{r}) = E_n(\mathbf{r}) - \int_{\mathcal{A}_a} k_a^2(\mathbf{r}_0)\, E(\mathbf{r}_0)\, G(\mathbf{r}|\mathbf{r}_0)\, d\mathbf{r}_0 \tag{B.22}$$

Since $k_a^2$ vanishes outside the anomalous domain $\mathcal{A}_a$, it is only necessary to evaluate the integrals in equations and (B.20) and (B.22) over $\mathcal{A}_a$ instead of the whole space. Equation (B.20) may be utilized to derive the electric field within the anomalous domain. Once, $E(\mathbf{r}_0)$ is known, equation (B.22) yields the electric field at any point outside of the anomalous domain, e.g., at the surface of the earth.

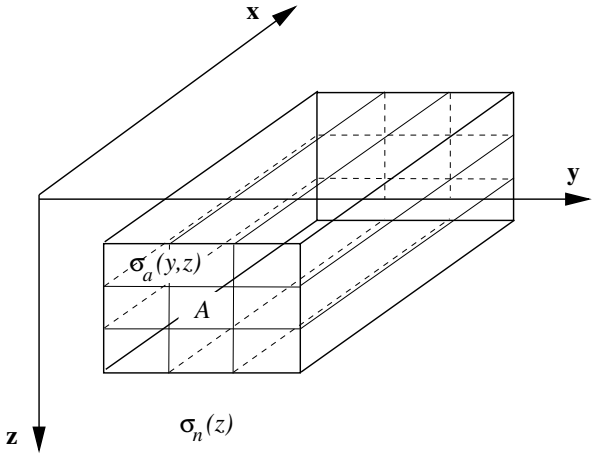


**Figure B.2.:** 2D anomalous domain $\mathcal{A}_a$ with anomalous conductivity $\sigma_a(y,z)$, which is embedded in a normal structure with only depth dependent conductivity $\sigma_n(z)$. The total conductivity at each point is $\sigma = \sigma_n + \sigma_a$.

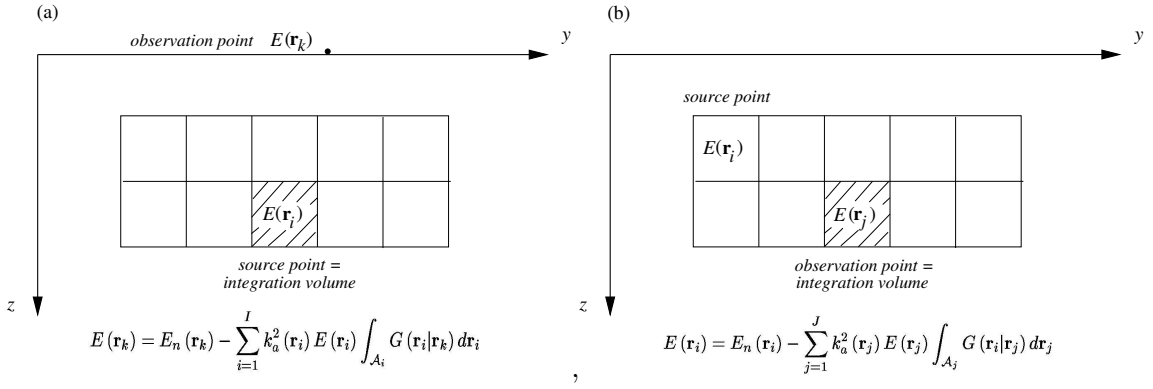


**Figure B.3.:** Sketch of the integral equations (B.20) and (B.22).

From Faraday's law the magnetic field components at the observation points $\mathbf{r}$ are determined from expression (B.22) as

$$\begin{aligned} H_z(\mathbf{r}) &= -\int_{\mathcal{A}_a} \sigma_a(\mathbf{r}_0)\, E(\mathbf{r}_0)\, \partial_y \left[G(\mathbf{r}|\mathbf{r}_0)\right] d\mathbf{r}_0 \\ H_y(\mathbf{r}) &= H_n(\mathbf{r}) + \int_{\mathcal{A}_a} \sigma_a(\mathbf{r}_0)\, E(\mathbf{r}_0)\, \partial_z \left[G(\mathbf{r}|\mathbf{r}_0)\right] d\mathbf{r}_0 \ , \end{aligned} \tag{B.23}$$

where only the Green's function must be differentiated.

## B.3. Standard solution of the integral equation

For a numerical solution of equations (B.20) and (B.22), the anomalous domain is split into $N$ rectangular cells as shown in Figures B.3a and b, respectively. Within each cell, the anomalous conductivity is taken constant, and the electric field is also assumed to be constant and represents the electric field in the center of the cell.

The inhomogeneous term $E_n$ may be calculated in a well known way for a given source field and normal structure. It remains to evaluate the Green's function for the $E-$Polarization problem, which depends only on the normal structure and is independent of the source field. It maybe readily calculated in wavenumber domain, and a fast Hankel transform is used to obtain the integral in space domain.

If the electric field is constant within each cell, the integral equation (B.20) reduces to the sum

$$E(\mathbf{r}_i) = E_n(\mathbf{r}_i) - \sum_{j=1}^{N} k_a^2(\mathbf{r}_j) E(\mathbf{r}_j) \int_{\mathcal{A}_j} G(\mathbf{r}_i|\mathbf{r}_j)\, d\mathbf{r}_j \ , \tag{B.24}$$

where $\mathbf{r}_i$, $\mathbf{r}_j \in \mathcal{A}_a$. The individual addends in equation (B.29) contain the integral of the Green's function with respect to the cell $\mathcal{A}_j$ due to a line current in cell $\mathcal{A}_i$.

Equation (B.29) has then the linear form

$$x_i = \sum_j a_{ij} x_j + g_i \ , \tag{B.25}$$

where $x_i = E_i$, $a_{ij} = k_a^2(\mathbf{r}_j) \int_{\mathcal{A}_j} G(\mathbf{r}_i|\mathbf{r}_j)\, d\mathbf{r}_j$ and $g_i = E_{n,i}$. The system of linear equations may be solved by iterative techniques, e.g. the Gauss-Seidel iteration scheme or directly from

$$\sum_j [\delta_{ij} - a_{ij}] x_j - g_i = 0 \ , \tag{B.26}$$

where

$$\delta_{ij} = \begin{cases} 0\,, & i \neq j \\ 1\,, & i = j \end{cases} \ .$$

Once, the electric field within the anomalous domain $\mathcal{A}_a$ is known, the electric field at the observation points $\mathbf{r}_k$ is derived from equation (B.22), which reads as

$$E(\mathbf{r}_k) = E_n(\mathbf{r}_k) - \sum_{i=1}^{I} k_a^2(\mathbf{r}_i) E(\mathbf{r}_i) \int_{\mathcal{A}_i} G(\mathbf{r}_i|\mathbf{r}_k)\, d\mathbf{r}_i \ . \tag{B.27}$$

assuming a constant electric field within each cell. Here, the integration of the Green's function is done with respect to the cells $\mathcal{A}_i$, in which the line current is placed (cf. Figure B.3b). In discrete notation, equation (B.27) is rewritten as

$$x_k = \sum_i a_{ki} x_i + g_k \ , \tag{B.28}$$

which gives directly the electric field $x_k$ at the observation points $k$.

We can now reformulate the standard solution in terms of the previously described Haar wavelet representation. For simplicity, I only consider lateral variations for the reformulation, while in vertical direction the standard description is kept. Thus, I consider the integral equation

$$E(y, z_w) = E_n(y, z_w) - \sum_w i\omega\mu_0 \int \sigma_a(y, z_w) E(y, z_w) K_w(y, z_w)\, dy \ , \tag{B.29}$$

where $w = 1\,, ...,\, W$ horizontal cell layers are assumed and $K_w(y, z_w) = \int_{z_w}^{z_{w+1}} G(\mathbf{r}_i|\mathbf{r}_j)\, dz$ is the depth integrated Green's function. Both the electric field and conductivity are in the standard

solution assumed to be constant within each cell, and are therefore entirely in the space of functions $V_j$ spanned by the the Haar scaling functions $\phi_{J,k}(y)$. The level $J$ is determined by the size of the cells in horizontal direction. Therefore, omitting the depth dependency $z_w$, the anomalous conductivity and the electric field are given by

$$\begin{aligned} \sigma_a(y) &= \sum_k \sigma_{a,k}^J \phi_{J,k}(y) \\ E(y) &= \sum_k E_k^J \phi_{J,k}(y) \ , \end{aligned} \tag{B.30}$$

where the Haar scaling function is

$$\phi_{J,k}(y) = \begin{cases} 2^{J/2} & \text{for} \quad 0 \le x < 2^J \\ 0 & \text{otherwise} \end{cases}$$

Inserting expression (B.30) into the integral equation (B.29) yields

$$E(y, z_w) = E_n(y, z_w) - \sum_w \sum_k i\omega\mu_0 \sigma_{a,k}^J(z_w) E_k^J(z_w) \int K_w(y, z_w)\, dy \tag{B.31}$$

This expression is the same as in equation (B.25), only the conductivity and electric field functions have been expressed in terms of the approximation coefficients in a wavelet basis spanned by the Haar scaling functions. Therefore, the standard solution can be considered as a particular (simple) version of a greater class of solutions, which maybe formulated in wavelet bases.

## B.4. Solution in wavelet domain

Let us first consider two functions $\sigma_a(y)$, $E_a(y)$, where we will assume, that the functions are elements of the subspace $V_J$, i.e.,

$$\begin{aligned} \sigma_a(y) &= \sigma_J(y) = \sum_k x_k^J \phi_{J,k}(y) = \sum_k x_k^{j_0} \phi_{j_0,k}(y) + \sum_{l=j_0}^{J-1} \sum_k w_k^l \psi_{l,k}(y) \\ E_a(y) &= E_J(y) = \sum_k y_k^J \phi_{J,k}(y) = \sum_k y_k^{j_0} \phi_{j_0,k}(y) + \sum_{l=j_0}^{J-1} \sum_k z_k^l \psi_{l,k}(y) \end{aligned} \tag{B.32}$$

and are decomposed into the trend at level $j_0$, given in terms of the coefficients $y_k^{j_0}$, and into details given in terms of the coefficients $z_k^l$ up to level $J-1$. Then, the product of the two functions is given by

$$\begin{aligned} J_J(y) &= \sigma_J(y) E_J(y) \\ &= \left( \sum_k x_k^{j_0} \phi_{j_0,k}(y) + \sum_{l=j_0}^{J-1} \sum_k w_k^l \psi_{l,k}(y) \right) \left( \sum_m y_m^{j_0} \phi_{j_0,m}(y) + \sum_{n=j_0}^{J-1} \sum_m z_m^n \psi_{n,m}(y) \right) \end{aligned} \tag{B.33}$$

which corresponds to the anomalous current density $J_a = \sigma_a E_a$ and is itself represented as

$$J_J(y) = \sum_k f_k^J \phi_{J,k}(y) = \sum_k f_k^{j_0} \phi_{j_0,k}(y) + \sum_{l=j_0}^{j-1} \sum_k d_k^l \psi_{l,k}(y) \ . \tag{B.34}$$

The coefficients $f_k^j$ and $d_k^l$ are obtained from the inner products

$$\begin{aligned} f_k^{j_0} &= \int_{-\infty}^{\infty} J_J(y)\phi_{j_0,k}(y)dy \\ d_k^l &= \int_{-\infty}^{\infty} J_J(y)\psi_{l,k}(y)dyx \ . \end{aligned} \tag{B.35}$$

The functions are connected via an integral equation of type (B.29) as

$$E_a(y) = \int_{-\infty}^{\infty} J_a(y')K(y,y')dy' + E_n \int_{-\infty}^{\infty} \sigma(y')K(y,y')dy' \tag{B.36}$$

where in the sequel paragraphs I write for notational simplicity $\sigma \equiv \sigma_a$, $J \equiv J_a = \sigma_a E_a$ and $E \equiv E_a$. $K$ is the depth integrated Green's function of E-Polarization multiplied by $-i\omega\mu_0$. The second integral in equation (B.36) is the Born approximation of the anomalous electric field, and the first integral accounts for self-induction. Equation (B.36) involves convolution integrals and is transformed to Fourier space as

$$\hat{E}(\kappa) = \hat{J}(\kappa)\hat{K}(\kappa) + E_n\hat{\sigma}(\kappa)\hat{K}(\kappa) \ . \tag{B.37}$$

The coefficients $y_k^{j_0}$ representing the trend of $E(x)$ at level $j_0$ are obtained from the inner product

$$\begin{aligned} y_k^{j_0} &= \int_{-\infty}^{\infty} E(y)\phi_{j_0,k}(y)dy \qquad (B.38) \\ &= \int_{-\infty}^{\infty} J(y') \int_{-\infty}^{\infty} K(y,y')\phi_{j_0,k}(y)dydy' + E_n \int_{-\infty}^{\infty} \sigma(y') \int_{-\infty}^{\infty} K(y,y')\phi_{j_0,k}(y)dydy' \end{aligned}$$

where the inner integral represents a convolution of the $K-$function with the scaled and translated scaling function. Let me denote $h^*_{j_0,k}(y') = \int_{-\infty}^{\infty} K(y,y')\phi_{j_0,k}(y)dy$ and apply Parseval's theorem

$$\begin{aligned} \int_{-\infty}^{\infty} J(y')h^*_{j_0,k}(y')dx' &= \frac{1}{2\pi}\int_{-\infty}^{\infty} \hat{J}(\kappa)\hat{H}^*_{j_0,k}(\kappa)d\kappa \\ \int_{-\infty}^{\infty} \sigma(y')h^*_{j_0,k}(y')dx' &= \frac{1}{2\pi}\int_{-\infty}^{\infty} \hat{\sigma}(\kappa)\hat{H}^*_{j_0,k}(\omega)d\kappa \end{aligned} \tag{B.39}$$

where

$$\hat{H}^*_{j_0,k}(\kappa) = \hat{K}(-\kappa)\hat{\phi}^*_{j_0,k}(\kappa) \tag{B.40}$$

making use of the convolution theorem and of the the fact, that the real and imaginary part of the scaling and wavelet function in Fourier domain are even and odd, respectively, i.e.,

$$\hat{\phi}_{j_0,k}(-\kappa) = \hat{\phi}^*_{j_0,k}(\kappa) \text{ and } \hat{\psi}_{j_0,k}(-\kappa) = \hat{\psi}^*_{j_0,k}(\kappa) \ . \tag{B.41}$$

Since

$$\begin{aligned} \hat{J}(\kappa) &= \sum_k f_k^{j_0}\hat{\phi}_{j_0,k}(\kappa) + \sum_{l=j_0}^{j-1}\sum_k d_k^l\hat{\psi}_{l,k}(\kappa) \\ \hat{\sigma}(\kappa) &= \sum_k x_k^{j_0}\hat{\phi}_{j,k}(\kappa) + \sum_{l=j_0}^{j-1}\sum_k w_k^l\hat{\psi}_{l,k}(\kappa) \ , \end{aligned} \tag{B.42}$$

the integrals in frequency domain maybe rewritten in terms of the approximation and detail coefficients $f_m^{j_0}$, $x_m^{j_0}$ and $d_m^l$, $w_m^l$, respectively, and lead to

$$\begin{aligned} y_k^{j_0} &= \frac{1}{2\pi}\sum_m \left(f_m^{j_0} + E_n x_m^{j_0}\right) \int_{-\infty}^{\infty} \hat{K}(-\kappa)\hat{\phi}_{j_0,k}^*(\kappa)\hat{\phi}_{j_0,m}(\kappa)d\kappa \\ &+ \frac{1}{2\pi}\sum_{l=j_0}^{j-1}\sum_m \left(d_m^l + E_n w_m^l\right) \int_{-\infty}^{\infty} \hat{K}(-\kappa)\hat{\phi}_{j_0,k}^*(\kappa)\hat{\psi}_{l,m}(\kappa)d\kappa \ . \end{aligned} \tag{B.43}$$

The detail coefficients $z_k^l$ are obtained from the inner product

$$\begin{aligned} z_k^l &= \int_{-\infty}^{\infty} E(y)\psi_{l,k}(y)dy \\ &= \int_{-\infty}^{\infty} J(y')\int_{-\infty}^{\infty} K(y,y')\psi_{l,k}(y)dydy' + E_n\int_{-\infty}^{\infty}\sigma(y')\int_{-\infty}^{\infty} K(y,y')\psi_{l,k}(y)dydy' \end{aligned} \tag{B.44}$$

where the inner integral now represents a convolution of the $K-$function with the scaled and translated wavelet function. Let me denote $D_{l,k}^*(y') = \int_{-\infty}^{\infty} K(y,y')\psi_{l,k}(y)dy$ and again apply Parseval's theorem

$$\begin{aligned} \int_{-\infty}^{\infty} J(y')D_{l,k}^*(y')dy' &= \frac{1}{2\pi}\int_{-\infty}^{\infty}\hat{J}(\kappa)\hat{D}_{l,k}^*(\kappa)d\kappa \\ \int_{-\infty}^{\infty} \sigma(y')D_{d,k}^*(y')dy' &= \frac{1}{2\pi}\int_{-\infty}^{\infty}\hat{\sigma}(\kappa)\hat{D}_{l,k}^*(\kappa)d\kappa \end{aligned} \tag{B.45}$$

where

$$\hat{D}_{l,k}(\kappa) = \hat{G}^*(-\kappa)\hat{\psi}_{l,k}(\kappa) \ . \tag{B.46}$$

Expanding expression (B.44-B.46) leads to

$$\begin{aligned} z_k^l &= \frac{1}{2\pi}\sum_m \left(f_m^{j_0} + E_n x_m^{j_0}\right) \int_{-\infty}^{\infty} \hat{K}(-\kappa)\hat{\psi}_{l,k}^*(\kappa)\hat{\phi}_{j_0,m}(\kappa)d\kappa \\ &+ \frac{1}{2\pi}\sum_{n=j_0}^{j-1}\sum_m \left(d_m^n + E_n w_m^n\right) \int_{-\infty}^{\infty} \hat{K}(-\kappa)\hat{\psi}_{l,k}^*(\kappa)\hat{\psi}_{n,m}(\kappa)d\kappa \ . \end{aligned} \tag{B.47}$$

The integral arising in expressions (B.43) and (B.47) are in the following denoted as

$$\begin{aligned} A_{k,l}^{j_0} &= \frac{1}{2\pi}\int_{-\infty}^{\infty} \hat{K}(-\kappa)\hat{\phi}_{j_0,k}^*(\kappa)\hat{\phi}_{j_0,m}(\kappa)d\kappa \\ B_{k,m}^{j_0,l} &= \frac{1}{2\pi}\int_{-\infty}^{\infty} \hat{K}(-\kappa)\hat{\phi}_{j_0,k}^*(\kappa)\hat{\psi}_{l,m}(\kappa)d\kappa \\ C_{k,m}^{l,j_0} &= \frac{1}{2\pi}\int_{-\infty}^{\infty} \hat{K}(-\kappa)\hat{\psi}_{l,k}^*(\kappa)\hat{\phi}_{j_0,m}(\kappa)d\kappa \\ D_{k,m}^{l,n} &= \frac{1}{2\pi}\int_{-\infty}^{\infty} \hat{K}(-\kappa)\hat{\psi}_{l,k}^*(\kappa)\hat{\psi}_{n,m}(\kappa)d\kappa \end{aligned} \tag{B.48}$$

Then, equations (B.43) and (B.47) can be combined in a matrix equation as

$$\begin{bmatrix} \mathbf{y}^{j_0} \\ \mathbf{z}^l \end{bmatrix} = \begin{bmatrix} \mathbf{A}^{j_0} & \mathbf{B}^{l,n} \\ \mathbf{C}^{j_0} & \mathbf{D}^{l,n} \end{bmatrix} \left( \begin{bmatrix} \mathbf{f}^{j_0} \\ \mathbf{d}^n \end{bmatrix} + E_n \begin{bmatrix} \mathbf{x}^{j_0} \\ \mathbf{w}^n \end{bmatrix} \right) \tag{B.49}$$

The left hand-side of equation (B.49) contains the wavelet coefficients of the anomalous electric field, the right hand-side involves the wavelet coefficients of the anomalous current density and the anomalous conductivity. Let me abbreviate for simplicity

$$\begin{aligned} \mathbf{c}_e &= \begin{bmatrix} \mathbf{y}^{j_0} \\ \mathbf{z}^l \end{bmatrix} \ , \ \mathbf{c}_j = \begin{bmatrix} \mathbf{f}^{j_0} \\ \mathbf{d}^n \end{bmatrix} \ , \ \mathbf{c}_\sigma = \begin{bmatrix} \mathbf{x}^{j_0} \\ \mathbf{w}^n \end{bmatrix} \ , \\ \mathbf{M} &= \begin{bmatrix} \mathbf{A}^{j_0} & \mathbf{B}^{l,n} \\ \mathbf{C}^{j_0} & \mathbf{D}^{l,n} \end{bmatrix} \ . \end{aligned} \tag{B.50}$$

The coefficients of the current density are intrinsically linked with the coefficients of the electric field via Ohm's law. Therefore, from $J = \sigma E$ follows in wavelet domain

$$\mathbf{R}\mathbf{c}_j = (\mathbf{I}\boldsymbol{\sigma})\,\mathbf{e} = (\mathbf{I}\mathbf{W}\mathbf{c}_\sigma)\,(\mathbf{W}\mathbf{c}_e) \ ,$$

and

$$\mathbf{c}_j = (\mathbf{I}\boldsymbol{\sigma})\,\mathbf{e} = \mathbf{R}^{-1}\,(\mathbf{I}\mathbf{W}\mathbf{c}_\sigma)\,(\mathbf{W}\mathbf{c}_e) = \mathbf{U}\mathbf{c}_e \ , \tag{B.51}$$

where $\mathbf{I}$ is the unity matrix, and $\mathbf{R}$ and $\mathbf{W}$ are the wavelet reconstruction and decomposition matrices, respectively (cf. equations (B.6,B.17)). Inserting equality (B.51) into equation (B.49) using abbreviations (B.50) leads to the inhomogeneous linear system of equations

$$\mathbf{c}_e = \mathbf{M}\mathbf{U}\mathbf{c}_e + E_n\mathbf{M}\mathbf{c}_\sigma \tag{B.52}$$

with the Born approximation as source term. Expression (B.52) can be solved for the wavelet coefficients $\mathbf{c}_e$ of the electric field by standard methods similar to the solution of equation (B.26).

## B.5. Computation of integral kernels

The Fourier transform of the wavelet and scaling functions are needed to evaluate the integrals $A, B, C, D$ in equation (B.48). Note that in case of using the Haar wavelet, the integral kernels either vanish or reduce to the Green's function. This leads to the standard evaluation of the integral kernels in the scope of the integral equation by means of a fast Hankel transform, and is not considered further here. Using more complicated wavelets, the wavelet and scaling functions have to be considered explicitely while evaluating the integral. They can, however, readily incorporated in Fourier domain as pointed out below.

Using the dilation and scaling property of the Fourier transform, we obtain from

$$\hat{\phi}_{k,j}(\kappa) = 2^{j/2}\int_{-\infty}^{\infty}\phi\left(2^j y - k\right)e^{-i\kappa y}dy = 2^{-j/2}\hat{\phi}\left(\frac{\kappa}{2^j}\right)e^{-i\kappa k/2^j} \tag{B.53}$$

the following formulae:

$$A^{j_0}_{k,m} = \frac{1}{2\pi}\frac{1}{2^{j_0}}\int_{-\infty}^{\infty}\hat{K}(-\kappa)\hat{\phi}^*\left(\frac{\kappa}{2^{j_0}}\right)\hat{\phi}\left(\frac{\kappa}{2^{j_0}}\right)e^{i\kappa(m-k)/2^{j_0}}d\kappa \tag{B.54}$$

$$B^{j_0,l}_{k,m} = \frac{1}{2\pi}\frac{1}{2^{(j_0+l)/2}}\int_{-\infty}^{\infty}\hat{K}(-\kappa)\hat{\phi}^*\left(\frac{\kappa}{2^{j_0}}\right)\hat{\psi}\left(\frac{\kappa}{2^{l}}\right)e^{i\kappa(k/2^{j_0}-m/2^{l})}d\kappa \tag{B.55}$$

$$C^{l,j_0}_{k,m} = \frac{1}{2\pi}\frac{1}{2^{(j_0+l)/2}}\int_{-\infty}^{\infty}\hat{K}(-\kappa)\hat{\psi}^*\left(\frac{\kappa}{2^{l}}\right)\hat{\phi}\left(\frac{\kappa}{2^{j_0}}\right)e^{i\kappa(k/2^{l}-m/2^{j_0})}d\kappa \tag{B.56}$$

$$D^{l,n}_{k,m} = \frac{1}{2\pi}\frac{1}{2^{(l+n)/2}}\int_{-\infty}^{\infty}\hat{K}(-\kappa)\hat{\psi}^*\left(\frac{\kappa}{2^{l}}\right)\hat{\psi}\left(\frac{\kappa}{2^{n}}\right)e^{i\kappa(k/2^{l}-m/2^{n})}d\kappa \tag{B.57}$$

These integrals may be conceived as inverse Fourier transform and numerically evaluated very efficiently using an inverse FFT.

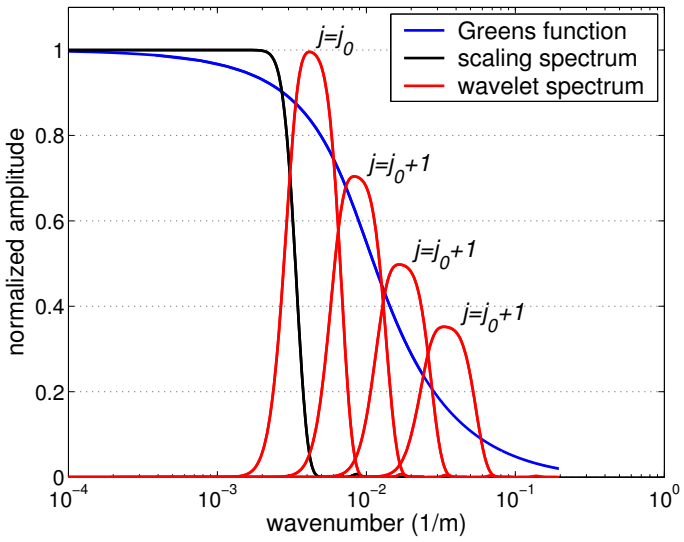


**Figure B.4.:** Normalized wavenumber spectrum of the Green's function, the scaling function of *db12* at level $j_0 = -10$ and wavelet functions *db12* at levels $j = j_0, ..., j_0+3$. Note, that the scaling function is a low-pass, and the wavelets are band-pass filter. The overlap of the spectra is only relevant for a limited number of levels.

**Integral $A_{k,m}^{j_0}$:** The integral $A_{k,m}^{j_0}$ has to be evaluated at scale $j_0$ for a number of dilations $k, m$. If the integrand is numerically evaluated at $N$ values within the range $[-\kappa_{ny}; \kappa_{ny} - \Delta\kappa]$, the inverse FFT yields values at $y_n = [0; (N-1)\pi/\kappa_{ny}]$, sampled at $\Delta y = \pi/\kappa_{ny}$. The result of the integral is then given at position $y_{k,m} = (k-m)/2^{j_0}$, which corresponds to the sample $n = (k-m)\kappa_{ny}/2^{j_0}\pi$, assuming the first sample is indexed with 0. Thus, it is advisable to choose $\kappa_{ny} = \pi 2^{j_0+u}$, $u \epsilon \mathbb{N}$, in order to find $n = (k-m)2^u$ at integers, i.e., every $2^u - th$ sample represents an integer dilation combination. For negative or vanishing$(k-m)$, the relation

$$f(-y) = \frac{1}{2\pi} \int_{-\infty}^{\infty} F(-\kappa) e^{i\kappa y} d\kappa \tag{B.58}$$

may be utilized to obtain $A_{k,m}^{j_0}$ for negative $y$ and$(k-m)$, respectively. However, the integrand of $A_{k,m}^{j_0}$ is an even function in $\kappa$, since the Green's function as well as $\phi^*\phi$ are even, and therefore $A_{k,m}^{j_0}$ is even in $(k-m)$, i.e. $A_{k,m}^{j_0} = A_{m,k}^{j_0}$.

Only a limited number $K$ of coefficients $y_k^{j_0}$ is sought for a given Number $M$ of coefficients $x_m^{j_0}$. Therefore, the integral has to be evaluated at positions $1-K, ..., M-1$, which makes a total number of $M+K-1$ values and thereby determines the spacing $\Delta\kappa$ in Fourier domain. In order to make use of the FFT, we determine the number of points, at which the Kernel of the integral is calculated, to the next higher power of 2 of $(M+K-1)2^u$. Note, that in this particular case, $M = K$, and that in practice, the integral vanishes for high dilation differences $(k-m)$.

**Integral $B_{k,m}^{j_0,l}$:** The integral $B_{k,m}^{j_0,l}$ is required for a number of scale combinations $j_0$; $l = j_0, j_0+1, ..., j-1$. In practice only few $l-$levels have to be considered, since the wavelet in the integrand is a band-pass, and wavelet spectra at high scales do not overlap with the scaling function. The

number of levels $l$ to be taken into account depends on the particular wavelet basis, but is for the wavelet $db12$ not more than $3$. This can be deduced from Figure B.4, where the absolute values of the wavenumber spectra of the vertically integrated Green's function, the scaling and the wavelet functions are depicted, the latter for four scales. Due to the low-pass and band-pass cascades used in the MRA, the overlap between consecutive wavelet spectra or scaling function and wavelet function is small, and only a limited number of adjacent scales contributes to the integrals.

Again, the integral for integer dilations is obtained from an inverse FFT, given now at $y_n = \left(k/2^{j_0} - m/2^l\right)$ corresponding to the sample $n = \left(2^{l-j_0}k - m\right)\kappa_{ny}/2^l\pi$. Selecting $\kappa_{ny} = \pi 2^{l+u}$, we obtain $n = \left(2^{l-j_0}k - m\right)2^u$, i.e., every $2^u - th$ sample represents an integer dilation combination, and among these, samples $\left(2^{l-j_0}k - m\right)$ are needed. For negative $\left(2^{l-j_0}k - m\right)$, the inverse FFT is computed using the relation (B.58), and the integral values are found at $n = -\left(2^{l-j_0}k - m\right)2^u$.

**Integral $C^{l,j_0}_{k,m}$:** The integral $C^{l,j_0}_{k,m}$ is similar to $B^{j_0,l}_{k,m}$, but has now to be evaluated now at $y_{k,m} = \left(k/2^l - m/2^{j_0}\right)$ corresponding to the sample $n = \left(k - 2^{l-j_0}m\right)\kappa_{ny}/2^l\pi$. Selecting $\kappa_{ny} = \pi 2^{l+u}$, $u\epsilon\mathbb{N}$, we obtain $n = \left(k - 2^{l-j_0}m\right)2^u$, i.e., every $2^u - th$ sample represents an integer dilation combination, and among these, samples $\left(k - 2^{l-j_0}m\right)$ are needed. For negative $\left(k - 2^{l-j_0}m\right)$, the inverse FFT is computed using the relation (B.58), and the integral values are the found at $n = -\left(k - 2^{l-j_0}m\right)2^u$.

**Integral $D^{l,n}_{k,m}$:** The integral $D^{l,n}_{k,m}$ has to be evaluated for a number of level combinations $l = j_0, j_0+1, ..., J$ and $n = j_0, j_0+1, ..., J$ and dilation combinations $\left(k/2^l - m/2^n\right)$. Because of the bandpass characteristic of the wavelet spectra, only neighboring levels $n = l \pm 1, l \pm 2, ...$ contribute to the integral at a given level $l$. For a given $l$, the inverse FFT is computed from the integral kernel, i.e.,

$$d\left(y\right) = F^{-1}\left\{\frac{1}{2^{(l+n)/2}}K(-\kappa)\hat{\psi}^*\left(\frac{\kappa}{2^l}\right)\hat{\psi}\left(\frac{\kappa}{2^n}\right)\right\}$$

and the sought result for an dilation combination is found at $y_{k,m} = \left(k/2^l - m/2^n\right)$. If $l \geq n$, we choose $\kappa_{ny} = \pi 2^{l+u}$, and the integral value is found at sample $n = \left(k - 2^{l-n}m\right)2^u$. On the other hand, if $l < n$ we choose $\kappa_{ny} = \pi 2^{n+u}$, but the integral value is now found at sample $n = \left(2^{n-l}k - m\right)2^u$.

- **Example:** Let $l = -10$ , $N = 2^9$, $u = 4$. Then, $\kappa_{ny} = \pi/2^6$ and $\Delta\kappa = \pi/2^{14}$. Assume, that a similar wavelet to the one used in Figure B.4 is used. So, the Kernel is sampled at $\kappa$=$\pi/2^{14}$ within $[-\pi/2^6; \pi/2^6 - \Delta\kappa]$. Note, that at level $-10$, $\hat{\psi}_{-10}\left(\kappa\right)$ approximately vanishes for wavenumber $|\kappa| > \pi/2^8$, i.e. the main lobe of the wavelet spectrum is in the interval $[-\pi/2^8; \pi/2^8]$. (The first side-lobe is in the interval $\pi/2^7 > |\kappa| > \pi/2^8$, the second within $\pi/2^6 > |\kappa| > \pi/2^7$, etc.. Compare also with Figure B.4.)

1. Assume $l - n = 0$: Then, every $2^u - th$ sample in $m-$ and $k-$direction is taken. Denote the first sample with $0$, the $1 * 2^u - th$ with $1$, the $2 * 2^u-$ sample with $2$ etc., then the

matrix $D$ is filled according to

$$D^{l,l}_{k,m} = (k-m)\,2^u = d\left(\begin{bmatrix} 0 & -1 & -2 & \cdots & -(M-1) \\ 1 & 0 & 1 & & \\ 2 & 1 & 0 & & \\ \vdots & & & \ddots & \\ K-1 & & & & 0 \end{bmatrix} 2^u\right)$$

2. Assume $l-n=1$: Then, every $2^{u-1}-th$ sample in $m-$ and $2^u-th$ sample in $k-$direction is taken. Denote the first sample with $0$, the $1*2^u-th$ with $1$, the $2*2^u-$ sample with $2$ etc., then the matrix $D$ is filled according to

$$D^{l,n}_{k,m} = (k-2m)\,2^u = d\left(\begin{bmatrix} 0 & -2 & -4 & \cdots & -2(M-1) \\ 1 & -1 & -3 & & \\ 2 & 0 & -2 & & \\ \vdots & & & \ddots & \\ K-1 & & & & \end{bmatrix} 2^u\right)$$

3. Assume $n-l=1$: Then, every $2^{u-1}-th$ sample in $m-$ and $2^u-th$ sample in $k-$direction is taken. Denote the first sample with $0$, the $1*2^{u-1}-th$ with $1$, the $2*2^{u-1}-$ sample with $2$ etc., then the matrix $D$ is filled according to

$$D^{l,n}_{k,m} = (m-2k)\,2^u = d\left(\begin{bmatrix} 0 & -1 & -2 & \cdots & -(M-1) \\ 2 & 1 & 0 & & \\ 4 & 3 & 2 & & \\ \vdots & & & \ddots & \\ 2(K-1) & & & & \end{bmatrix} 2^u\right)$$

4. Equivalently, matrix $D^{l,n}_{k,m}$ is constructed for $|l-n|>1$.

## B.6. Outlook

In the previous sections, the electromagnetic integral equation has been reformulated in terms of wavelet coefficients of the electric field and the conductivity distribution. In the derivation, I used the same wavelet to represent both functionals which is on a first sight convenient, but it is not necessary to do so. Note, that it was not necessary to specify the wavelet basis explicitely. Furthermore, it is not necessary to use orthogonal wavelets as I did. Using bi-orthogonal wavelets could also be a good choice, without changing the formulas in principle. Therefore, a general formulation of the integral equation solution has been established. It remains of course to justify the approach suggested here. In the scope of this work, I can only sketch some ideas.

The major impact of wavelets are its compression capabilities. This means, that in general less wavelet coefficients are necessary to represent functions than function values itself. This has been demonstrated in Figure (B.1) using a smooth function and a smooth wavelet. Therefore, it may be believed, that the size of the linear equation (B.52) of the electric field coefficients may be dramatically reduced, if the solution is only sought for significant coefficients. Unfortunately, the

significant coefficients are not known a priori. A possible strategy to circumvent this problem is to solve the linear system iteratively, starting at a course level, i.e. a high compression, and consecutively refine the solution while only keeping coefficients larger than a threshold. Then, the refined solution could be concentrated on areas, where a fine solution is required (which will be the case in the vicinity of large conductivity gradients).

A second advancement arises from the interpolation properties of wavelets itself. Using B-spline wavelets, for example, implies a spline-interpolation between function samples. It is evident, that a true field distribution could be approximated in a much more efficient way using spline functions instead of using piecewise constant functions as is done in the common solution of the integral equation. This property again leads to a reduction of the size of the system of linear equations and therefore to shorter computation times.

The wavelet representation could, thirdly, also be helpful in inverse calculations and sensitivity analysis. In sensitivity analysis, one investigates the effect of a small model parameter variation on the model response. The most simple way to accomplish this is to disturb the conductivity at one point (or within one cell), and consider the difference of the undisturbed and disturbed mode response as a measure of the sensitivity. Thus, the sensitivity to the change of the total value of one(!) cell is determined. In the scope of the wavelet representation, one can proceed one step further. Consider for instance a Haar decomposition of the conductivity structure, with the decomposition coefficients contained in the data vector $\mathbf{c}_\sigma$ in equation (B.52). These coefficients represent simply the mean of the conductivity function, taken on a certain distance determined by the level of decomposition, and the spatial fluctuations of the conductivity at different spatial scales (i.e. the detail coefficients). Manipulation of a detail coefficient yields a disturbed model response, which in comparison with the undisturbed model response can be considered as the sensitivity to a spatial change of the conductivity on a certain scale. It is deducible, that in a MT measurement, the sensitivity of the surface fields to small-scale conductivity changes in the deeper subsurface is small. By means of the wavelet transformation representation, a direct measure is given in terms of the sensitivity of the fields with respect to the detail coefficients of the conductivity function. Therefore, in inverse calculations, it will turn out, that less and less detail coefficients are required to represent the conductivity function with increasing depth. The resulting model will then be a smooth model, with increased smoothness in areas, in which spatial fluctuations do not affect the surface fields.

Only few possible applications of the novel approach have been outlined above. Though easily described, their numerical implementation is a difficult task, which was not accomplished in the time limit of this work.